Topics in Current Chemistry 348

Massimo Marcaccio
Francesco Paolucci *Editors*

Making and Exploiting Fullerenes, Graphene, and Carbon Nanotubes

Springer

348
Topics in Current Chemistry

Aims and Scope

The series Topics in Current Chemistry presents critical reviews of the present and future trends in modern chemical research. The scope of coverage includes all areas of chemical science including the interfaces with related disciplines such as biology, medicine and materials science.

The goal of each thematic volume is to give the non-specialist reader, whether at the university or in industry, a comprehensive overview of an area where new insights are emerging that are of interest to larger scientific audience.

Thus each review within the volume critically surveys one aspect of that topic and places it within the context of the volume as a whole. The most significant developments of the last 5 to 10 years should be presented. A description of the laboratory procedures involved is often useful to the reader. The coverage should not be exhaustive in data, but should rather be conceptual, concentrating on the methodological thinking that will allow the non-specialist reader to understand the information presented.

Discussion of possible future research directions in the area is welcome.

Review articles for the individual volumes are invited by the volume editors.

Readership: research chemists at universities or in industry, graduate students.

More information about this series at
http://www.springer.com/series/128

Massimo Marcaccio • Francesco Paolucci
Editors

Making and Exploiting Fullerenes, Graphene, and Carbon Nanotubes

With contributions by

P. Bachawala · L. Ballerini · M. Bonchio · S. Bosi ·
E. Cadelano · S. Campidelli · L. Colombo ·
C. Degli Esposti Boschi · F. D'Souza · A. Filoramo ·
P. Fornasiero · G. Gavrel · D.R. Jones · B. Jousselme ·
L. Kavan · W. Kutner · J. Mack · A. Mateo-Alonso ·
M. Melchionna · A. Migliori · V. Morandi · L. Ortolani ·
F. Paolucci · A. Pénicaud · M. Prato · P.S. Sharma

Springer

Editors
Massimo Marcaccio
Francesco Paolucci
Dept. of Chemistry G. Ciamician
University of Bologna
Bologna
Italy

ISSN 0340-1022 ISSN 1436-5049 (electronic)
ISBN 978-3-642-55082-9 ISBN 978-3-642-55083-6 (eBook)
DOI 10.1007/978-3-642-55083-6
Springer Heidelberg New York Dordrecht London

Library of Congress Control Number: 2014947108

© Springer-Verlag Berlin Heidelberg 2014
This work is subject to copyright. All rights are reserved by the Publisher, whether the whole or part of the material is concerned, specifically the rights of translation, reprinting, reuse of illustrations, recitation, broadcasting, reproduction on microfilms or in any other physical way, and transmission or information storage and retrieval, electronic adaptation, computer software, or by similar or dissimilar methodology now known or hereafter developed. Exempted from this legal reservation are brief excerpts in connection with reviews or scholarly analysis or material supplied specifically for the purpose of being entered and executed on a computer system, for exclusive use by the purchaser of the work. Duplication of this publication or parts thereof is permitted only under the provisions of the Copyright Law of the Publisher's location, in its current version, and permission for use must always be obtained from Springer. Permissions for use may be obtained through RightsLink at the Copyright Clearance Center. Violations are liable to prosecution under the respective Copyright Law.
The use of general descriptive names, registered names, trademarks, service marks, etc. in this publication does not imply, even in the absence of a specific statement, that such names are exempt from the relevant protective laws and regulations and therefore free for general use.
While the advice and information in this book are believed to be true and accurate at the date of publication, neither the authors nor the editors nor the publisher can accept any legal responsibility for any errors or omissions that may be made. The publisher makes no warranty, express or implied, with respect to the material contained herein.

Printed on acid-free paper

Springer is part of Springer Science+Business Media (www.springer.com)

Preface

Carbon nanostructures, or nanocarbons (CNSs), i.e. the low-dimensional nanomaterials that comprise 0D fullerenes, 1D nanotubes and 2D graphene, have emerged over the last two decades in the field of new molecular materials for their unique structural and electronic properties, prompting a huge interest worldwide both from the viewpoint of fundamental research and for their application in molecular electronics, materials science, energy storage and conversion, biomedicine, sensing and biosensing. The electronic properties of CNSs and their optical, spectroscopic and electrochemical behaviour depend markedly on their characteristic nanometric dimensions; the identification of specific quantities relative to individual nanostructures in the bulk phase has proved challenging and has required extreme ingenuity. Making solutions (or suspensions) of CNSs where the nanostructures could retain most of their pristine properties has been a prerequisite for either fundamental investigation or for the development of any viable technological exploitation of such properties. This was the case, for example, of the application of bandgap fluorescence spectroscopy of aqueous, micelle-like suspensions of single-walled carbon nanotubes (SWNTs) that has given access to the electronic energies of individual semiconducting SWNTs as a function of structure diameter and helicity. In such a context, the chapter “Solubilization of Fullerenes, Carbon Nanotubes and Graphene” by Alain Pénicaud describes the various ingenious approaches to solve the solubility issue and describes in particular how graphite, and modern nanocarbons, can be made soluble by reductive dissolution. A large part of the present volume concerns the merging of nanocarbons with nanotechnology and their impact on technical development in many areas. Fullerenes, carbon nanotubes, nanodiamond and graphene find, for instance, various applications in the development of solar cells, including dye sensitized solar cells. The chapter “Incorporation of Balls, Tubes and Bowls in Nanotechnology” by James Mack describes the recent development of the area of fullerene fragments, and corannulene in particular, and their direct applications to organic light emitting diode (OLED) technology, while, in the chapter “Exploiting Nanocarbons in Dye-Sensitized Solar Cells” by Ladislav Kavan, the exploitation of nanocarbons in the development of novel dye sensitized solar cells with improved efficiency, durability and costs is thoroughly reviewed.

The functionalization of CNSs has the invaluable advantage of combining their unique properties with those of other classes of materials. Supramolecular chemistry represents an elegant alternative approach for the construction of functional systems by means of noncovalent bonding interactions. In the chapter “Supramolecular Chemistry of Carbon Nanotubes” by Gildas Gavrel et al., the incredibly varied world of supramolecular, non-covalent functionalization of carbon nanotubes and their applications is examined and reviewed, and the synthetic strategies devised for fabricating mechanically-linked molecular architectures are described in the chapter “Fullerene-Stoppered Bistable Rotaxanes” by Aurelio Mateo-Alonso, which presents an overview of the different types of fullerene-stoppered bistable rotaxanes, their switching mechanism and their potential applications.

In the chapter “Catalysis-Material Crosstalk at Tailored Nano-Carbon Interfaces” by Michele Melchionna et al., carbon nanomaterials are described as supports for molecular and nanostructured catalysts, where their outstanding electronic and optical properties, high surface area and thermal and mechanical stability contribute to create a synergistic effect that leads to enhanced performance for a wide range of possible applications. Exploitation of nanocarbons in biology and biomedical applications has been increasingly proposed and, in particular, the chapter “Carbon Nanotubes in Tissue Engineering” by Susanna Bosi et al. explores applications of CNTs for tissue engineering purposes, where the tubes proved to be ideal materials for the growth and proliferation of many kind of tissues.

The local chemical reactivity, the mechanical properties and the electron transfer in graphene membranes have been shown to be strongly affected by the fold-induced curvature; thus in the chapter “Folds and Buckles at the Nanoscale: Experimental and Theoretical Investigation of the Bending Properties of Graphene Membranes” by Vittorio Morandi, a novel methodology to investigate the mechanical properties of folded and wrinkled graphene crystals, which combine transmission electron microscopy mapping and theoretical modelling, is described. Graphene and nanocarbons in general are intensively investigated as platforms for the development of sensing devices for the selective and highly sensitive detection of biohazards. The aim of the chapter “Graphene and Graphene Oxide Materials for Chemo- and Biosensing of Chemical and Biochemical Hazards” by Piyush Sindhu Sharma et al. is then to bring out important advances of graphene-based sensors, with particular attention to the rapid detection and quantization of toxins, explosives, pesticides and pathogens.

Because of the several and diverse technological applications so far proposed, and of the many more expected in the near future, the present volume is addressed to researchers from several different areas: chemistry and materials chemistry, nanotechnology, medicine and industrial research. We hope they will enjoy the presentations and find inspiration for their research activity in the fascinating field of nanocarbons.

Finally, we would like to thank Prof. Margherita Venturi who, as a member of the Editorial Board of Topics in Current Chemistry, promoted the preparation of a volume on this subject.

Bologna, Italy
November 2013

Massimo Marcaccio
Francesco Paolucci

Contents

Top Curr Chem (2014) 348: 1–36
DOI: 10.1007/128_2013_520

Solubilization of Fullerenes, Carbon Nanotubes, and Graphene

Alain Pénicaud

Abstract Processing of novel carbon forms, i.e. fullerenes, nanotubes and graphene, in solution is described. C_{60} and higher fullerenes appear to be the only truly soluble forms of pure carbon. Ways to disperse carbon nanotubes and graphene are reviewed. True solutions of carbon nanotubes and graphene can be obtained by reductive dissolution, leading to solution of polyelectrolyte nanocarbons of high concentrations without damaging the nanocarbon. Finally it is shown that these solutions allow to obtain high performing materials such as highly conducting transparent electrodes.

Keywords C_{60} · Carbon · Dissolution · Entropy · Fullerenes · GIC · Graphene · Graphenide · Graphite · Individualization · Nanotube salts · Nanotubes · Nanotubide · Solutions

Contents

A. Pénicaud (✉)
CNRS, Centre de Recherche Paul Pascal (CRPP), Université de Bordeaux, UPR 8641,
Pessac 33600, France
e-mail: penicaud@crpp-bordeaux.cnrs.fr

Abbreviations

AFM	Atomic force microscopy
CNT	Carbon nanotube
CoMoCAT	Process in which carbon nanotubes are synthesized with Co/Mo catalysts
DMSO	Dimethylsulfoxide
GIC	Graphite intercalation compound
GO	Graphene oxide
HiPCO	High pressure carbon monoxide process to synthesize carbon nanotubes
HOPG	Highly ordered pyrolytic graphene
NMP	*N*-Methylpyrrolidone
PAH	Polyaromatic hydrocarbon
RGO	Reduced graphene oxide
SCE	Standard calomel electrode
SEM	Scanning electron microscopy
SWCNT	Single-wall carbon nanotube
TEM	Transmission electron spectroscopy
THF	Tetrahydrofuran

1 Introduction

Excluding metallic elements, carbon is one of the few elements of the Periodic Table that has led to many fundamentally important materials. Unlike metals, carbon exhibits a variety of valence topology, depending on its hybridization sp, sp^2, or sp^3, and even intermediate hybridization. This has led to an amazing variety of nature, appearance, and properties within carbon materials. Let’s mention graphite and diamond, the former opaque, slippery, and conducting, the latter transparent, hard, and insulating. Important carbon materials are not restricted to graphite and diamond.

Carbon fibers and carbon black, which can be considered disordered forms of graphite, have a tremendous industrial importance in modern materials and composites [1]. Since the 1990s and 2000s, novel forms of carbon, often quoted now as nanocarbons, have emerged. They are the subject of this book: fullerenes, graphene, and carbon nanotubes.

One property that all carbon materials (apart from fullerenes) share is that they are insoluble. Why is solubility important? Solubility allows for easier and safer handling and processing. This chapter deals with solubilizing carbons. We will see that the molecular form of carbon, C_{60} and the other fullerenes are all soluble but that the larger carbon nanoforms, such as nanotubes and graphene, are not. We will see in this chapter how graphite and modern nanocarbons can be made soluble by *reductive dissolution*. In reductive dissolution, the carbon form is reduced, to make a salt, that salt being spontaneously soluble in polar organic solvents.

1.1 Size Is Important

The insolubility of nanocarbons has to do with size. That leads to the question of the fundamental unit in each carbon material, its size or molecular formula, its weight, and its chemical nature (Sect. 2). When it comes to solubility, the prototypical nanocarbon, the C_{60} molecule [2] and its analogs, the whole family of fullerenes, are different. They are indeed soluble and form the first truly soluble form of carbon [3]. They will be discussed in Sect. 3. All other forms of carbon are insoluble. Section 4 will review the varied strategies that have been designed to overcome this shortcoming. One can look at nanocarbons (carbon nanotubes and graphene) as macromolecules and see the implications about solubility. Thermodynamics can be advantageously used to promote true dissolution of macromolecules. By electrically charging nanotubes, i.e., by reduction or oxidation, charged macromolecules, i.e., polyelectrolytes, are obtained and those are found to be soluble in some organic solvents [4]. The resulting, soluble, nanotube salts are shown to be individualized in solution [5], allowing for easy processing, while keeping length integrity of the nanotubes, hence allowing for better performance/content ratio in composites. This will be the central subject of this chapter. The rationale, history, and procedure of reductive dissolution will be described in Sect. 5. Graphene has risen as the next ever-promising material. Section 6 is devoted to graphene solubilization, put in perspective with the other ways of obtaining graphene or so-called graphene. The only prerequisite for the reductive dissolution is the possibility to reduce (n-dope) nanocarbons. This has been found to be applicable to forms of carbon other than nanotubes or graphene, for examples, carbon nanohorns or nanocups, and will be described in Sect. 7. Oxidation (in the sense of p-doping) has been much less explored than reduction for nanocarbon dissolution. State of the art of the field will be described in Sect. 8. In Sect. 9, uses of reductive dissolution will be described, be it for controlled functionalization, catalysis, materials processing, etc., all the way to the recent commercialization of nanotubide inks.

2 From Diamond and Graphite to Nanocarbons or Nanocarbon Size Vs Solubility

Diamond crystal structure was determined in 1914 by Henry Bragg and Laurence Bragg, father and son [6]. Each carbon atom is in sp3 hybridization, and is tetrahedrally coordinated to four equivalent carbon atoms (Fig. 1). Diamond is thus an infinite molecule in all three directions forming a solid. Hence, there is no way that one could dissolve diamond. However, carbon nanoparticles with internal diamond structure, i.e., nanodiamonds, can be made soluble [7]. In nanodiamonds, volume is greatly reduced, and the surface, which is only a negligible defect in bulk diamond, acquires importance and the interaction between solvent and surface will lead or not lead to nanodiamond dissolution.

Graphite, although bulk, is made by the stacking in the third direction of two-dimensional sheets of *graphene* (Fig. 1). Covalent bonds govern the cohesion within a graphene plane whereas van der Waals interactions are responsible for intergraphene cohesion. The fundamental unit is then a graphene layer and we'll see that a graphene layer, if electrically charged, can indeed be dissolved. Likewise, fullerite and carbon nanotube soot are three dimensional arrangements of 0D fullerenes and 1D nanotubes (Fig. 1) where the fundamental nanocarbon can be dissolved, by reductive dissolution in the case of nanotubes.

2.1 Some Nomenclature

C_{60} was originally dubbed buckminsterfullerene since its structure was reminiscent of the geodesic constructions of the late architect R. Buckminsterfuller. That led to the nickname buckyball and the family of fullerenes. The correct, recommended name (IUPAC Gold book) is [60]fullerene. Logically, fullerenes soot was quoted as fullerite, fullerene ions were fullerides and fullereniums [10]. Nanotubes were first called helical microtubules of graphitic carbon [11], buckytubes, but soon enough, "nanotubes" became their name. Their anions have long been called nanotube salts. Recently, Shaffer, Skipper et al. proposed the term nanotubide [12] for the (poly) anion and likewise nanotubium for the (poly)cation [13]. Graphene was named long before it was ever isolated, since it was already a useful concept as either the fundamental unit plane of graphite or as the infinite limit of polyaromatic molecules. When reduced or oxidized, graphite leads to graphite intercalation compounds (GICs) [14], called either donor-GICS or acceptor-GICS, depending whether the intercalated species respectively donates electron to (as in KC_8) or accepts electrons from graphite. The recommended name for the corresponding, reduced, graphene sheet is graphenide [15, 16]. For the more exotic forms of carbon, the reader is referred to a recent essay on nanocarbon naming [17].

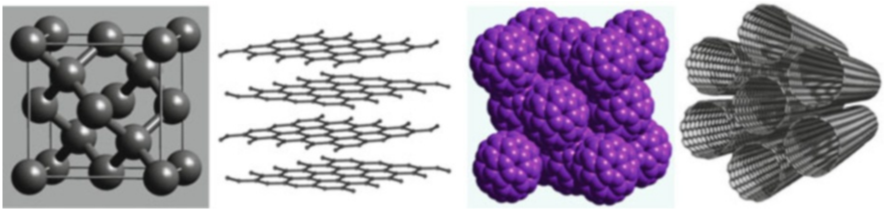

Fig. 1 Main carbon allotropes. From *left* to *right*: *Diamond* is a three dimensional covalently bonded solid (image from [8]). *Graphite* is made of the stacking of *graphene* sheets (image from Wikimedia). *[60]Fullerenes* pack in a cubic face centered lattice to form *fullerite* (image by Boris Pevzner). Single-walled carbon *nanotubes* packed in a bundle (image from [9])

Fig. 2 The C_{60} molecule

3 The Special Case of C_{60}

C_{60} created a surprise in 1985 when it was first observed [2] in a mass spectrum of 720 daltons (60 carbon atoms) and intellectually conceived (although some earlier reports have been spotted since then). In 1991, C_{60} was synthesized in "bulk" quantities (a few tens of milligrams in the first report) and was thus made available to the scientific community [3]. As C.A. Reed wrote, "It is truly remarkable that a new allotrope of carbon, especially one of such structural elegance, should appear this late in the exploration of the chemistry of the stable elements" [18]. C_{60} is a truncated icosahedron, made of 60 atoms (Fig. 2). All these atoms are equivalent as seen by the single NMR ^{13}C peak of C_{60} at 143 ppm [19]. With C_{60} came a whole family of *higher fullerenes*, C_{76}, C_{78}, C_{84}; see, for example, [20, 21]—they are all composed of 12 pentagons and a varying number of hexagons. They come as different isomers, depending on the topology of the pentagons. They are all allotropic forms of carbon.

C_{60} was the first soluble form of carbon. As neutral, pristine species, only C_{60} and its higher analogs, the fullerenes, are soluble species. It's actually because it was soluble in some organic solvents that Krätschmer, Huffman and colleagues

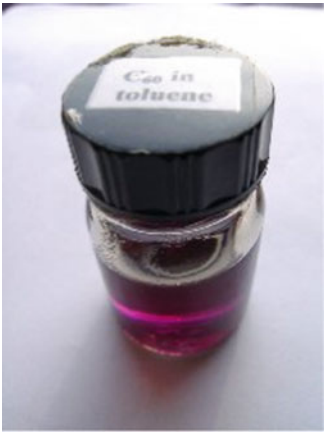

Fig. 3 A solution of C_{60}, the first ever soluble form of carbon (picture Jonathan Hare)

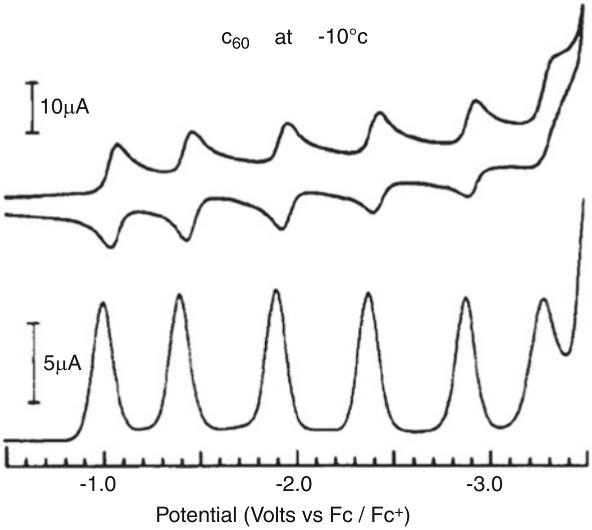

Fig. 4 Reversible electro-reduction of C_{60} observed by cyclic voltammetry (*top*) and differential pulse voltammetry (*bottom*) in CH_3CN/toluene at −10°C [24]

were able to extract C_{60} and some higher fullerenes in benzene from the remaining graphitic soot that composed 95% of their initial material [3]. Dissolving C_{60} yields a magenta colored solution (Fig. 3). Soon after the first isolation of C_{60}, UV–vis [22] and 13C NMR [19] solution spectra were recorded. Cyclic voltammograms followed [23], culminating in the record of six reversible reduction waves (Fig. 4) [24] and two oxidation process [25]. Tables have been published of C_{60} solubility in organic solvents (see Table 1).

Table 1 Solubility of C_{60} in various solvents (from [26])

Solvent	C_{60} (mg/mL)	mole fraction ($\times 10^4$)	n	ε	V ($cm^3\ mol^{-1}$)	δ ($cal^{1/2}\ cm^{-3/2}$)
Alkanes						
n-Pentane	0.005	0.008	1.36	1.84	115	7.0
Cyclopentane	0.002	0.003	1.41	1.97	93	8.6
n-Hexane	0.043	0.073	1.38	1.89	131	7.3
Cyclohexane	0.036	0.059	1.43	2.02	108	8.2
n-Decane	0.071	0.19	1.41	1.99	195	8.0
Decalins	4.6	9.8	1.48	2.20	154	8.8
cis-Decalin	2.2	4.6	1.48	–	154	8.8
trans-Decalin	1.3	2.9	1.47	–	158	8.6
Haloalkanes						
Dichloromethane	0.26	0.27	1.42	9.08	60	9.7
Chloroform	0.16	0.22	1.45	4.81	86	9.3
Carbon tetrachloride	0.32	0.40	1.46	2.24	80	8.6
1,2-Dibromoethane	0.50	0.60	1.54	4.79	72	10.4
Trichloroethylene	1.4	1.7	1.48	3.40	89	9.2
Tetrachloroethylene	1.2	1.7	1.51	2.46	102	9.3
Freon TF (dichorodifluoroethane)	0.020	0.042	1.36	–	188	–
1,1,2-Trichlorotrifluoroethane	0.014	0.017	1.44	–	118	–
1,1,2,2-Tetrachloroethane	5.3	7.7	1.49	8.20	64	9.7
Polars						
Methanol	0.000	0.000	1.33	33.62	41	14.5
Ethanol	0.001	0.001	1.36	24.30	59	12.7
Nitromethane	0.000	0.000	1.38	35.90	81	12.7
Nitroethane	0.002	0.002	1.39	28.00	105	11.1
Acetone	0.001	0.001	1.36	20.70	90	9.8
Acetonitrile	0.000	0.000	1.34	37.50	52	11.8
N-Methyl-2-pyrrolidone	0.89	1.2	1.47	–	96	11.3

(continued)

Table 1 (continued)

Solvent	C_{60} (mg/mL)	mole fraction ($\times 10^4$)	n	ε	V ($cm^3\ mol^{-1}$)	δ ($cal^{1/2}\ cm^{-3/2}$)
Benzenes						
Benzene	1.7	2.1	1.50	2.28	89	9.2
Toluene	2.8	4.0	1.50	2.44	106	8.9
Xylenes	5.2	8.9	1.50	2.40	123	8.8
Mesitylene	1.5	3.1	1.50	2.28	139	8.8
Tetralin	16	31	1.54	11.50	103	10.7
o-Cresol	0.014	0.029	1.54	11.50	103	10.7
Benzonitrile	0.41	0.71	1.53	25.60	97	8.4
Fluorobenzene	0.59	0.78	1.47	5.42	94	9.0
Nitrobenzene	0.80	1.1	1.56	35.74	103	10.0
Bromobenzene	3.3	4.8	1.56	5.40	105	9.5
Anisole	5.6	8.4	1.52	4.33	109	9.5
Chlorobenzene	7.0	9.9	1.52	5.71	102	9.2
1,2-Dichlorobenzene	27	53	1.55	9.93	113	10.0
1,2,4-Trichlorobenzene	8.5	15	1.57	3.95	125	9.3
Naphthalenes						
1-Methylnaphthalene	33	68	1.62	2.92	142	9.9
Dimethylnaphthalenes	36	78	1.61	2.90	156	9.9
1-Phenylnaphthalene	50	131	1.67	2.50	155	10.0
1-Chloronaphthalene	51	97	1.63	5.00	136	9.8
Miscellaneous						
Carbon disulfide	7.9	6.6	1.63	2.64	54	10.0
Tetrahydrofuran	0.000	0.000	1.41	7.60	81	9.1
Tetrahydrothiophene	0.030	0.036	1.50	2.28	88	9.5
2-Methylthiophene	6.8	9.1	1.52	2.26	96	9.6
Pyridine	0.89	0.99	1.51	12.30	80	10.7

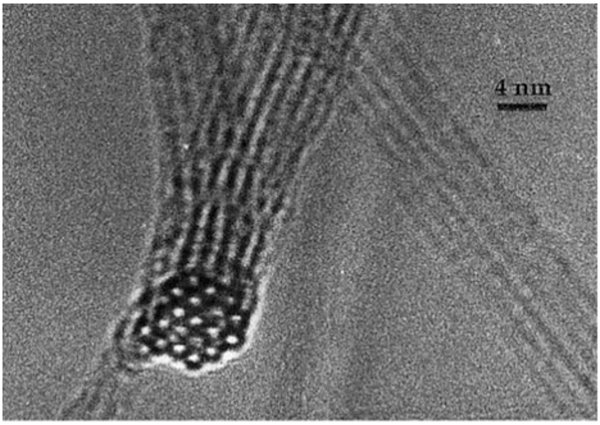

Fig. 5 High resolution transmission electron microscopy view of a bundle of single-walled carbon nanotubes. Image from [29]

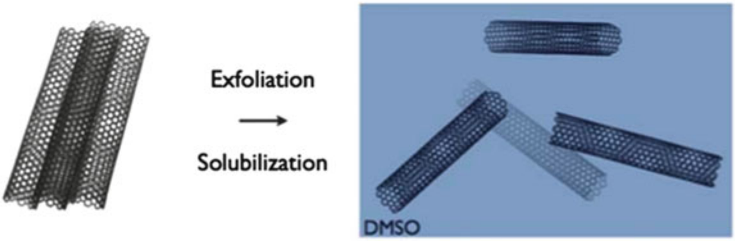

Fig. 6 Exfoliation of a bundle of SWCNTs into individualized nanotubes (from [31])

4 Strategies to Disperse Carbon Nanotubes

The beginning of the 1990s was an exciting time for carbon science. At the same time than C_{60} was made available as a compound, carbon nanotubes were observed in a transmission electron microscope, at first as multiwalled carbon nanotubes [11], later as single-walled carbon nanotubes [27, 28]. A few years afterwards, they also became available in “bulk” quantities through their synthesis by electric arc discharge [29] and laser ablation [30], the same techniques that had been used for C_{60} but with some catalyst added. Single-walled carbon nanotubes come in bundles (Fig. 5), much the same way graphene is stacked to form graphite. The fundamental unit to dissolve is thus one *single-walled nanotube* by separating it from its congeners (Fig. 6).

Nanotubes have roughly the same diameter as fullerenes (ca 1 nm) but they are 1,000 times longer on average (Fig. 7). As alluded to earlier, they can be considered as macromolecules, polydisperse in size, of molecular weight of the order of 1,000,000 daltons. Given the extraordinary properties of carbon nanotubes, in

Fig. 7 A model at scale of C_{60} and a CNT with L/D = 120. A real CNT might have an L/D ratio up to 20,000

Table 2 Dry extract from nanotube dispersions (see text and [34] for the dispersing protocol[a])

Solvent	mg L^{-1}
1,2-Dichlorobenzene	95
Chloroform	31
1-Methylnaphthalene	25
1-Bromo-2-methylnaphthalene	23
N-Methylpyrrolidinone	10
Dimethylformamide	7.2
Tetrahydrofuran	4.9
1,2-Dimethylbenzene	4.7
Pyridine	4.3
Carbon disulfide	2.6
1,3,5-Trimethylbenzene	2.3
Acetone	–[b]
1,3-Dimethylbenzene	–[b]
1,4-Dimethylbenzene	–[b]
Ethanol	–[b]
Toluene	–[b]

[a] The sonicator bath water temperature rose to ca 35°C over the course of 1 h

[b] Solubility in these solvents was <1 mg L^{-1}

particular mechanical and electrical properties, recognized from the very beginning and later optical, there was a strong driving force for dispersing carbon nanotubes, since they were found to be insoluble.

4.1 Dispersions in Organic Solvents

This is the simplest way to disperse carbon nanotubes. By sonicating them in a solvent, one is able to get a colored metastable suspension. Very early on in the field, it was found that SWCNTs disperse in amide solvents such as dimethylformamide (DMF) or *N*-methyl-pyrrolidone (NMP) [32–34]. A systematic screening of solvents for nanotube dispersion was published in 2001 (Table 2) [34]. Apparently better than NMP or DMF, several “fullerene-dissolving solvents” appear such as Me-naphthalene or 1,2-dichlorobenzene. Perhaps more surprisingly, chloroform is listed as a good dispersing solvent for nanotubes. Although this table gives an idea of solvents with better affinity for the graphenic surface of nanotubes, two points are worth noting: (1) reported “concentrations” are of the order or 10 mg/L, about 100–500 times less than what can be achieved with solutions of nanotube salts (cf. Sect. 5); (2) the suspensions are reported to reaggregate after ca 4 h to 3 days. This field of research is still active with papers appearing regularly [35–38].

4.2 Aqueous Suspensions

Likewise, SWCNTs were dispersed in water with the help of surfactants and sonication as early as 1998 [39]. Despite inherent metastability and the need for a stabilizing agent, this field has drawn a lot of attention due to simplicity, ease, and the fact that the solvent is water. Recent reviews can be consulted [40]. Noteworthy is the fact that bile salts surfactants dissolve SWCNTs without the need for sonication [41]. Water-based surfactant suspensions are also the basis for SWCNT sorting [42] via ultracentrifugation [43].

5 Reductive Dissolution of Nanotubes

While C_{60} is soluble, CNTs are not. We have seen in the preceding section that they can be dispersed in a liquid phase using sonication to obtain metastable systems. Inspiration to circumvent this problem came from outside the carbon world: $M_2Mo_6Se_6$ are inorganic solids made of infinite, polymeric chains of formula $(Mo_3Se_3\text{-})_\infty$. Electro-neutrality is assured by the counter ion M^+. In the case of Li^+, and to a lesser extent Na^+, exposure of $M_2Mo_6Se_6$ to polar solvents such as DMSO (or water) leads to swelling of the solid, forming first a gel and ultimately a solution [44]. Individual, rigid, polymeric chains of $(Mo_3Se_3^-)_\infty$ have been identified as the solute in those stable solutions. Nanotubes can be seen as similar rigid polymeric chains. Electrically charging them was no problem since doped nanotubes had been prepared soon after the discovery of nanotubes in order to explore their electronic properties [45, 46]. Lithium salts of nanotubes were prepared following the recipe of Petit et al. [49] and exposed to polar solvents, similar to solvents that dissolved $Li_2Mo_6Se_6$. Indeed, a spontaneous dissolution occurred that led to an opaque, air sensitive, black solution (Fig. 8) [4, 47]. Raman spectroscopy was performed on the solutions and showed that they contained carbon nanotubes, revealed by the G and D bands of the top spectrum of Fig. 9. Those nanotubes were negatively charged, leading to a broadening of the Raman signals and a strong decrease of intensity, even leading to the full disappearance of the RBM bands (top spectrum of Fig. 9) [48]. This decrease of intensity is due to the loss of the optical resonance between symmetrical van Hove singularities in the nanotube band structure, due to the filling of the upper levels by electrons during the reduction (Fig. 10) [46]. Upon air oxidation, the nanotubes lose their extra charge and revert to neutral, as seen in the middle spectrum of Fig. 9 where the G and D bands have narrowed and recovered intensity while the RBM bands are now visible.

Fig. 8 Picture of a drop of DMSO deposited onto nanotubes, under inert atmosphere. *Left*: a few seconds after contact. *Right*: at the end of the dissolution process, the drop is fully *black*. Adapted from [4]

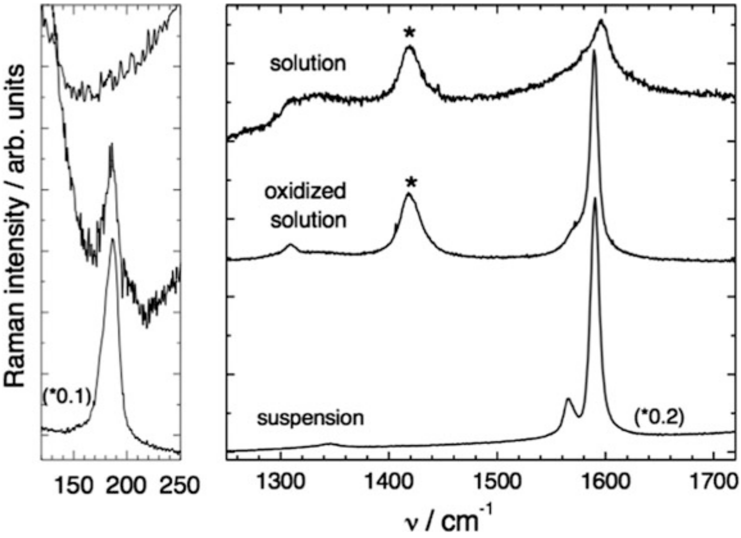

Fig. 9 Raman spectra of $[Na(THF)]_nNT$ in DMSO, taken with a 514.5-nm laser excitation. *Top*: $[Na(THF)]_nNT$ in DMSO. *Middle*: the same after air exposure. *Bottom*: for comparison, Raman spectrum of neutral SWCNTs dispersed with surfactants. The *starred bands* come from the solvent. Figure from [4]

5.1 Synthesis of Nanotube Salts

In the recipe of Petit et al. [49] a radical anion salt of a polyaromatic hydrocarbon (PAH) is obtained by mixing the corresponding PAH with an alkali metal in tetrahydrofuran. Depending on the PAH redox potential, solutions of varying reduction power can be obtained. In the work of Petit et al., a film of carbon nanotubes was exposed to these solutions and it has been shown that, starting from neutral CNTs, sequential quenching of the optical transitions of CNTs could be performed by suitable choice of the starting PAH [49]. CNT soot can also be treated with the radical anion solution and a bulk CNT salt is obtained [4]. Alternatively, CNT salts can be prepared by vapor phase doping of CNTs [50] or by electrochemistry [46], similarly to graphite intercalation compounds.

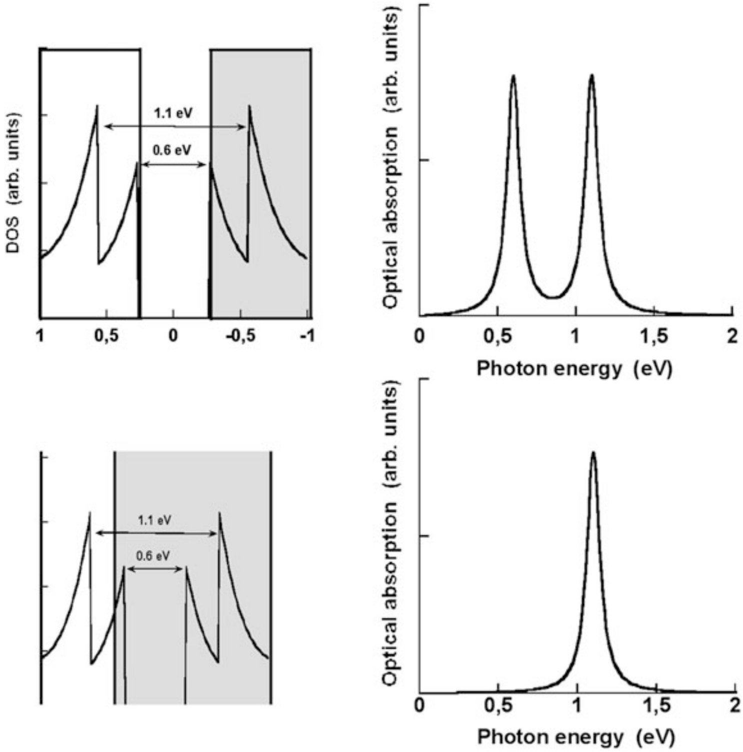

Fig. 10 *Top*: DOS of a neutral semiconducting SWCNT and the corresponding simulated optical absorption bands induced by transitions between van Hove singularities. *Bottom left*: DOS of the same semiconducting SWCNT after n-doping. The Fermi level being shifted above the first van Hove singularity, the transition of lowest energy is suppressed. *Bottom right*: corresponding simulated optical absorption spectrum. Figure and legend from [46]

5.2 Individualization

As described above, single-walled carbon nanotubes come in bundles. Once dissolved by the reductive dissolution, how exfoliated are those bundles? What is the degree of individualization of the nanotubes? This question was answered through height measurements by atomic force microscopy of drop casted nanotube salt solution (Fig. 11), first reported during NT'07 in Ouro Preto, Brazil, and published very recently [5]. In Fig. 12, two diameter distribution curves are shown – for raw nanotubes weakly dispersed in ethanol (red curve) and for salts of nanotubes dissolved in DMSO (black curve). DMSO is known to be a very poor solvent for dispersing nanotubes [33, 51]; hence raw nanotubes were dispersed in a more practical solvent, such as ethanol, that evaporates easily with the idea that dispersing the nanotubes in a bad solvent has the advantage of being the closest possible to the soot. A total of 99 measurements on clean parts of nanotube images,

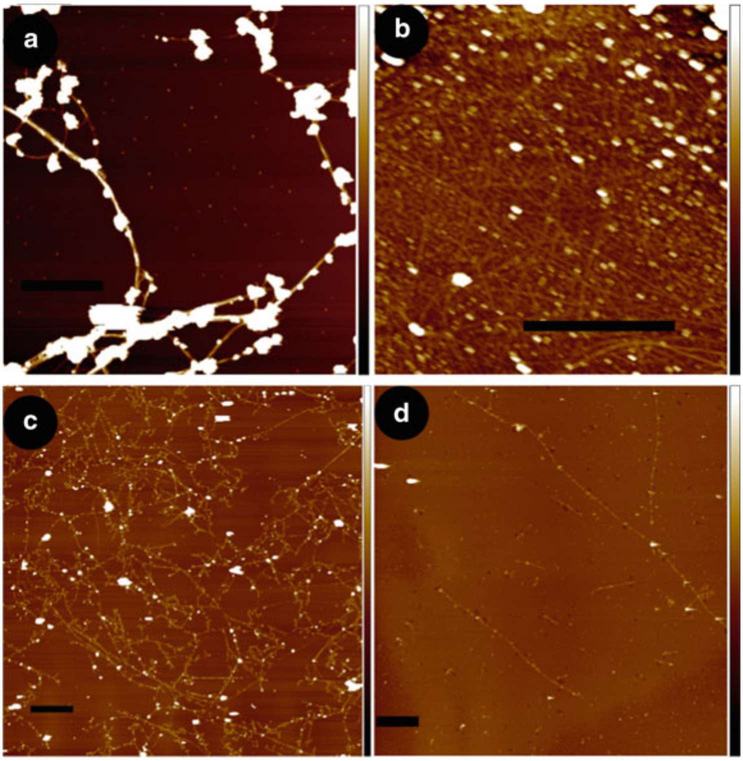

Fig. 11 AFM height images of drop-casted arc electric SWCNTs on mica. (**a**) Raw nanotubes dispersed in ethanol. (**b**)–(**d**) Nanotubides dissolved in DMSO, dilution by 10, 100, and 1,000 respectively. For each image, the *black line* stands for 1 μm lateral scale. Height scale for all images: 0 to 30 nm. Figure and legend from [5]

such as in Fig. 11a and similar figures, show that raw tubes are present as bundles with diameters varying from 1 to 25 nm. The distribution can be fitted with a lognormal law, yielding a mean diameter of 6 nm, corresponding to bundles of 20–30 tubes [5]. In contrast, 250 measurements on drop casted DMSO solutions of nanotube salts show a much narrower distribution of diameters, from 1 to 3 nm, peaking at 1.5 nm, close enough to the diameter (1.3 nm) of the electric arc nanotubes used in this experiment, taking into account a vdW radius of ca 0.3 nm. These data show that the reductive dissolution indeed leads to a spontaneous exfoliation of the CNT bundles [5]. A quite important point is that these solutions of individualized tubes are concentrated solutions, of concentration up to 2 mg/mL. By using crown ether to complex the alkali ions, Marti et al. have been able to obtain solutions of concentration up to ca 9 mg/mL [52]. Having at hand solutions of individualized nanotubes, it has been possible to perform spectro-electrochemical studies of single tubes to determine the Fermi level at neutrality and their oxidation and reduction potential as a function of SWCNT diameters (Fig. 13) [53].

Fig. 12 Distribution of diameters for raw nanotubes (*full red squares*, 99 objects) and dissolved nanotubes (*full black circles*, 251 objects), each normalized with respect to the area below the curve, and fitted with a log-normal law. Figure and legend from [5]

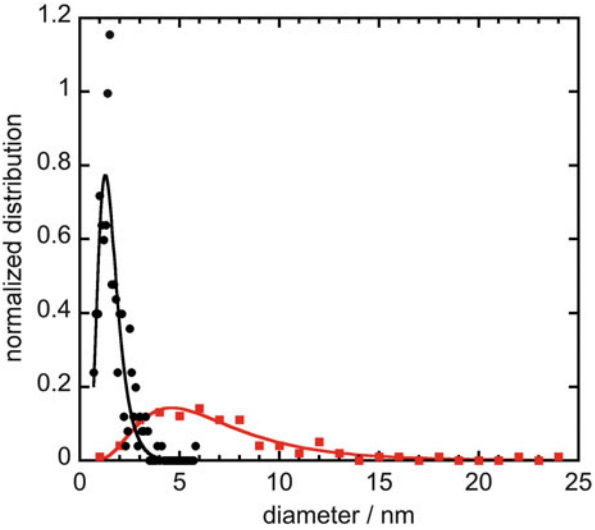

5.3 Dissolution Mechanism

Carbon nanotubes can be conceived as polymers. Charged polymers are known as polyelectrolytes. In an effort to unravel the mechanism of dissolution of nanotube salts and the reason behind the spontaneous dissolution, experimentally measured concentrations were used to fit a model of polyelectrolyte dissolution. Unlike conventional polyelectrolytes, it is easy to control the level of charges on reduced carbon nanotubes by simply varying the C/alkali metal ratio when preparing the salt [31]. Concentrations at saturation were measured as a function of the charges on the CNTs (black squares in Fig. 14). The experimental points were used to fit a general curve deduced from the calculated free energy of mixing a carbon nanotube salt with DMSO ΔG_{mix} where $\Delta G_{\text{mix}} = \Delta H_{\text{mix}} - T\,\Delta S_{\text{mix}}$. The enthalpic part is related to the solvent-nanotube interaction vs nanotube–nanotube (and solvent–solvent) interaction. It is always unfavorable but can be less unfavorable in polar solvents such as DMSO, DMF, NMP, etc. On the other hand, the favorable entropic contribution of the counterions dominates in polar solvents and is the driving force behind the spontaneous dissolution of carbon nanotube salts in those solvents. The interested reader is referred to [31] for a full discussion.

In short, rather than electrostatic repulsion between chains bearing same sign charges, often stated as the reason for dissolution, the entropy gain due to countercation solvation is the true driving force for nanotube salts dissolution.

It should be noted in Fig. 14 that, for high concentrations, experiments and models differ rather dramatically. This is to be expected since the model does not take into account inter-tube interaction. In that range of concentration, one is already well over the semi-dilute regime concentration (ca 0.01 mg/mL) and nanotubes are expected to interact with each other. Interestingly enough,

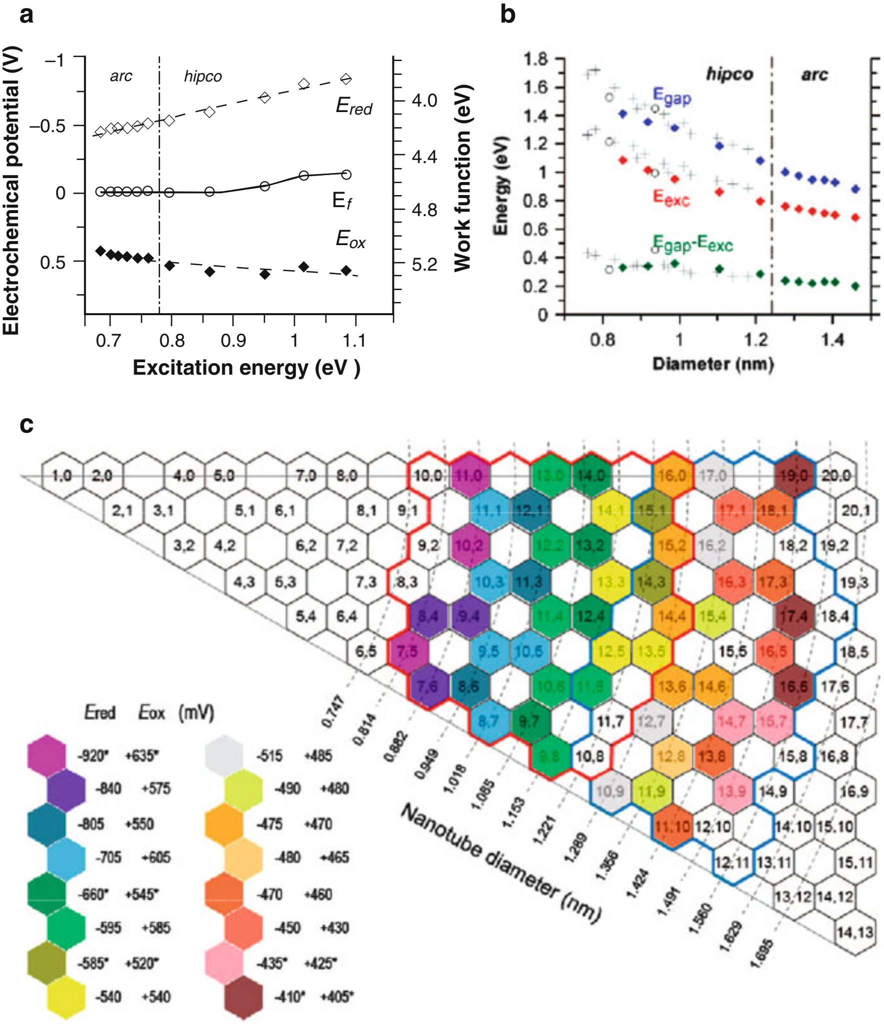

Fig. 13 (**a**) Oxidation (*solid diamonds*) and reduction (*open diamonds*) standard potentials and Fermi levels (*open circles*) of semiconducting SWCNTs, as a function of the excitation energy. Potential data were plotted with reference to either the SCE electrode (*left axis*) or the vacuum level (*right axis*), assuming that the latter is located at 4.68 eV with respect to SCE.42. (**b**) The electrochemical gap (*blue diamonds*), the excitation energy (*red diamonds*), and the exciton binding energy (*green diamonds*) plotted as a function of the nanotube diameters, calculated from excitation energies. (**c**) Chirality map displaying the average standard potentials associated to each of the SWCNT structures identified in this work. HiPco SWCNTs are located inside the *red line*, while arc-discharge SWCNT are inside the *blue line*. *Starred values* were extrapolated (see [53]). Figure and legend from [53]

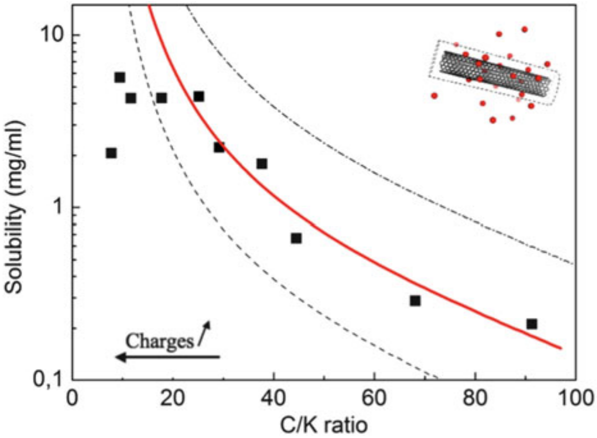

Fig. 14 Solubility of the reduced single-walled SWCNTs measured (*black squares*) and fitted (*red solid line*) yields $\overline{\Delta H_{\text{mix}}} = 18.8$ mJ m^{-2}. Additional lines were plotted for slightly different values of $\overline{\Delta H_{\text{mix}}}$: 17.5 mJ m^{-2} (*dashed-dotted line*) and 20 mJ m^{-2} (*dashed line*). *Inset* (*upper right*): Representation of the polyelectrolyte nanotubes in solution with potassium cations in *red*. Adapted from [31]

Marti and co-workers, by adding a crown ether to the dissolution medium, succeeded in obtaining much higher concentrations (ca 15 mg/mL) and evidence for a nematic phase [52].

5.4 Multiwalled Nanotubes

Multi-walled carbon nanotubes are made of concentric single-walled nanotubes. Solubilizing or dispersing them requires putting the entire multiwalled nanotube into solution. MWNTs are far more defective than single-walled nanotubes and their volume/surface ratio is much higher. Nevertheless, small multiwalled nanotubes of ca 10–15 nm diameter can be dissolved by the reductive dissolution route (Fig. 15) [54]. Obviously there should be a limit where MWNTs are too large and don't dissolve any more. The entropic factor, described above, is constant per surface area. When the volume increase without increase of surface, the whole free energy balance should be unfavorable and the MWNTs should not dissolve. It remains to be seen up to what diameter MWNTs can be dissolved.

5.5 Reduced Nanotubes for Functionalization

In parallel to the first experiments on dissolution of reduced nanotubes, electrophilic addition onto nanotubes had been explored by the Billups' team. Liang et al. [55] and Chattopadhyay et al. [56] were followed by several works of groups

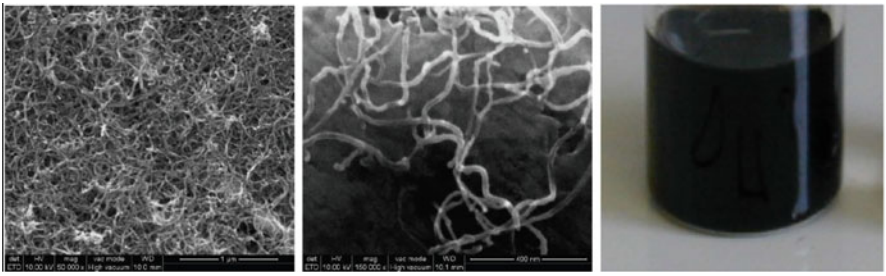

Fig. 15 Scanning electron microscope images of concentrated (*left*) and diluted (*middle*) solutions drop-casted on an aluminum substrate. *Right*: a concentrated solution of multi-walled nanotubes in DMSO. Adapted from [54]

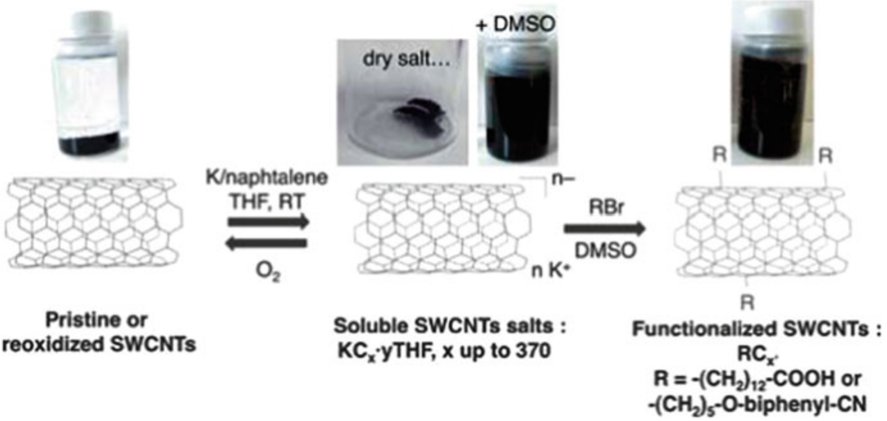

Fig. 16 A reaction scheme for the isolation of reduced SWCNTs salts and further functionalization through alkylation. The stoichiometry of the salt is adjustable, while remaining soluble. Figure and legend from [60]

such as those of Hirsch [57], Simard [58, 59], and others. By varying the amount of negative charges on the nanotubes, it has been possible to control the number of addends grafted onto the tubes (Fig. 16). An often quoted problem with functionalization is its deleterious influence on the opto-electronic properties of nanotubes. By electrophilic addition of nanotubides of low charge contents, it has been possible to functionalize nanotubes while keeping their band structure virtually unchanged (Fig. 17) [60], opening a wealth of possibilities for ad hoc functionalized nanotubes retaining the electrical and optical properties of pristine tubes.

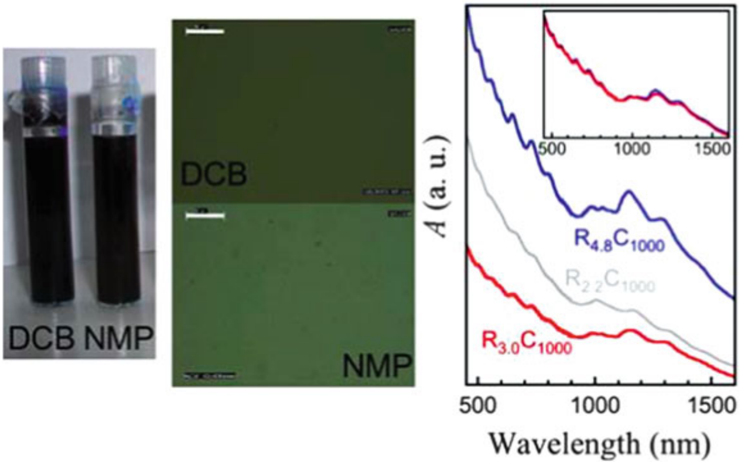

Fig. 17 *Left*: solutions of functionalized SWCNTs in dichlorobenzene and NMP. *Middle*: optical microscopy observations solutions showing the absence of aggregates. The *scale bar* is 50 µm. *Right*: vis-NIR spectra of SWCNTs functionalized with R. 40-cyano[1,10-biphenyl]-4-oxypentyl. The *inset* shows two spectra after normalization. Images and legend from [60]

5.6 Sorting Nanotubes

As A.G. Rinzler once wrote, “perhaps the most wonderful feature of carbon nanotubes is that they are synthesized in both metallic and semiconducting variants, and perhaps the most problematic feature is that they are synthesized in both metallic and semiconducting variants” [61]. Since the first report on nanotube sorting by electronic character [62], there has been quite a lot of effort to obtain SWCNTs of only metallic character or only semiconducting character (and the same electronic gap) [42]. Although today one can buy suspensions of semiconducting single-walled carbon nanotubes in 99% purity (see Nanointegris at http://www.nanointegris.com/), sold by the milligram, the issue is far from being resolved for industrial-scale application. Reductive dissolution of carbon nanotubes might prove to be the way to go. Starting from raw nanotubes, the problem is threefold: (1) removal of non-nanotube impurities, particularly the carbonaceous ones, that have similar chemical and spectroscopic responses, (2) individualization in order to be able to treat metallic and semiconducting tubes separately, and (3) actual separation of semiconducting and metallic tubes. Shaffer, Skipper et al. showed that the reductive dissolution offers a way to remove carbonaceous impurities, either through chemical [12] or electrochemical [13, 63] reduction of the tubes. Individualization of the tubes have been observed [4, 12] and quantified [5]. It should be added that, since no sonication is needed to dissolve the tubes, length is preserved, an important asset of carbon nanotubes. Furthermore, concentrated solutions can be obtained, hence allowing for optimal processing if a viable separation process can be designed. “Concentrated” should be understood here to indicate 10^0 mg/mL [4, 5, 12, 31] to 10^1 mg/mL [52] order of magnitude concentrations. This might not appear very high when compared to surfactant-aided suspensions that can easily attain concentrations in the 10–50 mg/mL range. However, when dealing with individualized tubes, concentrations are several orders of magnitude lower, between 1 and 10 μg/mL [51, 64, 65].

In a first step towards efficient sorting of nanotubes, Fogden et al. have shown preferential dissolution of metallic tubes by reductive dissolution, exemplified by Raman and absorption spectra (Fig. 18) [12]. And this without the need for functionalization/defunctionalization, a popular route exploiting the enhanced reactivity of metallic tubes compared to semiconducting ones.

5.7 Electrochemical Synthesis

As has long been known for GICs, reduced nanocarbons can be made electrochemically, by vapor phase doping [50] or in solution, using a reducing intermediate such as naphthalene [4] or electrides [12]. Hodge et al. have recently obtained nanotubide solutions via an electrochemical route, thus eliminating the need for alkali metal handling and offering a handy control over the required amount of reduction (Fig. 19) [63].

6 Graphenide Solutions

Graphene has come out in recent years as a wonder material [66] due to its high mechanical strength, high electronic mobility, lightness, flexibility, single-atom thickness, and near-transparency, the first three properties (at least) being shared with carbon nanotubes. These properties make graphene a very promising charge for composites, thin films, electromagnetic shielding, barrier films, sensors, as well as other applications. In order to process graphene, as is the case for carbon nanotubes, one has to be able to disperse it. Ideally, one would like to be able to dissolve it, i.e., deal with separated graphenes rather than aggregated ones or few layered graphite.

There are a number of ways to synthesize graphene (Table 3). Some of them yield true graphene, i.e., "a single carbon layer of the graphite structure, describing its nature by analogy to a polycyclic aromatic hydrocarbon of quasi infinite size,"[1] and some of them yield something close to graphene, either few layered or still containing some oxygen atoms (reduced graphene oxide). Methods 1–3 in Table 3 are surface methods and are not suitable for solution processing which is the subject of this chapter. Methods 4–6 give a powder of "graphene," each having their

---

[1] IUPAC definition of "graphene" in the IUPAC Gold Book : http://goldbook.iupac.org/.

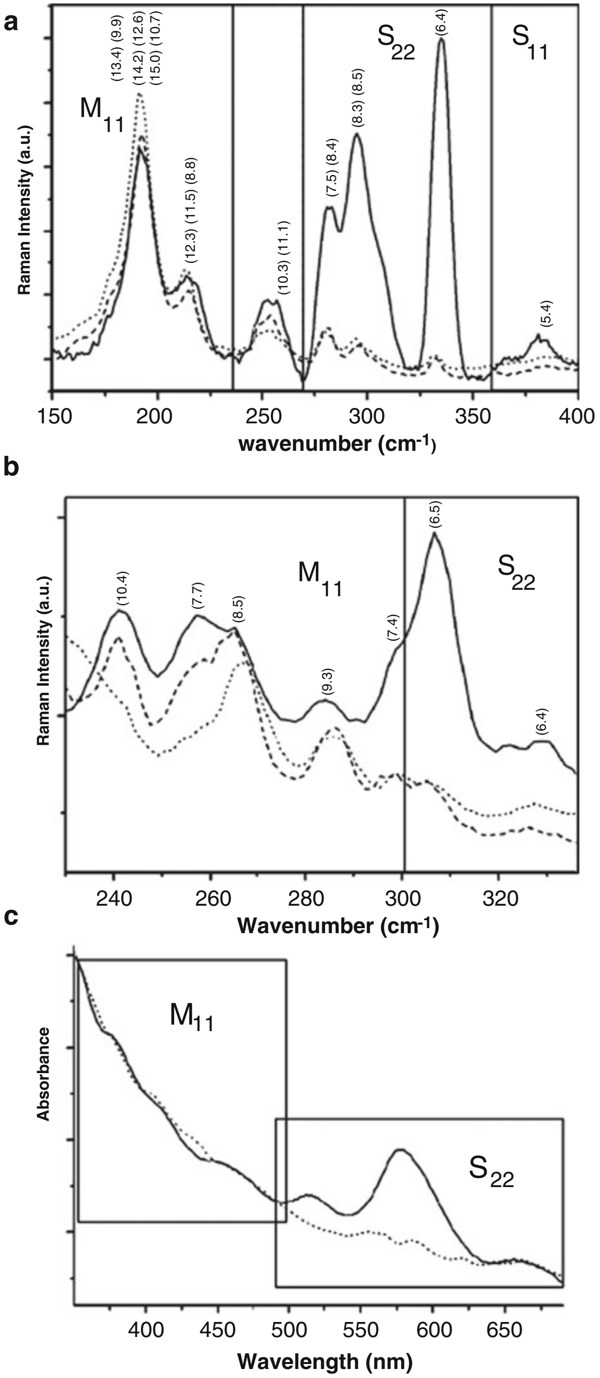

Fig. 18 Optical characterization of SWCNT fraction spontaneously dissolved into DMF at the M:C ratio 1:10. (**a**) *Red* (633 nm) RBM Raman spectra of as-received CoMoCAT SWCNTs (*solid line*), the spontaneously dissolved CoMoCAT fraction (*dashed line*), and the spontaneously dissolved CoMoCAT fraction following vacuum annealing (*dotted line*). The *shaded area* represents the crossover between the metallic and semiconducting SWCNTs. (**b**) *Green* (532 nm) RBM Raman spectra of as-received CoMoCAT SWCNTs (*solid line*), the spontaneously dissolved CoMoCAT fraction (*dashed line*), and the spontaneously dissolved CoMoCAT fraction followed by vacuum annealing (*dotted line*). (**c**) UV/vis spectra of as-received CoMoCAT SWCNTs (*solid line*) and spontaneously dissolved fraction (*dotted line*). Images and legend from [12]

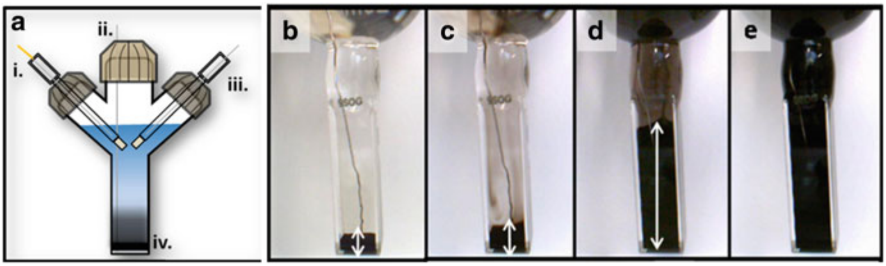

Fig. 19 Electrochemical dissolution process. (**a**) Schematic illustration of the electrochemical process showing *i*) Ag/Ag^+ reference electrode, (*ii*) Pt plate working electrode, (*iii*) Pt wire counter electrode, (*iv*) SWCNT powder. (**b**)–(**e**) Electrochemical dissolution of 20 mg of raw HiPco SWCNT powder in 1 mM TBAP/DMF at −2.3 V over 5 days. The *white arrows* indicate the significant degree of swelling of the SWCNT powder bed. For smaller loadings (<10 mg), the dissolution process can be performed within 24 h, without agitation, to generate >1 mg mL^{-1} solutions. Images and legend from [63]

Table 3 Methods of graphene synthesis

#	Method	Quality	Quantity	Advantages	Disadvantages	References
1	Mechanical exfoliation	+++	+	Single objects of lateral size up to 50 μm and high quality	Unsuitable for upscaling	[85]
2	Reconstruction of SiC surface	+++	++	High quality wafer-like graphene	Expensive, attached to substrate	[86]
3	CVD on metal surfaces	++	++	Very large surface (m^2), upscalable	Expensive	[87]
4	Growth of powdered graphene	+	+++	Large quantities	Quality?	[74–76]
5	CNT unzipping	+	+	Route for obtaining ribbons	Defective	[69–73]
6	Total (chemical) synthesis	+++	+	Monodisperse in size, high quality, ribbons	Small sizes, expensive	[67, 68]
7	Graphite oxide reduction	+	+++	Cheap, large quantities	Defective	[77–79]
8	Graphite dispersions	+	++	cheap	Incomplete exfoliation	[80–82]
9	Graphene salts solutions	++	++	Individualized sheets	Inert atmosphere	[89–91]
10	Superacids (see Sect. 8)	++	++	Individualized sheets	Dry atmosphere	[88]

advantages and disadvantages. Total synthesis (method 6) is intellectually very pleasing, gives monodisperse polyaromatic species, i.e., C_nH_m molecules with n being large (already higher than 200) and $n >> m$ (Fig. 20) [67]. These are true

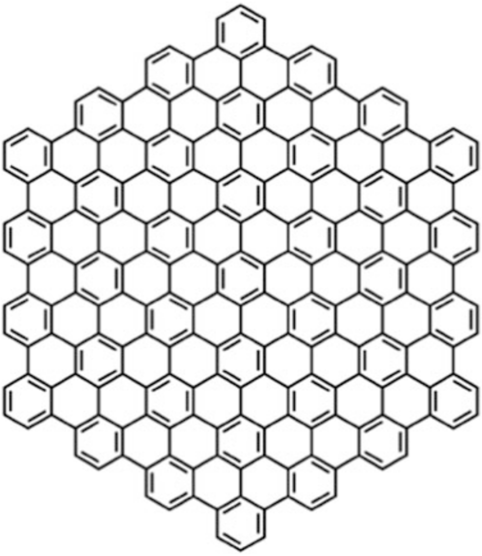

Fig. 20 The $C_{222}H_{36}$ molecule. From [67]

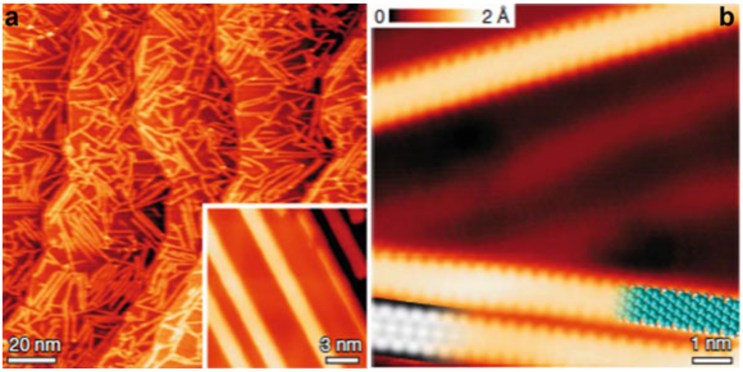

Fig. 21 Straight graphene nanoribbons. (**a**) Overview STM image of straight GNRs. The *inset* shows a higher-resolution STM image taken at 35 K. (**b**) High-resolution STM image with partly overlaid molecular model (*blue*) of the ribbon. At the *bottom left* is a DFT-based STM simulation of the ribbon shown as a grey-scale image. Images and legend adapted from [68]

molecular species that bridge the gap between classical polyaromatic hydrocarbons (PAHs) and graphene. They can also be synthesized as ribbons (Fig. 21) [68]. CNT unzipping (method 5) is a very good way of obtaining ribbons, albeit at the cost of defective objects [69–73]. Varied methods have been developed to obtain a powder of graphene or graphene-like material in scalable quantities [74–76]. Defect-less graphene in large quantity is graphite, and hence the amount of defects in those powdered graphene is to be watched. However, this might prove to be a method of choice for large volume applications such as composites. All three methods, though, give a solid form, which needs to be solubilized in order to process it. Solubilizing methods (methods 7–10) start from graphite but could also be applied to the resulting material from methods 4–6.

Graphene oxide (method # 7) is by far the large scale route, applicable in large volume and cheap. Graphite is oxidized in a strongly oxidizing medium, based in sulfuric acid and potassium permanganate. This graphite oxide (with a C/O ratio close to 2) is dispersible and exfoliated in water, giving dispersions of graphene oxide (GO). GO has then to be reduced to remove most of the oxygen atoms. A large amount of work has been devoted to finding ways of reducing graphene without losing all solubility in water. Conductivity can be restored by several orders of magnitude but, up to now, that of graphite/graphene cannot be recovered. GO and RGO (reduced graphene oxide) have been covered in various reviews and will not be further described here [77–79].

Dispersions of graphite (method 8) are of two kinds: in organic solvents [80] and in water with surfactants [81, 82]. In both cases, sonication is used to bring energy to the system and break the graphite particles sufficiently small so that they can be dispersed either with surfactants or in solvents that have affinity for the graphenic surface. The advantages are that it is a cheap method, easily transferable to any laboratory. The disadvantage is the use of sonication or high shearing that breaks the flakes into smaller fragments [83]. Use of bath sonication allows less degradation of the flakes, albeit at the cost of longer times [84]. It is certainly a good way to disperse thin graphite into a liquid. It remains to be seen whether it can effectively and predominantly unravel the fundamental constituents, graphenes, from graphite.

Graphenide solutions (method 9) [89–93], i.e., solutions of negatively charged graphene sheets, allow for rather concentrated solutions (ca 0.5 mg/mL). Graphenide solutions are prepared by exposure to a suitable solvent such as NMP [89, 94], THF [91, 95], or 1,2-dimethoxyethane (DME) [92], of a graphite intercalation compound (Fig. 22). Although a detailed analysis like the one that has been performed on nanotubes [31] has not been attempted, by analogy it is expected that both the entropy gain with counterions dissolution and a rather favorable graphenide–solvent interaction lead to these thermodynamically stable solutions. Graphenides have been shown to be individualized in solution [91, 95]. Absorption spectra in NMP show a strong peak at 300 nm (4.1 eV), characteristic of negatively charged graphene sheets (Fig. 23) [94]. Spectro-electrochemistry has shown that graphenides could be reversibly undoped (re-oxidized) and the redox potential of graphene has been determined at +22 mV vs a standard calomel electrode (SCE), very close to the work function of graphite [94].

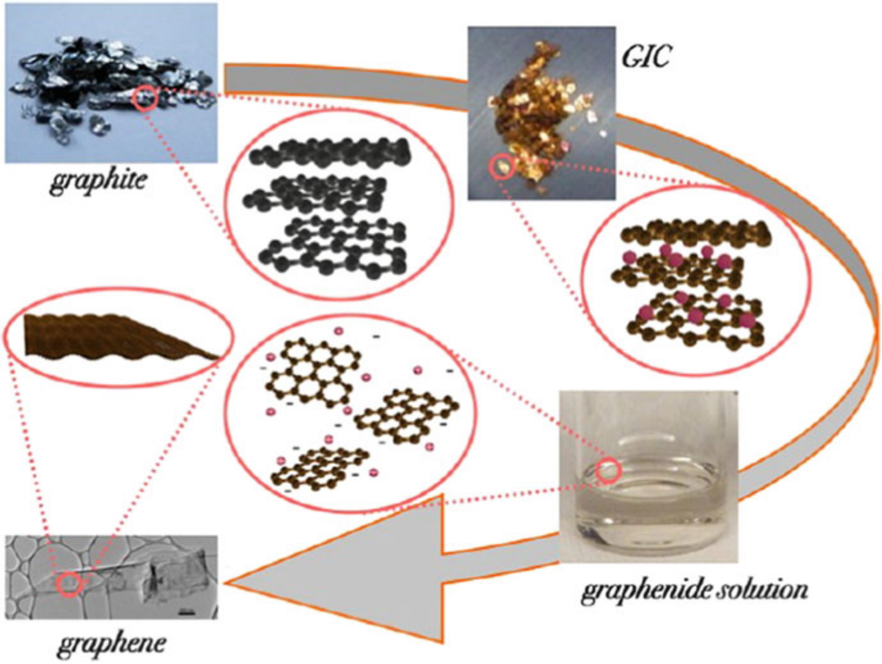

Fig. 22 From graphite to graphene via dissolution of graphite intercalation compounds. Reprinted from [90]

7 Nanocones Dissolution

7.1 Carbon Nanocones

In 1999, Yudasaka, Iijima and co-workers synthesized a new carbon form that they described as "nano-aggregates of single-walled graphitic carbon nano-horns" [96]. Following a recent editorial in Carbon [17], which attempted to rationalize the vast amount of "new" carbon forms, they would be described as aggregated single-walled nanocones. The single unit here is a nanocone, which should be attainable by disrupting the dahlia-shaped aggregates (Fig. 24).

Another form of nanocones, opened at their apex, is the so-called *cup-stacked carbon nanocones* (Fig. 25) [97]. They appear to stack together to form hollow core cup stacked carbon nanotubes. The fundamental unit to dissolve here is the nanocone itself, as has been shown by Fukuzumi et al. [98].

Reductive dissolution is a choice method to obtain solutions of individualized single-walled nanotubes, multi-walled nanotubes, graphenes, etc.; it requires electronic levels that can be filled with electrons in order to form a salt. It actually works very well with C_{60} [10], but in that case, since the neutral molecule itself is soluble (see Sect. 3), there's no need to synthesize fulleride salts. An intermediate

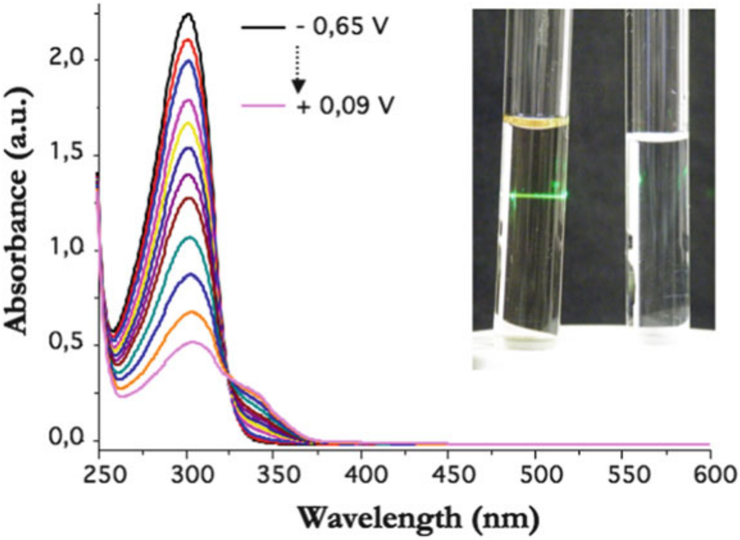

Fig. 23 Absorption spectra of an NMP solution of negatively charged graphene flakes from KC_8 dissolved in NMP. *Black*: starting solution. All other spectra were recorded while raising the electrochemical potential of the solution to less negative potentials. The intensity of the 300 nm peak could be fitted using the Nernst equation and yielded a reduction potential of +22 mV vs SCE for graphene. *Inset*: the graphene solution scatters light from a laser beam, indicating the presence of particles of colloidal size (Tyndall effect), whereas the same laser is invisible through the pure solvent. Images and legend adapted from [90, 94]

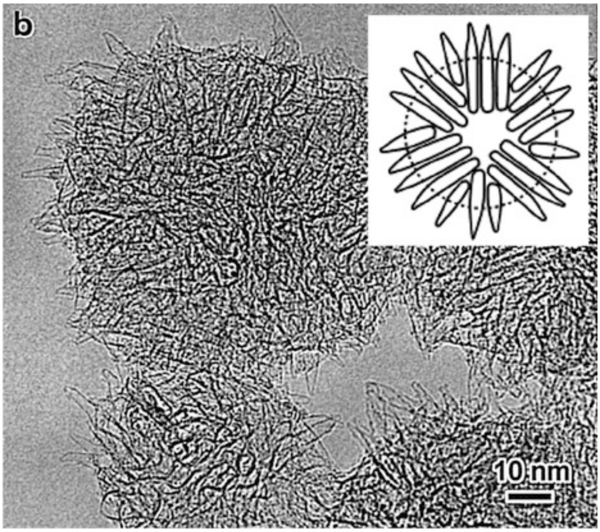

Fig. 24 Dahlia shaped carbon nanohorns aggregates. *Inset*: schematic representation of the packing of nanohorns. Images from [96]

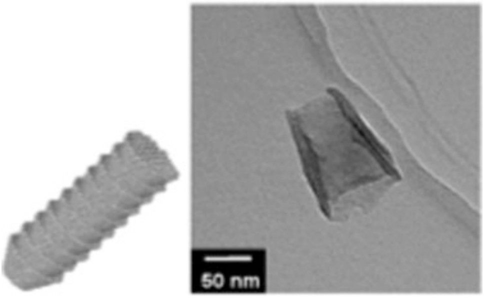

Fig. 25 *Left*: schematic model of cup-stacked nanocones. *Right*: TEM image of dodecylated, individualized cup-shaped carbons. Images from [98]

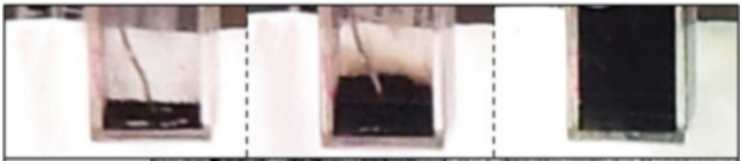

Fig. 26 Spontaneous electrochemical dissolution of nanotubium species under potentiostatic control in 1 mM $LiAsF_6$/propylene carbonate, at +1.6 V vs Ag/Ag. for 120 h. Figure and legend from [13]

case between the molecular size of C_{60} and the macromolecular size of carbon nanotubes or graphene, nanocones, and nanohorns can also be dissolved by reductive dissolution.

Starting from cup-stacked carbon nanocones, Fukuzumi et al. obtained individualized and alkylated carbon nanocups (open nanocones) using reduction by sodium naphthalide followed by reaction with iododecane in DMF (Fig. 25) [98].

Likewise, carbon nanohorns can be individualized by reductive dissolution and concentrated solutions of nanohorn salts can be obtained in a variety of organic solvents: starting from pristine nanohorn aggregates (Dahlia shaped aggregates), reduction affords salts of nanohorns that are soluble in several polar solvents, attaining concentrations as high as 30 mg/mL in DMSO [99, 100].

8 Oxidative Dissolution of Nanocarbons

Oxidation has also been used to dissolve nanocarbons. Oxidation here is to be understood as removal of electrons (or p-doping in physics language). Hodge et al. have succeeded in dissolving nanotubes electrochemically in a similar manner to their electroreductive dissolution: the nanotube soot is placed on and in contact with a metal electrode. This working electrode is then polarized towards positive potentials and SWCNT dissolution is observed (Fig. 26) [13].

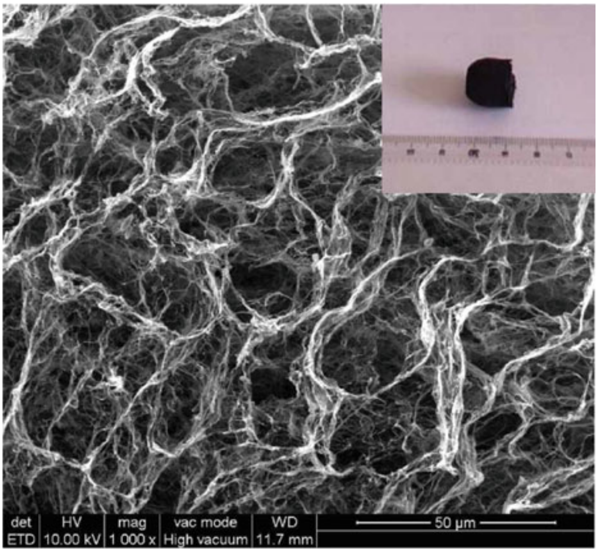

Fig. 27 A typical scanning electron microscopy image of an SWCNT cryogel. Large pores are observed of typical size around 20 m. Walls between the pores are made of SWNT fishnet with holes of ca 100 nm. *Inset*: optical photograph of a cryogel. Note the shape, reminiscent of the test tube in which the solution was freeze-dried. Figure and legend from [5]

Although it has been reported as protonation rather than oxidation, nanotubes [101] and graphite [88] have both been dissolved spontaneously in superacids such as chlorosulfonic acid, yielding solutions that, in the case of nanotubes, allowed spinning into fibers.

9 Applications and Materials from Nanocarbide Solutions

Reductive dissolution is a way to dissolve and individualize nanocarbons without the deleterious consequences of using sonication. The downside is that an inert atmosphere is needed to handle the highly reducing nanocarbides that can react with water or oxygen. Nevertheless, it has already been used in research labs and in R&D labs to prepare materials:

9.1 Cryogels

By freeze-drying solutions of nanotubide in DMSO, a cryogel is obtained, the macroscopic form of which is that of the solution before freeze-drying (Fig. 27, inset) [5]. The resulting foam-like material has very large interconnected pores of ca 20 µm diameter (Fig. 27). Its density can be as low as 2 g/L making it one of the lightest materials in the world. Applications are foreseen as electrode materials or decontamination materials (due to the hydrophobic surface) among others.

9.2 Field Effect Transistors

While studying field effect transistors on individual tubes, Ahlskog et al. have monitored the doping of a single tube by a solution of lithium naphthalenide solution, showing full reversibility of the doping process and pointing to reductive dissolution as an efficient way to prepare carbon nanotube-based devices [102].

9.3 Catalysts

Nanocarbides are synthesized by filling electronic levels with electrons donated by alkali metals. The resulting, reduced species are in turn highly potent reducing agent. They have been used as such to prepare metallic nanoparticles of palladium or platinum that have shown efficient catalytic activity upon Suzuki, Stille and Heck reactions [99, 100, 103].

9.4 Transparent Conducting Films

Indium tin oxide (ITO) is used in the vast majority of flat screens all over the world as a transparent electrode. ITO shows a very good conductivity vs transparency, of ca 10 ohm/square surface resistivity for 90% transparency. ITO brings a number of problems, however, such as its scarcity, its price, the need for high temperature processing, and its rigidity. Substitutes are being actively sought all over the world. Carbon nanotubes, graphene, and metal nanowires, in particular silver nanowires, are among the best candidates [104]. Silver nanowires give by far the best performances but carbon nanotubes or graphene show excellent chemical inertness, a crucial factor against aging in any viable industrial product. Long nanotubes can be dissolved by reductive dissolution without sacrificing their length. Hence they can retain very large aspect ratios of 10,000 or more. This has important consequences for transparent electrodes. Indeed, by using longer tubes one can diminish the required quantity of nanotubes to obtain a percolating network and hence obtain more transparent films for a given conductivity [105]. Based upon results from Shaffer et al. and ourselves, the Linde company has recently succeeded in obtaining films of superior performances, of ca 130 ohm/square surface resistivity for 90% transparency (Fig. 28) with nanotubides of up to 20 μm length. The corresponding ink, named SEER^{e-} ink, is now commercially available (see the Linde Nanomaterials website: http://www.linde-gas.com/en/products_and_supply/electronic_gases_and_chemicals/carbon_nanotubes/index.html).

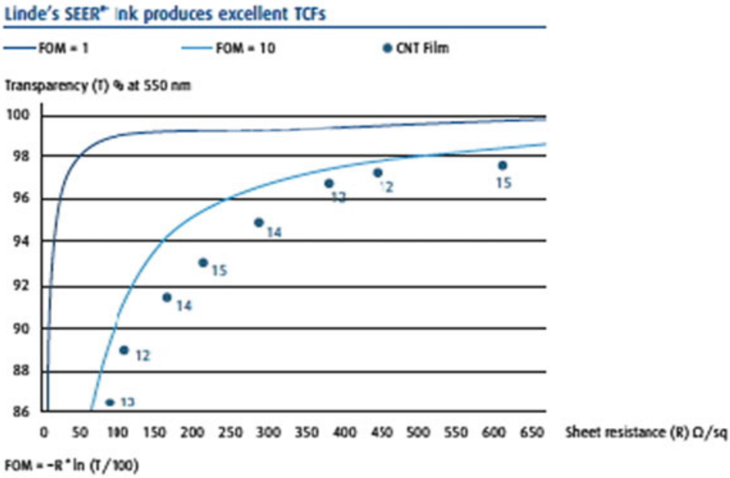

Fig. 28 Transparency vs resistivity for transparent conducting films made from solutions of nanotubes salts. Data and figure from the Linde Nanomaterials website: http://www.linde-gas.com/en/products_and_supply/electronic_gases_and_chemicals/carbon_nanotubes/index.html

10 Conclusion and Perspectives

Although spotted in the 1970s [106], carbon nanotubes have been the subject of an intense research effort since 1991 [11] and specifically since 1996 after gram scale synthesis methods were published [29, 30]. After close to 20 years of fundamental research on carbon nanotubes and activity still going on, graphene is now quoted as the next marvel material. One may wonder what would be the situation if graphene had appeared in the 1990s and nanotubes some years ago; no doubt these wonderful “rolled up graphene cylinders” would be the new wonder material. Science is not totally immune to fashion considerations and both materials share extraordinary properties. These include electrical conductivity, mechanical resistance, lightness, chemical nature (i.e., carbon rather than metals, think of the recycling of electronic circuits full of rare earth materials). As is no surprise to scientists, research takes time and it might take a few more years before these promising carbon nanomaterials are incorporated into real life objects [107]. Carbon nanotubes and graphene have both shown wonderful fundamental science. On the technological side, besides exciting announcements (I am personally waiting for bicycle frames that incorporate graphene), some real applications are now commercialized using carbon nanotubes, mostly due to their conductivity preventing electric discharge, e.g., in conductive plastic fuel pumps in the automotive industry, in hard disks packaging, etc.

Two bottlenecks have slowed down nanotubes usage, in spite of their extraordinary technological potential: processing and sorting. Graphene shares the problem of processing while there’s no sorting to be made on graphene (as long as graphene ribbons do not exist in workable quantities). The reductive dissolution, described in this chapter is one solution to the processing problem. It doesn't bring defects to the processed nanocarbon, it preserves its aspect ratio, and, most important of all, it yields individualized objects, enabling one to take full advantage of them. The price to pay for these great advantages is having to work under an inert atmosphere, which has slowed down the generalization of reductive dissolution. For those willing to take these extra precautions, solutions of nanotubides or graphenides constitute systems where the true individual objects can be processed to the best of their potential.

Acknowledgements Most of the experimental work described here has been performed by Dr. C. Vallés, Dr. A. Catheline, Dr D. Voiry, Dr F. Dragin, and Yu Wang, in collaboration with Dr Olivier Roubeau, Dr Carlos Drummond, the group of Prof. F. Paolucci from the University of Bologna (in particular, Dr. M. Marcaccio, Dr. M. Iurlo, Dr. G. Valenti, and Dr S. Rapino), and with Dr L. Ortolani and Dr. V. Morandi (CNR, Bologna). Prof. Eric Anglaret (Laboratoire Charles Coulomb, Montpellier), Dr. M. Monthioux (CEMES, Toulouse), and Dr. C. Furtado (CDTN, Belo Horizonte), as well as Prof. M. Pimenta, Dr. A. Righi, and Dr. C. Fantini are also gratefully acknowledged as well as all the researchers and students from the "carbon nanotubes and graphene" team at CRPP. Support from the Agence Nationale de la Recherche (TRICOTRA and GRAAL Projects), Région Aquitaine (collaboration project with Emilie Romagne 2012–2014), Arkema and Linde is acknowledged. This work has been performed within the framework of the GDR-I 3217 "graphene and nanotubes."

References

1. Delhaes P (2012) Carbon science and technology: from energy to materials. Wiley, Hoboken
2. Kroto HW, Heath JR, O'Brien SC, Curl RF, Smalley RE (1985) C_{60}: buckminsterfullerene. Nature 318:162–163
3. Krätschmer W, Lamb LD, Fostiropoulos K, Huffman DR (1990) Solid C_{60}: a new form of carbon. Nature 347:354–358
4. Pénicaud A, Poulin P, Derré A, Anglaret E, Petit P (2005) Spontaneous dissolution of a single wall carbon nanotube salt. J Am Chem Soc 127:8–9
5. Pénicaud A, Dragin F, Pécastaings G, He M, Anglaret E (2013) Concentrated solutions of individualized single walled carbon nanotubes. Carbon. http://dx.doi.org/10.1016/j.carbon.2013.10.006
6. Bragg WH, Bragg WL (1913) The structure of the diamond. Nature 91:557
7. Kuznetsov O et al (2012) Water-soluble nanodiamond. Langmuir 28:5243–5248
8. Pénicaud A (1999) Les Cristaux, fenêtres sur l'invisible. Ellipses, Paris
9. Hirsch A (2002) Functionalization of single-walled carbon nanotubes. Angew Chemie Int Ed 41:1853–1859
10. Reed CA, Bolskar RD (2000) Discrete fulleride anions and fullerenium cations. Chem Rev 100(3):1075–1120
11. Iijima S (1991) Helical microtubules of graphitic carbon. Nature 354:56–58
12. Fogden S, Howard CA, Heenan RK, Skipper NT, Shaffer MSP (2012) Scalable method for the reductive dissolution, purification, and separation of single-walled carbon nanotubes. ACS Nano 6:54–62

13. Hodge SA, Bayazit MK, Tay HH, Shaffer MSP (2013) Giant cationic polyelectrolytes generated via electrochemical oxidtion of single-walled carbon nanotubes. Nat Commun 4:1989
14. Dresselhaus MS, Dresselhaus G (1981) Intercalation compounds of graphite. Adv Phys 30:139–326
15. Stumpp E et al (1994) IUPAC paper. Pure Appl Chem 66(9):1893–1901
16. McCleverty JA, Connelly NG (2001) Nomenclature of inorganic chemistry II: recommendations 2000. The Royal Society of Chemistry, Cambridge
17. Suarez-Martinez I, Grobert N, Ewels CP (2012) Nomenclature of sp^2 carbon nanoforms. Carbon N Y 50:741–747
18. Boyd PDW, Bhyrappa P, Paul P, Stinchcombe J, Bolskar R, Sun Y, Reed CA (1995) The C_{60}^{2-} fulleride ion. J Am Chem Soc 117:2907–2914
19. Taylor R, Hare JP, Abdul-sada AK, Kroto HW (1990) Isolation, separation and characterisation of the fullerenes CG0 and CT0: the third form of carbon. J Chem Soc Chem Commun 1423–1425. doi:10.1039/C39900001423
20. Azamar-Barrios JA, Muñoz EP, Pénicaud A (1997) Electrochemical generation of minute quantities (<100 μg) of the higher fullerene radicals $C_{76}^{\cdot}$-, $C_{78}^{\cdot}$- and $C_{84}^{\cdot}$- under O_2-and-H_2O-free conditions and their observation by electron spin resonance. Faraday Trans 93:3119
21. Azamar-Barrios JA, Dennis TJS, Sadhukan S, Shinohara H, Scuseria G, Pénicaud A (2001) Characterization of six isomers of [84]fullerene C_{84} by electrochemistry, electron spin -resonance spectroscopy and molecular energy levels calculations. J Phys Chem A 105(19):4627–4632
22. Hare JP, Kroto HW, Taylor R (1991) Preparation and UV/visible spectra of the fullerenes C_{60} and C_{70}. Chem Phys Lett 177:394
23. Allemand PM, Koch A, Wudl F, Rubin Y, Diederich F, Alvarez MM, Anz SJ, Whetten RL (1991) Two different fullerenes have the same cyclic voltammetry. J Am Chem Soc 113(3):1050–1051
24. Xie Q, Pérez-Cordero E, Echegoyen L (1992) Electrochemical detection of C_{60}^{6-} and C_{70}^{6-}: enhanced stability of fullerides in solution. J Am Chem Soc 114:3978–3980
25. Bruno C et al (2003) Electrochemical generation of C_{60}^{2+} and C_{60}^{3+}. J Am Chem Soc 125:15738–15739
26. Ruoff RS, Tse DS, Malhotra R, Lorents DC (1993) Solubility of C_{60} in a variety of solvents. J Phys Chem 97:3379–3383
27. Iijima S, Ichihashi T (1993) Single-shell carbon nanotubes of 1-nm diameter. Nature 363:603–605
28. Bethune DS et al (1993) Cobalt-catalysed growth of carbon nanotubes with single-atomlc-layer walls. Nature 363:605–607
29. Journet C et al (1997) Large-scale production of single-walled carbon nanotubes by the electric-arc technique. Nature 388:756–758
30. Thess A et al (1996) Crystalline ropes of metallic carbon nanotubes. Science 273:483–487
31. Voiry D, Drummond C, Pénicaud A (2011) Portrait of carbon nanotube salts as soluble polyelectrolytes. Soft Matter 7:7998
32. Liu J et al (1999) Controlled deposition of individual single-walled carbon nanotubes on chemically functionalized templates. Chem Phys Lett 303:125–129
33. Ausman KD, Piner R, Lourie O, Ruoff RS, Korobov M (2000) Organic solvent dispersions of single-walled carbon nanotubes: toward solutions of pristine nanotubes. J Phys Chem B 104(38):8911–8915
34. Bahr JL, Mickelson ET, Bronikowski MJ, Smalley RE, Tour JM (2001) Dissolution of small diameter single-wall carbon nanotubes in organic solvents? Chem Commun 2:193–194
35. Furtado CA, Kim UJ, Gutierrez HR, Pan L, Dickey EC, Eklund PC (2004) Debundling and dissolution of single-walled carbon nanotubes in amide solvents. J Am Chem Soc 126:6095–6105

36. Ham HT, Choi YS, Chung IJ (2005) An explanation of dispersion states of single-walledcarbon nanotubes in solvents and aqueous surfactant solutions using solubility parameters. J Colloid Interface Sci 286:216–223
37. Detriche S, Zorzini G, Colomer JF, Fonseca A, Nagy JB (2008) Application of the Hansen solubility parameters theory to carbon nanotubes. J Nanosci Nanotechnol 8:6082–6092
38. Coleman JN (2009) Liquid-phase exfoliation of nanotubes and graphene. Adv Funct Mater 19:3680–3695
39. Liu J et al (1998) Fullerene pipes. Science 280:1253–1256
40. Mkumar T, Mezzenga R, Geckeler KE (2012) Carbon nanotubes in the liquid phase: addressing the issue of dispersion. Small 8:1299–1313
41. Wenseleers W et al (2004) Efficient isolation and solubilization of pristine single-walled nanotubes in bile salt micelles. Adv Funct Mater 14:1105–1112
42. Martel R (2008) Sorting carbon nanotubes for electronics. ACS Nano 2:2195–2199
43. Arnold MS, Stupp SI, Hersam MC (2005) Enrichment of single-walled carbon nanotubes by diameter in density gradients. Nano Lett 5:713–718
44. Tarascon JM, DiSalvo FJ, Chen CH, Carrol PJ, Walsh M, Rupp L (1985) First example of monodispersed (Mo_3Se_3) clusters. J Solid State Chem 58:290–300
45. Lee RS, Kim HJ, Fischer JE, Thess A (1997) Conductivity enhancement in single-walled carbon nanotube bundles doped with K and Br. Nature 388:255–257
46. Pénicaud A, Petit P, Fischer JE (2012) Doped carbon nanotubes. In: Monthioux M (ed) Carbon meta-nanotubes: synthesis, properties and applications, 1st edn. Wiley, Hoboken, pp 41–111
47. Pénicaud A, Poulin P, Derré A (2003) Procédé de dissolution de nanotubes de carbone, CNRS, WO 2005/073127; PCT/FR04/03383
48. Bendiab N, Anglaret E, Bantignies JL, Zahab A, Sauvajol JL, Petit P, Mathis C, Lefrant S (2001) Phys Rev B 64:245424
49. Petit P, Mathis C, Journet C, Bernier P (1999) Tuning and monitoring the electronic structure of carbon nanotubes. Chem Phys Lett 305:370–374
50. Vigolo B et al (2009) Direct revealing of the occupation sites of heavy alkali metal atoms in single-walled carbon nanotube intercalation compounds. J Phys Chem C 113:7624–7628
51. Giordani S, Bergin SD, Nicolosi V, Lebedkin S, Kappes MM, Blau WJ et al (2006) Debundling of single-walled nanotubes by dilution: observation of large populations of individual nanotubes in amide solvent dispersions. J Phys Chem B 110(32):15708–15718
52. Jiang C, Saha A, Xiang C, Young C, Tour JM, Pasquali M et al (2013) Increased solubility, liquid crystalline phase and selective functionalization of single-walled carbon nanotube polyelectrolyte dispersions. ACS Nano 7:4503–4510
53. Paolucci D, Melle Franco M, Iurlo M, Marcaccio M, Prato M, Zerbetto F, Pénicaud A, Paolucci F (2008) Singling out the electrochemistry of individual single-walled carbon nanotubes in solution. J Am Chem Soc 130:7393–7399
54. Voiry D, Vallés C, Roubeau O, Pénicaud A (2011) Dissolution and alkylation of industrially produced multi-walled carbon nanotubes. Carbon N Y 49:170–175
55. Liang F, Sadana AK, Peera A, Chattopadhyay J, Gu Z, Hauge RE, Billups WE (2004) Nano Lett 4:1257–1260
56. Chattopadhyay J et al (2005) Carbon nanotube salts: arylation of single-wall carbon nanotubes. Org Lett 7:4067–4069
57. Graupner R et al (2006) Nucleophilic-alkylation-reoxidation: a functionalization sequence for single-wall carbon nanotubes. J Am Chem Soc 128:6683–6689
58. Martínez-Rubí Y, Guan J, Lin S, Scriver C, Sturgeon RE, Simard B (2007) Rapid and controllable covalent functionalization of single-walled carbon nanotubes at room temperature. Chem Commun 48:5146–5148
59. Guan J, Martinez-Rubi Y, Dénommée S, Ruth D, Kingston CT, Daroszewska M et al (2009) About the solubility of reduced SWCNT in DMSO. Nanotechnology 20(24):245701

60. Voiry D, Roubeau O, Pénicaud A (2010) Stoichiometric control of single walled carbon nanotubes functionalization. J Mater Chem 20:4385
61. Chen Z, Wu Z, Sippel J, Rinzler AG (2004) Metallic/semiconducting nanotube separation and ultra-thin, transparent nanotube films. In: Electronic properties and synthesis of nanostructures B. Series of AIP conference proceedings, New York, vol 723, pp 69–74
62. Krupke R, Hennrich F, von Löhneysen H, Kappes MM (2003) Separation of metallic from semiconducting single-walled carbon nanotubes. Science 301:344–347
63. Hodge SA, Fogden S, Howard CA, Skipper NT, Shaffer MSP (2013) Electrochemical processing of discrete single-walled carbon nanotube anions. ACS Nano 7:1769–1778
64. O'Connell MJ, Bachilo SM, Huffman CB, Moore VC, Strano MS, Haroz EH et al (2002) Band gap fluorescence from individual single-walled carbon nanotubes. Science 297:593–596
65. Islam MF, Rojas E, Bergey DM, Johnson AT, Yodh AG (2003) High weight fraction surfactant solubilization of single-wall carbon nanotubes in water. Nano Lett 3(2):269–273
66. Geim AK (2009) Graphene: status and prospects. Science 324:1530–1534
67. Wu J, Pisula W, Müllen K (2007) Graphenes as potential material for electronics. Chem Rev 107:718–747
68. Cai J et al (2010) Atomically precise bottom-up fabrication of graphene nanoribbons. Nature 466:470–473
69. Cano-Márquez AG et al (2009) Ex-MWNTs: graphene sheets and ribbons produced by lithium intercalation and exfoliation of carbon nanotubes. Nano Lett 9:1527–1533
70. Paiva MC et al (2010) Unzipping of functionalized multiwall carbon nanotubes induced by STM. Nano Lett 10:1764–1768
71. Janowska I et al (2009) Catalytic unzipping of carbon nanotubes to few-layer graphene sheets under microwaves irradiation. Appl Catal A 371:22–30
72. Jiao L, Zhang L, Wang X, Diankov G, Dai H (2009) Narrow graphene nanoribbons from carbon nanotubes. Nature 458:877–880
73. Kosynkin DV et al (2009) Longitudinal unzipping of carbon nanotubes to form graphene nanoribbons. Nature 458:872–876
74. Campos-Delgado J et al (2008) Bulk production of a new form of sp(2) carbon: crystalline graphene nanoribbons. Nano Lett 8:2773–2778
75. Ning G et al (2011) Gram-scale synthesis of nanomesh graphene with high surface area and its application in supercapacitor electrodes. Chem Commun (Camb) 47(5976–8)
76. Sun Z et al (2010) Growth of graphene from solid carbon sources. Nature 468:549–552
77. Zhu Y et al (2010) Graphene and graphene oxide: synthesis, properties, and applications. Adv Mater 22:3906–3924
78. Dreyer DR, Park S, Bielawski W, Ruoff RS (2010) The chemistry of graphene oxide. Chem Soc Rev 39:228–240
79. Krishnamoorthy K, Veerapandian M, Yun K, Kim S (2013) The chemical and structural analysis of graphene oxide with different degrees of oxidation. Carbon N Y 53:38–49
80. Hernandez Y et al (2008) High-yield production of graphene by liquid-phase exfoliation of graphite. Nat Nanotechnol 3:563–568
81. Lotya M et al (2009) Liquid phase production of graphene by exfoliation of graphite in surfactant/water solutions. J Am Chem Soc 131:3611–3620
82. Guardia L et al (2011) High-throughput production of pristine graphene in an aqueous dispersion assisted by non-ionic surfactants. Carbon N Y 49:1653–1662
83. Cravotto G, Cintas P (2010) Sonication-assisted fabrication and post-synthetic modifications of graphene-like materials. Chem Eur J 16:5246–5259
84. Khan U, O'Neill A, Lotya M, De S, Coleman JN (2010) High-concentration solvent exfoliation of graphene. Small 6:864–871
85. Novoselov KS, Geim AK, Morozov SV, Jiang D, Zhang Y, Dubonos SV, Grigorieva IV, Firsov AA (2004) Electric field effect in atomically thin carbon films. Science 306:666–669

86. Berger C et al (2004) Ultrathin epitaxial graphite: 2D electron gas properties and a route toward graphene based nanoelectronics. J Phys Chem B 108:19912–19916
87. Bae S et al (2010) Roll-to-roll production of 30-inch graphene films for transparent electrodes. Nat Nanotechnol 5:574–578
88. Behabtu N et al (2010) Spontaneous high-concentration dispersions and liquid crystals of graphene. Nat Nanotechnol 5:406–411
89. Vallés C et al (2008) Solutions of negatively charged graphene sheets and ribbons. J Am Chem Soc 130:15802–15804
90. Pénicaud A, Drummond C (2013) Deconstructing graphite: graphenide solutions. Acc Chem Res 46:129–137
91. Milner EM et al (2012) Structure and morphology of charged graphene platelets in solution by small angle neutron scattering. J Am Chem Soc 134:8302–8305
92. Englert JM et al (2011) Covalent bulk functionalization of graphene. Nat Chem 3:279–286
93. Kelly KF, Billups WE (2013) Synthesis of soluble graphite and graphene. Acc Chem Res 46:4–13
94. Catheline A et al (2011) Graphene solutions. Chem Commun (Camb) 47(5470–2)
95. Catheline A et al (2012) Solutions of fully exfoliated individual graphene flakes in low boiling point solvents. Soft Matter 8:7882
96. Iijima S et al (1999) Nano-aggregates of single-walled graphitic carbon nano-horns. Chem Phys Lett 309:165–170
97. Endo M et al (2002) Structural characterization of cup-stacked-type nanofibers with an entirely hollow core. Appl Phys Lett 80:1267
98. Saito K, Ohtani M, Fukuzumi S (2006) Electron-transfer reduction of cup-stacked carbon nanotubes affording cup-shaped carbons with controlled diameter and size. J Am Chem Soc 128:14216–14217
99. Voiry D, Pagona G, Tagmatarchis N, Pénicaud A (2007) Solutions of carbon nanohorns, method for making same, and uses thereof, WO 2011/154894, demande de brevet européen du 7 juin 2010, N° EP 10165108.1
100. Voiry D, Pagona G, del Canto E, Ortolani L, Morandi V, Noé L, Melle Franco M, Monthioux M, Tagmatarchis N, Penicaud A Individualized single-wall carbon nanohorns: a new form of metal free carbon nanomaterial, in preparation
101. Davis VA et al (2009) True solutions of single-walled carbon nanotubes for assembly into macroscopic materials. Nat Nanotechnol 4:830–834
102. Yotprayoonsak P, Hannula K, Lahtinen T, Ahlskog M, Johansson A (2011) Liquid-phase alkali-doping of individual carbon nanotube field-effect transistors observed in real-time. Carbon N Y 49:5283–5291
103. Lorençon E, Ferlauto AS, de Oliveira S, Miquita DR, Resende RR, Lacerda RG, Ladeira LO (2009) Appl Mater Interfaces 1:2104–2106
104. Hecht DS, Hu LB, Irvin G (2011) Emerging transparent electrodes based on thin films of carbon nanotubes, graphene, and metallic nanostructures. Adv Mater 23(13):1482–1513
105. Pénicaud A, Catheline A, Gaillard P (2011) Procédé de préparation de films transparents conducteurs à base de nanotubes de carbone, FR2011/051352
106. Monthioux M, Kuznetsov V (2006) Who should be given the credit for the discovery of carbon nanotubes? Carbon 44:1621–1623
107. Zakri C, Penicaud A, Poulin P (2013) Les nanotubes: des fibres d'avenir. Dossiers Pour la Sci 79:86

Top Curr Chem (2014) 348: 37–52
DOI: 10.1007/128_2013_519

Incorporation of Balls, Tubes, and Bowls in Nanotechnology

Derek R. Jones, Praveen Bachawala, and James Mack

Abstract The development of nanotechnology has been spearheaded by the development and discovery of new materials. The earliest materials theorized to be used in nanotechnology were fullerenes and nanotubes. Although fullerenes and nanotubes have a rich history in the area of nanotechnology, fullerene fragments, which share some the same properties as fullerenes and nanotubes, show potential in the field of nanotechnology as well. Fullerene fragments were synthesized close to 20 years prior to the discovery of fullerenes; however due to their complex synthesis they remained in relative obscurity in the field of nanotechnology. More recently, improved syntheses of corannulene and other fullerene fragments on an industrial scale have led to their potential in industrial applications. With the mass production of corannulene finally being realized, many new structures and exciting properties are making its way into the chemical literature.

Keywords Corannulene · Light Emitting diodes · Nanotechnology

Contents

D.R. Jones, P. Bachawala, and J. Mack (✉)
Department of Chemistry, University of Cincinnati, Cincinnati, OH 45221-0172, USA
e-mail: james.mack@uc.edu

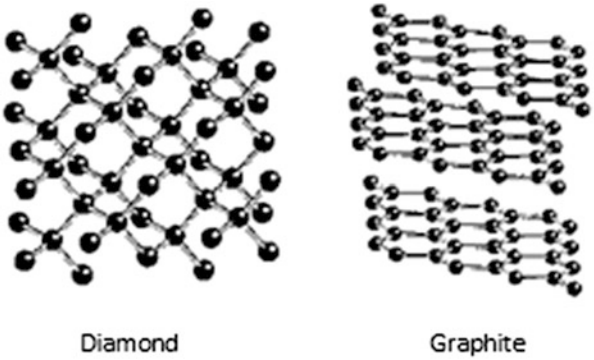

Fig. 1 Structures of a diamond lattice and graphite

1 Nanotechnology

Nanotechnology is a broad term that encompasses a wide range of topics within the scientific world. The idea of nanotechnology was conceived by physicist Richard Feynman at an American Physical Society meeting in 1959 with the idea that you could manipulate one set of atoms or molecules in order to build and control another proportionally smaller set of atoms or molecules [1]. The term nanotechnology was first coined by Professor Norio Taniguchi in a 1974 conference, describing it as "the processing of, separation, consolidation, and deformation of materials by one atom or one molecule." In 1981 the invention of instruments such as the scanning tunneling microscope helped to move the concept of nanotechnology forward [2]. Shortly thereafter fullerenes and nanotubes were discovered, thus bringing carbon into the exciting world of nanotechnology. Carbon is the 15th most abundant element in the Earth's crust, and the 4th most abundant element in the universe; considerable quantities occur in organic deposits of coal, oil, and gas and are the chemical basis of all known life. Until the twentieth century only two allotropes of carbon were known – diamond and graphite. Although both are forms of carbon, their physical properties differ greatly. Carbon atoms in diamonds are arranged in a face-centered cubic crystal structure called a diamond lattice and have strong covalent bonds between them, leading to the highest hardness and thermal conductivity of any bulk material. Diamond is also vastly transparent and is known for its unique optical properties. Graphite on the other hand has a layered, planar structure and its unique electrical conductivity is due to the high aromaticity leading to considerable electron delocalization between the carbon layers (Fig. 1). Graphite is the most stable form of carbon and is an excellent electrical conductor. Graphite is black in color and is most commonly used as "lead" in pencils and as lubricants.

Buckminsterfullerene (C_{60}) is a relatively new allotropic form of elemental carbon and is produced during the studies of nucleation in a carbon plasma formed by laser evaporation of graphite [3]. Buckminsterfullerene (C_{60}) was named after Richard Buckminster Fuller, a noted architectural modeler who popularized the geodesic dome. Fullerenes or "buckyballs" exhibits a closed carbon framework

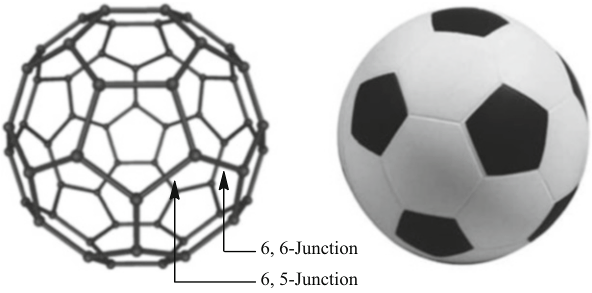

Fig. 2 Structural relationship of fullerene (C_{60}) and an American soccer ball

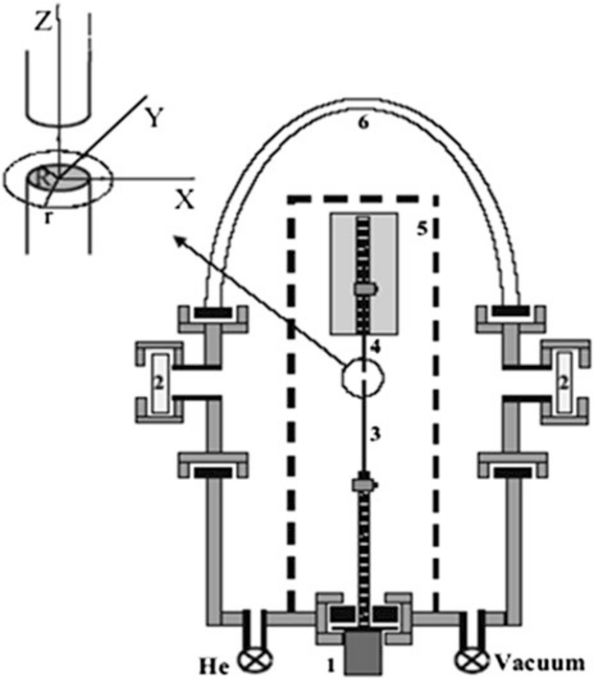

Fig. 3 Graphite electrode arc chamber: (*1*) motor for anode position control to maintain a constant inter-electrode distance, (*2*) quartz optical access ports for plasma spectroscopy, (*3*) anode, (*4*) cathode, (*5*) electrode holding platform, (*6*) glass dumbbell

with 20 hexagons and 12 pentagons (Fig. 2) and resembles an American soccer ball. Fullerene carbon atoms are sp^2 hybridized and form geodesic cages.

The C_{60} molecule has two different bond lengths. C–C bonds at 6–6 junctions (between two hexagons) can be considered as double bonds and measure 1.40 Å, whereas C–C bonds at 6–5 junctions (between a hexagon and a pentagon) are longer and measure 1.45 Å [4]. Although C_{60} is the most stable and abundant fullerene, higher fullerenes (i.e., C_{70}, C_{76}, C_{84}) are found as small impurities. In 1990 Kratschmer and Huffman developed a way to synthesize gram quantities of fullerenes by passing a current between two graphite electrodes in an atmosphere of helium, causing the graphite to vaporize (Fig. 3) [5]. At present, C_{60} is manufactured on a metric ton scale every year.

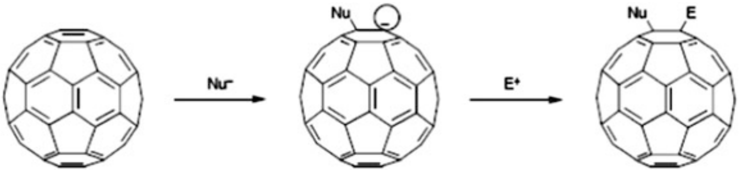

Scheme 1 Generic schematic of nucleophilic attack of C_{60} followed by quenching by electrophile

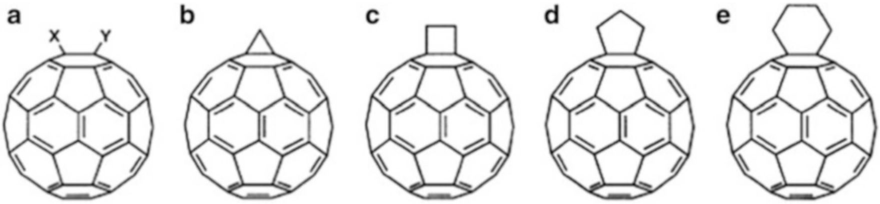

Fig. 4 Geometrical shapes of built onto a 6–6 ring junction of C_{60} (a) 1, 2 addition, (b) cyclopropanation, (c) 2+2 addition, (d) 3+2 addition, (e) 4+2 addition

Unlike diamond and graphite, fullerenes (C_{60}) are chemical reactive, having the chemical reactivity similar to that of an electron deficient olefin. C_{60} reacts readily with nucleophiles and is a reactive component in cycloadditions. The majority of reactants attack the 6–6 ring junctions of C_{60}, which possess more electron density. The insertions into 5–6 ring junctions have been reported only as rearrangements following a 6–6 junction attack. Adducts of C_{60} can be achieved by addition of a nucleophile followed by quenching with an acid or an electrophile (Scheme 1). Usually a 1,2-addition is observed, with many different adducts possible (Fig. 4).

Since their first detection and bulk production, fullerenes have played a leading role in the development of nanotechnology. Fullerenes are of great interest in this emerging field because they possess unique structural and electrical properties. The unique properties of fullerenes are desirable for various fields including nanoelectronics and materials science [6]. Fullerenes have numerous applications which include incorporation into polymers to obtain electroactive polymers or polymers with optical limiting properties, incorporation into thin films, and the design of novel molecular electronic devices. Furthermore, fullerenes have also been selected for potential uses in medicine including enzyme inhibition, photodynamic therapy, and electron transfer [7]. Its unusual closed geodesic structure can also be used for the entrapment of molecules.

2 Nanotubes

Carbon nanotubes are allotropes of carbon that were originally discovered in 1991 by Sumio Iijima [8]. Several techniques have been developed to produce nanotubes in large quantities, including arc discharge. Nanotubes were first observed in the

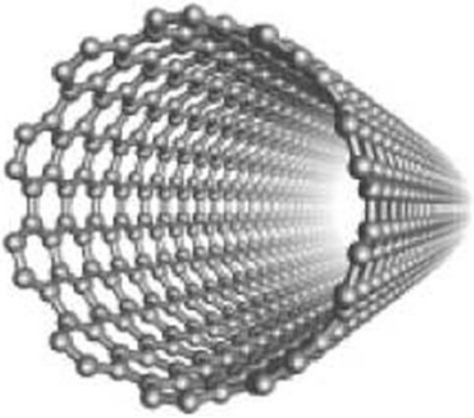

Fig. 5 Single-walled nanotube (SWNT)

carbon soot of graphite electrodes in an attempt to produce fullerenes, similar to the method used by Kratschmer and Huffman. This method is the most widely used to produce nanotubes with yields of up to 30% [9].

Nanotubes can be classified as "cylindrical fullerenes" and are usually only a few nanometers wide. Nanotubes can be classified as single-walled nanotubes (SWNTs) or multi-walled nanotubes (MWNTs) (Fig. 5).

Since nanotubes are in the same class of molecules as fullerenes, they possess similar properties and applications. Nanotubes have properties that include high tensile strength, high electrical conductivity, high ductility, high resistance to heat, and relative chemical inactivity. Although fullerenes and nanotubes have the above-mentioned unique structural and physical properties, current methods in which they are synthesized make it difficult to modify them chemically for specific tasks. Since their discovery, there have been thousands of publications and patents exploring their unique properties; however, progress towards tailoring them for specific chemical tasks has been slow [10, 11]. The "difficult processability" of fullerenes and complex mixtures prove troublesome for specific applications. Furthermore, the inability to reproduce single walled nanotubes consistently is still a major concern. It is these issues that limit the implementation of these molecules into viable uses in nanotechnology.

3 Corannulene

The advancement of nanotechnology is reliant on the discovery of new and promising materials. The area of fullerene fragments has been around for nearly 40 years, but has mostly been overlooked in the field of nanotechnology due to the original lengthy synthesis and small quantities produced. Corannulene, which represents one third of C_{60}, consists of a cyclopentane ring fused with five benzene rings. Corannulene was first synthesized in the 1960s by Barth and Lawton. The

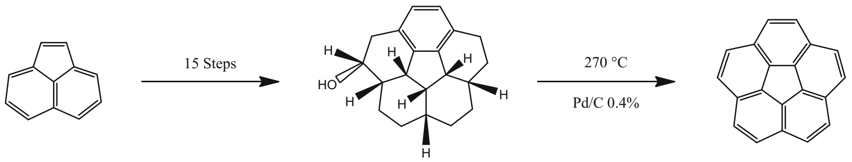

Scheme 2 Barth and Lawton's multi-step synthesis of corannulene (1)

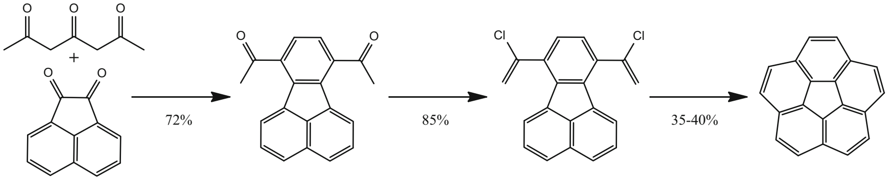

Scheme 3 Flash vacuum pyrolysis of corannulene

original synthesis was long and cumbersome with an overall yield of only 0.4% (Scheme 2) [12, 13].

Barth and Lawton were able to determine a bowl shaped geometry for corannulene, resulting in unusual strain associated with the central five-member ring. Furthermore, they concluded that all ten hydrogens on the outer rim of corannulene were equivalent, resulting in a singlet in the ^{1}H NMR spectrum.

Corannulene research went nearly dormant for over 2 decades. The original 17-step synthesis hindered any further insight into the chemical behavior of the novel hydrocarbon. The discovery of fullerenes and nanotubes renewed interest in this unique molecule. In the early 1990s, Scott (Scheme 3), Siegel, Rabideau and others proposed much shorter higher yielding syntheses of corannulene, making this unique molecule more available [14–19].

Although corannulene could be produced in larger quantities it was still far behind the commercialization of fullerenes and nanotubes. Therefore it was integral that a solution-based model be developed in order to obtain large scale quantities.

It is of great importance that macroscale quantities of corannulene be produced in order for its unique properties to be fully explored, leading to its implementation into the field of nanotechnology. Recently Siegel and co-workers have demonstrated the ability to produce kilogram quantities of corannulene (Scheme 4) [20].

Corannulene is of great interest because it has similar properties to that of fullerenes and nanotubes. Corannulene's structure is similar to C_{60} in that it maps perfectly onto its surface, as shown in Fig. 6.

Corannulene is one of only a few hydrocarbons to have a strong dipole moment, which is 2.07 D [21]. In comparison, water has a dipole moment of 1.8 D and ammonia that of 1.5 D. It also has a curved structure with its electron density localized in the center of the bowl, shown here in Fig. 7.

Furthermore, corannulene is one of only a few organic molecules to possess electrochromic properties. Electrochromism refers to the reversible color change

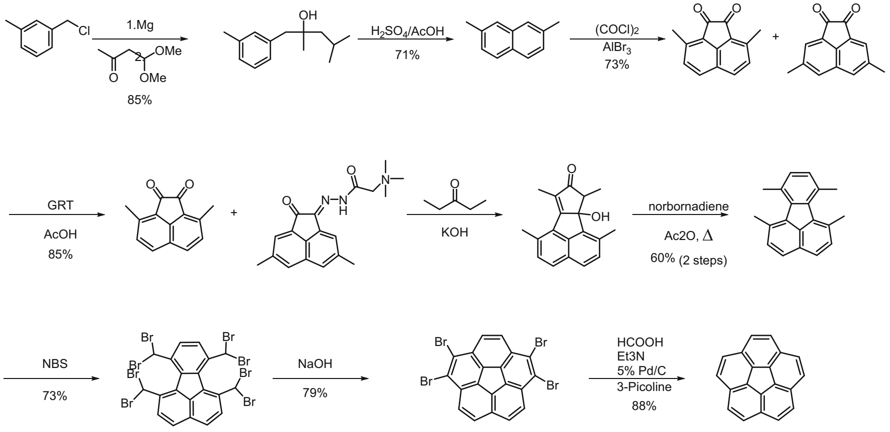

Scheme 4 Large scale synthesis of corannulene synthesis of corannulene

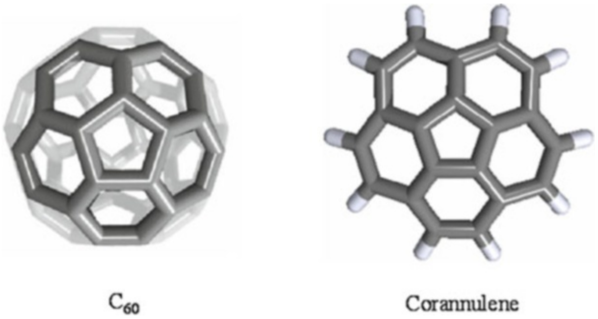

Fig. 6 Structural relationship between C_{60} and corannulene

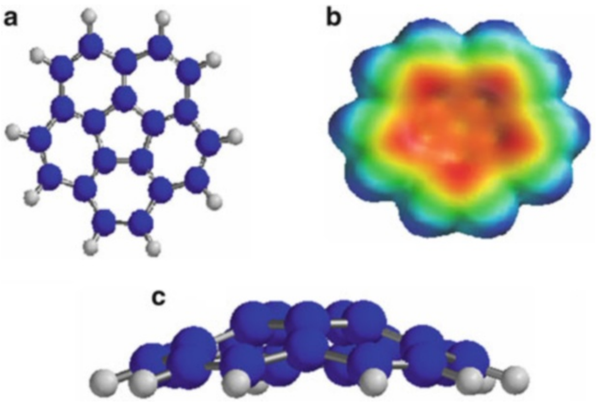

Fig. 7 (**a**) Molecular structure of corannulene. (**b**) Electron-density of corannulene. (**c**) Curvature of corannulene

associated with a chemical or electrochemical reduction. C_{60} has a triply degenerate low lying LUMO and has been shown to be electrochemically reduced six times, with reduction potentials of −0.98, −1.37, −1.87, −2.35, −2.85, and −3.26 eV [22–24]. Similarly, corannulene has a doubly degenerate low lying LUMO that can accept up to four extra electrons. In 1967, the first two reductions of corannulene were discovered and reported to be 1.88 and 2.36 eV [25]. Additionally, noticeable color changes associated with each reduction were observed. The first reduction gives a green color and the second reduction is associated with a bright red species. Attempts at this point to obtain a third and fourth reduction were unsuccessful. It was also noticed that the oxidations produced a polymeric product that blocked further oxidation. The third and fourth reductions were achieved later using lithium wire [26]. The third reduction gave a color change to purple, while the fourth reduction gave a brownish color. To date, the electrochemical reduction potentials of the third and fourth reductions are absent from the literature since the experiments were done using NMR. One field in which the electrochromic nature of coannulene would show great promise is in the area of organic electronics.

Organic electronics have been of interest in several fields such as chemistry and physics for more than 50 years [27]. Until recently, the electronic and optical phenomenon of these materials was restricted to academic research because of their limited practical applications. For example, electroluminescence from anthracene crystals manifested in 1960 by Pope et al. disclosed the phenomenon of organic electroluminescence [28]. Unfortunately, the application of organic light emitting diodes (OLEDs) was still unrealistic due to high operating voltage and catastrophic decay of light in just few minutes of operation [29, 30]. However, the ability of synthetic chemists to modify the chemical structure in ways that directly impact the properties of the materials when deposited in thin film form has provided a new direction to this field. A breakthrough was made by Tang et al. and Slyke at Kodak, who demonstrated the use of a low voltage and highly efficient thin film light emitting diode [31]. Their double-layer design soon became a landmark achievement and a prototypical structure in OLEDs. Even though results reported were not on par with existing technology, their discovery opened the door for the possible use of organic thin films based on light emitting diodes (OLED) as a platform for future generations to come. In the last 15 years the field of organic semiconductors has transformed itself rapidly from a topic of academic research interest to a wide range of applications, which include polymers LEDs [32], small molecule-based OLEDs [33, 34], organic lasers [35], organic transistors [36], and solar cells [37]. The commercial success of OLEDs is driven purely because of their low production cost, flexibility, and lower power consumption. However, key issues like control over desired emission colors with high emission intensity, efficiency, and the ability to display both electrical and optical stability for longer periods of time remain a bottleneck for today's synthetic chemists in designing these materials. More importantly, the synthesis of stable blue electroluminescent organic molecules with high efficiency and good color purity at practical levels of brightness remains a challenge [38].

Although the OLEDs have come a long way there are still major hurdles which must be addressed in order to advance the field further. A major concern that plagues OLED display is their shorter lifetimes, especially for blue OLED materials [27, 38]; typical lifetimes are 46,000–230,000 h in the case of red and green OLEDs but only 14,000 h for blue OLEDs. As OLED devices display pictures with high brightness, such a phenomenon would lead to higher voltages across a larger band gap, especially for blue emitting materials in comparison to their green and red counterparts, and hence, would result in faster degradation of blue emitting materials compared to green and red. Another issue is uneven color balance; over the period of time OLED material which produces a blue color tends to degrade faster than the rest, resulting in poor picture quality with unnatural color saturations.

Hence the future and thereby market capitalization of OLED-based display technology relies greatly on synthesizing more robust, thermally stable, easily processed and high quantum yield blue emitting OLEDs. Typically carbon is a poor conductor of electricity; however, carbon-based systems could act as good conductors when arranged in the form of a conjugated π system. Conduction of electricity followed by its electroluminescence properties are based on band gaps, ionization potentials, and the differences between energies of highest occupied molecular orbital (HOMO) and lowest unoccupied molecular orbital (LUMO). The difference between these two MOs is known as the HOMO–LUMO energy gap and is related to the minimum energy needed to excite an electron in a molecule. The energy required for an electronic transition corresponds to the molecules' wavelength of radiation. An alkene bond is described by two π orbitals of different energies, bonding and antibonding. In a conjugated molecule there is an effective overlap of π orbitals, resulting in a π–π conjugated system. Each additional alkene bond extending conjugation creates two new energy levels allowing the HOMO-LUMO gap to lessen. The decreased gap requires less energy to excite an electron and bathochromically (red shift) shifts the wavelength of emission possibly into the visible region; hence it is a vital tool to control and fine tune emission color.

Looking at the band gap comparison of polyenes, acenes, fullerenes, and corrannulene, we observe drawbacks for the use of aromatics in OLED fields (Fig. 8) [39].

Let us take a moment to examine various carbon-based conjugated system with reference to their band gap, commercial availability, and processability issues.

Initially, poly(*p*-phenylene-vinylene) (PPV) was used as an active material in fabrication of an OLED (Fig. 9) [40]. PPV is insoluble and difficult to process, and its incorporation into an OLED was via a soluble precursor method. This technique often involved intensive labor hours and generated high cost.

In an attempt to improve processability, PPV derivatives bearing long alkyl chains [41], alkoxy substituents [41, 42], and even metals [43, 44] were introduced following classical synthetic organic methods. However, steric repulsions between side chains cause a marked twisting of polymer backbones leading to very short conjugation lengths and corresponding aggregation leading to a shift of emission into UV region. Additionally, conjugated polymeric materials are difficult to

Fig. 8 Band-gap comparison of different π-conjugated system

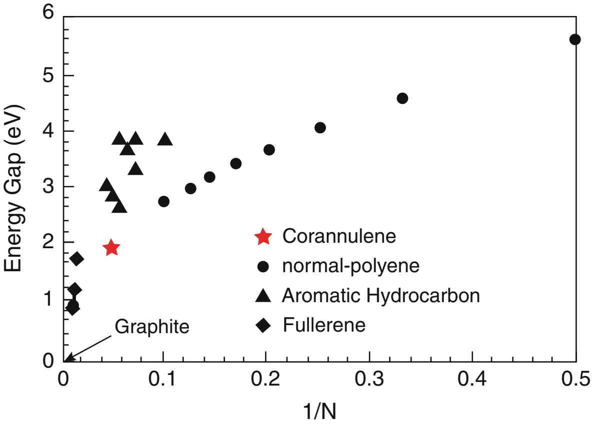

Fig. 9 Poly(*p*-phenylene vinylene)

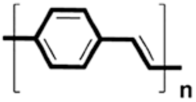

synthesize and purify. Once an impurity is built in, it can either be removed by chemical treatment or thermal conversion.

Next in the series are cyclic conjugated acenes: anthracene, tetracene, pentacene, hexacene, etc. With increasing numbers of benzenoid rings, the band gap rapidly decreases and so does chemical stability. For example, both green-hexacene and violet-pentacene must be handled under an inert atmosphere. Similarly, dark-green heptacene has never been obtained in a pure state due to rapid oxidation in air [45]. Moreover, strong π–π interactions are responsible for their aggregation in solution phase, thereby raising concerns over their processing to produce thin films. To help improve processability in the case of anthracene, bulky substituents were introduced at the 9, 10- positions [46, 47]. Substituents introduce steric strain to help limit intermolecular π–π interactions and enhance solubility. Literature proceedings also suggest that anthracene derivative-based devices showed recrystallization during device operation because of high voltage, leading to device failure [48].

Fullerenes also show photophysical properties but these properties are not easily modified. They absorb strongly in the ultra-violet region of the electromagnetic spectrum, with slight trailing into the visible region, as depicted in Fig. 10 [49]. However, attempts to lower band gap by connecting two fullerene units together with an acetylene bridge introduce an sp^3 hybridized carbon which disrupts the overall conjugation. Hence, even though two fullerenes are connected, because of disruption in π-communication each fullerene unit acts independently from each other. As a result there is no net reduction of band gap.

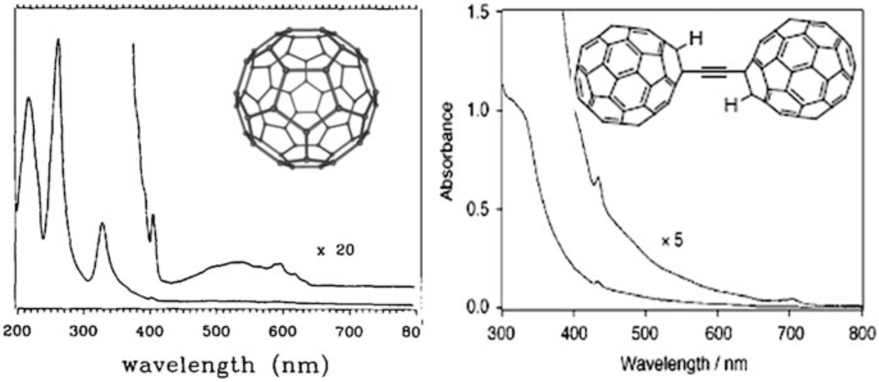

Fig. 10 UV-vis spectra of fullerene and difullerenylacetylene

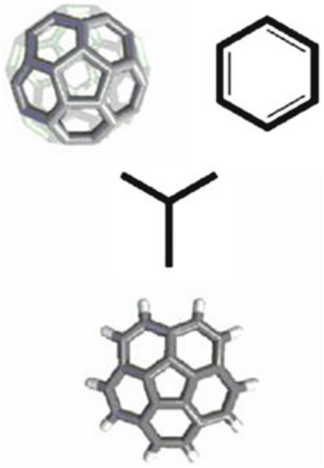

Fig. 11 Structural and chemical similarities of (**1**) with fullerene [C_{60}] and benzene

Carbon nanotubes are allotropes of carbon rolled into the form of cylindrical nanostructures exhibits exceptional thermal conductivity, mechanical and electrical properties. Its ability to exhibit such extraordinary properties stems from combination of the discrete angle created during its roll up and the radius formed. The inability to produce consistently carbon nanotubes that are tailored for specific needs remains a major bottleneck. Moreover, functionalization of carbon nanotubes to enhance their processability is often non-regioselective [50].

Because corannulene has the properties of both fullerenes and benzene, it possesses unique electronic properties more related to fullerenes as well as the ability to be modified like benzene (Fig. 11).

Corannulene has fluorescent properties and organic molecules using its framework could have a large impact on a variety of fields, including the display

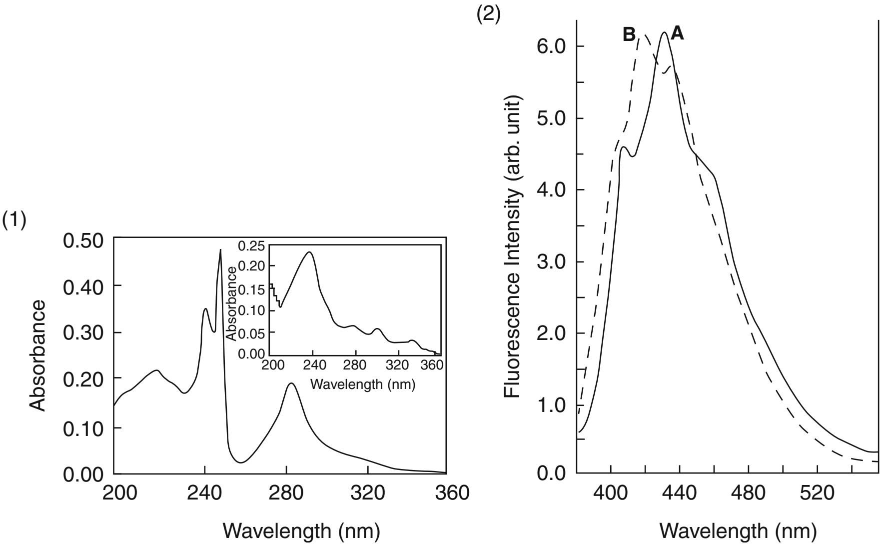

Fig. 12 (**a**) Absorption spectrum of cyclopentacorannulene in cyclohexane. (*Inset*) Absorption spectrum of corannulene in cyclohexane. (**b**) Fluorescence spectra of purified samples of (*A*) cyclopentacorannulene and (*B*) corannulene. Excitation wavelength = 285 nm

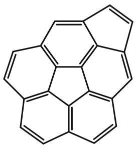

Fig. 13 Cyclopentacorannulene

industry [51]. It has been observed that the phosphorescence and fluorescence of corannulene has a lifetime of 2.6 ns and 10.3 ns, respectively [52]. The corannulene bowl inverts at a rate of approximately 200,000 times per second [53] and the fluorescence and phosphorescence spectra of corannulene is an average of the continuous bowl inversions (Fig. 12). The absorption and steady-state fluorescence measurements of corannulene and cyclopentacorannulene were examined to help determine the spectroscopic properties [54].

Cyclopentacorannulene consists of two additional carbon atoms attached to the outer rim of corrannulene, forming a cyclopentene ring (Fig. 13). The additional carbon atoms extend conjugation and increase rigidity and bowl depth to 1.05 Å (by comparison corannulene has a bowl depth of 0.89 Å). The observed bathochromic shift from corannulene to cyclopentacorannulene can be attributed to the additional π-electrons that extend the overall conjugation of the corannulene ring system. The bathochromic shift of the fluorescence spectrum of cyclopentacorannulene compared to corannulene can also be attributed to the additional π-electrons.

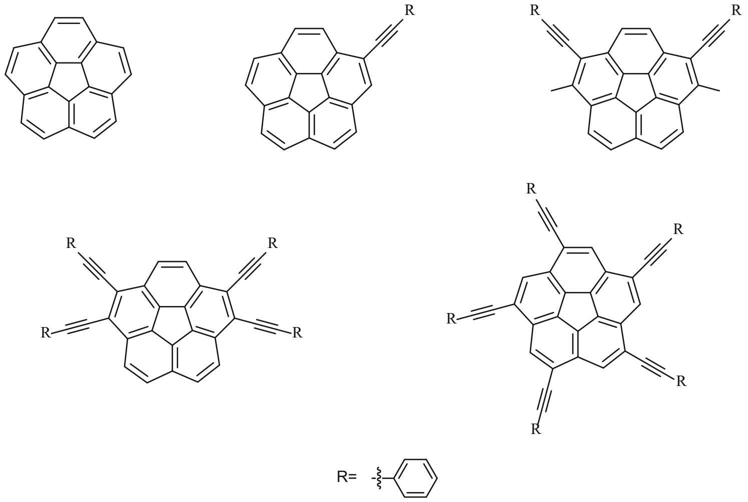

Fig. 14 Comparison study of multiethynylphenyl derivatives of corannulene

However, one major drawback to corannulene and cyclopentacorannulene being utilized as fluorescent materials are their low fluorescent quantum yields of (0.07) and (0.01), respectively. However, unlike fullerenes and nanotubes, linking corannulene with ethynyl bridges does not introduce an sp^3 hybridized carbon. Functionalizing corannulene in this manner allows for the ability to change the HOMO–LUMO gap and thereby changing the fluorescence properties. For these reasons – and many more – it is worth investigating the hidden properties of corannulene which would be highly beneficial in designing systems which could emit blue color with high quantum yields/thermal stability. With the ability to produce larger quantities of corannulene, more has been learned about the photophysical properties of this unique molecule. Bicorannlenylacetylene – an example of a monosubstituted corannulene derivative synthesized by Siegel's group – exhibits strong blue fluorescence with quantum yields of 0.57, more than eight times that of the parent corannulene [55]. However, bicorannulenylacetylene is unstable and quickly decomposes even at $-16°C$. Results clearly show that π-conjugation can be extended between corannulene units if tethered by triple bonds and show predominant red shift (302 nm) in the absorption spectrum. On the other hand, more recent reports from Siegel et al. highlight the expansion of ethnyl derivatives of disubstituted, tetrasubstituted, and pentasubstituted alkynyl corannulene derivatives [56].

Interesting absorption/quantum yield trends of multiethynyl corannulene derivatives have been presented (Fig. 14). Surprisingly, longer wavelength absorption was noticed for tetrasubstituted followed by disubstituted in comparison to highly symmetric pentasubstituted corannulene derivatives. Possible reasons for such an anomaly could be symmetry forbidden transition states and the presence of multiple non-radiative relaxation modes in ground states with higher rates of decay. Meanwhile the Mack group reported the synthesis/photophysical properties of a series of

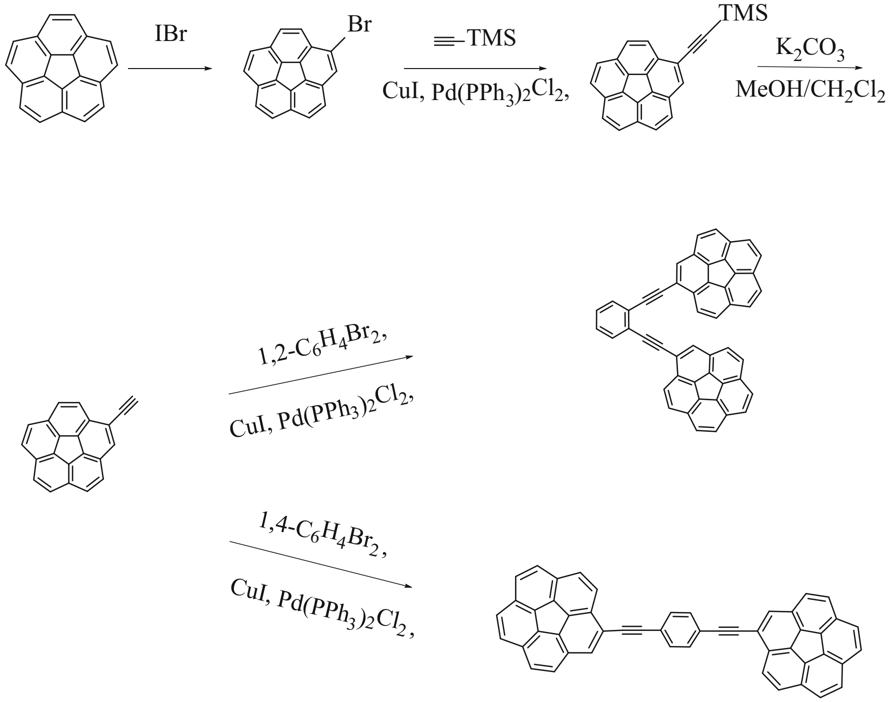

Scheme 5 Synthesis of 1,2-bis(corannulenylethynyl)benzene and 1,4-bis(corannulenylethynyl) benzene

o, *p*-substituted bis(corannulenylethynyl)benzenes (Scheme 5) [57]. The reason behind their synthesis was to examine the photophysical and thermal properties of these materials in comparison to bicorannuleneylacetylene. Surprisingly, none of these materials showed any signs of decomposition even at 300°C. As expected, both *ortho* and *para* substitution showed enhanced conjugation (299,371 nm).

These findings raise an important question with reference to the nature of linker and corresponding conjugating site. In benzene it is an established fact that groups placed in *ortho* and *para* positions are always in conjugation whereas in *meta* they are not. A detailed investigation related to site specificity on corannulene's rim have to be undertaken in order to understand which substitutions resemble *o*/*p* and *meta*. The data generated from these types of studies would certainly help in designing materials with extremely robust and thermally stable blue LEDs.

4 Conclusion

Corannulene and other fullerene fragments have considerable potential for uses in many applications. These properties can be directly applied to organic light emitting diode (OLED) technology. Improvements in the syntheses of these molecules can potentially make these structures viable building blocks in the development of nanotechnology. As bigger and more diverse carbon-based structures are synthesized, more properties of these unique molecules will be discovered. The development of carbon-based materials will potentially be the bridge between current problems and possible solutions.

References

1. Feynman RP (1960) Caltech Eng Sci 23(5):22–36
2. Binning G, Rohrer H, Gerber C, Weibel E (1993) In: Neddermeyer H (ed) Perspectives in condensed matter physics, vol 6. Springer, The Netherlands, pp 31–35
3. Kroto H, Heath J, O'Brien S, Curl R, Smalley R (1985) Nature 318:162–163
4. David WI, Ibberson RM, Matthewman JC, Prassides K, Dennis TJ, Hare JP, Kroto HW, Taylor R, Walton DR (1991) Nature 353:147–149. doi:10.1038/353147a0
5. Kraetschmer W, Lamb LD, Fostiropoulos K, Huffman DR (1990) Nature (Lond) 347:354
6. Prato M (1997) J Mater Chem 7:1097–1109
7. Jensen AW, Wilson SR, Schuster DI (1996) Bioorg Med Chem 4:767–779
8. Iijima S (1991) Nature 354:56–58
9. Collins P, Avouris P (2000) Sci Am 283:62–69
10. Langa F, Nierengarten J (2007) Fullerenes: principles and applications. Royal Society of Chemistry, Cambridge
11. Reich S, Thomsen C, Maultzsch J (2009) Carbon nanotubes: an introduction to the basic concepts and physical properties. Wiley-VCH, Cambridge
12. Barth W, Lawton R (1966) J Am Chem Soc 88:380–381
13. Lawton R, Barth W (1971) J Am Chem Soc 93:1730–1745
14. Scott L, Hashemi M, Meyer D (1991) J Am Chem Soc 113:7082–7084
15. Scott LT, Cheng P, Hashemi MM, Bratcher MS, Meyer DT, Warren HB (1997) J Am Chem Soc 119:10963–10968
16. Seiders TJ, Elliott EL, Grube GH, Siegel JS (1999) J Am Chem Soc 121:7804–7813
17. Mehta G, Panda G (1997) Tetrahedron Lett 38:2145–2148
18. Sygula A, Rabideau P (2000) J Am Chem Soc 122:6323–6324
19. Sygula A, Rabideau PW (1999) J Am Chem Soc 121:7800–7803
20. Butterfield AM, Gilomen B, Siegel JS (2012) Org Process Res Dev 16:664–676
21. Lovas F, McMahon R, Grabow J (2005) J Am Chem Soc 12:4345–4349
22. Xie Q, Perez-Cordero E, Echegoyen L (1992) J Am Chem Soc 114:3978–3980
23. Xie Q, Arias F, Echegoyen L (1993) J Am Chem Soc 115:9818–9819
24. Echegoyen L, Echegoyen LE (1998) Acc Chem Res 31:593
25. Janata J, Gendell J, Ling C, Barth WE, Backes L, Lawton RG (1967) J Am Chem Soc 89:3056–3058
26. Baumgarten M, Gherghel L, Wagner M, Weitz A, Rabinovitz M, Cheng P, Scott LT (1995) J Am Chem Soc 117:6254–6257
27. Aziz H, Popovic ZD (2004) Chem Mater 16:4522–4532
28. Pope M, Kallmann HP, Magnante P (1963) J Chem Phys 38:2042–2043
29. Helfrich W, Schneider WG (1965) Phys Rev Lett 14:229–231
30. Vincett PS, Barlow WA, Hann RA, Roberts GG (1982) Thin Solid Films 94:171–183
31. Tang CW, VanSlyke SA (1987) Appl Phys Lett 51:913–915
32. Cao Y, Parker ID, Yu G, Zhang C, Heeger AJ (1999) Nature 397:414–417
33. Tang CW, VanSlyke SA, Chen CH (1989) J Appl Phys 65:3610–3616
34. Baldo MA, Thompson ME, Forrest SR (2000) Nature 403:750–753
35. Schon JH, Meng H, Bao Z (2001) Nature 413:713–716

36. Schön JH, Kloc C, Dodabalapur A, Batlogg B (2000) Science 289:599–601
37. Huynh WU, Dittmer JJ, Alivisatos AP (2002) Science 295:2425–2427
38. Kulkarni AP, Jenekhe SA (2003) Macromolecules 36:5285–5296
39. Morii K, Fujikawa C, Kitagawa H, Iwasa Y, Mitani T, Suzuki T (1997) Mol Cryst Liq Cryst Sci Technol Sect A 296:357–364
40. Burroughes JH, Bradley DD, Brown AR, Marks RN, Mackay K, Friend RH, Burns PL, Holmes AB (1990) Nature 347:539–541
41. Andersson MR, Yu G, Heeger AJ (1997) Synth Met 85:1275–1276
42. Schwartz BJ, Hide F, Andersson MR, Heeger AJ (1997) Chem Phys Lett 265:327–333
43. Chuah BS, Hwang D, Kim ST, Moratti SC, Holmes AB, de Mello JC, Friend RH (1997) Synth Met 91:279–282
44. Kim ST, Hwang D, Li XC, Grüner J, Friend RH, Holmes AB, Shim HK (1996) Adv Mater 8:979–982
45. Boggiano B, Clar E (1957) J Chem Soc 2681–2689
46. Subramanian S, Park SK, Parkin SR, Podzorov V, Jackson TN, Anthony JE (2008) J Am Chem Soc 130:2706–2707
47. Kim YH, Shin DC, Kim SH, Ko CH, Yu HS, Chae YS, Kwon SK (2001) Adv Mater 13:1690–1693
48. Kim Y, Kwon S, Yoo D, Rubner MF, Wrighton MS (1997) Chem Mater 9:2699–2701
49. Tanaka T, Komatsu K (1999) J Chem Soc Perkin Trans 1 1671–1676
50. Balasubramanian K, Burghard M (2005) Small 1:180–192
51. Tucker SA, Fetzer JC, Harvey RG, Tanga MJ, Cheng PC, Scott LT (1993) Appl Spectrosc 47:715–722
52. Verdieck JF, Jankowski WA (1969) In: Benjamin WA (ed) Mol Lumin Int Conf, Inc, pp 829–36
53. Scott LT, Hashemi MM, Bratcher MS (1992) J Am Chem Soc 114:1920–1921
54. Dey J, Will AY, Agbaria RA, Rabideau PW, Abdourazak AH, Sygula R, Warner IM (1997) J Fluoresc 7:231–236
55. Jones CS, Elliott E, Siegel JS (2004) Synlett 1:187–191
56. Wu Y, Bandera D, Maag R, Linden A, Baldridge KK, Siegel JS (2008) J Am Chem Soc 130:10729–10739
57. Mack J, Vogel P, Jones D, Kaval N, Sutton A (2007) Org Biomol Chem 5:2448–2452

Top Curr Chem (2014) 348: 53–94
DOI: 10.1007/128_2013_447

Exploiting Nanocarbons in Dye-Sensitized Solar Cells

Ladislav Kavan

Abstract Fullerenes, carbon nanotubes, nanodiamond, and graphene find various applications in the development of solar cells, including dye sensitized solar cells. Nanocarbons can be used as (1) active light-absorbing component, (2) current collector, (3) photoanode additive, or (4) counter electrode. Graphene-based materials have attracted considerable interest for catalytic counter electrodes, particularly in state-of-the-art dye sensitized solar cells with Co-mediators. The understanding of electrochemical charge-transfer at carbon surfaces is key to optimization of these solar cells, but the electrocatalysis on carbon surfaces is still a subject of conflicting debate. Due to the rich palette of problems at the interface of nanocarbons and photovoltaics, this review is selective rather than comprehensive. Its motivation was to highlight selected prospective inputs from nanocarbon science towards the development of novel dye sensitized solar cells with improved efficiency, durability, and cost.

Keywords Dye sensitized solar cells · Carbon nanotubes · Graphene · Fullerenes · electrochemical impedance spectroscopy · Electrocatalysis

Contents

L. Kavan (✉)
J. Heyrovský Institute of Physical Chemistry, Academy of Sciences of the Czech Republic, v.v.i., Dolejškova 3, 182 23 Prague 8, Czech Republic
e-mail: kavan@jh-inst.cas.cz

1 Introduction

The increasing world's demand for electricity, confronted with inherent limitations of fossil and nuclear fuels, highlights renewable resources as the only energetic perspective for modern society. These topics represent one of the main tasks for science and technology of the twenty-first century. The sun is a unique source of renewable energy, providing the necessary terawatt power on global scale. Si-based photovoltaics was pioneered by Bell Labs in 1954, and since that time has developed into the standard technology of solar energy conversion. The dye sensitized solar cell (DSC), also called the Graetzel cell, represents an attractive alternative to solid-state photovoltaics, offering high efficiency at low cost and ease of fabrication [1–5]. The DSC is based on two grounds: (1) electrochemistry at semiconductor electrodes and (2) spectral sensitization of wide-band gap semiconductors to visible light. The first theme has been studied since 1960s [6–9] and the research accelerated after the seminal paper of Fujishima and Honda in 1972 [10].

The second theme, i.e., the spectral sensitization of wide-band gap semiconductors by dyes, has been explored since 1970s [11–13]. Graetzel et al. [14] pioneered in 1985 a sensitization of polycrystalline TiO_2 (anatase) electrodes by adsorption of Ru–bipyridine complex, and this subject attracted tremendous academic and commercial feedback during the next 3 decades [1–4, 15, 16]. Despite worldwide endeavours, the state-of-the-art devices are still based on the original concepts and materials. A pivotal material is nanocrystalline TiO_2 (anatase). Its application in DSC and similar electrochemical devices is, indeed, unique [17–22].

Optimization of DSC performance consists of several interconnected tasks, among which the materials engineering of both the TiO_2 photoanode and the counter electrode are key issues. The development of the TiO_2 electrode has been the subject of many studies (for review see [17–21]), but, until recently, the counter electrode of DSC has been investigated less extensively. The reason is obvious: whereas the nano-architecture of TiO_2 has a critical impact on DSC efficiency, the counter electrode (cathode) exhibited acceptable electrochemical performance even in the simplest variants used during the initial stages of DSC research.

The cathode of dye sensitized solar cells is often fabricated from conducting oxides, such as F-doped SnO_2 (FTO) or indium-tin oxide (ITO) which are modified with platinum to promote the electrocatalytic activity. The amount of Pt is so small that it almost does not influence the optical transmission of the conducting oxide support. FTO is also frequently used as a support for TiO_2 in the construction of photoanodes [1–4]. The second material of choice, e.g., for flexible DSCs, is Ti metal, albeit we lose, of course, the optical transparency of photoanode [3, 4]. Some of the above-mentioned materials, viz. Pt, FTO, and ITO, are problematic due to their high cost and limited natural abundance (In, Pt). Nevertheless, many practical DSCs still use noble metals (Ru-dyes, Pt catalyst) and the low cost stems from the fact that only small amounts of precious metals are required in the final devices.

The key process in DSC is sensitization, i.e., excitation of dye molecule adsorbed on TiO_2, $S|TiO_2$ by a photon of visible light. The subsequent event is injection of electrons from photoexcited dye, $S^*|TiO_2$ into the conduction band of TiO_2 (with quantum efficiency, η_{inj}):

$$S|TiO_2 + h\nu \rightarrow S^*|TiO_2 \rightarrow S^+ + e^-_{cb}(TiO_2) \tag{1}$$

As a result of this process, the dye molecule becomes oxidized (S^+). There is, however, also a parasitic effect, called recombination, i.e., back electron transfer:

$$S^+ + e^-_{cb}(TiO_2) \rightarrow S|TiO_2 \tag{2}$$

For proper function of DSC, the reaction at (2) must be hindered. To block recombination, holes must be rapidly removed from S^+ by a certain process which is kinetically competitive to (2). This is achieved either by (1) hole transport through a solid medium contacting the photoanode towards the counter electrode (solid-state DSC) or by (2) redox reaction with a suitable redox couple (mediator, shuttle, M) in the electrolyte solution contacting the photoanode (liquid-junction DSC):

$$S^+ + M \rightarrow S + M^+ \tag{3}$$

To close the regenerative loop, the oxidized mediator, M^+ must again be reduced back to M. This occurs at the counter electrode through the electron (originally e^-_{cb} (TiO_2)) after its passage through the external circuit towards the cathode:

$$M^+ + e^- \rightarrow M \tag{4}$$

In the first case of solid-state DSC, hole conductors like CuI and CuSCN were used, but the most effective hole-transporting medium is 2,2′,7,7′-tetrakis[*N*,*N*-di(4-methoxyphenyl)amino]-9,9′-spirobifluorene (*spiro*-OMeTAD) introduced by Bach and Graetzel in 1998 [15]. In the second case, the reduction of oxidized dye is carried out by iodide, I^-, i.e., the corresponding redox couple (M^+/M in (3)) is I_3^-/I^-. The traditional I-mediated DSC is schematically sketched in Fig. 1. The I_3^-/I^- mediator became very popular after the initial work by Graetzel et al. [23]. It was unrivalled for more than 20 years, when almost all liquid-junction DSCs relied on this redox shuttle. However, new discoveries in 2010/2011 highlighted alternative redox couples to I_3^-/I^-, which even generated a slogan *The end of iodide* [24].

The replacement of I_3^-/I^- by other M^+/M couples with more positive electrochemical potentials [25–28] such as $Co^{3+/2+}$ complexes [24, 28–37] resulted in the

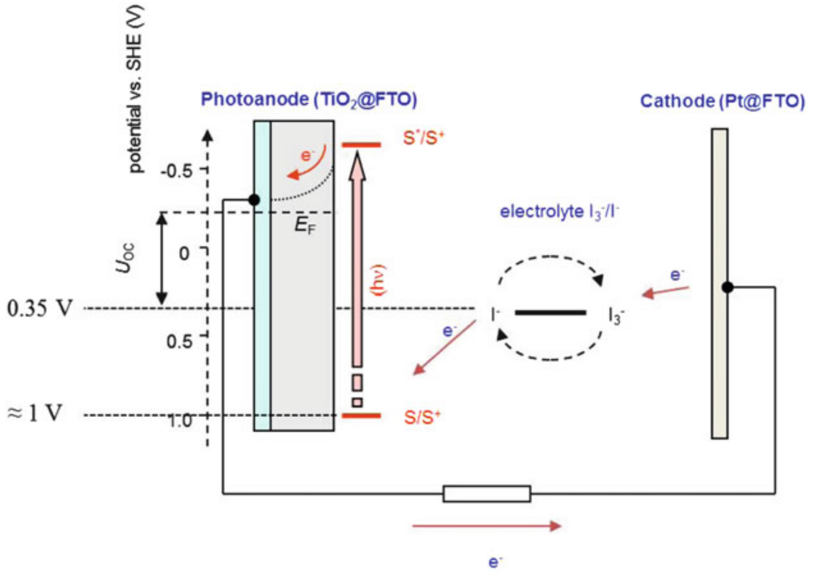

Fig. 1 Scheme of dye sensitized solar cell. A classical I-mediated liquid-junction solar cell is sketched with F-doped SnO_2 (FTO) as current collector both in TiO_2 photoanode and in the Pt cathode. S is sensitizer, S* is photoexcited sensitizer, and S^+ is oxidized sensitizer

record efficiency of 12.3% in 2011 [29]. These works are now considered as a *renaissance of DSC* [31]. Later on there was another breakthrough in the field, when Snaith et al. [38] reported on a hybrid solar cell based on meso-superstructured organometal halide perovskite (MSSC). Their device achieved remarkable efficiency of 10.9% utilizing some ideas and materials from solid-state DSC (TiO_2 as photoanode component and *spiro*-OMeTAD as hole conductor) but there are also fundamentally new concepts. The photoexcited electron is not assumed to be injected into the conduction band of photoanode, i.e., the perovskite is not considered "sensitizer" as in the traditional DSC.

1.1 Optimization of DSC Performance: Fundamentals

1.1.1 Photoanode

The optimization of the photoanode's nano-architecture can be simply illustrated by model calculation of the so-called "incident photon to current conversion efficiency" (IPCE). This quantity provides the number of electrons generated in a solar cell per one incident photon:

$$\mathrm{IPCE} = \frac{i_{\mathrm{ph}} hc}{P e \lambda} \tag{5}$$

where i_{ph} is the photocurrent density, h is Planck's constant, λ is the photon wavelength, c is the velocity of light, P is the incident light power density, and e is the electron charge. Sometimes we also find in the literature an analogous quantity, APCE (absorbed photon to electron conversion efficiency), which was introduced to consider inherent losses caused by light reflection and scattering in real cells. Some authors also use the terms "external quantum efficiency" (EQE) and "internal quantum efficiency" (IQC), but there is no fundamental difference between IPCE and EQE or between APCE and IQE. We shall continue to use the term IPCE because it is the most popular quantity to characterize the spectral response of a solar cell.

If we approximate the photoactive medium by a monolayer of a dye (with extinction coefficient ε and surface coverage Γ) we can also express the IPCE as follows:

$$\mathrm{IPCE} = \eta_{\mathrm{inj}} \cdot \eta_{\mathrm{coll}} \cdot (1 - 10^{-r_{\mathrm{f}}\Gamma\varepsilon}) \tag{6}$$

where η_{inj} is the efficiency of electron injection from the photoexcited dye into the TiO_2 conduction band, η_{coll} is the efficiency of collection of the injected electron by the back contact of photoanode, and r_{f} is the so-called roughness factor, defined as the ratio of total physical area of the electrode material divided by the projected cross-sectional area of the electrode. The last term in (6) is actually the efficiency of light absorption (light harvesting) which is quantified by the Lambert–Beer law.

For a good TiO_2 electrode we can approximate $\eta_{\mathrm{inj}} \cdot \eta_{\mathrm{coll}} \approx 1$. Assuming $r_{\mathrm{f}} = 1$, that is for a perfectly flat TiO_2 surface, and for the typical parameters of Ru–bipyridine dyes ($\varepsilon \approx 1.3 \times 10^7$ cm^2/mol, $\Gamma \approx 9.1 \times 10^{-11}$ mol/cm^2) we can calculate IPCE $\approx 0.27\%$; (the experimental value for anatase single crystal was 0.11%) [39]. On the other hand, assuming $r_{\mathrm{f}} = 1{,}000$, which is typical value for nanocrystalline films of TiO_2, (6) provides IPCE $\approx 93\%$. This efficiency is, indeed, achievable experimentally for optimized TiO_2 nano-architectures [1, 3, 4]. However, is says little about the efficiency of the conversion of solar light to electricity in a solar cell.

The reason is that the solar light is naturally white, ranging from UV to NIR radiation. Hence, one would require that the absorption band of the dye is broad enough to get large IPCE values for all the solar photons. There is a simple relation between IPCE (defined for monochromatic light, see (5)) and the overall photocurrent for white solar light: The short circuit photocurrent density for DSC illuminated by solar light, I_{SC} is given by the sum of individual contributions from IPCEs, integrated over the whole solar spectrum:

$$I_{\mathrm{SC}} = \int_0^{\infty} \mathrm{IPCE}(\lambda) \cdot P_{\mathrm{sun}}(\lambda)\mathrm{d}\lambda \tag{7}$$

where $P_{\mathrm{sun}}(\lambda)$ is the solar power density at the wavelength λ. The state-of-the-art DSC can achieve values I_{SC} of about 20 mA/cm^2 under full sun illumination [3, 4]. Such photocurrents were obtained as a result of development of photoanode material which is both the dye and the TiO_2 structure. Among other parameters, the values of ε, Γ and r_f play a significant role in the photocurrent optimization.

The photocurrent density, I_{SC}, together with the cell voltage define the efficiency of conversion of white (solar) light to electrical energy, Φ_{sol}. This solar conversion efficiency is expressed as the maximum electric power output per solar cell area, divided by the white light solar power density, P_{sol} (for AM 1.5, the conventionally used value of P_{sol} is 100 mW/cm^2):

$$\Phi_{sol} = \frac{I_{SC}U_{OC}}{P_{sol}} \cdot F_F \tag{8}$$

where U_{OC} is the open-circuit voltage. The parameter F_F is the so-called fill factor describing the non-ideality of the practical current/voltage profile:

$$F_F = \frac{I_{pmax}U_{pmax}}{I_{SC}U_{OC}} \tag{9}$$

with I_{pmax} being the photocurrent density and U_{pmax} being the voltage for which the Φ_{sol} is maximal. (Typical values of F_F are around 70%.) Obviously the efficiency Φ_{sol} is, for fundamental reasons, smaller than the well-known Shockley Queisser limit ($\Phi_{sol} \lesssim 32\%$) because DSC is a typical single-junction device [3, 4, 31].

1.1.2 Redox Mediator

Whereas the achievable current density, I_{SC}, is, to a great extent, dictated by the dye optical absorption spectrum and photoanode nanostructure (by the parameters ε, Γ, and r_f; see (5), (6), and (7)), the other crucial variable, i.e., the cell voltage, is mostly controlled by the redox mediator. For the assumed value of $U_{pmax} = 1$ V, we would theoretically get the “dream” efficiency of 20% (for AM 1.5 solar light, $P_{sol} = 100$ mW/cm^2) if we keep the photocurrent density, I_{pmax} of 20 mA/cm^2; see Sect. 1.1.1.

To address the voltage problem, we can approximate that U_{OC} is given by the difference between the quasi-Fermi level position, E_F, in TiO_2 and the position of energy level corresponding to the redox potential of a mediator (cf. Fig. 1). Consequently the cell voltage can be enhanced in two ways: either by (1) upshift of the Fermi level of TiO_2 or by (2) downshift of the redox level of mediator (this means *enhancement* of its redox potential in the electrochemical scale). In the first case the available shifts in band energetics are limited to tens of meV through engineering of the TiO_2 structure [40]. (Analogous shifts of ca. 0.1–0.3 eV are introduced by electrolyte additives, like 4-*tert*-butylpyridine, which adsorbs on TiO_2, or by insertion of Li^+ [3, 4].) On the other hand, the mediator selection is theoretically limited only by the electrochemical potential of the dye’s ground state, which is typically near 1 V vs SHE [1, 3, 4, 37]. The reason is that the mediator’s redox potential must be reasonably smaller than the dye’s redox potential ($\lesssim$1 V vs SHE) to leave some overpotential (driving force) for dye regeneration (3) [37].

This discussion leads to the simple conclusion that the I_3^-/I^- redox couple is hardly the optimum mediator for DSC due to its relatively low redox potential. It amounts to ca. 0.35 V vs SHE, i.e., the corresponding overpotential for dye regeneration (≈0.7 V) is too high (cf. Fig. 1) [24, 27, 28, 31]. Among other possible redox shuttles [27, 28] the Co-polypyridine complexes, coupled with donor-bridge-acceptor sensitizers, turned out to be particularly promising [24, 28–37, 41, 42]. For instance, the standard redox potential of $[\mathrm{Co(bpy)_3}]^{3+}/[\mathrm{Co(bpy)_3}]^{2+}$ (bpy is 2,2′-bipyridine) equals 0.56 V vs SHE, and this redox shuttle provided solar cells with U_{OC} near 0.9 V [24, 28–31, 33]. A still larger voltage of DSC ($U_{\mathrm{OC}} = 1.03$ V) is accessible with $[\mathrm{Co(bpy\text{-}pz)_2}]^{3+/2+}$; bpy-pz is 6-(1*H*-pyrazol-1-yl) 2,2′-bipyridine [37, 42] which has the standard redox potential of 0.86 V vs SHE.

The vast majority of work on Co-mediated DSCs has dealt with the traditional solar cell architecture with TiO_2 functioning as photoanode (Fig. 1). However, the Co-mediators can also be used in reverse devices, in which the sensitized semiconductor is used as photocathode; an example is p-doped nickel oxide, NiO [43].

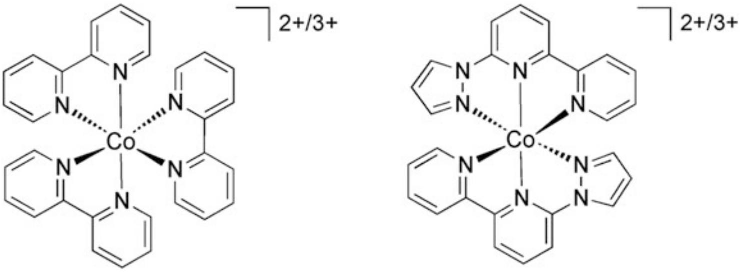

Structural formulae of two Co-polypyridine complexes used as redox couples in dye sensitized solar cells: $[\mathrm{Co(bpy)_3}]^{2+/3+}$ and $[\mathrm{Co(bpy\text{-}pz)_2}]^{3+/2+}$

The $[\mathrm{Co(bpy)_3}]^{3+}/[\mathrm{Co(bpy)_3}]^{2+}$ redox mediator in conjunction with an optimized combination of dyes as sensitizers demonstrated DSC with power conversion efficiency of 12.3%, which is the current world record DSC performance [29]. Most Co-mediated solar cells, including the champion (12.3%)-cell [29] still rely on the Pt-FTO cathode [29, 33–37, 44] but materials like conducting polymers (PEDOT or PProDOT) [30, 32, 37] and various form of nanocarbons have attracted considerable interest. The latter theme will be discussed in Sect. 3.3.4.

1.1.3 Counter Electrode

The role of counter electrode (cathode) in liquid-junction DSC consists in keeping the charge balance through the reduction of the oxidized state of the mediator, M^+, back to M (4). Ideally, the rate of mediator's reduction at the cathode should be comparable to the rate of dye regeneration by M at the photoanode. The latter is described by (3) and practically expressed by the photocurrent density, I_{SC}.

To avoid losses at the counter electrode, the exchange current density equivalent to reaction (4) should be comparable to I_{SC}.

In general, the electrocatalytic quality of an electrode is described by the exchange current density, j_0. An alternative quantity to assess the electrode activity is charge transfer resistance, R_{CT}, which can be obtained, e.g., from electrochemical impedance spectroscopy. Both quantities are related:

$$j_0 = \frac{RT}{nFR_{CT}} \tag{10}$$

where R is the gas constant, T is temperature, n is a number of electrons, and F is the Faraday constant. Assuming typical photocurrent densities on the TiO_2 photoanode working under full sun illumination [3] to be ca. 20 mA/cm^2 (Sect. 1.1.1), (10) provides an estimate of R_{CT} of 1.3 Ω cm^2 for the same j_0 value on the cathode. Such exchange current densities are accessible for I_3^-/I^- on a Pt@FTO cathode [45–47] as well as on thick carbon layers [45, 48, 49]. Due to the small amounts of Pt deposited on FTO (ca. 10 μg/cm^2), this traditional counter electrode is optically transparent which is beneficial for certain practical applications, albeit not mandatory for proper function of DSC [31, 50].

For the sake of completeness, we should mention that the exchange current density is also a function of mediator concentration (c_{ox} is a concentration of M^+, c_{red} is a concentration of M). This is described by the following equation:

$$j_0 = Fk_0\left(c_{ox}^{1-\alpha} \cdot c_{red}^{\alpha}\right) \tag{11}$$

where k_0 is the formal (conditional) rate constant of the electrode reaction and α is the charge-transfer coefficient. The rate constant, k_0, is yet another variable to assess the electrocatalytic activity of an electrode. It is the rate constant of electrochemical system at equilibrium, i.e., at the condition when the rate constants of anodic reaction and cathodic reaction are identical.

2 Carbon Nanostructures in Solar Cells Beyond DSC: General Overview

Nanocarbons (fullerenes, nanotubes, graphene, nanodiamond) are fascinating materials for a variety of reasons. Particularly in the field of this review is a fact that their structure-dependent electronic properties find applications in various types of solar cells, which have been developed since the early 1990s. This theme has been reviewed by several authors recently [51–59], so below only the main highlights are briefly summarized. The next section (Sect. 3) will specifically cover the field of nanocarbons in DSC. Treatment of this subject is compatible with the cited reviews [51–59] because they have concentrated on other types of solar cells and/or they did not cover the recent achievements in DSC research.

2.1 Fullerenes

Fullerene (C_{60} or C_{70}) is a good electron acceptor, representing a generic molecule for bulk heterojunction (BHJ) solar cells. These cells are also called organic photovoltaics (OPV) to stress the fact that all the active components are organic molecules. The concept of BHJ consists in an interpenetrating mixture of donor and acceptor molecules in the same medium. Fullerene is typically interfaced to semiconducting polymers like poly(phenylene vinylene) (PPV) or poly-3-hexylthiophene (P3HT) which act as electron donor and as a medium absorbing the majority of light. The pioneering work in 1995 [60] employed as acceptor the soluble fullerene derivative, viz. phenyl C_{61} butyric acid methyl ester ($PC_{61}BM$), and even the recently optimized systems still rely on these molecules ($PC_{61}BM$ or $PC_{71}BM$) [54, 61, 62]. The state-of-the-art solar cells of this type now achieve a power conversion efficiency (Φ_{sol}) of over 10% [54, 61, 63] (for a recent review see [63]).

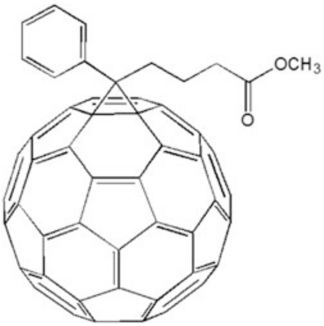

Structural formula of $PC_{61}BM$ molecule: [6,6]-phenyl-C_{61}-butyric acid methyl ester

2.2 Single-Walled Carbon Nanotubes

Single-walled carbon nanotubes (SWNTs) are attractive in the field of solar cells for two reasons. First, they represent ideal nanowires for electron transport, because the latter is ballistic, i.e., the electron is not scattered in the solid over a long distance. Second, they may act as active light-absorbing medium in solar cells. SWNT was considered as a current collector for transparent conducting thin films to replace ITO. Nanotubes in thin films may combine good electrical conductivity with high optical transparency, although the parameters of ITO are difficult to reach (for review see [64]).

SWNT are either semiconducting or metallic depending on the geometry of rolling (chirality). The existence of Van Hove singularities in the density of states defines a certain optical gap in the visible to near-infrared region, which brings salient inputs for electrochemistry and spectroelectrochemistry of SWNT [65, 66]. Particularly attractive is the fact that the usual SWNTs, having diameters between ca. 0.7 and

1.2 nm, provide the optical gap of 1.0–1.3 eV, which is close to the Shockley–Queisser optimum of photovoltaics devices. (We should note that most organic or organometallic dyes used in current DSCs have a considerably larger optical gap (HOMO/LUMO spacing) than this optimum [1–4].) Hence, SWNTs, particularly their semiconducting variant (s-SWNT), may serve as active optical absorbers in solar cells covering the near-IR part of the solar spectrum [67–70].

However, the efficiencies (Φ_{sol}) of sensitization through s-SWNT are still low, typically below 1%. One of the problems is the fact, that the photogenerated e^-/h^+ pair is bound in s-SWNT as an exciton. The dissociation of an exciton is crucial in solar cells, but is difficult to achieve in s-SWNT due to the large binding energy, which usually exceeds the thermal activation energy, k_bT. To overcome this problem the exciton dissociation must be driven by an external field, induced, e.g., by the presence of fullerenes or certain polymers acting as acceptors or donors, respectively [67–69]. The second main problem of SNWT, considered as a light absorber, is the fact that the usual samples are mixtures of semiconducting and metallic nanotubes. The metallic tubes effectively quench the excited state and hence purification of samples is necessary for the actual applications.

2.3 Graphene

Graphene is attractive due to its high mobility for electrons and holes associated with the well-known optical transmittance of 97.7%. This makes graphene a material of choice for a transparent current collector. Practically useful are films made from reduced graphene oxide [57, 71]. However, the sheet resistances achieved so far are typically between 1 and 0.1 kΩ/sq, i.e., still below those of ITO (1–10 Ω/sq). This situation is quite reminiscent of SWNT thin films (see Sect. 2.2).

Graphene also finds application in classical solid-state photovoltaics. Graphene forms Schottky junctions with a variety of semiconductors like CdS, CdSe, and Si. The efficiency of 8.6% was reported for the junction of n-Si with graphene which was doped with bis-(trifluoromethanesulfonyl)amide (TFSA) [72]. Graphene, together with other carbonaceous nanostructures, actually provide all the necessary functions to design an *all-carbon solar cell*. Indeed, it is possible to construct a solar cell, in which all the active components are nanocarbons only (fullerenes, SWNTs, and graphene or graphite) [73–75]. A device composed of $PC_{71}BM$, semiconducting SWNT, and reduced graphene oxide (rGO) achieved the record efficiency (Φ_{sol}) of 1.3% [75]. Figure 2 shows a schematic sketch of this solar cell.

In the all-carbon solar cell, the main light absorbing medium is $PC_{71}BM$ which harvests photons in the visible part of solar spectrum (Fig. 2c, black curve). The holes from photoexcited $PC_{71}BM$ are transported through reduced graphene oxide toward semiconducting SWNT. This device obviously uses the design of BHJ cells (see Sect. 2.1). The hole transfer is facilitated by the existence of Schottky barriers at each of the interfaces in the assembly $PC_{71}BM$/rGO/SWNT. Furthermore, semiconducting SWNT also takes over the function of a second light absorber,

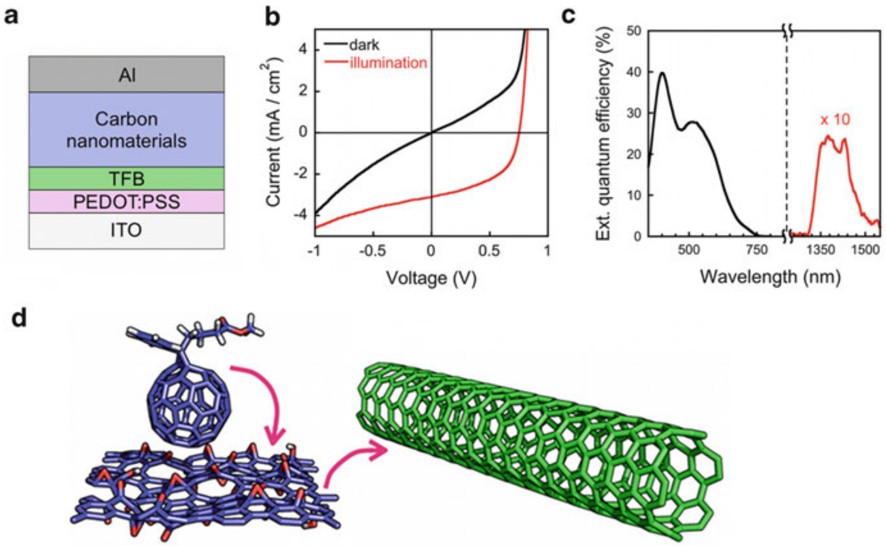

Fig. 2 Scheme of all-carbon solar cell. (**a**) Structure of the device, ITO = indium tin oxide, PEDOS:PSS = poly(3,4-ethylenedioxythiophene) poly(styrenesulfonate) acting as hole conducting layer, TFB = poly[(9,9-dioctylfluorenyl-2,7-diyl)-*co*-(4,4′-(*N*-(4-*s*-butylphenyl)) diphenylamine)] acting as an electron blocking layer. (**b**) Current–voltage characteristics in the dark and under illumination with full sun (AM 1.5). (**c**) External quantum efficiency (a quantity similar to IPCE) as a function of wavelength. (**d**) Scheme of cell interfaces; *pink arrows* show the pathway of photogenerated holes from $PC_{71}BM$ (phenyl C_{71} butyric acid methyl ester) through reduced graphene oxide to SWNT. Reprinted with permission from M. Bernardi et al. *ACS Nano* **6**, 8896 (2012). Copyright (2012) American Chemical Society

which harvests photons in the near-IR region of the solar spectrum. This is expressed by the red curve in Fig. 2c, which is a plot of EQE vs wavelength (for discussion of EQE and IPCE see Sect. 1.1.1 and (5)). Strictly speaking, this device is not “truly all-carbon” because it requires other auxiliary materials, viz. ITO and Al for electrical contacts and certain polymers as electron/hole blocking media (see Fig. 2a) [75]. Further research is needed to test whether or not the all-carbon solar cell is just a laboratory curiosity or a new technological perspective of solar conversion. It has been predicted that efficiencies similar or larger than those of the traditional BHJ cells (9–13%) might be accessible [75].

Graphene is also attractive for the possibility of tuning the band gap in certain size-controlled structures like nanoribbons. While the bulk graphene has a zero band gap, the size engineering of small nanoplatelets allows, in principle, tuning of the band gap from 0 to that of benzene. In this way, one could theoretically cover the whole solar spectrum by graphene quantum dots. Yan et al. [76] demonstrated that size-engineered graphene quantum dots can even be used as regular sensitizer in DSC. They proved the principle using graphene instead of the traditional Ru–bipyridine sensitizer in the I-mediated DSC. While their device exhibited at AM 1.5 illumination quite reasonable U_{OC} of 0.48 V and F_F of 0.58, the I_{SC} was only 0.2 mA/cm^2, i.e., two orders of magnitude smaller than the current densities observed in standard DSCs with organometallic sensitizers.

2.4 Nanodiamond

There have only been a few attempts to use boron-doped (p-doped) nanocrystalline diamond as a current collector to replace ITO in ordinary OPV cells. The O-terminated p-doped diamond is attractive for anode current collector, due to well-matching band energetics with polymers like P3HT, and intrinsic hole-acceptor characteristics of nanodiamond [77]. Similarly, the H-terminated p-doped nanocrystalline diamond was chemically modified by covalent grafting of bi-thiophene-C_{60}; this electrode exhibited promising photoresponse compared to that of reference devices with ITO-supported active material [78]. However, the solar conversion efficiency is still not competitive with that of fully optimized OPV devices.

3 Carbon Nanomaterials in DSC

Carbon nanomaterials are frequently used for fabrication of DSC electrodes, both cathodes and anodes, but there are also sporadic reports about the application of nanocarbons as additives in the electrolyte. For instance, graphene oxide was recently used as gelator of 3-methoxypropionitrile electrolyte solutions for application in quasi-solid-state dye sensitized solar cells [79]. Various forms of nanostructured carbons (carbon black, nanotubes, graphene) can be found in DSC electrodes. Here, they have four basically different functions: (1) active light absorbing medium, (2) current collector, (3) additive material in TiO_2 photoanode, and (4) electrocatalyst in counter electrode. The first option has already been mentioned for semiconducting SWNT (Sect. 2.2) and for graphene-based quantum dots (Sect. 2.3). Although this application of nanocarbons is certainly challenging scientifically, the performance of actual devices is still too low to be competitive with those of standard sensitizers, i.e., organic or organometallic dyes and inorganic quantum dots. Below we shall concentrate on the remaining three functions, the last one being, obviously, the most promising application of nanocarbons in DSCs.

3.1 Nanocarbons as Current Collectors in TiO_2 Photoanodes

There have been only few attempts at using carbon instead of FTO, ITO, or Ti as the photoanode current collector in DSCs. The reason is recognizable: due to significant electrocatalytic activity of carbon for the I_3^-/I^- redox mediator (and even larger for the Co^{3+}/Co^{2+} redox mediators, see Sect. 3.3.4), carbonaceous support of mesoporous TiO_2 photoanode would accelerate the undesired recombination

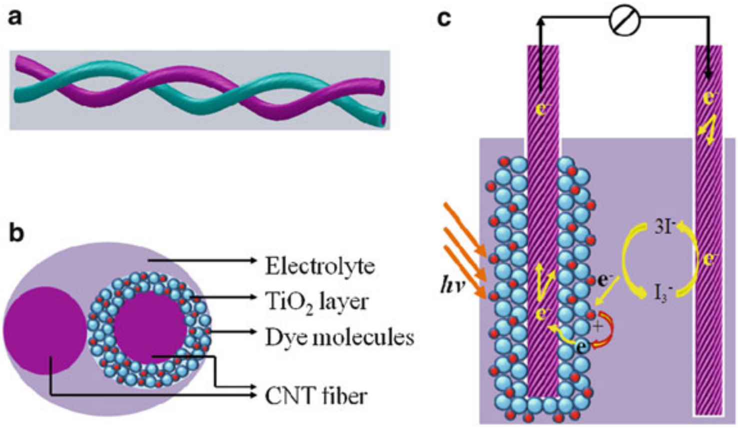

Fig. 3 Scheme of intertwined nanotube-based dye sensitized solar cell. The cell is fabricated from two nanotube fibers acting as current collectors both in photoanode and cathode. (**a**) Side view. (**b**) Top view. (**c**) Scheme of operation with electron flow. Reprinted with permission from T. Chen et al. *Nano Letters* **12**, 2568 (2012). Copyright (2012) American Chemical Society

reaction (2) at all the sites where carbon is contacting the electrolyte solution in the mesopores of titania matrix. Consequently, carbonaceous current collectors could find prospective applications in DSCs which do not require redox mediators in electrolyte solution, like in solid-state DSC.

An exception to this rule was, however, reported by Chen et al. [80] who developed a liquid-junction DSC using I_3^-/I^- redox mediator, where a carbon nanotube served as current collector both in the photoanode and in the cathode. Their photoanode was a layer of TiO_2 nanoparticles deposited directly on a carbonaceous fiber made from aligned carbon nanotubes. The fiber-shaped photoanode was spined with another fiber from pure nanotubes acting as the counter electrode. Figure 3 shows a scheme of this solar cell. It is based on the traditional platform of DSC, i.e., I-mediated hole transport in the electrolyte solution and Ru–bipyridine complex as the sensitizer of TiO_2. However, this unconventional geometry of intertwined two-wire cables can be used for manufacturing woven fabrics. This DSC can be fabricated in the form of photoactive textiles with a variety of potentially attractive applications in portable devices, such as in clothing-integrated solar cells.

However, the attained efficiency $\Phi_{sol} = 2.94\%$ of the "textile-like" solar cell is still considerably smaller than the efficiency of the same DSC, but with FTO-supported TiO_2. It was not quantified, whether or not recombination was responsible for the loss of efficiency, but the geometry of woven cloth is surely of interest for future developments. In this design, carbon nanotube served both as a current collector and as a cathode catalyst. Zhang et al. [81] developed a conceptually analogous device from woven fabric, in which carbon nanotube yarn served as a counter electrode, Ti wire coated with CdSe was the photoanode and polysulfide the electrolyte mediator. Their solar cells achieved efficiencies in the range from 1% to 2.9%. Hence, further optimization is needed to decide whether or not "woven photovoltaics" is the prospective application of semiconducting nanowires and carbon nanotubes.

Guo et al. [82] used carbon fiber as current collector underneath a TiO_2 photoanode. They grew rutile nanorods by a hydrothermal route on top of carbon fiber substrate. This photoanode architecture was implemented in traditional DSC with N719 sensitizer and I_3^-/I^- mediator in the electrolyte solution, and demonstrated 1.28% conversion efficiency. In some cases, nanocarbons, such as nanotubes or graphene, might also serve as local current collectors interconnecting individual TiO_2 nanoparticles either mutually or with the FTO support of the photoanode. This theme will be discussed in Sect. 3.2.

3.1.1 Graphene as Current Collector

Graphene is an attractive material for the current collector of FTO-free, solid-state DSCs because it forms transparent, conductive, and stretchable thin-film electrodes [57, 83–85]. We also note that the calculated work functions of graphene (4.42 eV) and FTO (4.4 eV) are quite close [86]. For comparison, the work function of transparent conductive MWNT sheets, which might be also considered as an alternative current collector, equals 5.2 eV [87]. Müllen et al. [86] have pioneered the use of graphene as a current collector layer underneath a TiO_2 photoanode. Their device was solid-state dye sensitized solar cell with *spiro*-OMeTAD as a hole conductor. The graphene layer used had a conductivity of 550 S/cm and optical transparency of more than 70% within the 1,000–3,000 nm wavelengths region, but it dropped down to ca. 50% at 400 nm. Direct comparison of graphene- and FTO-based cells indicated a factor of 3 smaller efficiency of the former, due to lower conductivity and optical transparency of the graphene used [86]. However, there is certainly room for improvement, which would eventually avoid the expensive FTO in solid-state DSCs.

The use of graphene as a cathode current collector in liquid-junction I-mediated DSC was investigated recently by Lee et al. [88]. They prepared graphene by the conventional CVD route with Cu-catalyst. However, they found that graphene is sensitive to delamination from the support in contact with the I-containing electrolyte. To avoid direct contact with the electrolyte solution, graphene was overcoated with a conducting polymer (PEDOT). In this example of a Pt- and FTO-free electrode, the conducting polymer takes over the catalytic function, and graphene enhances the electron transport, i.e., decreases the sheet resistivity of the cathode.

Recently, Chen et al. [89] reported that a film of graphene current collector can even act as an efficient recombination-blocking layer, acting even better than the standard TiO_2 underlayer made by hydrolysis of $TiCl_4$. They grew graphene by hydrazine reduction of GO and interspersed it between TiO_2 and FTO. The solar conversion efficiency of their DSC improved remarkably from 5.80% to 8.13%.

3.2 Nanocarbons as Additives to TiO_2 Photoanode

Graphitic thin films, single-walled carbon nanotube (SWNT), or graphene are incorporated in TiO_2 electrodes, where they are supposed to serve as electron-transporting scaffolds [90–94]. The motivation for making such a composite photoanode is increasing the electron diffusion length and thus improving the electron collection. It is rationalized by the fact that charge transport in a DSC photoanode is driven by electron diffusion. The electron diffusion length, L_e is given by

$$L_\mathrm{e} = \sqrt{D_\mathrm{e}\tau_\mathrm{e}} \tag{12}$$

where D_e is the electron diffusion coefficient and τ_e is the electron lifetime. Hence, the electron collection efficiency, η_coll (see also (6)) equals

$$\eta_\mathrm{coll} = 1 - \frac{\tau_\mathrm{d}}{\tau_\mathrm{e}} \tag{13}$$

where τ_d is the electron transport time constant. Unfortunately, the ideal *scenario* that graphitic films, SWNT, or graphene act as charge transport channels to move photogenerated electrons from a TiO_2 nanoparticle to the next TiO_2 particle or to the current collector (e.g., FTO) is perturbed by the easy recombination of electrons in carbons with electrolyte acceptors (like I_3^-) at sites where carbon surface is contacting the electrolyte solution. Consequently, the improvement in collection efficiency is observed only in composites with very small amounts of carbon in TiO_2 (usually less than ≈0.5 wt%). A second perturbation mechanism was analyzed recently by Chen et al. [95]. They pointed out the effect of the Schottky junction which is formed at the SWNT/TiO_2 interface. The Schottky barrier height, Φ_B equals

$$\Phi_\mathrm{B} = W_\mathrm{m} - \chi \tag{14}$$

where W_m is the work function of the supporting material ($W_\mathrm{m} \approx 4.4$ eV for FTO or ≈4.6–5.2 eV for nanotubes [87, 95, 96]) and χ is the electron affinity of TiO_2 ($\chi \approx 4.2$ eV). Consequently, the height of the Schottky barrier is only 0.2 eV for TiO_2/FTO interface but up to ≈0.8 eV for TiO_2/SWNT interface. Furthermore, this picture changes as a result of illumination intensity and actual output voltage of the DSC [95]. In spite of these limitations, the rationally designed TiO_2/SWNT composite might demonstrate some improvement in electron collection efficiency.

3.2.1 Carbon Nanotube and Graphene as Photoanode Additives

Among various questions to be addressed in the optimization of carbonaceous additives in TiO_2, the notorious problem of SWNT is that the ordinary samples are mixtures of metallic and semiconducting tubes, and they are usually bundled, so that their electronic and electrochemical [65, 66] properties vary over a broad range. Dang et al. [97] found that the effect of SWNT bundling was negative, i.e., the strongly bundled SWNTs exhibited lower performance in a DSC photoanode. Second, these authors demonstrated that the metallic and semiconducting SWNT had affected the DSC performance in contrasting ways: the addition of 0.2 wt% of semiconducting SWNT to TiO_2 increased the short-circuit photocurrent from ca. 15 mA/cm^2 to ca. 19 mA/cm^2 (at AM 1.5 illumination), but 0.2 wt% of metallic tubes caused a drop of short-circuit full sun photocurrent to ca. 12 mA/cm^2 [97]. Some authors further combined the carbonaceous composite photoanode with a nanotube-based counter electrode [98].

Graphene was also successfully tested for the same purpose. Yang et al. [94] incorporated reduced graphene oxide into a nanocrystalline TiO_2 photoanode and found considerable efficiency increase to 6.97% (from 5.01% originally found for the blank TiO_2). Again, there was a certain optimum of graphene loading (≈0.6 wt%) after which the performance dropped considerably. In this study, graphene turned out to be more efficient than carbon nanotubes, which were simultaneously tested in parallel experiments. The beneficial effect of graphene was ascribed to enhanced electron collection efficiency (cf. (13)), together with higher light scattering [94]. Specifically, the light scattering and improved light harvesting in the visible region of the solar spectrum was found to be decisive for enhancement of DSC efficiency by other authors [99].

In similar work, Tang et al. [93] reported on a factor of 5 improvement of ITO-supported TiO_2 photoanode via molecular grafting with graphene. They explained it in terms of electron-transport cascade due to offset between the TiO_2 conduction band edge (−4.2 eV), the graphene work function (−4.4 eV), and ITO work function (−4.7 eV). Furthermore, they also claimed improved dye loading in graphene/TiO_2 composite. As in the previous examples, the beneficial effect manifested itself only in the narrow region of relatively small concentrations of graphene in TiO_2. Analogous work on graphene oxide confirmed the optimum loading to be 0.75 wt% in titania for optimized DSC performance [100].

Song et al. [101] prepared an alternative assembly of photoanode materials, in which a layer of rGO was placed between TiO_2 and the dye. They found improved DSC performance (6.06% vs 5.09% efficiency) and ascribed it to a similar electron cascade between all the used materials, namely to the Schottky barrier junction between TiO_2 and rGO. Neo and Ouyang [102] recently found that a small amount of GO (0.8 wt%) in TiO_2 could even improve the mechanical properties of titania film on FTO, providing crack-free TiO_2 layers by single printing.

3.3 Nanocarbons in Cathode of DSC

The most promising application of carbonaceous materials is surely in the fabrication of cathode (counter electrode) of liquid-junction DSC. Here, carbons serve as electrocatalyst for the mediator reduction (4), as a current collector or both as electrocatalyst *and* current collector. This subject was pioneered in 1996 by Kay and Graetzel [103] in their work aimed at the design of a module of monolithically series-interconnected DSCs. The central motivation of this work was to decrease the device cost, because the module required porous counter electrode, for which Pt would be too expensive [103]. They found good electrocatalytic activity of graphite/carbon black mixture for the I_3^-/I^- mediator. This discovery was subsequently adopted by Murakami et al. [45], who prepared highly active cathodes from carbon black supported by FTO.

The initial work on classical carbons, viz. graphite, carbon black and active carbon, for I-mediated DSCs was reviewed by Papageorgiou [104] and Murakami [105]. Although it was not always explicitly discussed in individual works, none of the presented electrodes was likely to be optically transparent (similar to Pt@FTO) because the thickness of the carbon layer was quite large to obtain electrocatalytic activity comparable to that of platinum. The carbon layers on the electrode were usually tens of micrometers to a hundred micrometers thick [45, 48, 49, 106–108].

The optical transmission of the cathode is, nevertheless, mandatory for certain DSCs which cannot be illuminated from the photoanode side. This is a typical geometry of plastic solar cells, in which the photoanode current collector is usually made from thin non-transparent foil of Ti metal or stainless steel [3, 4]. The so-called tandem dye-sensitized solar cells also require an optically transparent counter electrode; this geometry was introduced to expand the photoresponse into the red and near-IR region, and it was realized by stacking two DSCs together [3, 4].

In the traditional FTO-based solar cells the optical transparency of the complete cell is also beneficial for certain other applications such as windows, roof panels, decorative indoor installations, etc. [3, 4]. Hence, there is a clear motivation to search for an optically transparent, Pt-free, and FTO-free carbon film of similar properties. The target parameters of this film were quantified by Trancik et al. [109]. They stipulated that a carbonaceous film, which would eventually replace Pt@FTO in a cathode of liquid-junction DSC, should have the following three parameters: 80% optical transparency at a wavelength of 550 nm, R_{CT} of 2–3 $\Omega\ cm^2$ (cf. (10) and (11)), and sheet resistance of 20 Ω/sq. Such a film has not yet been demonstrated experimentally because all three benchmark parameters are difficult to obtain simultaneously. The highly active and optically transparent carbon cathodes are mostly fabricated on top of the FTO support. Hence the construction of an optically transparent, highly conductive, and electrocatalytically active all-carbon cathode is still a challenge.

3.3.1 Characterization in Symmetrical Dummy Cells

The electrocatalytic performance of various nanocarbons of interest for DSC-cathodes can be conveniently tested using so-called symmetrical dummy cells [41, 42, 50, 110–114]. Figure 4 shows a schematic sketch of this device. There is a thin layer of electrolyte solution (thickness δ) sandwiched between two identical electrodes to be tested as DSC cathodes. Hence, the geometry of the

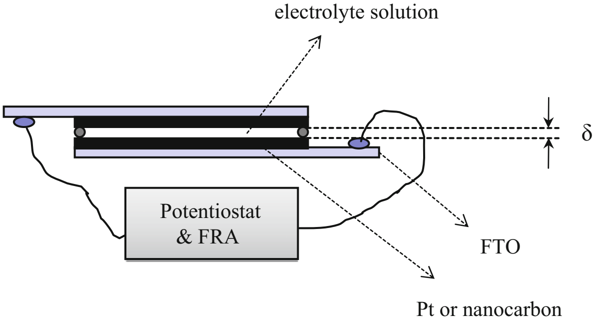

Fig. 4 Scheme of symmetrical dummy cell used for testing of electrocatalytic performance of DSC cathodes. *FRA* frequency response analyzer, *FTO* F-doped SnO_2

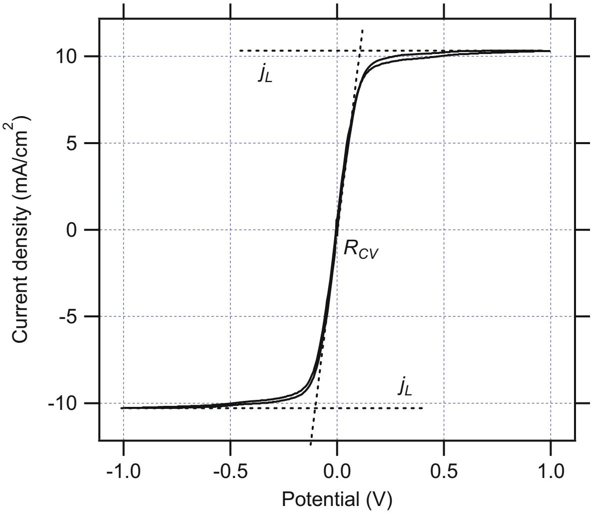

Fig. 5 Example of cyclic voltammogram measured on symmetrical dummy cell. The cell is composed of two identical electrodes from FTO-supported graphene nanoplatelets; the redox mediator is $[Co(bpy)_3]^{3+/2+}$ where bpy is 2,2′-bipyridine. Reprinted with permission from L. Kavan et al. *Nano Letters* **11**, 5501 (2011). Copyright (2011) American Chemical Society

symmetrical dummy cell is mimicking that of an ordinary liquid-junction solar cell. The performance of the carbonaceous cathode is investigated under simulated operating conditions of DSC by methods like cyclic voltammetry, chronoamperometry, and impedance spectroscopy, but without any interference from a TiO_2 photoanode. To this end, the dummy cell is interfaced to a potentiostat and a frequency response analyzer, FRA, as shown in Fig. 4 (the latter is needed for impedance spectra measurement). In the ideal case of a fast electrochemical reaction, which is not limited by mass transport in the electrolyte solution, the current response in the cyclic voltammogram should be a simple straight line following Ohm’s law.

This ideal situation is sometimes observed in sufficiently thin dummy cells and at small overvoltages [41, 42, 46, 110, 111, 114]. An example voltammogram is shown in Fig. 5, which was selected as a pattern of a Co-mediated system [41]. Liberatore et al. [114] have proposed that the inverse slope of the linear part in the region of “quasi-ohmic voltammogram” at the potential of 0 V (dashed line in Fig. 5)

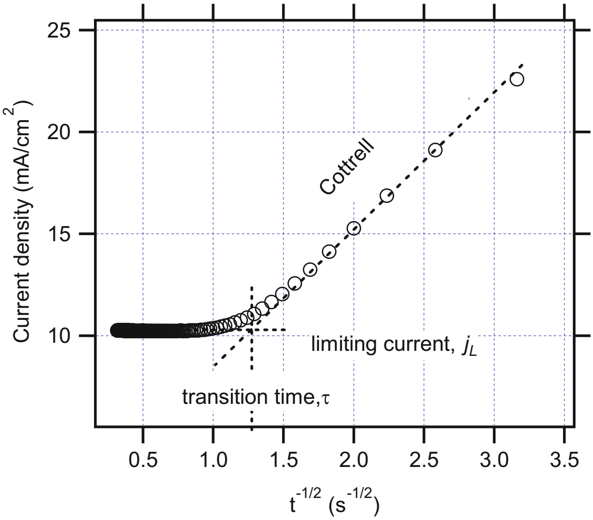

Fig. 6 Example of potential-step chronoamperometry measured on symmetrical dummy cell. The cell is composed of two identical electrodes from FTO-supported graphene nanoplatelets; the redox mediator is $[Co(L)_2]^{3+/2+}$; where L is 6-(1*H*-pyrazol-1-yl)-2,2′-bipyridine. Reprinted with permission from L. Kavan et al. *ACS Nano* **5**, 9171 (2011). Copyright (2011) American Chemical Society

characterizes the catalytic activity of an electrode. It is, actually, the overall cell resistance (R_{CV}) which can be attained at low current densities. We should note that the R_{CV} is fundamentally different from R_{CT} in (10), albeit both quantities characterize the electrocatalytic quality of a counter electrode.

The other limiting situation occurs when the mass transport controls the voltammetric current through the diffusion coefficient of the mediator, D. In this case the voltammogram extends to a constant plateau current density, j_L:

$$j_L = \frac{2nFcD}{\delta} \tag{15}$$

where n is the number of electrons (in practical systems, like for I_3^-/I^- or $Co^{3+/2+}$, $n = 1$) c is the concentration of transport limited species (either M or M^+), D is the diffusion coefficient, and δ is the distance between the electrodes in a dummy cell. This condition is illustrated in Fig. 5. Here the transport-controlling species was $[Co(bpy)_3]^{3+}$ ($c = 50$ mmol/L) and $\delta = 53$ μm. Equation (15) thus allows one to calculate the diffusion coefficient from the data in Fig. 5 to be $D = 6.2 \times 10^{-6}$ cm^2/s.

The mass transport can also be conveniently studied in a symmetrical dummy cell by potential-step chronoamperometry [114]. Figure 6 shows an example plot. Shortly after the potential step, the current density follows the semi-infinite decay according to the Cottrell equation:

$$j_{Cott} = nFc\sqrt{\frac{D}{\pi t}} \tag{16}$$

The current drops linearly with $t^{-1/2}$ (t is time) as long as the concentration profiles in front of each electrode in the dummy cell merge to form a single linear profile. In the limiting case of infinite time, the current density attains a constant value, j_L, which is also observed in cyclic voltammograms ((15) and Fig. 5). If we extrapolate both linear components of the chronoamperometric plot we get the intersection at the so-called transition time, τ, which defines the diffusion coefficient, D. From a condition $j_{Cott} = j_L$ ((15) and (16)) we obtain

$$D = \frac{\delta^2}{4\pi\tau} \tag{17}$$

As τ is independent of concentration, it is useful for alternative determination of the diffusion coefficient, D. Compared to I-mediated systems, the mass transport is much more important for Co-mediated DSCs [115]. The ionic diffusion here is expected to be slower due to the larger size of Co-polypyridine molecules compared to iodide anions. Furthermore, the limiting current (15) cannot be increased by concentration, c, due to the low solubility of Co(III) species [24, 27]. The problem of diffusion in Co-mediated DSCs has been recently addressed by Tsao and Graetzel [116]. The critical limitations caused by mass transport are obviously located in the mesoporous matrix of the photoanode; hence its layer thickness, porosity, particle size, and pore size have to be optimized [116].

Useful electrochemical techniques for investigation of electrocatalytic activity and mass transport in dummy cells are based on application of small sinusoidal perturbation of the cell voltage (with a varied frequency ω). This technique, called "electrochemical impedance spectroscopy" (EIS) is also a powerful tool for characterization of a complete DSC, where it allows, under certain conditions, individual characterization of all the important parts and interfaces in the solar cell, i.e., the TiO_2 photoanode, counter electrode, electrode supports, and electrolyte solution or hole transporting medium [3, 4]. If EIS is measured at various applied biases and illumination intensities, it provides detailed information about the solar cell, but the correct use and interpretation of EIS is not trivial. In principle, we can obtain all the relevant information about the counter electrode from measurements on complete DSC, but the use of a symmetrical dummy cell simplifies the interpretation of experimental data.

The first EIS studies of counter electrodes in a symmetrical dummy cell with an I_3^-/I^- redox couple were carried out by Papageorgiou et al. [117] and Hauch and Georg [46], who investigated the classical platinum (Pt@FTO) electrode and by Murakami and Graetzel [45], who investigated the electrode composed of carbon black/TiO_2 mixture. In the latter case, an asymmetric dummy cell was used, which contained Pt@FTO and carbon black/TiO_2@FTO in one dummy cell. This somewhat complicated assembly could still be analyzed, due to the fact that the impedances of Pt@FTO and carbon black/TiO_2@FTO are distinguishable in the spectrum at various frequencies [45, 105]. More specifically, Pt@FTO appears at ω between 1 and 100 kHz, whereas carbon black lowers the frequency response to 1–100 Hz.

In all the studies mentioned [45, 46, 105, 117], the authors fitted their impedance spectra to a traditional equivalent circuit based on serial combination of charge transfer resistance, R_{CT}, and double layer capacitance (C_{dl}) or constant phase element, CPE. The use of double layer capacitance is an acceptable approximation for the Pt@FTO electrode [46], where we can neglect surface roughness. However, the use of CPE is mandatory for carbon electrodes because the deviations from the ideal capacitance are significant. CPE is not a real electrical element but merely a mathematical model of a non-intuitive circuit component which is used to fit the experimental EIS spectra. The impedance of CPE equals

$$Z_{\mathrm{CPE}} = B(i\omega)^{-\beta} \tag{18}$$

where B and β are frequency-independent parameters of the CPE ($0 \leq \beta \leq 1$). Obviously CPE transforms to pure capacitor (C_{dl}) for $\beta = 1$ and to pure resistor (R) for $\beta = 0$. The standard R_{CT}/CPE equivalent circuit is completed by serial resistance, R_{s}, which characterizes the ohmic resistance of electrodes, electrical contacts, and electrolyte (with dominating contribution of the FTO substrate's resistance) and the Nernst diffusion impedance (also called Warburg impedance), Z_{W}, which describes the diffusion transport in the electrolyte solution. The Warburg impedance is diagnostic for mass transfer in DSC. Hence, it is useful to express it as follows:

$$Z_{\mathrm{W}} = \frac{W}{\sqrt{i\omega}} \tan h \sqrt{\frac{i\omega}{K_{\mathrm{N}}}} \tag{19}$$

(where W is the Warburg parameter accessible from the EIS fitting). The parameter K_{N} equals

$$K_{\mathrm{N}} = \frac{4D}{\delta^2} \tag{20}$$

Equations (19) and (20) thus provide yet another experimental routine for determination of diffusion coefficient (in addition to (15) and (17)). This description of the symmetrical dummy cell was further upgraded by Roy-Mayhew et al. [112], who pointed out that the Nernst diffusion impedance in pores of the electrode material, $Z_{\mathrm{W,pore}}$, should also be taken into account. This contribution is usually negligible for Pt@FTO, but must be considered in highly porous carbon electrodes, particularly those having a large layer thickness (≈tens of micrometers). Ignoring $Z_{\mathrm{W,pore}}$ could, in this case, lead to misinterpretation of EIS data, specifically to underestimation of charge transfer resistance of a carbon electrode [112]. On the other hand, the $Z_{\mathrm{W,pore}}$ might be negligible for virtually "non-porous" carbonaceous electrodes such as FTO-supported graphene-based particles [41, 42, 110, 111]. To decide whether or not $Z_{\mathrm{W,pore}}$ can be neglected, the EIS should be measured at various applied biases to a dummy cell [41, 42, 111–113].

A generalized equivalent circuit for fitting the impedance spectra of symmetrical dummy cells is shown in Fig. 7. Here all the elements, except Z_{W}, are considered to be the parameters of one electrode in the sandwich dummy cell (that is why we have

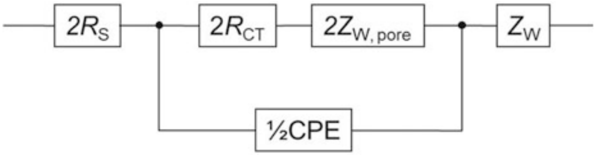

Fig. 7 Equivalent circuit used for fitting of electrochemical impedance spectra measured on symmetrical dummy cell. R_s is ohmic serial resistance, R_{CT} is charge transfer resistance, $Z_{W,pore}$ is Nernst diffusion impedance in pores, CPE is constant phase element, and Z_W is Warburg impedance of ionic transport in the electrolyte solution

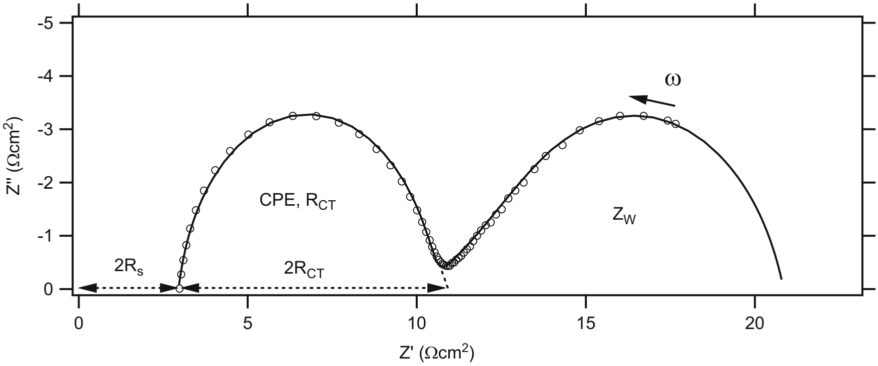

Fig. 8 Example of electrochemical impedance spectrum (EIS) measured on symmetrical dummy cell. R_s is ohmic serial resistance, R_{CT} is charge transfer resistance, $Z_{W,pore}$ is Nernst diffusion impedance in pores, CPE is constant phase element, Z_W is Warburg impedance of ionic transport in the electrolyte solution, and ω is frequency. The cell is composed of two identical electrodes made from FTO-supported graphene oxide modified by heat treatment; the redox mediator is $[Co(bpy)_3]^{3+/2+}$ where bpy is 2,2′-bipyridine. Reprinted with permission from L. Kavan et al. *ACS Applied Materials & Interfaces* **4**, 6999 (2012). Copyright (2012) American Chemical Society

to double R_s, R_{CT}, $Z_{w,pore}$, and to halve CPE). Each of these five quantities is measurable by the single EIS experiment, and the values found are diagnostic for the given electrode material. This is particularly important for R_{CT} because it characterizes the electrocatalytic activity of the electrode material; see (10). As discussed above, charge transfer resistances of 1–3 Ω cm^2 are required to minimize losses at the counter electrode, assuming the current densities equal ca. 20 mA/cm^2 in DSC illuminated by AM 1.5 solar radiation.

Figure 8 shows an example of the impedance spectrum of a symmetrical dummy cell in the format of a so-called Nyquist plot which is the imaginary part of impedance, Z'', vs the real part of impedance, Z'. The actual data are shown for $[Co(bpy)_3]^{3+/2+}$ mediator in electrolyte solution, and the electrodes are fabricated from thermally reduced graphene oxide on top of FTO [111]. This kind of impedance spectrum is quite frequently observed in dummy cells with Pt@FTO electrodes in various electrochemical environments [46, 110] and also for other graphene-based materials deposited on FTO [41, 42, 110] provided the amount of graphene on FTO is so small that we can neglect the Nernst diffusion impedance in the pores, $Z_{\mathrm{W,pore}}$.

The spectrum in Fig. 8 can be analyzed by fitting the experimental impedances (open points) to the equivalent circuit shown in Fig. 7 (without $Z_{\mathrm{W,pore}}$). The fit is plotted as a full line in Fig. 8. Generally the low frequency semicircle characterizes ionic diffusion in the electrolyte solution (described by Z_{W}; see (19)) and the high energy semicircle is representative for interfacial charge transfer (described by R_{CT}, CPE, or ultimately by C_{dl}). The cross section of this high-frequency semicircle with the bottom axis (at $Z'' = 0$ and the maximal ω) provides the ohmic serial resistance, $2R_{\mathrm{s}}$, and the diameter of this high-frequency semicircle provides an estimate of $2R_{\mathrm{CT}}$ as shown in Fig. 8.

3.3.2 Some Notes About the Electrocatalytic Activity of Carbon

Understanding the electrochemical kinetics of the redox mediator at the carbon electrode and at other electrode materials (Pt, TiO_2, FTO, etc.) is key to the development of liquid junction DSCs. The reason is that we require a high rate of charge transfer at the cathode (see (4), (10), and (11) and discussion above) but a slow rate of the same reaction at the anode to minimize recombination (3). As the electrochemical charge transfer is localized at the surface, the "chemical defects" which are involved in the *termination* of the carbon surface play a role. The core question in both cases is where the catalytic activity of carbon surface comes from? More specifically: how the carbon surface can catalyze electrochemical reactions of the used mediators, such as I_3^-/I^-, Co(III)/(II) or other redox couples, commonly used in DSC?

Such a problem is often bypassed by a hypothesis that "defects" and "oxygen-containing groups" are the catalytically active sites, but were never clearly identified. Roy-Mayhew et al. [112] proposed that carbons for a DSC cathode could be optimized by enhancement of the amount of specific catalytic sites and by eliminating inactive defects if they were known. At the carbon surface, all possible oxygen functional groups might occur; they are not only hydroxyls, –OH, carbonyls, =O, and carboxyls, –COOH, but also their mutual combinations and variants, like epoxy, lactone, ester, ether, etc. Some of these groups are reducible chemically or electrochemically. A model of such a surface is graphene oxide (GO) and, therefore, its electrochemistry attracts relevant attention [57, 118–120]. The reduction of GO in aqueous electrolyte solution also requires protons, which can be schematically depicted as follows:

$$\mathrm{GO} + 2\mathrm{H}^+ + 2\mathrm{e}^- \rightarrow \mathrm{rGO} + \mathrm{H_2O} \tag{21}$$

Nevertheless, there is a surprising difference between GO and rGO if we compare the electrocatalytic activity in a practical DSC electrolyte solution with $[Co(bpy)_3]^{3+/2+}$ redox mediator [111]. Contrary to expectation, the material with the largest concentration of oxidic functionalities (pristine GO) is quite sluggish, whereas the rGO made by hydrazine reduction or simply by calcination in inert atmosphere exhibits a strong increase in activity. Since the concentration of oxidic functionalities is known to decrease during both chemical reduction and heat treatment [71], this would lead to a hypothesis that the catalytically active sites are created by irreversible removal of the oxidic functionalities from GO rather than by their presence. A carbon surface can also be terminated (apart from oxidic groups discussed above) by hydrogen, C–H, or just by a dangling bond. Velten et al. [121] proposed that the electrocatalytic active sites in carbonaceous DSC cathode are actually dangling bonds and "sharp atomic edges" in analogy to edge-plane pyrolytic graphite [122, 123]. Although this is qualitatively consistent with the comparison of GO and rGO, there are still many open issues to be addressed.

A comprehensive review of the electrochemistry of carbon electrode materials ("classical" carbons, nanotubes, and nanodiamond) was presented by McCreery [124]. Electrochemistry of diamond was reviewed by Fujishima et al. [125] and carbons for electrochemical energy storage and conversion were treated by Beguin and Frackowiak [126]. Critical discussion about the electrocatalytic activity of carbon nanotubes [122] and graphene [118] was presented by Pumera. In general, electrocatalysis through "defect's" and "carbon-oxygen surface functionalities" is a contradictory subject with many opposing claims [122, 124, 127].

Specifically in carbon nanotubes, the influence of metallic impurities is of paramount importance because these metals are residua from catalysts needed for their synthesis. Their complete removal from ordinary samples is very difficult. Otherwise the electrochemical activity of carbon nanotubes is assumed to be similar to that of other graphite-like carbons, although there were also claims for "inherent" activity specific for nanotubes only. A critical discussion of inherent catalytic activity of nanotubes was presented by Pumera [122] and Banks et al. [123].

Graphene and graphene-related materials like graphene oxide and reduced graphene oxide (cf. (21)) recently attracted great attention from the scientific community, including electrochemists [57, 58, 118]. The electrocatalytic activity of bulk graphene is expected to be similar to that of highly ordered pyrolytic graphite (HOPG) which is a model sp^2 carbon, resembling the single crystal graphite. HOPG therefore allows individual addressing of the basal plane, i.e., the (0001) face in crystallographic notation, and edge planes (i.e., $(10\bar{1}0)$, $(1\bar{1}00)$, $(01\bar{1}0)$) which are perpendicular to it. The edge planes are obviously assumed to be full of defects, and thus more active electrochemically. The similarity between defect-free graphene and basal plane HOPG is further corroborated by the fact that the electrochemical response of graphene is independent of the number of layers which are stacked in multilayer assemblies of graphene [128]. The heterogeneous electron transfer rate constant (cf. (11)) was reported to be of the order of ≈0.01 cm/s for edge plane HOPG but $\approx 10^{-9}$ cm/s for basal plane HOPG and still smaller for graphene [128]. Specifically, the behavior of basal plane HOPG in practical electrolyte solution for DSCs with $[Co(bpy)_3]^{3+/2+}$ redox mediator was very poor [111].

This more or less coherent picture of HOPG surface was recently questioned by Lai et al. [127] who developed a novel technique called scanning electrochemical cell microscopy (SECCM). Using this method, they have found surprisingly large electron-transfer rate constants of >0.5 cm/s on the basal plane HOPG. These values are actually comparable to those predicted from Marcus theory (>1 cm/s). Furthermore, Lai et al. [127] claim that the defects, i.e., step sites at basal plane, show only a slight increase of activity, the local currents at defects being higher by ca. 2–3% only. Hence, there is a sharp contrast between this work [127] and the generally accepted opinion about negligible electrocatalytic activity of basal plane HOPG or graphene, and the catalytic role of defects [123, 128]. The discrepancy was discussed in terms of impurities, adsorption, and surface-blocking in "ordinary" macroscopic electrochemical experiments, but further work is needed to addresses these conflicts.

Another closely related general problem of electrocatalytic reaction at DSC electrodes is whether or not their activity is likely to change during the lifetime of solar cells? Ideally one would require no cathode's activity loss as a result of aging over some years of operation in DSCs under illumination in variable environmental conditions like temperature, air humidity, etc. This aging (also termed "poisoning" of electrocatalyst) is known to occur on various practical materials used in DSC cathodes such as Pt [46, 50, 110] and metal selenides [50] in I-mediated DSCs as well as on Pt [42] and graphene [41, 42, 111] cathodes in Co-mediated DSCs. However, the chemistry behind poisoning is unknown in all cases [41, 42, 46, 50, 110]. (Some authors noted dissolution of platinum in certain electrolyte solutions used in DSCs [129], but this is hardly a complete picture of the multifaceted problem of electrocatalyst aging.)

The instability of carbon electrodes in Co-mediated systems was first reported by Sapp et al. [44] in 2002, i.e., long before the advent of Co-mediators for highly efficient DSCs [29, 33, 37]. These authors found good electrocatalytic activity of gold, glass-like carbon, or graphite nanoparticle electrodes for Co(III/II) couples, but surprisingly poor activity of platinum for the same reactions. The loss of activity of graphite nanoparticles was ascribed to mechanical damage of the active layer during the electrode operation [44]. These findings were also reproduced for graphene nanoplatelets (GNP) by Kavan et al. [41, 42]. The active layer from GNP is mechanically unstable and hence nanoplatelets detaching from the support are responsible not only for the loss of electrochemical activity but also for higher dark current in DSC, and thus for lower open-circuit voltage (cf. Sect. 3.3.4 for further discussion). The aging and dark current can be minimized by using composite materials from GNP with graphene oxide, or from graphene oxide alone, which were mechanically more stable [111].

3.3.3 I-Mediated DSC

There is, presumably, no other counter electrode material which would beat Pt@FTO in electrocatalytic activity for the I_3^-/I^- redox reaction, along with its high optical transparency [27, 110]. Although the necessary amount of Pt on the cathode is very low, ca. 10–100 μg/cm^2 [47, 104, 105, 130], there is a challenge for substituting platinum by cheaper materials. The palette of alternative non-carbon materials comprises conducting polymers [131–133] or polymer/Pt or polymer/carbon composites [134] (for review see [105]). Materials like Au, Cu_2S, and RuO_2 were also occasionally mentioned [104, 117, 135]. Later on, high activities of surface-nitrided nickel [136] and CoS [137] were reported, the latter material allowing fabrication of an optically transparent counter electrode on plastic substrates. Recently Gong et al. [50] discovered that a cobalt selenide exhibited significant electrocatalytic activity for I_3^-/I^- and their DSC with a $Co_{0.85}Se$@FTO cathode actually performed better than with the Pt-FTO cathode. Wu et al. [138] presented systematic screening of carbides, nitrides, and oxides of various transition metals, pointing at good performance of vanadium carbide, VC, particularly if the electrocatalyst was embedded in mesoporous carbon. In another study, Wu et al. [139] demonstrated high activity of molybdenum carbide and tungsten carbide, outperforming platinum cathodes in DSCs [139].

Carbon is the second most widely studied material for DSC cathode after platinum. This research was triggered by Kay and Grätzel [103] who used graphite/carbon black mixtures. Subsequently, various kinds of carbon were studied by others, such as hard carbon spherules [106], activated carbon [107], colloidal graphite [140], carbon black [141], mesoporous carbon [49, 142], nanocarbon [48], graphene [110, 142–149], nitrogen-doped graphene [150], MoS_2-graphene nanocomposite [151], graphene-activated carbon composite [152], graphene/polymer composites [153, 154], single-walled carbon nanotubes [155, 156], multi-walled carbon nanotubes (MWNT) [156–160], N-doped nanotubes [161], electrospun nanofibers [162], and carbon black/TiO_2 composite [45]. MWNT were also assembled in composites with conducting polymer [157] and TiN [108]. (In the latter case, however, the presence of TiN requires further proof, due to possible mismatch of TiN with titanium oxynitrides under the used synthetic conditions [163]. We may also note the beneficial effect of TiN as an electrolyte additive [164] and TiO_2 additive [165]). A systematic screening of nine different carbon materials for a cathode of I-mediated DSC was presented by Wu et al. [166]. They tested the following materials: mesoporous carbon, activated carbon, carbon black, conductive carbon, carbon dye, carbon fiber, carbon nanotube, discarded printer toner, and fullerene (C_{60}). This study confirmed that activity approaching that of Pt is accessible for certain carbons.

To get the same activity as platinum, carbon-based counter electrodes must have sufficiently high surface area. This requirement confirms the intuitive assumption that the number of active sites for the I_3^-/I^- redox reaction scales with the carbon electrode area [45, 105, 109, 123]. Even so, carbonaceous electrodes which would be superior to Pt were reported only rarely [107]. Promising activity similar to that of Pt was also found for MWNT cathodes [109, 159, 160, 167], although there is a debate as to whether or not the high activity of MWNT comes from the residual metal or metal oxide catalyst particles in the samples (cf. Sect. 3.3.4) [109, 159, 168]. Occasionally we can also find reports about optically semitransparent MWNT film used in DSC cathode [158]. In this particular case, a reasonably good conversion efficiency of 7.59% was reported, but comparison with Pt cathode was not made.

Graphene Cathode for I-Mediated DSC

Perfect graphene does not seem to be the right candidate for the DSC cathode in view of the limited number of active sites for I_3^- reduction on the basal plane (0001) [45, 105, 109]. Nevertheless, small graphene nanoplatelets, made, e.g., by thermal annealing of GO, behave better [112, 144, 145]. Such a defect-rich graphene-based material seems to be favored over MWNT for a transparent DSC cathode because the amount of active sites per one π-electron in carbonaceous skeleton is larger. (We assume that inner tubes in MWNT do not contribute to electrochemical activity, but absorb light.) Zhang et al. [144] reported on a graphene nanosheet cathode for DSC, but the solar conversion efficiencies were only 0.71–2.94%. Analogously, Choi et al. [145] reported on a rather poor performance of the graphene cathode, but a composite of graphene with MWNT exhibited enhanced activity, giving 3% solar conversion efficiency in DSC.

Roy-Mayhew et al. [112] further upgraded the work on graphene-based materials by using functionalized graphene sheets, FGS. (Their FGS material seems to be close to reduced graphene oxide fabricated by thermal treatment.) In contrast to earlier reports [112, 144, 145], these authors obtained good solar conversion efficiency (≈5%) in their solar cells with FGS@FTO cathode. (A reference solar cell with Pt@FTO cathode exhibited efficiency of ≈5.5%.) They also presented a plastic-supported (Mylar) carbonaceous cathode showing 3.8% efficiency [112]. However, none of the FGS electrodes seems to be optically transparent. The catalytic activity of FGS correlated with the amount of oxygen in carbonaceous skeleton, until a certain limit when the electrical conductivity became performance-controlling [112]. The follow up studies of graphene cathode for I-mediated DSC essentially confirmed that performance comparable to Pt is hard to achieve [56, 113, 148, 149, 166, 169–175] (for a review of graphene counter electrodes in I-mediated DSCs see [149]).

There are only a few reports explicitly presenting optically transparent graphene-based cathodes [110, 146, 151, 154, 174, 175] or carbon nanotube cathodes [161]. Systematic work was carried out with graphene nanoplatelets (GNP) deposited on FTO [110]. GNP is a commercial product consisting of several sheets of graphene with an overall thickness of approximately 5 nm (ranging from 1 to 15 nm) and particle diameters less than 2 μm. This study revealed an empirical rule that the optical absorbance of the electrode (GNP@FTO) is directly proportional to exchange current density, j_0 (or $1/R_{CT}$; cf. (10)). The rule obviously illustrates the assumption that catalytic activity scales with the physical area of the carbonaceous material. This confirms that the optical density of GNP film is proportional to amount of graphene nanoparticles in it. Velten et al. [176] reported on a reversible photoinduced bleaching of the I_3^-/I^- electrolyte solution specifically in contact with the few-layer graphene nanoribbons.

The performance of an actual I-mediated DSC with transparent GNP@FTO cathode is demonstrated in Fig. 9, right chart. Here the solar cell provided 5.00% or 6.89% efficiency for GNP@FTO or Pt@FTO cathodes, respectively. Obviously, the main problem of this cell is the large $R_{CT} = 308\ \Omega\ \text{cm}^2$ of the cathode, which

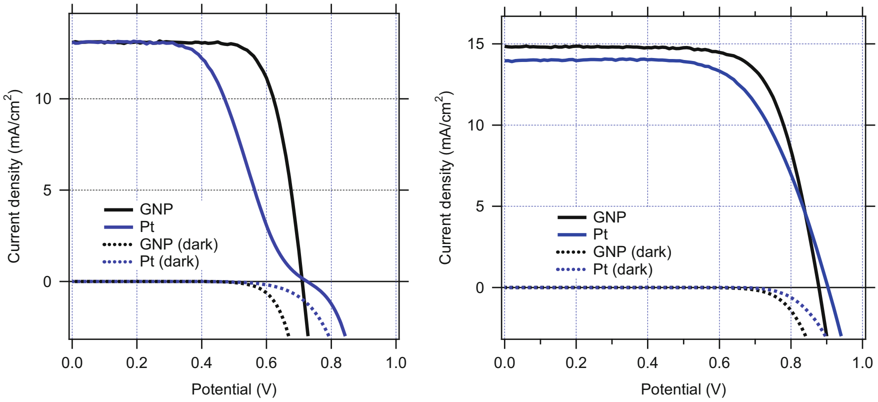

Fig. 9 Current–voltage characteristics of dye sensitized solar cell in the dark and under illumination with full sun (AM 1.5). The cathode is fabricated either from graphene nanoplatelets (GNP, *black curves*) or Pt (*blue curves*). *Left chart*: N-719 sensitized TiO_2 photoanode and I_3^-/I^- as the redox mediator (electrolyte solution Z946 – see text for details). The GNP film had optical transmission of 87% at 550 nm wavelength. Adapted with permission from L. Kavan et al. *ACS Nano* **5**, 165 (2011). Copyright (2011) American Chemical Society. *Right chart*: Y123 sensitized TiO_2 photoanode and $[Co(bpy)_3]^{3+/2+}$ (bpy is 2,2′-bipyridine) as the redox mediator. The GNP film had optical transmission of 66% at 550 nm wavelength. Adapted with permission from L. Kavan et al. *Nano Letters* **11**, 5501 (2011). Copyright (2011) American Chemical Society

is responsible for poor performance at potentials near U_{OC} [110]. Interestingly, the electrocatalytic activity of GNP@FTO for the I_3^-/I^- redox reaction was considerably better in the electrolyte based on ionic liquid compared to that in the traditional electrolyte solution in organic solvent. The latter solution (coded Z946) was 1 M 1,3-dimethylimidazolium iodide + 0.15 M iodine + 0.5 M *N*-butylbenzoimidazole + 0.1 M guanidine thiocyanate in 3-methoxypropionitrile. The alternative ionic liquid medium (coded Z952) was 1,3-dimethylimidazolium iodide + 1-ethyl-3-methylimidazolium iodide + 1-ethyl-3-methylimidazolium tetracyanoborate + iodine + *N*-butylbenzoimidazole + guanidinium thiocyanate (molar ratio 12/12/16/1.67/3.33/0.67). The electrocatalytic activity, quantified as j_0 or $1/R_{CT}$, (cf. (10)) was found to be larger by a factor of about 5–6 for the Z952 electrolyte compared to that for the Z946 electrolyte [110].

One might argue that the concentration of electroactive species is different in Z946 vs Z952, and different exchange currents, j_0, are expected to follow simply from different concentrations as it is quantified by (11). Nevertheless, the calculation of $c_{ox}{}^{1-\alpha}\cdot c_{red}{}^{\alpha}$ using the actual electrolyte compositions mentioned above shows the ratio of exchange currents in Z952/Z946 to be 1.75 only. Hence the found factor of 5–6 enhancement of j_0 in Z952 is *not* a simple concentration effect. The reason for this striking improvement of electrocatalytic activity in ionic liquid medium [110] is still unclear, but we may note that a very similar improvement in solvent-free electrolyte was recently also found for another carbonaceous material, LPAH [172].

The LPAH is a "large-effective-surface-area polyaromatic hydrocarbon" and it was used by Lee et al. [172] for construction of a "truly" carbonaceous (that is without FTO) cathode for DSC. The material is grown in a soot from hydrogen arc discharge, which is also used for the synthesis of nanotubes. The LPAH film was deposited on top of graphite with the aid of amphiphilic triblock copolymer Pluronic P123. This cathode exhibited excellent performance in I-mediated DSC with plastic electrolyte. Although it was not clearly specified in the cited paper [172] what is meant by "plastic electrolyte," one can assume that *N*-methyl-*N*-butylpyrrolidium iodide doped succinonitrile plastic crystal was used. In this medium, the LPAH@graphite cathode clearly outperformed Pt@FTO. The corresponding DSCs exhibited efficiencies of 8.63% or 7.15%, for LPAH@graphite or Pt@FTO cathodes, respectively. Surprisingly, the LPAH@FTO provided only 7.50% under the same conditions [172]. Besides pure graphene, composites of graphene with conducting polymers were also tested as catalytic counter electrodes in DSC; for a recent review see [154].

3.3.4 Co-Mediated DSC

The use of $Co^{3+/2+}$ redox couple instead of I_3^-/I^- as the DSC mediator is rationalized in terms of the different and easily tuneable redox potentials of the former (cf. Sect. 1.1.2 and Fig. 1). The pioneering work was carried out by Nusbaumer et al. [177] in 2001, but there was no significant progress during the next decade. The reason was that the performance of the initial Co-mediated devices was quite poor with solar conversion efficiency of 2.2% at full sun illumination [177]. One of the reasons was the fast recombination of TiO_2-conduction band electrons with the Co(III) species in the electrolyte solution, which is supposed to be much faster than the recombination with I_3^- (cf. (2)).

In 2010, Feldt et al. [33] made an important step forward by showing that the recombination can be minimized by proper molecular engineering of dye sensitizers. More specifically, they replaced the traditional Ru–bipyridine sensitizers by purely organic triphenylamine-based dyes. The best performing dye in their study (coded D35) in conjunction with $[Co(bpy)_3]^{3+/2+}$ redox mediator provided the solar conversion efficiency of 6.7% (at AM 1.5) and the remarkable $U_{OC} = 0.92$ V [33]. (To be honest, however, similar U_{OC} is also accessible for a solar cell with D35-sensitized TiO_2 in I_3^-/I^- containing medium by proper tuning of the electrolyte composition aimed at conduction band shift and electron lifetime increase [33].)

In 2011, Yella et al. [29] demonstrated the best solar cell so far using the same $[Co(bpy)_3]^{3+/2+}$ redox mediator, but they interfaced it to a novel zinc porphyrin dye of the general structural motif of donor-π-bridge-acceptor (D-π-A). This dye had a better spectral response, harvesting sunlight up to ca. 750 nm wavelength. (The D35 dye was active by ca. 620 nm wavelength only.) The D-π-A structural design is also involved in another dye, similar to D35 but with broader absorption band (coded Y123; see the structural formula below) [34].

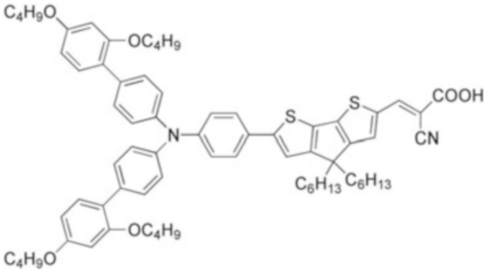

Structural formula of the Y123 dye. Chemical name: 3-[6-[4-[bis(2′,4′-dihexyloxybiphenyl-4-yl) amino-]phenyl]-4,4-dihexylcyclopenta-[2,1-b:3,4-b]dithiophene-2-yl]-2-cyanoacrylic acid. In the structure, triphenylamine is donor (D), dithiophene species is the π-bridge, and CN(COOH) is the acceptor (A)

The use of Y123 as a Co-sensitizer to Zn-porphyrin dye further improved the response around 550 nm, i.e., near the peak of solar spectrum, and this combination provided the record DSC with 12.3% solar conversion efficiency [29].

Most Co-mediated solar cells, including the champion (12.3%)-cell [29] still rely on Pt@FTO cathode [29, 33–37, 44] and occasionally also conducting polymers (PEDOT or PProDOT) were used with interesting results [30, 32, 37]. The application of Pt counter electrode for Co-mediated DSC is, nevertheless, quite debatable, due to sluggish and irreversible electrochemistry of the $Co^{3+/2+}$ redox couple in complexes with a variety of bipyridine, terpyridine, and phenanthroline ligands [44]. On the other hand, these complexes exhibit fast electrochemical kinetics on gold electrodes as well as on graphite or glass-like carbon electrodes [44, 178]. Feldt et al. [33] reported that the electrocatalytic activity of Pt (expressed as j_o or $1/R_{CT}$; see (10)) further decreased for Co-bipyridines with bulky substituents on the ligands. These authors predicted in their seminal paper [33] that “alternative, cheap electrode materials will become available.”

The first application of an alternative cathode material (other than Pt) in Co-mediated DSC was demonstrated by Sapp et al. [44]. They combined different Co-polypyridine mediators with gold sputtered on FTO. However, they used the classical Ru–bipyridine sensitizer (N3); that is why their efficiencies were around only 1%. A carbon cathode was employed in Co-mediated DSC for the first time in 2010 by the same group [178], but again, due to the improper use of Ru-bipyridine sensitizers (N3 or Z907), the efficiency was only 1.2%. This particular work used a screen-printed carbon ink counter electrode [178].

Graphene Cathode for Co-Mediated DSC

The application of a graphene-based counter electrode for Co-mediated DSC was pioneered by Kavan et al. [42] in 2011. They utilized the same optically transparent GNP electrode, which was previously tested for I-mediated DSC with moderate success [110] (cf. Sect. 3.3.3 and Fig. 9). This electrode turned out to be highly active for Co-mediated DSC using $[Co(bpy\text{-}pz)_2]^{3+/2}$ (see above for the chemical formula) [42]. Their solar cell with Y123-sensitized photoanode provided U_{OC} over 1 V due to the higher redox potential of this mediator. A parallel study of Yum et al. [37] confirmed that $U_{OC} > 1$ V can be achieved in these solar cells independent of the counter electrode material (Pt, GNP or PProDOT) [37, 42].

A comparative test of platinum and graphene cathodes in the DSCs with Y123-sensitized photoanode gave 8.1% and 9.3% efficiencies for Pt@FTO and GNP@FTO, respectively [42]. This finding is consistent with the R_{CT} values found (cf. (10)) of 4.7 and 0.7 Ω cm^2 for the Pt@FTO and GNP@FTO cathodes used, respectively [42]. Analogous comparison of Pt@FTO and PProDOT@FTO provided 9.52% and 10.08% for Pt@FTO and PProDOT@FTO, respectively [37]. Again, there is consistency with the reported factor of 20 smaller R_{CT} value (cf. (10)) found for the conductive polymer [37]. We should note that actual efficiencies of the two reference cells with Pt cathodes do not match due to different properties of the photoanode used in the cited works [37, 42]. Nevertheless, the relative comparison confirms beneficial properties of both the Pt-free cathodes, i.e., graphene and PProDOT. The cell with GNP@FTO cathode outperforms that with Pt@FTO particularly in fill factors and in the efficiency at higher illumination intensities, but there is also a slight increase of dark current for GNP-based device, which reduces efficiency at smaller light intensities and the U_{OC} [42].

There was no explicit discussion of the optical properties of PProDOT cathodes [32, 37, 131] in Co-mediated DSCs, but the GNP cathode was optically transparent (similar to Pt@FTO) [41, 42]. A systematic study confirmed the existence of an empirical rule, which is also known from I-mediated systems (see Sect. 3.3.3 and [110]). This rule says that the optical absorbance of the electrode is linearly proportional to the exchange current density (j_0) or $1/R_{CT}$. However, the exchange currents for $[Co(bpy\text{-}pz)_2]^{3+/2+}$ couple on GNP-electrode are larger by a factor of ca. 25 or 160 than those for the I_3^-/I^- couple on the same electrode (depending on the reference electrolyte used, either ionic liquid or classical electrolyte solution; cf. Sect. 3.3.3 [42, 110]). This again confirms that the concentration of catalytically active sites for $Co^{3+/2+}$ reaction scales linearly with the physical surface area of GNP, although the mechanism of electrocatalysis is unknown in all cases (see Sect. 3.3.2).

A logical continuation of the study of $[Co(bpy\text{-}pz)_2]^{3+/2+}$ complex on GNP was the corresponding investigation of the $[Co(bpy)_3]^{3+/2+}$ mediator, which manifested itself in the champion (12.3%) cell [29]. Kavan et al. [41] confirmed that, indeed, this complex is extremely fast on the GNP electrode. They estimated $R_{CT} \approx 0.08$ Ω cm^2 for a GNP electrode with optical transmittance of 85% at a 550 nm wavelength. (Note that this electrode would actually meet all the benchmark parameters outlined by Trancik et al. [109]; cf. Sect. 3.3, albeit it requires FTO as the electrode support.)

Solar cells with Y123-sensitized TiO_2 photoanode, $[Co(bpy)_3]^{3+/2+}$ mediator, and GNP@FTO cathode outperform, as expected, those with the Pt@FTO cathode, particularly in fill factors and conversion efficiency at higher illumination intensities [41]. Figure 9 (right chart) shows the corresponding current–voltage characteristics at AM 1.5 illumination. The improvement for the GNP@FTO cathode is an obvious effect of higher electrocatalytic activity (higher j_0 or smaller R_{CT}). The photocurrent at high illumination intensity decays with time for the Pt@FTO cathode but it is stable for the GNP-FTO cathode for as yet unclear reasons [41]. However, there is again a marked increase of dark current for the GNP-based device, found also for the $[Co(bpy\text{-}pz)_2]^{3+/2+}$ mediated DSCs [42] (see above). This dark current reduces the open-circuit voltage and efficiency (cf. Fig. 9), particularly at smaller light intensities [41, 42].

The difference in dark current for GNP@FTO and Pt@FTO cathodes (cf. Fig. 9) is difficult to understand, because the dark current should be controlled by the electron flow from the nanocrystalline TiO_2 film into the redox electrolyte and not by the flow of electrons at the counter electrode. Inspection of the previously reported DSC characteristics for $[Co(bpy\text{-}pz)_2]^{3+/2+}$ complex [41] and I_3^-/I^- [110] mediated systems confirms that the dark current near U_{OC} is always larger in cells with the GNP-FTO cathodes. Several authors [111, 113] suggested a hypothesis that graphene nanoplatelets detaching from the cathode might be transported through the electrolyte to the TiO_2 photoanode, where they deposit and subsequently catalyze the undesired recombination reactions (2).

Further upgrade of the work on graphene cathode for Co-mediated DSC was presented recently by Roy-Mayhew et al. [113]. They actually adopted a strategy similar to that of Kavan et al. [41, 42, 110], i.e., they revisited their previously developed cathode for I-mediated systems, viz. a porous FGS electrode [112] (see Sect. 3.3.3). They further optimized the composition of their FGS electrode; the main distinction from earlier work [112] was that the new electrode was formulated with binders (ethyl cellulose, Pluronic-type copolymers, and polyethylene oxide) which were only party pyrolyzed at moderate temperatures, leaving ca. 20 wt% of residuum after heat treatment [113]. This residuum acted as spacer of the FGS particles, thus improving the structural stability and surface area of the composite, albeit the residue itself did not have significant catalytic activity [113]. Similarly, the composite of ca, 20% GNP with pyrolyzed polyacrylonitrile showed good electrocatalytic activity with $R_{CT} \approx 1\ \Omega\,cm^2$ for $Co(bpy)_3{}^{3+/2+}$ and improved stability against that of pure GNP deposit on FTO [179]. The dye sensitized solar cell using this cathode also had enhanced efficiency and fill factor compared to those of DSC with a Pt@FTO cathode [179].

The FGS composite with unpyrolyzed residuum is attractive because of its universal applicability in three fundamentally different types of DSC distinguished by the mediator: (1) the classical I_3^-/I^- electrolyte solution interfaced to N719 sensitized photoanode, (2) the state-of-the-art Co-mediator, $[Co(bpy)_3]^{3+/2+}$ interfaced to D35 sensitized photoanode, and (3) the alternative S-containing mediator (5-mercapto-1-methyltetrazole and its dimer) [25] interfaced to D35. The FGS composite turns out to be a versatile replacement of Pt@FTO in all these three model DSCs providing: (1) identical performance (I-mediated DSC, 6.8% vs 6.8%) or (2) slightly better performance (Co-mediated DSC, 4.5% vs 4.4%) or considerably better performance (S-mediated DSC, 3.5% vs 2.0%)

[113]. In a recent related study on thiolate/disulfide redox couple, Liu et al. [180] confirmed the high activity of hydrazine-reduced GO with remarkable DSC efficiency of 6.55% (referenced to 3.22% for DSC with a Pt cathode).

Inspired by this success of FGS-composites with partly pyrolyzed residuum [113], Kavan et al. [111] developed a new type of composite using graphene oxide (GO) as a source of binder and/or catalytic component. Graphene nanoplatelets (GNP) which have been investigated in their earlier works [41, 42, 110] are highly active as cathode catalysts, but unfortunately insoluble in any solvent, and they do not adhere well to FTO. On the other hand, the single-layer graphene oxide (GO) is soluble in water, and the mixed aqueous solutions of GO/GNP are also quite stable against flocculation [111].

The amphiphilic character of GO stems from the presence of oxidic functional groups on the condensed aromatic backbone. GO is known to act as surfactant, which enables one to make colloidal solutions of carbon nanotubes and nanotubes/fullerene-C_{60} mixtures in water [74]. The same surfactant-aided dissolution occurs, presumably, also in the GO/GNP mixture [111]. Furthermore, the solution-processable films deposited on FTO glass from GO or GO/GNP mixtures are robust and wear resistant, due to intimate interaction of hydrophilic functionalities in GO with the hydroxylated surface of FTO. The films from pure GO are not very active catalytically, but can be activated either by chemical reduction with hydrazine or by simple calcination in inert atmosphere [111]. The later treatment is reminiscent of the thermal activation of FGS-composites mentioned above [113], and is also applicable to the activation of GO/GNP composites [111].

This GO/GNP fabrication protocol provided improved optically transparent cathode for dye sensitized solar cells [111]. Compared to films from pure graphene nanoplatelets, the GO or GO/GNP based electrodes showed better mechanical and electrochemical stability, but without any significant drop in electrocatalytic activity for $[Co(bpy)_3]^{3+/2+}$. The aging-induced loss of activity was smaller for GO-based electrodes compared to that for pure GNP-electrodes [111]. The performance of GO-containing films was demonstrated in dye-sensitized solar cells with Y123-sensitized TiO_2 photoanodes and $[Co(bpy)_3]^{3+/2+}$ as the redox mediator [111]. Figure 10 shows representative data for cathodes from pure graphene oxide upon thermal activation (coded GO-HT) and Pt@FTO for comparison. The efficiencies of solar cells with GO-HT@FTO cathode are similar to the efficiencies of solar cells with Pt@FTO cathode [111]. Specifically, the solar cell shown in Fig. 10 provided at 0.095 sun the efficiency of 10.1% and 10.0% for GO-HT and Pt, respectively. Analogously at 1 sun illumination, the corresponding efficiencies were 8.8% and 9.0% for GO-HT and Pt, respectively (Fig. 10 and [111]).

A systematic screening of GO/GNP composites with varying optical transmissions (total carbon loading) and varying GO/GNP ratios pointed at the optimum material containing 50 wt% of each GO and GNP components [111]. The actual thin-film electrode (optical transmission 90% at 550 nm wavelength) exhibited the charge transfer resistance $R_{CT1} = 0.23\ \Omega\ cm^2$ and $R_{CT2} = 0.38\ \Omega\ cm^2$

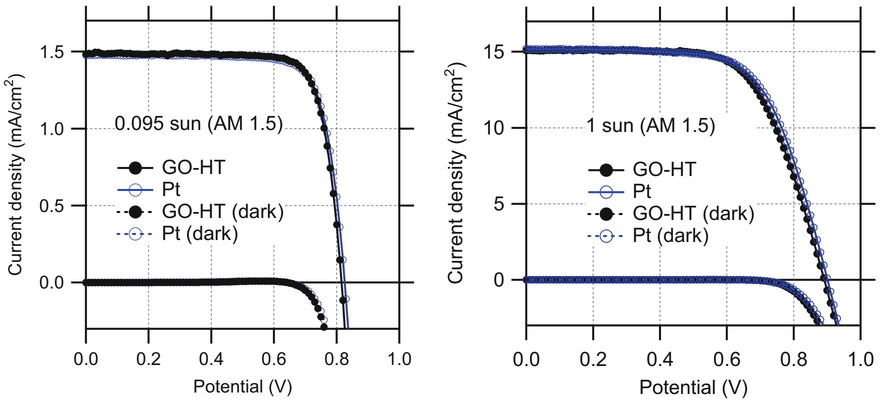

Fig. 10 Current–voltage characteristics of dye sensitized solar cell with Y123 sensitized TiO_2 photoanode and $[Co(bpy)_3]^{3+/2+}$ (bpy is 2,2′-bipyridine) as the redox mediator in the dark and under illumination with 0.095% sun (*left chart*) and full sun (*right chart*). The cathode is fabricated either from heat treated graphene oxide (GO-HT *black curves*) or Pt (*blue curves*). The GO-HT film had optical transmission of 86% at 550 nm wavelength. Adapted with permission from L. Kavan et al. *ACS Applied Materials & Interfaces* **4**, 6999 (2012). Copyright (2012) American Chemical Society

which are the best values from all of those GO/GNP composites. (Note that the EIS of the composite cannot be fitted to the equivalent circuit as in Fig. 7, because the spectra distinguish both electrode components separately.) Nevertheless, the solar tests of DSCs with GO/GNP composite cathodes are expectedly less sensitive to individual differences between cathodes having such a high activity. The deviations found are rather statistical than systematic, with no clear trends, except, perhaps, for slightly larger currents, but smaller voltages for most DSCs with GO-based cathodes [111].

Furthermore, the solar cells with GO-based cathodes do not show the problem with enhanced dark current anymore, which was previously identified as one of the drawbacks of GNP-electrodes [41, 42, 110]. Blocking of dark current in GO-HT-based solar cells is also visible in Fig. 10, if we compare it to Fig. 9. The decrease of dark current can be explained by improved film structure and firm bonding of GO-based films to FTO, which prevents peeling of carbonaceous particles from the electrode support [41, 113]. The same effect is also responsible for slower aging of the GO-HT and GO/GNP referenced to the aging-induced loss of activity for pure GNP cathodes [41, 42, 111].

3.3.5 Sulfur-Mediated DSC

Carbon electrodes show particularly promising electrocatalytic activity for redox mediators based on organosulfur molecules. In 2010, Graetzel et al. [25] introduced a redox shuttle based on disulfide/thiolate, T_2/T^-, where T^- is 5-mercapto-1-methyltetrazole and T_2 its dimer, i.e., bis(1-methyltetrazol-5-yl) disulfide.

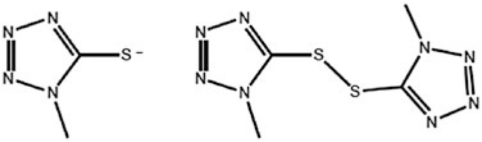

Structural formulae of T^-: 5-mercapto-1-methyltetrazol and T_2: bis(1-methyltetrazol-5-yl) disulfide

Their DSC with a classical Pt@FTO cathode provided 6.4% solar conversion efficiency, which was the highest value in an iodine-free system at that time [25]. Later on, an efficiency of 7.9% was reported for a similar DSC employing PEDOT as the counter electrode [181]. Other organosulfur compounds based on disulfide, polysulfides, thiourea, cysteine, etc. were also tested in DSCs but the T_2/T^- couple or its ethyl homologue [180] usually exhibited the best performance [27, 28, 32, 181, 182].

Wu et al. [182] reported that the graphite counter electrode was considerably more efficient than that with Pt@FTO cathode in sulfur-mediated DSC. The same conclusion was also made about counter electrodes fabricated from vertically aligned SWNT [183], carbon black [184], and composites of carbon black with PEDOT [185].

Roy-Mayhew et al. [113] compared the activity of FGS in a composite with partly pyrolyzed organic binder (see Sect. 3.3.4.1) in conjunction with T_2/T^- and two other model systems, i.e., I_3^-/I^- and $[Co(bpy)_3]^{3+/2+}$. They concluded that FGS composite is a versatile replacement of Pt@FTO in all three model DSCs with D35 sensitizer providing: (1) identical performance (I-mediated DSC, 6.8% vs 6.8%) or (2) slightly better performance (Co-mediated DSC, 4.5% vs 4.4%) or considerably better performance (S-mediated DSC, 3.5% vs 2.0%) [113].

Recently, Liu et al. [180] tested hydrazine-reduced graphene oxide (rGO) mixed with carbon black as counter electrode material for DSC with 5-mercapto-1-ethyltetrazol/bis(1-ethyltetrazol-5-yl) disulfide, i.e., the ethyl homologue of the T_2/T^-. They found a remarkable solar conversion efficiency of 6.55% (referenced to 3.22% for DSC with Pt cathode). The factor of 2 improvement in efficiency is the highest value found in the literature on sulfur mediated DSC, as well as on DSCs using other redox shuttles. This makes a viable promise that platinum could eventually be replaced in practical solar cells by cheaper counter electrode materials based on nanocarbons.

4 Conclusion

This review illustrates natural links between dye sensitized solar cells and carbon science in general and between DSCs and modern nanocarbons in particular. The implementation of nanocarbons in solar cells, not only in DSCs but also in similar devices like BHJ cells and solid-state photovoltaics, is a vital scientific discipline with numerous challenges. Due to the broad scope of these problems, this review is selective rather than comprehensive.

A significant theme, which also seems to be close to practical applications, is the use of graphene-based materials as catalytic cathode in the state-of-the-art Co-mediated solar cells. The history of Co-mediated DSCs per se represents a fascinating lesson about the development of solar cells, and the decade of research on Co-mediated cells is a rich source of general scientific and philosophical inputs.

Another "evergreen story," closely related to DSC research, is the discussion of electrochemical charge transfer and electrocatalytic activity of a carbon surface. Again, this subject, which extends from the area of DSCs to many other branches of electrochemistry and materials science, has passed 2 decades of intriguing scientific efforts, but it has also generated opposite claims and conflicting discussions at the same time. Hence, the problem of electrocatalysis on carbon is still open for fundamental research addressing the currently existing contradictions.

Furthermore, there are several novel ideas like all-carbon solar cells, nanocarbon-based sensitizers, nanodiamond, etc., which still have to be explored to decide whether or not they have the potential to generate novel technological platforms of solar energy conversion. Concerted efforts of electrochemists and carbon specialists will surely bring new discoveries in the field of DSC.

Acknowledgement This work was supported by the Grant Agency of the Czech Republic (contract No. 13-07724S).

References

1. Grätzel M (2001) Nature 414:338
2. O'Regan B, Grätzel M (1991) Nature 353:737
3. Hagfeldt A, Boschloo G, Sun L, Kloo L, Pettersson H (2010) Chem Rev 110:6595
4. Kalyanasundaram K (2010) Dye sensitized solar cells. CRC, Boca Raton
5. Gong J, Liang J, Sumathy K (2012) Renew Sustain Energy Rev 16:5848
6. Gerischer H (1990) Electrochim Acta 35:1677
7. Wrington MS (1979) Acc Chem Res 12:303
8. Finklea HO (1988) In: Finklea HO (ed) Semiconductor electrodes. Elsevier, Amsterdam, pp 44–145
9. Bard AJ (1980) Science 207:139
10. Fujishima A, Honda K (1972) Nature 238:37
11. Hamnett A, Dare-Edwards MP, Wright RD, Seddon KR, Goodenough JB (1979) J Phys Chem 83:3280
12. Clark WDK, Sutin N (1977) J Am Chem Soc 99:4676
13. Anderson S, Constable EC, Dare-Edwards MP, Goodenough JB, Hamnett A, Seddon KR, Wright RD (1979) Nature 280:571
14. Desilvestro J, Grätzel M, Kavan L, Moser J, Augustynski J (1985) J Am Chem Soc 107:2988
15. Bach U, Lupo D, Comte P, Moser J, Weissortel F, Salbeck J, Spreitzer H, Grätzel M (1998) Nature 395:583
16. Bai Y, Cao Y, Zhang J, Wang M, Li R, Wang P, Zakeeruddin SM, Grätzel M (2008) Nat Mater 7:626

17. Berger T, Monllor-Setoca D, Jankulovska M, Lana-Villarreal T, Gomez R (2012) Chemphyschem 13:2824
18. Froeschl T, Hoermann U, Kubiak P, Kucerova G, Pfanzelt M, Weiss CK, Boehm RJ, Husing N, Kaiser U, Landfester K, Wohlfahrt_Mehrens M (2012) Chem Soc Rev 41:5313
19. Kavan L (2012) Chem Rec 12:131
20. Kavan L (2012) Int J Nanotechnol 9:652
21. Kavan L (2010) In: Kalyanasundaram K (ed) Dye-sensitized solar cells. CRC, Boca Raton, pp 45–81
22. Pelouchova H, Janda P, Weber J, Kavan L (2004) J Electroanal Chem 566:73
23. Vlachopolous N, Liska P, Augustynski J, Grätzel M (1988) J Am Chem Soc 110:1216
24. Hamann TW (2012) Dalton Trans 41:3111
25. Wang M, Chamberland N, Breau L, Moser J, Humphry-Baker R, Marsan B, Zakeeruddin SM, Grätzel M (2010) Nat Chem 2:385
26. Daeneke T, Kwon TH, Holmes AB, Duffy NW, Bach U, Spiccia L (2011) Nat Chem 3:211
27. Hamann TW, Ondersma JW (2011) Energy Environ Sci 4:370
28. Cong J, Yang X, Kloo L, Sun L (2012) Energy Environ Sci 5:9180
29. Yella A, Lee HW, Tsao HN, Yi C, Chandiran AK, Nazeeruddin MK, Diau EWG, Yeh CY, Zakeeruddin SM, Grätzel M (2011) Science 334:629
30. Tsao HN, Burschka J, Yi C, Kessler F, Nazeeruddin MK, Grätzel M (2011) Energy Environ Sci 4:4921
31. Hardin BE, Snaith HJ, McGehee MD (2012) Nat Photonics 6:161
32. Ahmad S, Bessho T, Kessler F, Baranoff E, Frey J, Yi C, Grätzel M, Nazeeruddin MK (2012) Phys Chem Chem Phys 14:10631
33. Feldt SM, Gibson EA, Gabrielsson E, Sun L, Boschloo G, Hagfeldt A (2010) J Am Chem Soc 132:16714
34. Tsao HN, Yi C, Moehl T, Yum J-H, Zakeeruddin SM, Nazeeruddin MK, Grätzel M (2011) ChemSusChem 4:591
35. Zhou D, Yu Q, Cai N, Bai Y, Wang Y, Wang P (2011) Energy Environ Sci 4:2030
36. Liu J, Zhang J, Xu M, Zhou D, Jing X, Wang P (2011) Energy Environ Sci 4:3021
37. Yum J-H, Baranoff E, Kessler F, Moehl T, Ahmad S, Bessho T, Marchioro A, Ghadiri E, Moser JE, Nazeeruddin MK, Grätzel M (2012) Nat Commun 3:631
38. Lee MM, Teuscher J, Miyasaka T, Murakami TN, Snaith HJ (2012) Science 338:643
39. Kavan L, Grätzel M, Gilbert SE, Klemenz C, Scheel HJ (1996) J Am Chem Soc 118:6716
40. Laskova B, Zukalova M, Kavan L, Chou A, Liska P, Wei Z, Bin L, Kubat P, Ghadiri E, Moser JE, Grätzel M (2012) J Solid State Electrochem 16:2993
41. Kavan L, Yum J-H, Grätzel M (2011) Nano Lett 11:5501
42. Kavan L, Yum J-H, Nazeeruddin MK, Grätzel M (2011) ACS Nano 5:9171
43. Gibson EA, Smeigh AL, Pleux LL, Hammarstrom L, Odobel F, Boschloo G, Hagfeldt A (2011) J Phys Chem C 115:9772
44. Sapp SA, Elliot M, Contado C, Caramori S, Bignozzi CA (2002) J Am Chem Soc 124:11215
45. Murakami TN, Ito S, Wang Q, Nazeeruddin MK, Bessho T, Cesar I, Liska P, Humphry-Baker R, Comte P, Pechy P, Grätzel M (2006) J Electrochem Soc 153:A2255
46. Hauch A, Georg A (2001) Electrochim Acta 46:3457
47. Chen CM, Chen CH, Wei TC (2010) Electrochim Acta 55:1687
48. Ramasamy E, Lee WJ, Lee DY, Song JS (2007) Appl Phys Lett 90:173103
49. Wang G, Xing W, Zhou S (2009) J Power Sources 194:568
50. Gong F, Wang H, Xu X, Zhou G, Wang ZS (2012) J Am Chem Soc 134:10953
51. Dai L, Chang DW, Baek JB, Lu W (2012) Small 8:1166
52. D'Souza F, Ito O (2012) Chem Soc Rev 41:86
53. Guldi DM, Sgobba V (2011) Chem Commun 47:606
54. Moule AJ (2010) Curr Opin Solid State Mater Sci 14:123
55. Po R, Carbonera C, Bernardi A, Tinti F, Camaioni N (2012) Solar Energy Mater Solar Cells 100:97

56. Dubacheva GV, Liang CK, Bassani DM (2012) Coord Chem Rev 256:2628
57. Guo S, Dong S (2011) Chem Soc Rev 40:2644
58. Sun Y, Wu Q, Shi G (2011) Energy Environ Sci 4:1113
59. Zhu H, Wei J, Wang K, Wu D (2009) Solar Energy Mater Solar Cells 93:1461
60. Yu G, Gao J, Hummelen JC, Wudl F, Heeger AJ (1995) Science 270:1789
61. Liang Y, Xu Z, Xia J, Tsai ST, Wu Y, Li G, Ray C, Yu L (2010) Adv Mater 22:E135
62. Sun Y, Welch GC, Leong WL, Takacs CJ, Bazan GC, Heeger AJ (2012) Nat Mater 11:44
63. Li G, Zhu R, Yang Y (2012) Nat Photonics 6:153
64. Hu L, Hecht DS, Gruner G (2010) Chem Rev 110:5790
65. Kavan L, Dunsch L (2007) Chemphyschem 8:974
66. Kavan L, Dunsch L (2011) Chemphyschem 12:47
67. Bindl DJ, Wu MY, Prehn FC, Arnold MS (2011) Nano Lett 11:455
68. Ren S, Bernardi M, Lunt RR, Bulovic V, Grossman JC, Gradecak S (2011) Nano Lett 11:5316
69. Bindl DJ, Safron NS, Arnold MS (2010) ACS Nano 10:5657
70. Bissett M, Barlow A, Shearer C, Quinton J, Shapter JG (2012) Carbon 50:2431
71. Becerril HA, Mao J, Liu Z, Stoltenberg RM, Bao Z, Chen Y (2008) ACS Nano 2:463
72. Miao X, Tongay S, Petterson MK, Berke K, Rinzler AG, Appleton BR, Hebard AF (2012) Nano Lett 12:2745
73. Klinger C, Patel Y, Postma HWC (2012) PLoS One 7:e37806
74. Tung VC, Huang JH, Tevis I, Kim F, Kim J, Chu CW, Stupp SI, Huaong J (2011) J Am Chem Soc 133:4940
75. Bernardi M, Lohrman J, Kumar PV, Kirkeminde A, Ferralis N, Grossman JC, Ren S (2012) ACS Nano 6:8896
76. Yan X, Cui X, Li B, Li LS (2010) Nano Lett 10:1869
77. Lim CHYX, Zhong YL, Janssens S, Nesladek M, Loh KP (2010) Adv Funct Mater 20:1313
78. Zhong YL, Midya A, Ng Z, Chen ZK, Daenen M, Nesladek M, Loh KP (2008) J Am Chem Soc 130:17218
79. Neo CY, Ouyang J (2013) Carbon 54:48
80. Chen T, Qiu L, Cai Z, Gong F, Yang Z, Wang Z, Peng H (2012) Nano Lett 12:2568
81. Zhang L, Shi E, Ji C, Li Z, Li P, Shang Y, Li Y, Wei J, Wang K, Zhu H, Wu D, Cao A (2012) Nanoscale 4:4954
82. Guo W, Xu C, Wang X, Wang S, Pan C, Lin C, Wang ZL (2012) J Am Chem Soc 134:4437
83. Kim KS, Zhao Y, Jang H, Lee SY, Kim JM, Kim KS, Ahn JH, Kim P, Choi JY, Hong BH (2009) Nature 457:706
84. Nair RR, Blake B, Grigorenko AN, Novoselov KS, Booth TJ, Stauber T, Peres NMR, Geim AK (2008) Science 320:1308
85. Li X, Cai W, An J, Kim S, Nah J, Yang D, Piner R, Velamakanni A, Jung I, Tutuc E, Banerjee SK, Colombo L, Ruoff RS (2009) Science 324:1312
86. Wang X, Zhi L, Muellen K (2008) Nano Lett 8:323
87. Zhang M, Fang S, Zakhidov AA, Lee SB, Aliev AE, Williams CD, Atkinson KR, Baughman RH (2005) Science 309:1215
88. Lee KS, Lee Y, Lee JY, Ahn JH, Park JH (2012) ChemSusChem 5:379
89. Chen T, Hu W, Song J, Guai GH, Li CM (2012) Adv Funct Mater 22:5245
90. Kamat PV, Tvrdy K, Baker DR, Radich JG (2010) Chem Rev 110:6664
91. Nath NCD, Sarker S, Ahammad AJS, Lee JJ (2012) Phys Chem Chem Phys 14:4333
92. Jang YH, Xin X, Byun M, Jang YJ, Lin Z, Kim DH (2012) Nano Lett 12:479
93. Tang YB, Lee CS, Xu J, Liu ZT, Chen ZH, He Z, Cao YL, Yuan G, Song H, Chen L, Luo L, Cheng HM, Zhang WJ, Bello I, Lee ST (2010) ACS Nano 4:3482
94. Yang N, Zhai J, Wang D, Chen Y, Jiang L (2010) ACS Nano 4:887
95. Chen J, Li B, Zheng J, Zhao J, Zhu Z (2012) J Phys Chem C 116:14848
96. Paolucci D, Franco MM, Iurlo M, Marcaccio M, Prato M, Zerbetto F, Penicaud A, Paolucci F (2008) J Am Chem Soc 130:7393

97. Dang X, Yi H, Ham MH, Qi J, Yun DS, Ladewski R, Strano MS, Hammond PT, Belcher AM (2011) Nat Nanotechnol 6:377
98. Kyaw AKK, Tantang H, Wu T, Ke L, Wei J, Demir HV, Zhang Q, Sun XW (2012) J Phys D: Appl Phys 45:165108
99. Durantini J, Boix PP, Gervaldo M, Morales GM, Otero L, Bisquert J, Barea EM (2012) J Electroanal Chem 683:43
100. Fan J, Liu S, Yu J (2012) J Mater Chem 22:17027
101. Song J, Yin Z, Yang Z, Amaladass P, Wu S, Ye J, Zhao Y, Deng WQ, Zhang H, Liu XW (2011) Chem Eur J 17:10832
102. Neo CY, Ouyang J (2013) J Power Sources 222:161
103. Kay A, Grätzel M (1996) Solar Energy Mater Solar Cells 44:99
104. Papageorgiou N (2004) Coord Chem Rev 248:1421
105. Murakami TN, Grätzel M (2008) Inorg Chim Acta 361:572
106. Huang Z, Liu X, Li K, Li D, Luo Y, Li H, Song W, Chen L, Meng Q (2007) Electrochem Commun 9:596
107. Imoto K, Takahashi K, Yamaguchi T, Komura T, Nakamura J, Murata K (2003) Solar Energy Mater Solar Cells 79:459
108. Li G, Wang F, Jiang Q, Gao X, Shen P (2010) Angew Chem Int Ed 49:3653
109. Trancik JE, Barton SC, Hone J (2008) Nano Lett 8:982
110. Kavan L, Yum J-H, Grätzel M (2011) ACS Nano 5:165
111. Kavan L, Yum J-H, Grätzel M (2012) ACS Appl Mater Interfaces 4:6999
112. Roy-Mayhew JD, Bozym DJ, Punckt C, Aksay A (2010) ACS Nano 10:6203
113. Roy-Mayhew JD, Boschloo G, Hagfeldt A, Aksay IA (2012) ACS Appl Mater Interfaces 4:2794
114. Liberatore M, Petrocco A, Caprioli F, La Mesa C, Decker F, Bignozzi CA (2010) Electrochim Acta 55:4025
115. Nelson JJ, Amick TJ, Elliott CM (2008) J Phys Chem C 112:18255
116. Tsao HN, Comte P, Yi C, Grätzel M (2012) Chemphyschem 13:2976
117. Papageorgiou N, Maier WE, Grätzel M (1997) J Electrochem Soc 144:876
118. Pumera M (2010) Chem Soc Rev 39:4146
119. Ambrosi A, Bonanni A, Sofer Z, Cross JS, Pumera M (2011) Chem Eur J 17:10763
120. Chua CK, Sofer Z, Pumera M (2012) Chem Eur J 18:13453
121. Velten J, Mozer AJ, Li D, Officer D, Wallace G, Baughman RH, Zakhidov AA (2012) Nanotechnology 23:085201
122. Pumera M (2009) Chem Eur J 15:4970
123. Banks CE, Davies TJ, Wildgoose GG, Compton RG (2005) Chem Commun 829
124. McCreery RL (2008) Chem Rev 108:2646
125. Fujishima A, Einaga Y, Rao TN, Tryk DA (2005) Diamond electrochemistry. Elsevier, Tokyo
126. Beguin F, Frackowiak E (2009) Carbons for electrochemical energy storage and conversion systems. Taylor & Francis, New York
127. Lai SCS, Patel AN, McKelvey K, Unwin PR (2012) Angew Chem Int Ed Engl 51:5405
128. Goh MS, Pumera M (2010) Chem Asian J 5:2355
129. Olsen E, Hagen G, Lindquist SE (2000) Solar Energy Mater Solar Cells 63:267
130. Liberatore M, Decker F, Burtone L, Zardetto V, Brown TM, Reale A, Di Carlo A (2009) J Appl Electrochem 39:2291
131. Ahmad S, Yum J-H, Butt HJ, Nazeeruddin MK, Grätzel M (2010) Chemphyschem 11:2814
132. Ahmad S, Yum J-H, Xianxi Z, Grätzel M, Butt HJ, Nazeeruddin MK (2010) J Mater Chem 20:1654
133. Tian H, Yu Z, Hagfeldt A, Kloo L, Sun L (2011) J Am Chem Soc 133:9422
134. Hong W, Xu Y, Lu G, Li C, Shi G (2008) Electrochem Commun 10:1555
135. Zhang Q, Zhang Y, Huang S, Huang X, Luo Y, Meng Q, Li D (2010) Electrochem Commun 12:327

136. Jiang QW, Li GR, Liu S, Gao XP (2010) J Phys Chem C 114:13397
137. Wang M, Anghel AM, Marsan B, Cevey Ha NL, Pootrakulchote N, Zakeeruddin SM, Grätzel M (2009) J Am Chem Soc 131:15976
138. Wu M, Lin X, Wang L, Guo W, Qi D, Peng X, Hagfeldt A, Grätzel M, Ma T (2012) J Am Chem Soc 134:3419
139. Wu M, Lin X, Hagfeldt A, Ma T (2011) Angew Chem Int Ed 50:3520
140. Veerappan G, Bojan K, Rhee SW (2011) ACS Appl Mater Interfaces 3:857
141. Liu Y, Jennings JR, Parameswaran M, Wang Q (2011) Energy Environ Sci 4:564
142. Hsieh CT, Yang BH, Lin JY (2011) Carbon 49:3092
143. Choi H, Kim H, Hwang S, Han Y, Jeon M (2011) J Mater Chem 21:7548
144. Zhang DW, Li XD, Chen S, Li HB, Sun Z, Yin XJ, Huang SM (2010) In: Chu PK (ed) Proceeding of the 3rd international nanoelectronics conference (INEC). IEEE, Hong Kong, pp 610–611
145. Choi H, Kim H, Hwang S, Choi W, Jeon M (2010) Solar Energy Mater Solar Cells 95:323
146. Wan L, Wang S, Wang X, Dong B, Xu Z, Zhang X, Bing Y, Peng S, Wang J, Xu C (2011) Solid State Sci 13:468
147. Xu Y, Bai H, Lu G, Li C, Shi G (2008) J Am Chem Soc 130:5856
148. Zhang DW, Li XD, Li HB, Chen S, Sun Z, Yin XJ, Huang SM (2011) Carbon 49:5382
149. Wang H, Hu YH (2012) Energy Environ Sci 5:8182
150. Xue Y, Liu J, Chen H, Wang R, Li D, Qu J, Dai L (2012) Angew Chem Int Ed Engl 51:12124
151. Lin JY, Chan CY, Chou SW (2013) Chem Commun 49:1440
152. Wu MS, Zheng YJ (2013) Phys Chem Chem Phys 15:1782
153. Hong W, Xu Y, Lu G, Li C, Shi G (2008) Electrochem Commun 10:1555
154. Sun Y, Shi G (2013) J Polym Sci, Part B: Polym Phys 51:231
155. Suzuki K, Yamaguchi M, Kumagai M, Yanagida S (2003) Chem Lett 32:28
156. Mei X, Cho JC, Fan B, Ouyang J (2010) Nanotechnology 21:395202
157. Fan B, Mei X, Sun K, Ouyang J (2008) Appl Phys Lett 93:143103
158. Ramasamy E, Lee WJ, Lee DY, Song JS (2008) Electrochem Commun 10:1087
159. Lee WJ, Ramasamy E, Lee DY, Song JS (2009) ACS Appl Mater Interfaces 1:1145
160. Seo SH, Kim SY, Koo BK, Cha SI, Lee DY (2010) Langmuir 26:10341
161. Tantang H, Kyaw AKK, Zhao Y, Park MBC, Tok AIY, Hu Z, Li LJ, Sun XW, Zhang Q (2012) Chem Asian J 7:51
162. Joshi P, Zhang L, Chen Q, Galipeau D, Fong H, Qiao Q (2010) ACS Appl Mater Interfaces 2:3572
163. Zukalova M, Prochazka J, Bastl Z, Duchoslav J, Rubacek L, Havlicek D, Kavan L (2010) Chem Mater 22:4045
164. Lee CP, Lin LY, Vittal R, Ho KC (2011) J Power Sources 196:1665
165. Lee CP, Lin LY, Tsai KW, Vittal R, Ho KC (2011) J Power Sources 196:1632
166. Wu M, Lin X, Wang T, Qiu J, Ma T (2011) Energy Environ Sci 4:2308
167. Zhu G, Pan L, Lu T, Liu X, Lv T, Xu T, Sun Z (2011) Electrochim Acta 56:10288
168. Sljukic B, Banks CE, Compton RG (2006) Nano Lett 6:1556
169. Guai GH, Song QL, Guo CX, Lu ZS, Chen T, Ng CM, Li CM (2012) Solar Energy 86:2041
170. Lee JS, Ahn HJ, Yoon JC, Jang JH (2012) Phys Chem Chem Phys 14:7938
171. Yeh MH, Sun CL, Su JS, Lin JY, Lee CP, Chen CY, Wu CG, Vittal R, Ho KC (2012) Carbon 50:4192
172. Lee B, Buchholz DB, Chang RPH (2012) Energy Environ Sci 5:6941
173. Choi H, Kim H, Hwang S, Han Y, Jeon M (2011) J Mater Chem 21:7548
174. Kim H, Choi H, Hwang S, Kim Y, Jeon M (2012) Nanoscale Res Lett 7:53
175. Choi H, Hwang S, Bae H, Kim S, Kim H, Jeon M (2011) Electron Lett 47:281
176. Velten JA, Carreterro-Gonzales J, Castillo-Martinez E, Bykova J, Cook A, Baughman RH, Zakhidov AA (2011) J Phys Chem C 115:25125
177. Nusbaumer H, Moser J, Zakeeruddin SM, Nazeeruddin MK, Grätzel M (2001) J Phys Chem B 105:10461

178. Ghamouss F, Pitson R, Odobel F, Boujtita M, Caramori S, Bignozzi CA (2010) Electrochim Acta 55:6517
179. Morgan S, Yum JH, Hu Y, Graetzel M (2013) J Mater Chem. doi:10.1039/c3ta01635h
180. Liu G, Li X, Wang H, Rong Y, Ku Z, Xu M, Liu L, Hu M, Yang Y, Han H (2013) Carbon 53:11
181. Burschka J, Brault V, Ahmad S, Breau L, Nazeeruddin MK, Marsan B, Zakeeruddin SM, Grätzel M (2012) Energy Environ Sci 5:6089
182. Wu H, Lv Z, Chu Z, Wang D, Hou S, Zou D (2011) J Mater Chem 21:14815
183. Hao F, Dong P, Zhang J, Zhang Y, Loya PE, Hauge RH, Li J, Lou J, Lin H (2012) Sci Rep 2:368
184. Wang L, Wu M, Gao Y, Ma T (2011) Appl Phys Lett 98:221102
185. Zhang J, Long H, Mirrales SG, Bisquert J, Fabergat-Santiago F, Zhang M (2012) Phys Chem Chem Phys 14:7131

Top Curr Chem (2014) 348: 95–126
DOI: 10.1007/128_2013_450

Supramolecular Chemistry of Carbon Nanotubes

Gildas Gavrel, Bruno Jousselme, Arianna Filoramo, and Stéphane Campidelli

Abstract This chapter aims to present recent examples of supramolecular functionalization of carbon nanotubes. The non-covalent functionalization appears as a solution for the future applications in nanotechnologies since it allows the functionalization and manipulation of nanotubes without the introduction of sp^3 defects in the π-conjugated system. Thus, the optical and electronic properties of the nanotubes remain preserved. In the first part of this chapter, we present the use of surfactant for the dispersion of nanotubes and its application for sorting. Then we report several examples of functionalization of nanotubes based on π-stacking interactions with pyrene derivatives. Finally, in the last part we review the wrapping of photo/electroactive polymers around the nanotube sidewalls. We put a particular focus on polyflurorene-based polymers and we show their utilization for the separation of nanotubes in diameter and chirality.

Keywords Carbon nanotubes · Nanotube sorting · Non-covalent functionalization · Photoactive materials · Supramolecular assembly

Contents

G. Gavrel, A. Filoramo, and S. Campidelli (✉)
Laboratoire d'Electronique Moléculaire, CEA, IRAMIS, SPEC (CNRS URA-2464),
CEA Saclay, 91191 Gif-sur-Yvette, France
e-mail: stephane.campidelli@cea.fr

B. Jousselme
Laboratoire de Chimie des Surfaces et Interfaces, CEA, IRAMIS, SPCSI, CEA Saclay,
91191 Gif-sur-Yvette, France

1 Introduction

Due to their outstanding properties, carbon nanotubes (CNTs) are particular class of materials which are still extensively studied. However, the processing of CNTs and their integration into real applications are severely limited by a number of inherent shortcomings like polydispersity and purity of the samples, difficulties of manipulation, and low solubility of the nanotubes. Indeed, as-produced nanotubes also contain non-negligible quantities of amorphous carbon and metal catalyst residues; the quantity of each depends notably on the fabrication technique used to produce the nanotubes and can vary for the same kind of nanotubes from one batch to another. Moreover, a sample of carbon nanotubes is composed of many different tubes of different lengths, diameters, and properties. For example, single-wall carbon nanotubes (SWNTs) can be either metallic or semiconducting depending on their structures (i.e., on how the sheet of graphene has rolled up to form the hollow tube). Therefore great attention has been paid in the past to the purification, separation, and functionalization of carbon nanotubes and this research field is still very active.

The functionalization of carbon nanotubes offers the invaluable opportunity to combine the properties of the nanotubes with those of other classes of materials, and that for many applications. To add new functions onto nanotubes, two general strategies have been explored: (1) covalent functionalization of the sp^2 framework of the nanotubes or the derivatization of oxygenated functions created by oxidative treatments of the nanotubes and (2) non-covalent functionalization through supramolecular interactions between the nanotubes and other chemical objects.

This chapter deals with the latter functionalization technique. In particular, we will describe the principal approaches explored to functionalize non-covalently the nanotubes and we will discuss some of their applications.

2 Carbon Nanotubes Hybrids

Many different synthetic protocols have been optimized for the functionalization of CNTs. Basically, either a noncovalent or a covalent approach can be used. The two methodologies differ in that the supramolecular chemistry does not interfere, or very slightly, with the extended π-electron system of the CNTs. Instead, an extensive covalent functionalization transforms sp^2 carbons in sp^3, thus interrupting the π-conjugation.

2.1 Carbon Nanotube and Surfactants

In the following section we do not want to give an exhaustive list of surfactants which have been used for carbon nanotube dispersions; we chose to give a few examples of nanotube dispersion and individualization, to discuss the organization of the molecules around the nanotubes, and to show their applications for nanotube sorting.

2.1.1 Suspension of Single Wall Carbon Nanotubes (Why, How, and What For)

As mentioned before, SWNTs can be either semiconducting or metallic depending on their atomic structure geometry (diameter and chirality). This particular feature and their nanometer range diameter make them ideal candidates for future nanoelectronics. However, as-produced SWNT samples display a not negligible distribution, both in diameter and in chirality. In addition, they have the tendency to aggregate into bundles/ropes (due to the substantial van der Waals tube–tube interactions). These facts represent important issues for applications of carbon nanotubes. Chronologically, the first problem to solve is the presence of aggregates. This bundling disturbed the study of their electronic properties and complicated attempts in separating nanotubes by size, type, or chirality, finally avoiding the possibility to consider and use them as single macromolecular species.

The first works reporting individual SWNTs used organic solvents for fabricating a solution of pristine or chemically modified nanotubes [1–4]. In these cases the debundling was facilitated by chemical modifications. However, the chemical attacks of the nanotube sidewalls create defects in the sp^2 graphene lattice and partially destroy their outstanding electronic properties [5]. In contrast, it is generally admitted that the use of surfactants is an effective and non-aggressive method for debundling nanotubes. The idea is that surfactants disperse nanotubes and successfully suspend them through supramolecular interactions, preserving (or very slightly modifying) their electronic properties [6]. Pioneering studies showed that anionic sodium dodecylsulfate (SDS) or non-ionic triton (TX100) could form stable colloidal suspensions of single wall nanotubes in water [7]. However, more systematic studies of the dispersion efficiency of various surfactants only started in 2003. These efforts concerned mainly laser ablation [8], $\mathrm{HiP_{CO}}$ [8, 9], and CoMoCat [10] SWNTs.

Islam et al. [8] reported on the exceptional capability of sodium dodecylbenzenesulfonate (NaDBS) surfactant to suspend high concentration of SWNTs. In more detail, they compared the effectiveness of various surfactants for suspending commercially purified $\mathrm{HiP_{CO}}$ nanotubes. To fabricate the suspensions they used surfactant concentrations always exceeding the nominal critical micelle concentration (cmc) and a single step process consisting in a mild bath sonication (12 W, 55 kHz, 20 h). Then they checked the aggregation status and stability of the solutions obtained both by macroscopic observation of flocculation/precipitation in the solutions and by AFM imaging of the deposited products onto silicon surfaces. It is worth noting that the AFM technique has some limitations since the imaging analysis does not allow definitively excluding the presence of small bundles of few nanotubes (due to the tip deconvolution effect) [11]. According to their report, NaDBS gives the best results, enabling raising of the SWNT concentration for stable suspensions up to 20 mg/mL, while for all the other surfactants this does not exceed the range of 0.1–0.5 mg/mL.

Moore et al. [9] studied the ability of suspending as-produced $\mathrm{HiP_{CO}}$ nanotubes by (2 wt%) aqueous anionic, cationic, or nonionic surfactants and polymers. To achieve their suspension they used high-shear mixing and ultrasonication followed by ultracentrifugation. The decant obtained was studied by UV–vis-NIR absorption, photoluminescence, Raman spectroscopy and cryo-electron microscopy (cryo-TEM) imaging. Note that the combination of these techniques permits one to be more confident concerning the absence of bundles (for example photoluminescence is a typical signature of isolated semiconducting SWNTs [6]). Their results reported a final nanotube concentration varying within the range 10–20 mg/L for all the tested surfactants or polymers.

In the same period, Matarredona et al. [10] investigated the effect of chemical pre-treatment of CoMoCat carbon nanotubes on their interactions with NaDBS surfactant. Their studies were based on the electrical charge of the nanotube surface, which varied with the pH of the surrounding media (Point of Zero Charge or PZC effect) and could be greatly affected by the nanotube purification method. They purified the as-produced CoMoCat sample by a protocol using in its final step an acid (HF) or a basic (NaOH) treatment. As expected, the purified sample presented different PCZ (due probably to the presence of fluorine or sodium on the nanotube sidewalls). The idea was to study the coulombic interactions in surfactant/nanotube hybrids by performing the experiments at different pH. Their experiments demonstrated that the hydrophobic interactions dominated and that coulomb forces could play a role only at extreme pH values.

These three works reported various hypotheses and suggestions concerning the supramolecular organization of the surfactants around the nanotube sidewalls. The consensus is that surfactants disperse SWNTs in aqueous solution mainly via hydrophobic/hydrophilic interactions. The hydrophobic part of the surfactant is adsorbed onto the sidewall while the hydrophilic head associates with water. The presence of an aromatic ring in the hydrophobic chain is supposed to reinforce the interaction with the nanotube sidewalls due to π–π stacking. For non-ionic surfactants and polymers, Moore and coworkers suggested that the ability to suspend nanotubes was related to the size of the hydrophilic group (enhanced steric stabilization), while for the ionic ones this property was generally associated with the electrostatic repulsion of their charged ions. Actually, different kinds of organization were proposed and this point still remains a topic of debate. The organization scheme ranges from encapsulation in cylindrical micelles [6, 10, 12], adsorption of hemispherical micelles (also called hemi-micelles) [8, 13], to random adsorption [14]. Experimentally, surfactant organization has been studied by HR-TEM [13], small angle neutron scattering (SANS) [14], and more recently by cryo-TEM [12]. The experimental data demonstrated results consistent with the situation in cylindrical micelles (Fig. 1a) [12], in hemi-micelles (Fig. 1b) [13], or in random adsorption (Fig. 1c) [14] as materialized in Fig. 1, depending on the experimental protocol used to prepare the suspensions.

In some cases, two different behaviors were reported for the same surfactant. In particular, for SDS Richard et al. [13] reported on hemi-micellar configuration while Yurekli et al. [14] found the signature of random adsorption. In spite of this apparently contradictory experimental situation, numerical simulations helped one to understand and could elucidate the differences [15, 16]. The simulations revealed that a dynamic balance existed for the surfactant molecule between three states: (1) isolated in solution, (2) in micelle in the solution, and (3) adsorbed onto the SWNT. Simulations suggested that this was particularly true and important for low surfactant concentrations. As an example, Calvaresi et al. [15] reported that for all

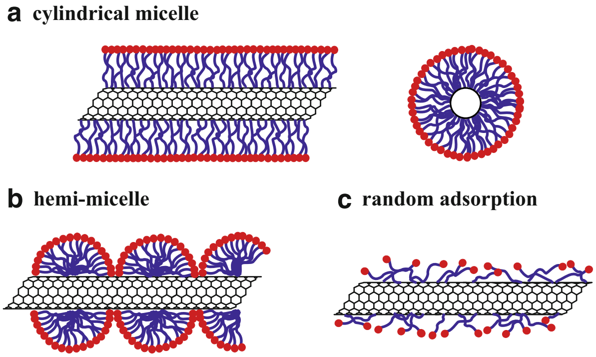

Fig. 1 Surfactant organization onto SWNTs. Three situations are possible: (**a**) encapsulation in cylindrical micelles; (**b**) adsorption of hemispherical micelles; or (**c**) random organization

surfactant concentrations the coverage of the nanotube started by collisions between the SWNT and preformed micelles in the liquid. At very low surfactant concentration the micelles interacted dynamically and weakly with the CNT, while when increasing the surfactant concentration the micelles started to adsorb and cover the SWNT. In this case, it was predicted that the micelles spread randomly on the surface and remained in a dynamical equilibrium on it. As far as the surfactant concentration increased, simulations showed that it started to self-assemble in stable superstructures (hemi-micelles). Then the hemi-micelles were replaced by cylindrical micelles at higher concentration. These results converged with the concentration-dependent study of Matarredona et al. [10] who reported about two stable plateaus that were assigned to random face-on adsorption of the surfactants and to their ordered edge-on adsorption. These results are also supported by the study of Wallace et al. [17] and, more recently, by the study of Pang et al. [18], showing through coarse-grained molecular dynamics calculations that the surfactant structure around SWNTs is concentration dependent. However, it is worth noting that in the work of Calvaresi the nanotube was a simple isolated cylinder and chirality was not taken into account while this parameter could influence the interaction and organization of the surfactant.

Recently several papers examined for single-tail vs double-tail molecules and also for gemini surfactants (two hydrophobic tails and two polar heads) the relationship between the structures and their stability on SWNTs [17, 19, 20]. Thus, in 2011, Fontana and co-workers [19] pointed out the ability of gemini surfactants (derived from *N*-[*p*-(*n*-dodecyloxybenzyl)]-*N*,*N*,*N*-trimethylammonium [*p*DOTABr]) to exfoliate and stabilize suspensions of SWNTs for surfactant/nanotube ratios 4–7 times lower than usual surfactant, such as CTAB, SDS, or SDBS, and for concentrations well below their CMC values. The good SWNT dispersing ability of that class of surfactant was attributed to their higher charge capacity, their stronger adsorption ability, and their compact alignment on the SWNT surfaces. Such compactness resulted in the fact that only the ammonium head was exposed to the aqueous solution whereas both the aromatic part and the two alkyl chains interacted with the nanotube backbone by π–π stacking and Van der Waals interactions.

Recently, several reports focused more deeply into the differences observed when varying the nanotube batches. It was noticed that even when a standard identical procedure for dispersion was used, different results in suspensions were obtained due to differences in SWNT batches. In particular, smaller diameter HiP$_{CO}$ presented higher solubility and dispersibility than bigger diameter tubes [21, 22]. In this sense, simulations predicted that small diameter SWNTs had weaker van der Waals attraction than large diameter ones, rendering them easier to debundle and disperse [23, 24]. In addition, smaller diameter nanotubes would permit a higher packing density of the surfactant tails and less electrostatic repulsion between headgroups [25].

The lessons to be learned here are that surfactant concentration is important but an effective dispersant for a particular batch of nanotubes will not perform in exactly the same way for another one.

Biomolecules were also used for producing high quality suspensions of SWNTs and, in particular, great attention was given to DNA. In 2003 Zheng and co-workers reported that single-stranded DNA (ssDNA) molecules wrapped helically around SWNTs [26]. They proposed that the aromatic part of the DNA nucleobases stacked onto the nanotube sidewall via π–π interactions and that the hydrophilic sugar-phosphate charged backbone ensured the nanotube suspension in water. In addition, the flexibility of ssDNA could permit low energy conformations to be found for the molecule when the base stacking matched with the underlying SWNT lattice structure. They also noted a difference depending on the basis sequence of the strand: poly(adenine) or poly(cytosine) sequences were less efficient to suspend nanotubes compared to poly(thymine). These features suggested that the ssDNA/SWNT interactions depended on both DNA sequence and SWNT structure as was also supported in the literature by simulations [27–29]. Interesting experimental results for SWNT solubilization by ssDNA oligomers were reported by Vogel et al. [30]. They demonstrated that short $d(GT)_3/d(AC)_3$ mixtures gave better results than longer $d(GT)_n/d(AC)_n$ or isolated $d(GT)_n$ oligomers for nanotube dispersion.

The understanding and control of the interactions between the nanotubes and the surfactants are important in view of future separation of the nanotubes. Once the individualization of the nanotubes is achieved in solution, the sorting process can take place. Different approaches were reported in the literature to sort SWNTs in length [31–35], diameter [33, 34, 36–42], chirality [43–49], metallic/semiconducting character [36, 39, 50–54], and handedness [55–57]. One of the most popular strategies reported in the literature took advantage of the differences in surfactant organization on suspended/encapsulated individual nanotubes. The method was based on the density gradient ultracentrifugation (DGU) technique. DGU is a method widely used in biochemistry for the purification of proteins and nucleic acids. In the present context, during the ultracentrifugation process the encapsulated SWNTs migrate into the density gradient medium until they reach their corresponding isopycnic points (the points where their buoyant density equals that of the surrounding medium) [39]. Thus objects with different buoyant density spatially separate in the gradient (overcoming the limitations of ultracentrifugation in a density constant medium). It is therefore easy to understand that the optimization of surfactant/nanotube interaction is crucial and that, in principle, small differences in surfactant packing around the nanotubes, depending on their structure, can enable the sorting process. Figure 2 shows the schematic representation of the DGU process [58]. First, an SWNTs/surfactant suspension was prepared by ultrasonication (Fig. 2a), big bundles were

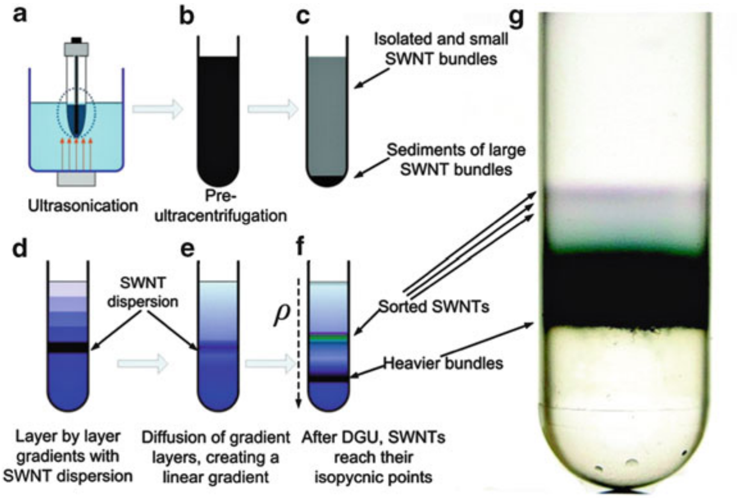

Fig. 2 Schematic representation of SWNTs sorting by DGU (**a**–**f**) and picture of the cell tube showing the separation SWNTs after DGU (**g**); extracted from [58], with permission of the *American Chemical Society*

removed by conventional ultracentrifugation (Fig. 2b), and the supernatant was recovered (Fig. 2c). Second, the step gradient for DGU was prepared by placing in several layers of gradient density media with decreasing concentration on top of each other. The SWNT dispersion was placed between two layers (Fig. 2d). A linear density gradient is formed spontaneously by diffusion (Fig. 2e). Finally, DGU led to SWNTs spatial separation in the ultracentrifuge cell (as schematized in Fig. 2f and demonstrated by a real photo of the DGU cell in Fig. 2g).

One famous result obtained by such a technique was reported in the literature by Hersam's group [39]. In their work they achieved a rich structure density relationship for sodium cholate (SC) encapsulated CoMoCat SWNTs that permitted their sorting by diameter and bandgap (Fig. 3). Note for DGU, Optiprep (60% w/v iodixanol solution in water) is very often used as gradient density medium.

For nanotube sorting by DGU, sodium cholate is often used as surfactant because of its ability to form close packed structures on nanotubes [59]; however, mixtures of surfactant (SDS, SDBS, SC, and other bile salts) can also be used [39, 60–63]. In particular, Maruyama and co-workers studied the influence of the surfactants in the separation by using mixtures of sodium deoxycholate (DOC) and SDS [62, 63]. The principle of the separation is mainly based on the relative affinities of the two surfactants to the SWNT sidewalls and the difference of density when wrapped on them. They demonstrated that the two surfactants (SDS and DOC) behaved differently with nanotubes. Indeed SDS interacts preferentially onto the metallic nanotubes, providing an electronic type separation [64], while DOC forms stable structures with small-diameter near-armchair nanotubes, inducing a separation in diameter. Moreover, because of the different packing of these

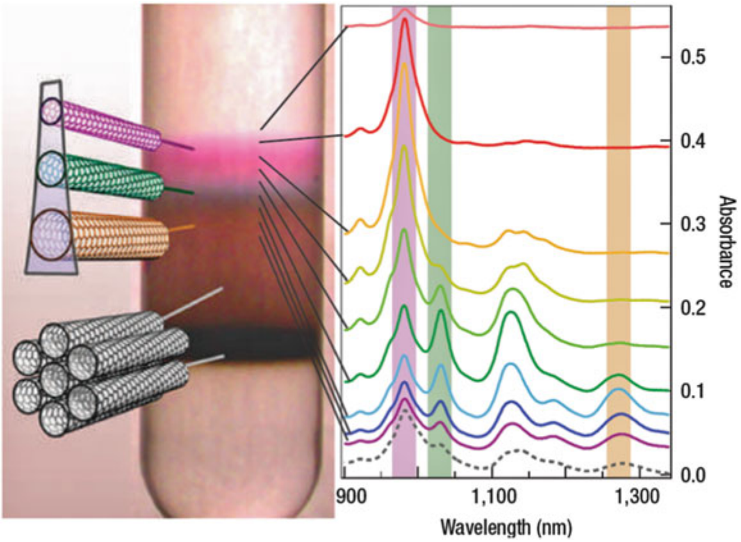

Fig. 3 Example of SC-encapsulated CoMoCat SWNTs (0.7–1.1 nm) sorted by diameter and energy bandgap using density gradient ultracentrifugation; adapted from [39], with permission of the *Nature Publishing Group*

surfactants on the nanotube sidewalls, the resulting SDS and DOC micelles exhibited different densities and then very different migrations in the gradient density medium. By carefully choosing the ratio SDS/DOC, the authors were able to improve the separation and well-resolved fractions of various narrow diameter distributions of s-SWNTs were obtained, simplifying the post-DGU fractionating procedure.

Another strategy that has been explored to achieve nanotube sorting is based on ion exchange chromatography (IEX). Ion exchange chromatography is a technique that it is commonly used to separate ions or polar molecules. It involves two main steps: first the molecules reversibly adsorb on oppositely charged resin and then desorption is brought about either by a change in the pH or by an increase in the salt concentration in the eluent. In this context the design of DNA sequences for specific recognition of SWNTs is of particular importance. The idea is that SWNT–DNA hybrids are negatively charged because of the DNA phosphate backbone and that their behavior in the column depends on their linear charge density. The effective net charge of the SWNT-DNA hybrids depends mainly on the linear charge density of the phosphate backbone along the nanotube axis (how ssDNA is arranged/packed on SWNTs). Note that the effective net charge is also influenced by the electronic properties of the nanotube (charge image/polarizability effect). In more detail, for a metallic nanotube the negative charges of DNA backbone induce positive screening by charge images of the nanotube and by consequence the net linear charge is reduced with respect to the value given by the wrapped DNA backbone alone. In contrast, for a semiconducting nanotube the lower polarizability of the nanotube,

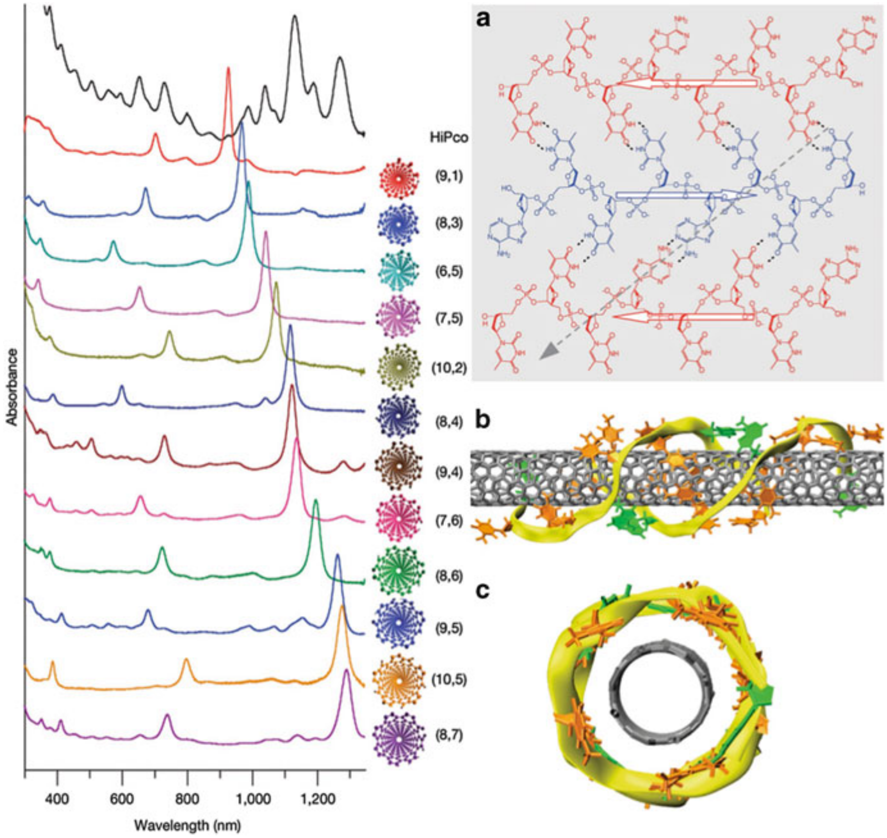

Fig. 4 *Left*: UV–vis-NIR absorption spectra of semiconducting SWNTs sorted by chirality (in color) and the starting $\mathrm{HiP_{CO}}$ mixture (in *black*). *Right*: (**a**) proposed organization of a 2D DNA sheet structure formed by three anti-parallel ATTTATTT strands; (**b**, **c**) schematic representation of the DNA barrel on a (8,4) nanotube formed by rolling up of the previous 2D DNA sheet; adapted from [47], with permission of the *Nature Publishing Group*

compared with the one of the surrounding water results in an increased effective linear charge.

These properties were used to fractionate ssDNA/nanotube solutions and the resulting nanotubes were characterized by optical absorption which is known to be distinct for each particular (n,m) nanotube. To reach such a result Zheng and co-workers [47] rationalized the exploration of ssDNA libraries and identified short DNA sequences that enabled SWNT single chirality separation as reported in Fig. 4, left. They observed that the successful sequences showed periodic purine pyrimidine patterns. They suggested that these purine pyrimidine patterns could form a two-dimensional sheet by hydrogen bonding, forming a well ordered three-dimensional barrel (when folded selectively onto nanotubes) (see Fig. 4, right).

2.2 π-Stacking Interactions

π-Conjugated molecules exhibit strong interactions with the sp^2 framework of nanotube sidewalls. Very early on, aromatic molecules bearing proper functionalization were proposed to disperse carbon nanotubes in aqueous and organic media. Due to the huge possibilities offered by organic chemistry and the versatility of the derivatization of polycyclic aromatic molecules, a wide variety of compounds have been synthesized and used to bring new functionalities to nanotubes. In the following section we will show a few examples from the recent literature.

2.2.1 Pyrene Derivatives

In their initial reports the group of Nakashima opened new avenues for nanotube functionalization. They demonstrated that in a family of aromatic compounds containing a polar head, polycyclic derivatives like phenanthrene and, even better, pyrene were able to give stable suspensions of SWNTs in water [65, 66]. In such systems the pyrene moiety ensured the interactions with the nanotube sidewalls while the trimethylammonium polar head allowed solubility in water. Rapidly 1-(trimethylammonium acetyl)pyrene bromide became popular and was used to anchor negatively charged molecules like porphyrin or polythiophene derivatives onto nanotubes (Fig. 5a, b) [67–70]. The chromophore/nanotube hybrids presented interesting photophysical properties and they were tested as photoactive materials for current generation in electrochemical cells.

In the SWNT/pyrene$^+$/porphyrin^{8-} composite systems (Fig. 5a), fluorescence and transient absorption studies in solutions showed rapid intrahybrid electron transfer, creating intrinsically long-lived radical ion pairs. Through analysis at several wavelengths it was possible to obtain lifetimes for the newly formed ion-pair state of about 0.65 and 0.4 μs for H_2P^{8-} and ZnP^{8-}, respectively [68]. The favorable charge separation features that result from the combination of SWNT with porphyrins in SWNT/pyrene$^+$/MP^{8-} ($M=H_2$ or Zn) were promising for the construction of photoactive electrode surfaces.

Using an electrostatically driven layer-by-layer (LBL) assembly technique, semitransparent ITO electrodes were realized from SWNT/pyrene$^+$/porphyrin^{8-} and SWNT/pyrene$^+$/polythiophene^{n-}. Photoelectrochemical cells were finally constructed using a Pt electrode connected to the modified ITO electrode. Upon illumination, electron transfers occurred from the porphyrins or the polythiophene to the nanotubes. The electrons are then injected into the ITO layer, then travelling to the Pt electrode. The oxidized electron donors were converted to their ground state through reduction via sodium ascorbate in the electrolyte, which was used as a sacrificial electron donor. These systems gave rise to promising monochromatic internal photoconversion efficiencies (IPCE) of up to 8.5% for porphyrin systems [71] and between 1.2% and 9.3% for one and eight sandwiched layers of SWNT/pyrene$^+$/polythiophene^{n-}, respectively [70].

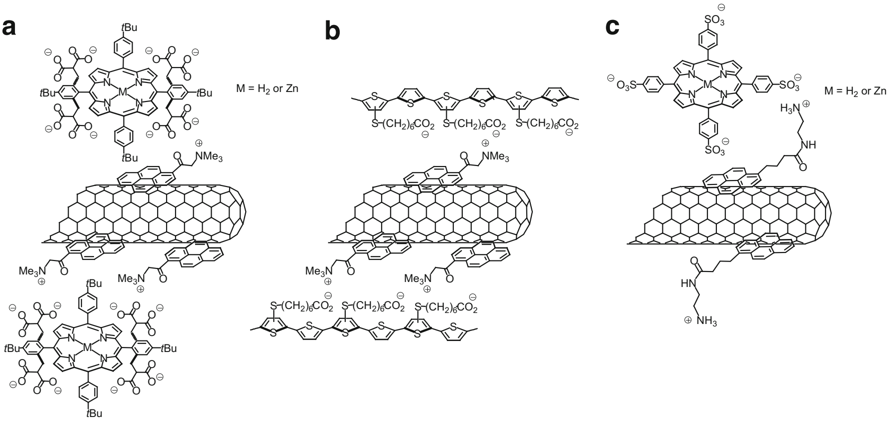

Fig. 5 Examples of supramolecular donor/acceptor assemblies formed by electrostatic interactions between positively charged pyrenes and negatively charged chromophores (**a**–**c**)

In a similar way, Sandanayaka et al. [72] described the assembly of anionic tetrasulfonatophenyl porphyrin sodium salts with positive pyrene anchored on SWNTs (Fig. 5c). The photophysical properties of the hybrids were characterized and photoinduced charge transfers from the porphyrins to the nanotubes were observed in the supramolecular system.

It was also demonstrated that charge inversion between the pyrene and the chromophore was possible. Indeed Guldi and co-workers described the functionalization of carbon nanotubes with negatively charged pyrenes (pyrene$^-$) followed by the anchoring of positively charged porphyrins (Fig. 6a) [73]. The interactions between SWNT and pyrene$^-$ were investigated by absorption spectroscopy. The maxima of the pyrene$^-$ transitions in the 200–400 nm region were shifted by about 2 nm, which suggested mutually interacting π-systems. Figure 6b shows the assembly of cationic tetra-*N*-methylpyridinium porphyrins on nanotubes containing 1-pyrenebutyric acid [72].

Positively-charged pyrenes were also used to assemble DNA and carbon nanotubes. Two recent examples in the literature should be mentioned; the first, in which SWNTs coated with 1-pyrenemethylamine hydrochloride were deposited on λ-DNA aligned on silicon surfaces (Fig. 7a) [74] and a second in which SWNTs coated with 1-(trimethylammonium acetyl)pyrene bromide were used to assemble 300 nm long double stranded DNA in solution (Fig. 7b) [75]. In the latter case it was demonstrated that the hybrid formation was a reversible process and that DNA can be voluntarily detached from SWNTs, by addition of a negatively charged pyrene, opening a new perspective for controlled assembly and de-assembly applications.

In the previous examples, electrostatic interactions were used to build supramolecular systems, adding new functions to carbon nanotubes. Different approaches based on host–guest complexation or axial complexation with transition metals were also reported. For example, the dispersion of SWNT with a pyrene derivative bearing an imidazol ring was achieved and the imidazoyl moiety was used for axial complexation of zinc porphyrin (ZnP) or naphthalocyanine (ZnNc)

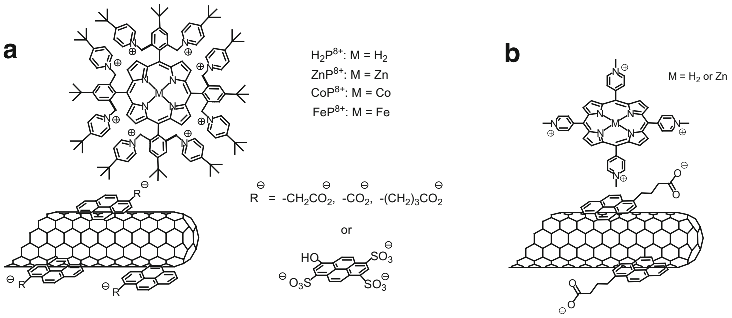

Fig. 6 SWNT with negatively charged pyrene and positively charged porphyrins

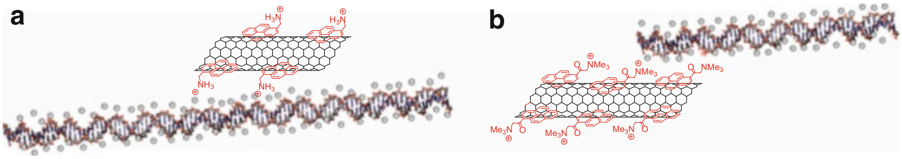

Fig. 7 Examples of association of SWNT/pyrene with double stranded DNA

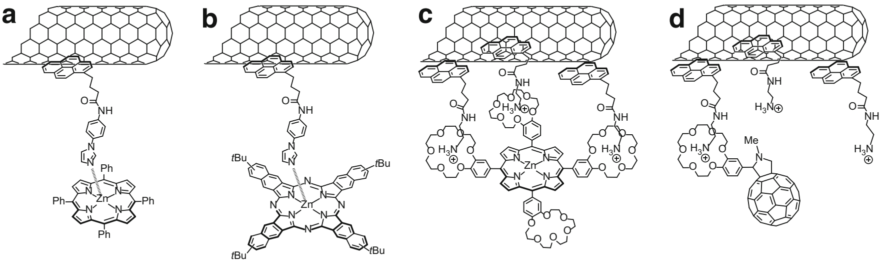

Fig. 8 SWNT-pyrene supramolecular assemblies axially complexed with zinc-porphyrins (**a**), zinc-naphthalocyanines (**b**), SWNT-porphyrins (**c**), and SWNT-fullerene hybrids (**d**) based on ammonium cation/crown ether self-assembly

derivatives in solution (Fig. 8) [76, 77]. Photophysical measurements showed efficient fluorescence quenching of the ZnP and ZnNc donors in the nanohybrids and revealed that the photoexcitation of the chromophores resulted in the one-electron oxidation of the donor unit with a simultaneous one-electron reduction of the SWNT. The experiments were also conducted in the presence of electron and hole mediators (dihexyl-viologen dication and 1-benzyl-1,4-dihydronicotinamide, respectively). Accumulation of the radical cation ($HV^{\bullet+}$) was observed in high yields, providing additional proofs for the occurrence of photoinduced charge separation.

The specific recognition of ammonium cation with benzo-18-crown-6-ether was also used to immobilize porphyrins and fullerene onto nanotubes [78, 79]. For the realization of the nanotube/porphyrin hybrids, SWNTs were first dispersed in DMF

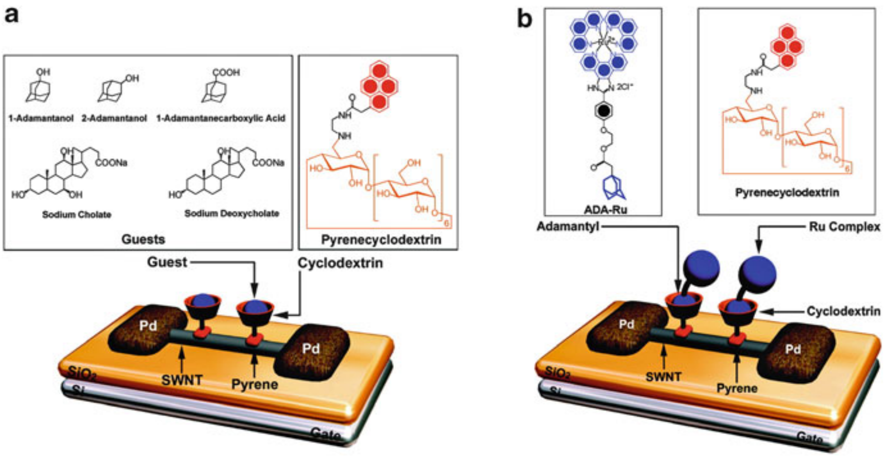

Fig. 9 Schematic representation of the pyrene-cyclodextrin-decorated CNT-FET devices; (**a**) chemical sensor and (**b**) photosensor; adapted from [83], with permission of the *American Chemical Society*

using a pyrene derivative bearing an ammonium cation and then complexed with porphyrins containing one or four benzo-18-crown-6-ether moieties, the latter offering more complexation sites which was expected to result in more stable ensembles owing to the cooperative binding effect (Fig. 8c). Steady-state and time-resolved emission studies revealed an efficient quenching of the singlet excited state of the porphyrins which was attributed to charge transfers between the porphyrins to the nanotubes [78]. The same strategy was used to combine SWNT-pyrene ammonium with fulleropyrrolidine bearing the 18-crown-6-ether moiety (Fig. 8d); this time upon photoexcitation at 532 nm, a photoinduced electron transfer from the nanotube to the fullerene was observed [79]. The same work performed on (6,5) and (7,6) enriched SWNTs (i.e., commercially available CoMoCat-SWNTs) showed that the SWNT–ZnP hybrids (Fig. 8c) gave high IPCE of ca. 12% when incorporated in photoelectrochemical cells [80].

Stoddart and Grüner reported the fabrication of sensors based on carbon nanotube field effect transistors (CNT-FETs) using SWNTs decorated with pyrenes modified with a β-cyclodextrin [81–83]. An SWNT can be seen as a sheet of graphene rolled up to form a hollow tube; in a SWNT all the atoms of carbon are in contact with the environment which makes nanotubes an incredibly sensitive material. During the last decade SWNTs have been widely studied and used for the fabrication of field effect transistors and sensors [84–87].

Taking advantage of the sensitivity of the CNT-FETs and the recognition properties between β-cyclodextrin and adamantane derivatives [88], the authors fabricated chemical detectors (Fig. 9a) and photosensors (Fig. 9b). In the first case, electrical response of the device allowed the detection of the complexation events: the transistor characteristics of the CNT-FET shifted towards negative gate voltage and the magnitudes of the shifts depended greatly on the complex formation constants (K_S) between the organic molecule and the pyrene-cyclodextrin [81].

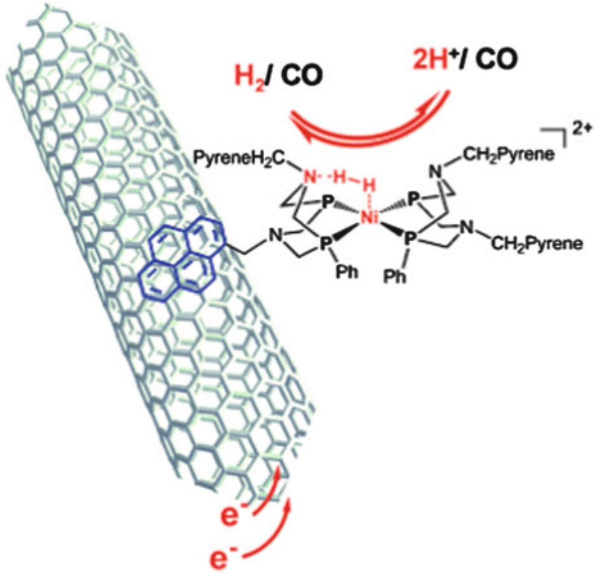

Fig. 10 Mechanism of the hydrogen evolution and uptake of the MWNTs modified with pyrene-functionalized nickel complexes, extracted from [115], with permission of *Wiley-VCH*

In the second case, the device was used as a tunable photosensor to sense a fluorescent adamantyl-modified ruthenium complex. When the light is on, the authors attributed the shift of the CNT-FET transfer characteristic to charge-transfer from the pyrene-cyclodextrin/Ru complexes to the SWNTs [82].

Pyrene-cyclodextrin-decorated nanotubes were also used to form SWNT hydrogels via host-guest complexations between the β-CDs of the SWNT/pyrene-cyclodextrin hybrids and dodecyl chains of a modified polyacrylic acid. The supramolecular SWNT hydrogel exhibited gel to sol transition by adding competitive β-CD guests (i.e., adamantyl derivatives) [89]. Very recently the complementary approach, i.e., the assembly of SWNT/adamantyl-modified pyrene with β-cyclodextrins–tethered ruthenium complexes was proposed [90]. The condensation ability of the nanotube-based supramolecular assembly with plasmid DNA was investigated and used as a non-viral gene delivery system with the ruthenium complexes as a fluorescent probe to monitor uptake of DNA by cells.

Addition of new moieties and/or new functionalities on carbon nanotubes can also be performed directly through the addition of a pyrene modified covalently with the molecules of interest. Many examples of pyrene modified with porphyrins [91–93], phthalocyanines [94–97], tetrathiafulvalenes [98–101], thiophenes [102], ferrocenes [103], fullerenes [104, 105], azobenzene and other chromophores [106–109], spiropyrans [110, 111], quantum dots (QDs) [112], glycodendrons [113], or glucosamines [114] were described during the last 5 years mainly for photoinduced charge transfer or sensing applications.

Jousselme and Artero reported the functionalization of multi-walled carbon nanotubes (MWNTs) with a nickel-based complex catalyst containing four pyrene moieties (Fig. 10) [115]. The nickel diphosphine catalysts anchored on the nanotubes were found to be efficient like commercial active layers containing highly dispersed platinum particles for hydrogen oxidation and proton reduction in a proton exchange membrane fuel cell (PEMFC). In addition, the system demonstrated great tolerance to the presence of carbon monoxide (CO) which is one of the limitations of the platinum-based electrocatalysts. This constitutes a breakthrough for the development of noble metal-free electrocatalytic materials for operative PEM devices.

The advantage of the preparation of covalently subsituted pyrene derivatives is a better control of the final structures since no sequential assembly is required. The evident disadvantage is the lack of versatility: each new pyrene derivative must be prepared independently and combined with the nanotubes.

To overcome this problem, commercially available activated pyrene (1-pyrenebutanoic acid succinimidyl ester) were used, first to disperse and/or functionalize carbon nanotubes and, in a second step, the molecules of interest containing amine groups were covalently attached to the activated carboxyl groups. This approach permitted the successful attachment of biomolecules (e.g., proteins, enzymes, antigens, DNA aptamers) [116–120], or QDs [121] onto carbon nanotube sidewalls. One of the interesting uses of this method is the facile immobilization of biomolecules on nanotubes for the realization of biosensors.

2.2.2 Other Cyclic Aromatic Compounds

Several examples of dispersion of carbon nanotubes using other polycyclic aromatic compounds like anthracene [122, 123], phenanthrene [66], extended pyrene [124], and coronene [125] have been reported in the literature. These compounds are, in general, less efficient than pyrene for nanotube functionalization. A solution for better dispersion of nanotubes and for their selection in chirality could come from the synthesis of specific aromatic bent structures which could follow the curvature of the nanotube sidewalls [126].

A few years ago Feng et al. [127] described the combination of carbon nanotubes with a perylene derivative (the *N*,*N*′-diphenyl glyoxaline-3,4,9,10-perylene tetracarboxylic acid diacidamide). The resulting nanocomposite was tested as active film for photocurrent generation. Recently, surfactants based on perylene diimides became very popular. In particular, the group of Hirsch reported the efficient individualization of SWNTs using perylene derivatives [128–131]. The surfactant was based on a perylene core containing water-soluble Newkome dendrons [132] as solubilizing counterparts (Fig. 11a). Perylene diimide-based surfactants are a particular class of compounds because they combine two important features: (1) good dispersion ability of nanotubes and (2) excellent electron accepting character. The perylene diimide derivative bearing two dendrons of first generation were used in a series of photophysical and spectroelectrochemistry experiments to probe the charge transfers between the nanotubes and the perylene [133].

Similarly, the groups of Reich and Haag reported the formation of a new energy transfer complex based on a perylene derivative bearing polyglycerol dendrons as the hydrophilic head and HiP$_{\mathrm{CO}}$ SWNTs (Fig. 11b) [134]. This perylene molecule

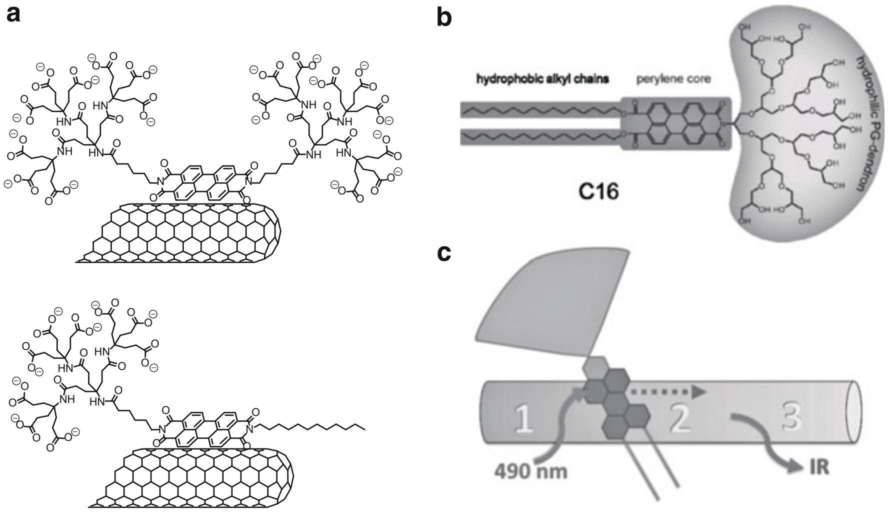

Fig. 11 (**a**) Examples of perylene-based surfactants used for SWNTs dispersion; (**b**) chemical structure of the perylene-imido-diester; (**c**) schematic representation of the energy transfer process between the perylene surfactant and the nanotube; extracted from [134], with permission of *Wiley-VCH*

acted as a surfactant and was able to individualized efficiently SWNTs in water. Upon excitation of the adsorbed perylene unit, an emission from the nanotubes was observed, indicating a successful energy excitation transfer from the perylene to the nanotubes (Fig. 11c).

2.2.3 Porphyrins and Derived Structures

Aromatic macrocycles such as porphyrins or phthalocyanines are also suitable for nanotube dispersion. In particular, several groups demonstrated that monomeric [135–143] or polymeric porphyrins [144–147] as well as fused porphyrins [148, 149] could stack to the nanotube surface by π-stacking interactions. Few examples with monomeric phthalocyanines or its derivatives were also reported in the literature [141, 150–153].

In 2005, Chichak et al. [154] reported on the functionalization of SWNTs with supramolecular porphyrin polymers. The polymer formation was based on the spontaneous complexation of 5,15-bis(4-pyridyl)-porphyrin with *cis*-palladium complexes (Fig. 12). While neither the porphyrin nor the palladium complexes were able to disperse efficiently the nanotubes in water, the supramolecular polymers, in the presence of SWNTs, gave stable dispersion. The electronic effect of the supramolecular structure was probed within a nanotube field-effect transistor device. Using the same porphyrin they demonstrated later that SWNT/porphyrin-FET could act as a light detector by detecting photoinduced electron transfers within the donor/acceptor system [155].

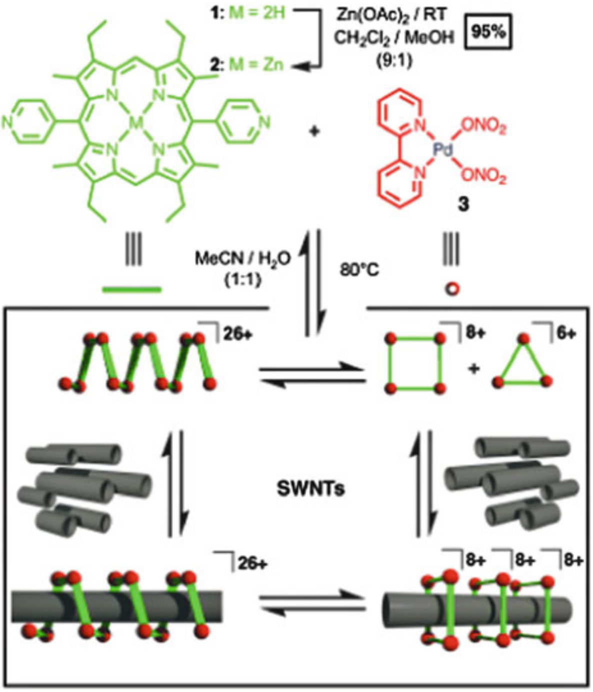

Fig. 12 Example of supramolecular structures formation around SWNTs; extracted from [154], with permission of *Wiley-VCH*

Recently, a very smart application of π-stacking interactions between the porphyrins and the nanotube sidewalls was developed by Komatsu and his group [55, 56, 156–158]. They demonstrated the separation in chirality of SWNTs and not simply in diameter [39] using particular porphyrin derivatives. Chiral diporphyrin "tweezers" containing either 1,3-phenylene, 2,6-pyridylene, or 3,6-carbazolylene bridges were found to bind left- and right-handed helical nanotube isomers with different affinities to form complexes with unequal stabilities that could be readily separated by centrifugation (Fig. 13). Theoretical calculation showed that the difference of association enthalpies between a tweezer and the two enantiomers of a (6,5)-SWNT was 0.22 kcal/mol [56]. The diporphyrins could be liberated from the nanotubes afterwards to provide optically enriched SWNTs. Circular dichroism (CD) of the nanotube solutions revealed the presence of Cotton effects which were not due to the tweezers and were therefore attributed to the chirality of the nanotubes.

The same group went a step further with the rationalization of the design of their chiral nanotweezers for discrimination of the handedness and diameter of SWNTs simultaneously [159]. In this example the asymmetric porphyrin subunits were connected via a phenanthrene spacer. The dihedral angle made by two porphyrins was effective to tweeze out selectively (6,5)-SWNTs from CoMoCat-SWNTs. By CD, only (6,5)-SWNTs exhibit Cotton effects, indicating that a single enantiomer of (6,5)-SWNTs was enriched through molecular recognition with the tweezer.

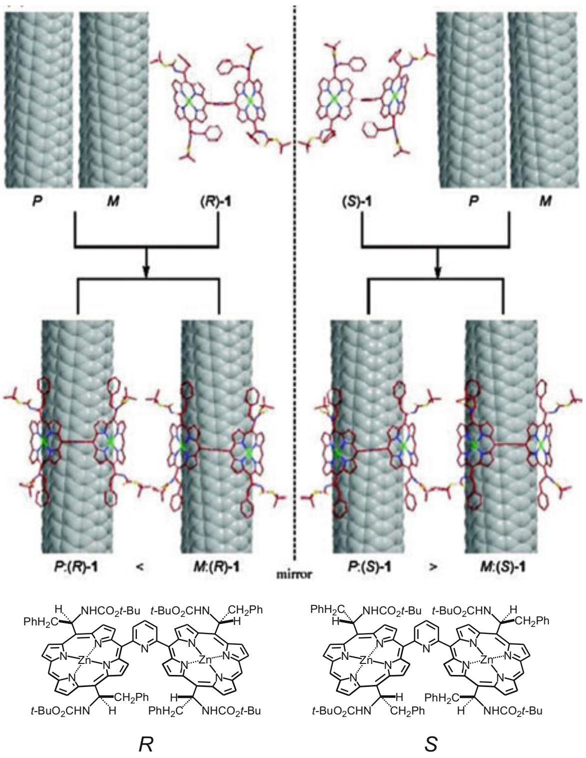

Fig. 13 Representation of the selection of chiral (6,5)-SWNTs with the *R* and *S* porphyrin tweezers; adapted from [56], with permission of the *American Chemical Society*

With the same goal and following a similar strategy, the groups of Komatsu [160] and Hirsch [161] designed new nanotweezers based either on pyrene or perylene moieties for π-stacking interaction with the nanotubes and containing carbazolylene or *m*-phenylene spacers.

2.2.4 Micelle Swelling

In 2008 Ziegler and co-workers showed that the incorporation of water-immiscible organic solvents in surfactant-stabilized aqueous SWNT suspensions gave rise to solvatochromic shifts in the absorbance and fluorescence spectra of the nanotubes (Fig. 14) [162]. They attributed this effect to the migration of the organic solvent in the hydrophobic core of the micelles. The micelles were then swelled by the solvent. Furthermore, the reversibility of those chemical shifts, observed for most of the surfactant, once the solvent is removed, showed that the surfactant structure returned to its former organization around the SWNTs.

Besides the influence on the fluorescence of the nanotubes, the swelling provided by the addition of organic solvents offers the unique possibility to immobilize hydrophobic molecules around the SWNTs in order to create new non-covalent nanohybrids [163].

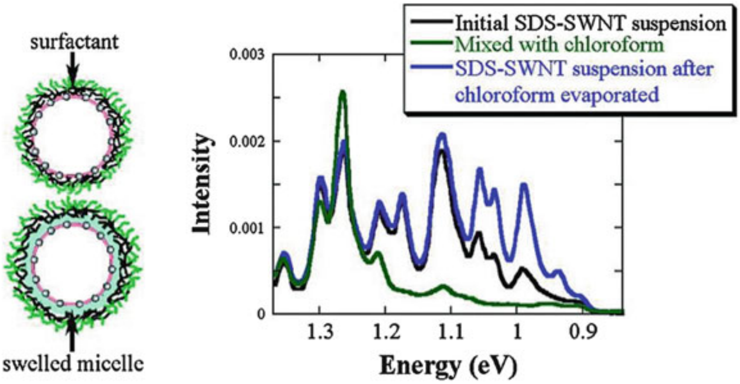

Fig. 14 Swelling of the hydrophobic core of the micelle surrounding a SWNT (*left*); NIR-fluorescence spectra of SDS-coated SWNT suspension after addition and removing chloroform (*right*), extracted from [162], with permission of the *American Chemical Society*

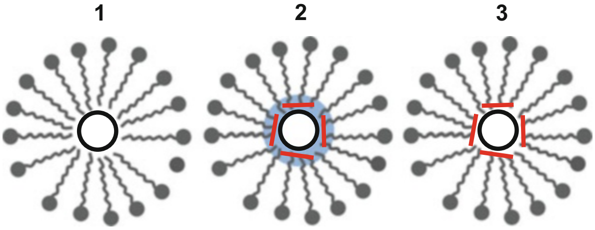

Fig. 15 Schematic representation of the micelle swelling method: the nanotubes are shown as *black circles* surrounded by the surfactant molecules in *gray* (step 1). A solution of porphyrins (*red sticks*) in dichloromethane in *blue* is added (step 2). After solvent removing, the functional nanotube hybrid is obtained (step 3)

In particular, taking advantage of the method developed by Ziegler, Roquelet et al. [140] reported functionalization of carbon nanotubes with tetraphenylporphyrins (TTP) through micelle swelling. They demonstrated that the synthesis of controlled and stable SWNT/porphyrin complexes can occur in micelles, pointing out the crucial role of the organic solvent for the insertion of the porphyrin molecules in the micelle core. Figure 15 shows the functionalization process. To a suspension of SWNTs is added TPP in solution in dichloromethane (step 1). The water immiscible solution enters in the micelles, carrying the porphyrin molecules with it (step 2). Then, the organic solvent is evaporated by the thermal energy brought by the sonication process leading to porphyrin molecules in close contact with the nanotube sidewalls (step 3). The photophysical properties of the resulting assemblies were investigated by steady state and transient absorption and emission spectroscopy [140, 164–167].

2.3 Polymers and Wrapping

In the following section we will focus on the association of carbon nanotubes with conducting and photo/electroactive polymers. Here we voluntarily do not consider nanotube composites for reinforcement applications. The latter is a field of intense research but beyond the scope of the present chapter. Note that the polymers usually employed for such reinforcement are mainly polyacrylates, polystyrenes, polyvinyls, etc., which are, in general, not appropriate for applications like nanotube sorting or optoelectronic devices. For readers who are interested in the field of nanotube composites, we recommend the following reviews [168, 169].

Basically, two strategies have been reported in the literature for combining carbon nanotubes with conducting polymers. The first consists in the direct ultrasonic mixing of the nanotubes and the polymers in organic solvent. The times of sonication have to be carefully controlled since under harsh conditions the nanotubes as well as the polymers can be broken into small pieces. The second method is based on the polymerization of the monomer in the presence of the nanotubes. Note that this method tends to form polymer aggregates around the nanotubes and thus the carbon nanotubes/polymer assemblies are less defined than in the first case.

The main advantages of using polymers instead of surfactant molecules for nanotube functionalization is that the polymers reduce the entropic penalty of micelle formation and have significantly higher interactions with nanotubes than small molecules. As previously discussed for DNA and surfactants, for polymers too the chemical structure of the chains as well as their flexibility, stiffness, hydrophobicity, combined with their electron affinity are directly responsible for the interactions between the polymer and the nanotubes.

Poly(*meta*-phenylenevinylene) (P*m*PV) was the first π-conjugated polymer found to wrap around the nanotubes [170–173]. Due to the *m*-phenylene linkage and the repulsive interactions between the alkoxy solubilizing groups, P*m*PV backbone adopts a helical structure suitable for wrapping around the nanotube sidewalls. The motivation for the realization of nanotube/P*m*PV composites is the combination of the photo-absorption properties of the polymer with the conductivity and charge mobility in the nanotubes. For example, by adding MWNTs to P*m*PV, the electrical conductivity of the polymer increased by 8 orders of magnitude [171]. On SWNTs, it was demonstrated that P*m*PV (or poly(*p*-phenyleneethynylene)-PPV copolymer) was able to pick up selectively (11,6), (11,7), and (12,6) nanotubes from an $\mathrm{HiP_{CO}}$ SWNT mixture [174, 175]. These nanotubes exhibited diameters of 1.19, 1.25, and 1.24 nm respectively; the tubes with smaller diameters were gradually removed under centrifugation. In contrast, it was also demonstrated that introducing water-soluble groups, such as sulfonate, to P*m*PV improved drastically the diameter selectivity for small diameter nanotubes ($d \approx 0.80$ nm) [176]. The explanation of this phenomenon lies in the difference of π–π interactions between the polymer backbone and the SWNTs and in the polymer conformation around the nanotubes. Indeed, considering the impact of the solubilizing substituents on the conformation of the polymers, they pointed out that in P*m*PV containing hydrophobic alkoxy groups, the *p*-phenylene rings are free to rotate until reaching a parallel alignment on the SWNT surface, thus widening the cavity size. As a consequence, the polymer has the tendency to bind selectivity SWNTs of larger diameters. Conversely, for water-soluble P*m*PV, the conformation of the polymer is constrained by the presence of the hydrophilic groups which strongly interact with water, confining the conformational cavity to a hydrophobic pocket of ca. 1 nm diameter.

The backbone modification of the P*m*PV with *m*-pyridylene instead of *m*-phenylene gave the poly{(2,6-pyridinylenevinylene)-*co*-[(2,5-dioctyloxy-*p*-phenylene)vinylene]} (PPyPV). This polymer was also able to wrap and then disperse efficiently carbon nanotubes. Field effect transistors fabricated with SWNTs coated with P*m*PV or PPyPV demonstrated a photogating effect in I/V characteristics which could rectify or amplify current through the nanotubes [177]. Similarly, P*m*PV derivatives functionalized with alcohol, azide, thiol, or amino acid functions in the C-5 position of the *meta*-disubstituted phenylene rings were designed and synthesized. These poly{(5-alkoxy-*m*-phenylenevinylene)-*co*-[(2,5-dioctyloxy-*p*-phenylene)-vinylene]} derivatives (PA*m*PV) were able to disperse SWNT in organic solvents; the functional groups on the polymers were used to graft pseudorotaxane molecular machines along the walls of the nanotubes with a view to constructing arrays of molecular switches and actuators [178].

The polyphenylacetylene (PPA) is structurally equivalent to the polystyrene in which the saturated CH_2–CH_2 groups are replaced with CH=CH groups; the polyene backbone of the polymer allows the wrapping around nanotubes. The first example of nanotube/PPA hybrids was fabricated by in situ polymerization of the phenylacetylene monomer in the presence of MWNTs. This process gave stable suspension of MWNTs in common organic solvent such as chloroform, toluene, and tetrahydrofuran [179]. Later, PPAs modified either with pyrene [180] or with ferrocene [181] groups were synthesized, isolated, and then absorbed on MWNTs and SWNTs. The PPA/nanotube hybrids showed good optical-limiting properties, light-emitting behavior, and efficient photoinduced charge transfer performance. Recently, it was demonstrated that donor–acceptor interactions between carbon nanotubes and poly(phenylacetylene) functionalized with carbazole or fluorene led to enhancement of the dispersion of MWNTs in organic solvents [182].

To summarize, due to their particular structure, P*m*PV, PPyPV, and PPA polymers are able to wrap around nanotubes to give efficient dispersion in organic solvents. These nanotube/polymer hybrids open interesting perspectives for the realization of optoelectronic devices thanks to the combination of the electronic properties of the nanotubes with the optical properties of the polymers.

Regioregular poly-3-alkylthiophene (PT) commonly used as *p*-type materials in organic solar cell devices were wrapped around SWNTs [183–189]. Using scanning tunneling microscopy, Goh et al. [184] showed that monolayers of regioregular poly-3-hexylthiophene (P3HT) were adsorbed on SWNTs with an angle of 48° (±4°) with respect to the SWNT axis. Recently, Nicholas's group showed that

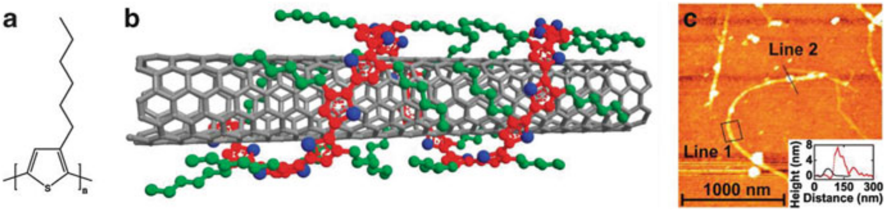

Fig. 16 (**a**) Chemical structure of P3HT; (**b**) Schematic representation of P3HT wrapping around a (6,5)-SWNT; (**c**) AFM image of the isolated nanotubes coated with P3HT; *inset*: heights of AFM slices marked on image, line 1 (*black*) and line 2 (*red*); extracted from [186], with permission of the *American Chemical Society*

P3HT could be used to individualize SWNTs (Fig. 16). Moreover, the presence of the nanotube improved the crystallinity of polythiophene, resulting in the reduction of the optical band gap and the increase of the carrier mobility in the polymer [185]. They also demonstrated using photoluminescence studies that highly efficient energy transfers, rather than charge transfers, occurred from P3HT to SWNTs, explaining the relatively poor performance of P3HT-SWNT solar cells. Nevertheless, the addition of excess P3HT led to long-lived charge separated states [186]. In order to improve the charge separation properties and then the photovoltaic properties of SWNT–P3HT hybrids, the solution was to add a barrier between the nanotubes and the polythiophene. The barrier is, in fact, a polyfluorene-*co*-benzothiadiazole (F8BT); this polymer possesses energy levels (HOMO-LUMO position and gap) that allow the transfer of electrons from P3HT to the nanotubes and prevent the transfer of holes [190].

In contrast to polythiophenes, which are able to wrap easily around the nanotubes, Chen et al. [191] suggested that short and rigid polymers like poly(*p*-phenyleneethynylene) (PPE) arranged parallel to the nanotube long axis. The substitution of methyl end groups of the alkoxy solubilizing chains of the PPE by sodium sulfonate led to poly[2,5-bis(3-sulfonatopropoxy)-1,4-ethynylphenylene-*alt*-1,4-ethynylphenylene] sodium salt (PPES) which allowed the solubilization of SWNTs coated with phenyleneethynylene in aqueous medium. In contrast to previous studies in which the *p*-phenyleneethynylene-based polymers were shown to organize parallel to the SWNT axis, the linear and conformationally restricted conjugated PPES polymer wrapped onto SWNTs forming a self-assembled helical super structure (Fig. 17) [192]. The anionic PPES/SWNT hybrids were assembled on a positively charged pre-patterned surface via electrostatic interactions. Patterned features were found to be electrically conducting with a low resistance value [193]. No information was given to explain the difference between PPE and PPES; however one can think that both polymers wrap around nanotubes but with smaller angles compared to P3HT and that, for short polymer chains, the wrapping is not clearly observed. Another explanation can be found if we refer to the works of Pang [174, 176]: this group reported the influence of the solubilizing group on the conformation of P*m*PV polymers. Indeed, different conformations can induce different organizations on the nanotube sidewalls.

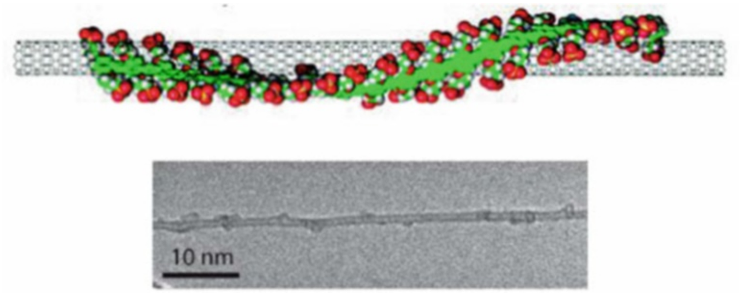

Fig. 17 Schematic representation (*top*) and TEM image (*bottom*) of the PPES/SWNT hybrids. Adapted from [192], with permission of the *American Chemical Society*

Similar to short PPE chains, it was reported that rigid Zn-porphyrin conjugated polymers assembled linearly onto SWNTs [144, 146, 147]. The polymers, formed by the porphyrins linked in meso position with 1,3-butadiyne bridges, enabled the exfoliation of nanotubes. The nanotube/porphyrin hybrid presented a broad absorption from the UV to the near-IR and potential application as light-harvesting systems in photovoltaics was foreseen for this system.

More recently, benzene rings of PPES polymers were replaced by naphthalene and the resulting poly[2,6-{1,5-bis(3-sulfonatopropoxy)}naphthylene]ethynylene sodium salt (PNES) was used to disperse SWNTs in aqueous or organic media. The solubility of the SWNT/PNES hybrids in organic solvents was obtained, thanks to the use of a phase transfer catalyst (i.e., the crown ether 18C6) which can complex the sodium counter-ions of the polymer [194, 195]. The efficient individualization of SWNTs was confirmed by steady-state electronic absorption spectroscopy, AFM, and TEM.

Electrochemical deposition of polypyrrole (PPy) onto an individual SWNT in field-effect transistor configuration was performed to study the electronic property of the SWNT/PPy composite [196]. The nanotube devices exhibited a drop of conductance for thin and moderate PPy coatings for both metallic and semi-conducting nanotubes that could be attributed to the covalent grafting of pyrrole on the nanotubes during the growth process. Other conducting polymers like polyaniline (PANI) [197–201] or poly-3,4-ethylenedioxythiophene:polystyrene-sulfonate (PEDOT:PSS) [202–208] were mixed with carbon nanotubes in order to modify the polymer conductivities and for thermoelectricity or photovoltaic applications. To the best of our knowledge, no morphological studies were performed on these composites as was the case for P*m*PV, PPE, PT, or polyfluorene (PFO) composites.

In the field of selective dispersions of SWNTs using polymers it was demonstrated that PFO and its copolymer derivatives were able to wrap SWNTs selectively with certain chiral angles or diameters depending on the chemical structures of the polymers [48, 49, 209–212]. Moreover, as theoretically demonstrated by Gao et al. [213] for PFO-SWNTs in toluene, the interactions between PFO and nanotubes are dominated by the alkyl–alkyl zipping mechanism

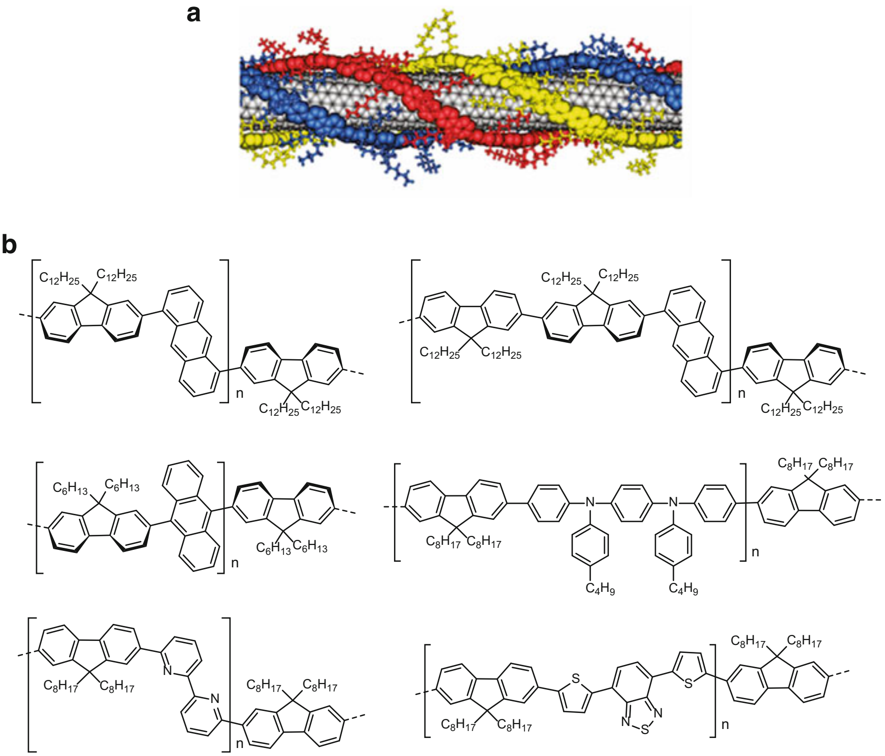

Fig. 18 (**a**) Nanotube wrapped helically with three PFO chains; extracted from [213], with permission of the *American Chemical Society*. (**b**) Examples of PFO-based copolymers used for SWNT dispersion and sorting

which locks the polymer chains around the nanotubes in a preferentially helical wrapping (Fig. 18a). The authors also highlighted the small role played by the fluorene–nanotube interaction in the polymer adsorption in the case of less constrained PFO-SWNT systems, such as PFO-(8,6) nanotube. The incorporation of other aromatic moieties like benzene, anthracene, electron poor benzothiadiazole, or electron rich *N*,*N*′-diphenyl-*N*,*N*′-di(*p*-butyloxyphenyl)-1,4-diaminobenzene moieties in the PFO backbone (Fig. 18b) allowed fine tuning of the interactions between the polymers and the nanotubes [214–219].

Initially limited to the sorting of small diameter nanotubes like CoMoCat and $\mathrm{HiP_{CO}}$ SWNTs, this approach was extended to larger diameter nanotubes ($d > 1.2$ nm). In order to change the selectivity of PFO for large diameters, Berton et al. [214] incorporated naphthalene, anthracene, or anthraquinone in the polyfluorene backbone. The diameter selectivity of the anthracene-1,5-diyl combined with the large chiral angle selectivity of the polyfluorene permitted extraction of large diameter SWNTs from a mixture of nanotubes produced by laser ablation. Similarly, Mistry et al. [219] introduced 2,2′-bipyridine and 9,10-anthracene in PFO. These polymers

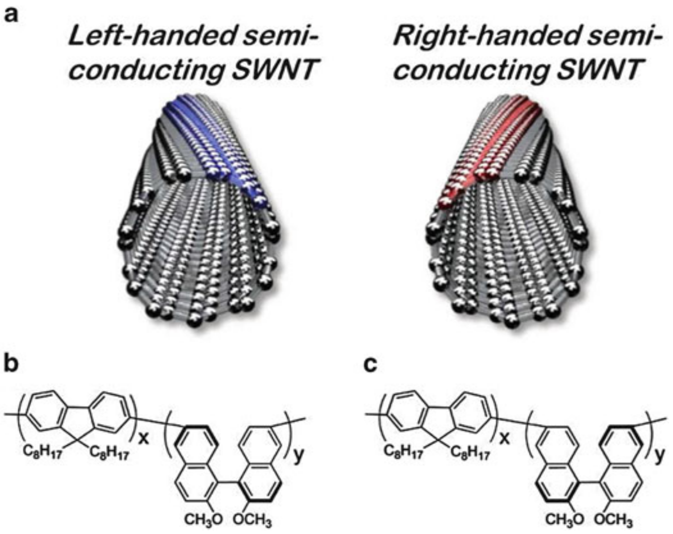

Fig. 19 Schematic representation of semiconducting SWNT enantiomers (**a**); chemical structures of $(PFO)_x(R\text{-}BN)_y$ (**b**) and $(PFO)_x(S\text{-}BN)_y$ (**c**); extracted from [216], with permission of the *American Chemical Society*

exhibited a strong selectivity for large diameter nanotubes; in addition PFO-anthracene demonstrated the particular ability to isolate exclusively narrow chirality dispersions of near-armchair semiconducting SWNTs (i.e., (n,m)SWNTs with $n - m = 3q + 2$). The high purity of semiconducting nanotubes provided by fluorene-based polymers sorting allowed consideration of nanotubes for high-efficiency field effect transistor [220, 221] and photovoltaic applications [222, 223].

After demonstrating a rational method for the selective recognition and solubilization of specific chirality of (n,m)SWNTs in 2011 [215], the group of Nakashima described the selective extraction of right- and left-handed s-SWNT enantiomers by integrating different proportions of chiral binaphthols (R-BN or S-BN) to the fluorene-based polymer (Fig. 19) [216]. The copolymers were able to extract either right- or left-handed semiconducting SWNT enantiomers with (6,5)- and (7,5)-enriched chirality. The separated materials were studied by circular dichroism, visible-near IR absorption, and photoluminescence spectroscopies.

In 2010 Imahori reported on the solubilization of SWNTs with azobenzene-based polymer and their release through the conformation changes induced by the photoisomerization of the azobenzene moieties [224]. This work constituted the first example of stimuli-responsive release of nanotubes after their wrapping with polymers; this issue is particularly important for nanotube sorting. Indeed PFO, for example, is extremely difficult to remove from the nanotube sidewalls after separation. In order to solve this problem, Mayor and Kappes reported on the synthesis of photocleavable copolymers containing different ratio of fluorene and *o*-nitrobenzylether [225]. The polymers were able to wrap selectively specific (n,m) SWNTs and upon light irradiation for few minutes the benzylether moieties could be easily cleaved, leading to the precipitation of the nanotubes. The same year Wang et al. [226] described the synthesis of degradable conjugated polymers based on fluorene backbone containing tetramethyl-, tetraphenyl, or dimethyldiphenyldisilane groups. The tetramethyldisilane-based copolymer was found to be selective for (8,7), (9,7), and (9,8) SWNTs. After sorting, the Si–Si bonds were cleaved by reacting the nanotube/polymer hybrids with aqueous hydrofluoric acid and the resulting fluorene-free semiconducting nanotubes were used for the fabrication of field effect transistor.

3 Conclusion

Supramolecular chemistry of carbon nanotubes gathers thousands of references; it was therefore impossible to review all the aspects of this field. The examples discussed here were taken from the recent literature and we have tried to give an overview of research pursued on non-covalent functionalization of carbon nanotubes. In this chapter, our main objective was to give useful information to the reader on different techniques of functionalization and their potential applications.

The already rich variety of CNT applications can be further improved when these carbon cylinders are functionalized. In addition, the recent development of nanotube sorting techniques as well as the commercialization of sorted SWNTs represents a real breakthrough. The possibility (very soon) to obtain a specific sample of (*n*,*m*)-SWNT excites the curiosity of physicists and chemists. Indeed, for the first time we can apprehend SWNT as molecules exhibiting homogeneous properties and reactivity.

References

1. Thess A, Lee R, Nikolaev P, Dai H, Petit P, Robert J, Xu C, Lee HY, Kim SG, Rinzler AG, Colbert DT, Scuseria GE, Tomanek D, Fischer JE, Smalley RE (1996) Science 273:483
2. Bockrath M, Cobden DH, McEuen PL, Chopra NG, Zettl A, Thess A, Smalley RE (1997) Science 275:1922
3. Martel R, Schmidt T, Shea HR, Hertel T, Avouris P (1998) Appl Phys Lett 73:2447
4. Chen J, Hamon MA, Hu H, Chen Y, Rao AM, Eklund PC, Haddon RC (1998) Science 282:95
5. Avouris P (2002) Acc Chem Res 35:1026
6. O’Connell MJ, Bachilo SM, Huffman CB, Moore VC, Strano MS, Haroz EH, Rialon KL, Boul PJ, Noon WH, Kittrell C, Ma J, Hauge RH, Weisman RB, Smalley RE (2002) Science 297:593
7. Liu J, Rinzler AG, Dai H, Hafner JH, Bradley RK, Boul PJ, Lu A, Iverson T, Shelimov K, Huffman CB, Rodriguez-Marcias F, Shon Y-S, Lee TR, Colbert DT, Smalley RE (1998) Science 280:1253
8. Islam MF, Pojas E, Bergey DM, Johnson AT, Yodh AG (2003) Nano Lett 3:269
9. Moore VC, Strano MS, Haroz EH, Hauge RH, Smalley RE (2003) Nano Lett 3:1379
10. Matarredona O, Rhoads H, Li Z, Harwell JH, Balzano L, Resasco DE (2003) J Phys Chem B 107:13357
11. Markiewicz P, Goh MC (1994) Langmuir 10:5
12. Nativ-Roth E, Regev O, Yerushalmi-Rozen R (2008) Chem Commun 2037
13. Richard C, Balavoine F, Schultz P, Ebbesen TW, Mioskowski C (2003) Science 300:775

14. Yurekli K, Mitchell CA, Krishnamoorti R (2004) J Am Chem Soc 126:9902
15. Calvaresi M, Dallavalle M, Zerbetto F (2009) Small 5:2191
16. Angelikopoulos P, Gromov A, Leen A, Nerushev O, Block H, Campbell EEB (2010) J Phys Chem C 114:2
17. Wallace EJ, Sansom MSP (2009) Nanotechnology 20:045101
18. Pang J, Xu G (2012) Comput Mater Sci 65:324
19. Di Crescenzo A, Germani R, Del Canto E, Giordani S, Savelli G, Fontana A (2011) Eur J Org Chem 5641
20. Lee H, Kim H (2012) J Phys Chem C 116:9327
21. Duque JG, Parra-Vasquez ANG, Behabtu N, Green MJ, Higginbotham AL, Price BK, Leonard AD, Schmidt HK, Lounis B, Tour JM, Doorn SK, Cognet L, Pasquali M (2010) ACS Nano 4:3063
22. McDonald TJ, Engttrakul C, Jones M, Rumbles G, Heben MJ (2006) J Phys Chem B 110:25339
23. Tangney P, Capaz RB, Spataru CD, Cohen ML, Louie SG (2005) Nano Lett 5:2268
24. Kamal C, Ghanty TK, Banerjee A, Chakrabarti A (2009) J Chem Phys 131:164708
25. Tummala NR, Striolo A (2009) ACS Nano 3:595
26. Zheng M, Jagota A, Semke ED, Diner BA, McLean RS, Lustig SR, Richardson RE, Tassi NG (2003) Nat Mater 2:338
27. Johnson RR, Johnson ATC, Klein ML (2008) Nano Lett 8:69
28. Wang Y (2008) J Phys Chem C 112:14297
29. Johnson RR, Kohlmeyer A, Johnson ATC, Klein ML (2009) Nano Lett 9:537
30. Vogel SR, Kappes MM, Hennrich F, Richert C (2007) Chem Eur J 13:1815
31. Duesberg GS, Muster J, Krstic V, Burghard M, Roth S (1998) Appl Phys A 67:117
32. Arnold K, Hennrich F, Krupke R, Lebedkin S, Kappes MM (2006) Phys Status Solidi B-Basic Solid State Phys 243:3073
33. Heller DA, Mayrhofer RM, Baik S, Grinkova YV, Usrey ML, Strano MS (2004) J Am Chem Soc 126:14567
34. Vetcher AA, Srinivasan S, Vetcher IA, Abramov SM, Kozlov M, Baughman RH, Levene SD (2006) Nanotechnology 17:4263
35. Strano MS, Zheng M, Jagota A, Onoa GB, Heller DA, Barone PW, Usrey ML (2004) Nano Lett 4:543
36. Zheng M, Jagota A, Strano MS, Santos AP, Barone PW, Chou SG, Diner BA, Dresselhaus MS, McLean RS, Onoa GB, Samsonidze GG, Semke ED, Usrey ML, Walls DJ (2003) Science 302:1545
37. Doorn SK, Strano MS, O'Connell MJ, Haroz EH, Rialon KL, Hauge RH, Smalley RE (2003) J Phys Chem B 107:6063
38. Arnold MS, Stupp SI, Hersam MC (2005) Nano Lett 5:713
39. Arnold MS, Grenn AA, Hulvat JF, Stupp SI, Hersam MC (2006) Nat Nanotechnol 1:60
40. Crochet J, Clemens M, Hertel T (2007) J Am Chem Soc 129:8058
41. Hennrich F, Arnold K, Lebedkin S, Quintillà A, Wenzel W, Kappes MM (2007) Phys Status Solidi B Basic Solid State Phys 244:3896
42. Nair N, Kim W-J, Braatz RD, Strano MS (2008) Langmuir 24:1790
43. Wei L, Wang B, Goh TH, Li L-J, Yang Y, Chan-Park MB, Chen Y (2008) J Phys Chem B 112:2771
44. Zheng M, Semke ED (2007) J Am Chem Soc 129:6084
45. Ju S-Y, Doll J, Sharma I, Papadimitrakopoulos F (2008) Nat Nanotechnol 3:356
46. Kim SN, Kuang Z, Grote JG, Farmer BL, Naik RR (2008) Nano Lett 8:4415
47. Tu X, Manohar S, Jagota A, Zheng M (2009) Nature 460:250
48. Nish A, Hwang J-Y, Doig J, Nicholas RJ (2007) Nat Nanotechnol 2:640
49. Chen F, Wang B, Chen Y, Li LJ (2007) Nano Lett 7:3013
50. Krupke R, Hennrich F, von Löhneyesen H, Kappes MM (2003) Science 301:344
51. Krupke R, Hennrich F, Weber HB, Kappes MM, von Löhneysen H (2003) Nano Lett 3:1019
52. Krupke R, Hennrich F, Kappes MM, von Löhneyesen H (2004) Nano Lett 4:1395

53. Krupke R, Linden S, Rapp M, Hennrich F (2006) Adv Mater 18:1468
54. Tanaka T, Jin H, Miyata Y, Fuji S, Suga H, Naitoh Y, Minari T, Miyadera T, Tsukagoshi K, Kataura H (2009) Nano Lett 9:1497
55. Peng X, Komatsu N, Bhattacharya S, Shimawaki T, Aonuma S, Kimura T, Osuka A (2007) Nat Nanotechnol 2:361
56. Peng X, Komatsu N, Kimura T, Osuka A (2007) J Am Chem Soc 129:15947
57. Gosh S, Bachilo SM, Weisman RB (2010) Nat Nanotechnol 5:443
58. Bonaccorso F, Hasan T, Tan PH, Sciascia C, Privitera G, Di Marco G, Gucciardi PG, Ferrari AC (2010) J Phys Chem C 114:17267
59. Lin S, Blankschtein D (2010) J Phys Chem C 114:15616
60. Green AA, Hersam MC (2008) Nano Lett 8:1417
61. Blackburn JL, Barnes TM, Beard MC, Kim Y-H, Tenent RC, McDonald TJ, To B, Coutts TJ, Heben MJ (2008) ACS Nano 2:1266
62. Zhao P, Einarsson E, Xiang R, Murakami Y, Maruyama S (2010) J Phys Chem C 114:4831
63. Zhao P, Einarsson E, Lagoudas G, Shiomi J, Chiashi S, Maruyama S (2011) Nano Res 4:623
64. Niyogi S, Densmore CG, Doorn SK (2009) J Am Chem Soc 131:1144
65. Nakashima N, Tomonari Y, Murakami H (2002) Chem Lett 638
66. Tomonari Y, Murakami H, Nakashima N (2006) Chem Eur J 12:4027
67. Guldi DM, Rahman GMA, Jux N, Tagmatarchis N, Prato M (2004) Angew Chem Int Ed 43:5526
68. Ehli C, Rahman GMA, Jux N, Balbinot D, Guldi DM, Paolucci F, Marcaccio M, Paolucci D, Melle-Franco M, Zerbetto F, Campidelli S, Prato M (2006) J Am Chem Soc 128:11222
69. Sgobba V, Rahman GMA, Guldi DM, Jux N, Campidelli S, Prato M (2006) Adv Mater 18:2264
70. Rahman GMA, Guldi DM, Cagnoli R, Mucci A, Schenetti L, Vaccari L, Prato M (2005) J Am Chem Soc 127:10051
71. Guldi DM, Rahman GMA, Prato M, Jux N, Qin S, Ford WT (2005) Angew Chem Int Ed 44:2015
72. Sandanayaka ASD, Chitta R, Subbaiyan NK, D'Souza L, Ito O, D'Souza F (2009) J Phys Chem C 113:13425
73. Guldi DM, Rahman GMA, Jux N, Balbinot D, Hartnagel U, Tagmatarchis N, Prato M (2005) J Am Chem Soc 127:9830
74. Xin H, Wooley AT (2003) J Am Chem Soc 125:8710
75. Chung C-L, Gautier C, Campidelli S, Filoramo A (2010) Chem Commun 6539
76. Chitta R, Sandanayaka AD, Schumacher AL, D'Souza L, Araki Y, Ito O, D'Souza F (2007) J Phys Chem C 111:6947
77. Das SK, Subbaiyan NK, D'Souza F, Sandanayaka ASD, Kakahara T, Ito O (2011) J Porphyr Phthalocyanines 15:1033
78. D'Souza F, Chitta R, Sandanayaka ASD, Subbaiyan NK, D'Souza L, Araki Y, Ito O (2007) Chem Eur J 13:8277
79. D'Souza F, Chitta R, Sandanayaka ASD, Subbaiyan NK, D'Souza L, Araki Y, Ito O (2007) J Am Chem Soc 129:15865
80. Sandanayaka ASD, Subbaiyan NK, Das SK, Chitta R, Maligaspe E, Hasode T, Ito O, D'Souza F (2011) ChemPhysChem 12:2266
81. Zhao Y-L, Hu L, Stoddart JF, Grüner G (2008) Adv Mater 20:1910
82. Zhao Y-L, Hu L, Grüner G, Stoddart JF (2008) J Am Chem Soc 130:16996
83. Zhao Y-L, Stoddart JF (2009) Acc Chem Res 42:1161
84. Avouris P, Chen Z, Perebeinos V (2007) Nat Nanotechnol 2:605
85. Avouris P, Freitag M, Perebeinos V (2008) Nat Photonics 2:341
86. Allen BL, Kichambare PD, Star A (2007) Adv Mater 19:1439
87. Grüner G (2006) Anal Bioanal Chem 384:322
88. Rekharsky MV, Inoue Y (1998) Chem Rev 98:1875
89. Ogoshi T, Takashima Y, Yamaguchi H, Harada A (2007) J Am Chem Soc 129:4878

90. Yu M, Zu S-Z, Chen Y, Liu Y-P, Han B-H, Liu Y (2010) Chem Eur J 16:1168
91. Kavakka JS, Heikkinen S, Kilpeläinen I, Mattila M, Lipsanen H, Helaja J (2007) Chem Commun 519
92. Satake A, Miyajima Y, Kobuke Y (2005) Chem Mater 17:716
93. Maligaspe E, Sandanayaka ASD, Hasode T, Ito O, D'Souza F (2010) J Am Chem Soc 132:8158
94. Bartelmess J, Ballesteros B, de la Torre G, Kiessling D, Campidelli S, Prato M, Torres T, Guldi DM (2010) J Am Chem Soc 132:16202
95. Ince M, Bartelmess J, Kiessling D, Dirian K, Martínez-Díaz MV, Torres T, Guldi DM (2012) Chem Sci 3:1472
96. Klyatskaya S, Galán Mascarós JR, Bogani L, Hennrich F, Kappes M, Wernsdorfer W, Ruben M (2009) J Am Chem Soc 131:15143
97. Urdampilleta M, Klyatskaya S, Cléziou J-P, Ruben M, Wernsdorfer W (2011) Nat Mater 10:502
98. Herranz MA, Ehli C, Campidelli S, Gutiérrez M, Hug GL, Ohkubo K, Fukuzumi S, Prato M, Martín N, Guldi DM (2008) J Am Chem Soc 130:66
99. Ehli C, Guldi DM, Herranz MA, Martín N, Campidelli S, Prato M (2008) J Mater Chem 18:1498
100. Canevet D, Pérez del Pino A, Amabilino DB, Sallé M (2011) Nanoscale 3:2898
101. Wurl A, Goossen S, Canevet D, Sallé M, Pérez EM, Martín N, Klinke C (2012) J Phys Chem C 116:20062
102. Klare JE, Murray IP, Goldberger J, Stupp SI (2009) Chem Commun 3705
103. Le Goff A, Moggia F, Debou N, Jégou P, Artero V, Fontecave M, Jousselme B, Palacin S (2010) J Electroanal Chem 641:57
104. Guldi DM, Menna E, Maggini M, Marcaccio M, Paolucci D, Paolucci F, Campidelli S, Prato M, Rahman GMA, Schergna S (2006) Chem Eur J 12:3975
105. D'Souza F, Sandanayaka ASD, Ito O (2010) J Phys Chem Lett 1:2586
106. Zhou X, Zifer T, Wong BM, Krafcik KL, Léonard F, Vance AL (2009) Nano Lett 9:1028
107. Huang C, Wang RK, Wong BM, McGee DJ, Léonard F, Kim YJ, Johnson KF, Arnold MS, Eriksson MA, Gopalan P (2011) ACS Nano 5:7767
108. Vijaykumar C, Balan B, Kim M-J, Takeuchi M (2011) J Phys Chem C 115:4533
109. Cicchi S, Fabbrizzi P, Ghini G, Brandi A, Foggi P, Marcelli A, Righini R, Botta C (2009) Chem Eur J 15:754
110. Guo X, Huang L, O'Brien S, Kim P, Nuckolls C (2005) J Am Chem Soc 127:15045
111. Setaro A, Bluemmel P, Maity C, Hecht S, Reich S (2012) Adv Funct Mater 22:2425
112. Hu L, Zhao Y-L, Ryu K, Zhou C, Stoddart JF, Grüner G (2008) Adv Mater 20:939
113. Wu P, Chen X, Hu N, Tam UC, Blixt O, Zettl A, Bertozzi CR (2008) Angew Chem Int Ed 47:5022
114. Sudibya HG, Ma J, Dong X, Ng S, Li L-J, Liu X-W, Chen P (2009) Angew Chem Int Ed 48:2723
115. Tran PD, Le Goff A, Heidkamp J, Jousselme B, Guillet N, Palacin S, Dau H, Fontecave M, Artero V (2011) Angew Chem Int Ed 50:1371
116. Chen RJ, Zhang Y, Wang D, Dai H (2001) J Am Chem Soc 123:3838
117. Besteman K, Lee J-O, Wiertz FGM, Heering HA, Dekker C (2003) Nano Lett 3:727
118. Li C, Curreli M, Lin H, Lei B, Ishikawa FN, Datar R, Cote RJ, Thompson ME, Zhou C (2005) J Am Chem Soc 127:12484
119. Maehashi K, Katsura T, Kerman K, Takamura Y, Matsumoto K, Tamiya E (2007) Anal Chem 79:782
120. Ramasamy RP, Luckarift HR, Ivnitski DM, Atanassov PB, Johnson GR (2010) Chem Commun 6045
121. Landi BJ, Evans CM, Worman JJ, Castro SL, Bailey SG, Raffaelle RP (2006) Mater Lett 60:3502
122. Sandanayaka ASD, Takaguchi Y, Uchida T, Sako Y, Morimoto Y, Araki Y, Ito O (2006) Chem Lett 35:1188

123. Zhang J, Lee J-K, Wu Y, Murray RW (2003) Nano Lett 3:403
124. Mateo-Alonso A, Ehli C, Chen KH, Guldi DM, Prato M (2007) J Phys Chem A 111:12669
125. Voggu R, Rao KV, George SJ, Rao CNR (2010) J Am Chem Soc 132:5560
126. Steinberg BD, Scott LT (2009) Angew Chem Int Ed 48:5400
127. Feng W, Fuji A, Ozaki M, Yosino K (2005) Carbon 43:2501
128. Backes C, Schmidt CD, Hauke F, Böttcher C, Hirsch A (2009) J Am Chem Soc 131:2172
129. Backes C, Schmidt CD, Rosenlehner K, Hauke F, Coleman JN, Hirsch A (2010) Adv Mater 22:788
130. Oelsner C, Schmidt C, Hauke F, Prato M, Hirsch A, Guldi DM (2011) J Am Chem Soc 2011:4580
131. Backes C, Hauke F, Hirsch A (2011) Adv Mater 23:2588
132. Newkome GR, Nayak A, Behera RK, Moorefield CN, Baker GR (1992) J Org Chem 57:358
133. Ehli C, Oelsner C, Guldi DM, Mateo-Alonso A, Prato M, Schmidt CD, Backes C, Hauke F, Hirsch A (2009) Nat Chem 1:243
134. Ernst F, Heek T, Setaro A, Haag R, Reich S (2012) Adv Funct Mater 22:3921
135. Murakami H, Nomura T, Nakashima N (2003) Chem Phys Lett 378:481
136. Chen J, Collier CP (2005) J Phys Chem B 109:7605
137. Rahman GMA, Guldi DM, Campidelli S, Prato M (2006) J Mater Chem 16:62
138. Tanaka H, Yajima T, Matsumoto T, Otsuka Y, Ogawa T (2006) Adv Mater 18:1411
139. Kauffman DR, Kuzmych O, Star A (2007) J Phys Chem C 111:3539
140. Roquelet C, Lauret J-S, Alain-Rizzo V, Voisin C, Fleurier R, Delarue M, Garrot D, Loiseau A, Roussignol P, Delaire JA, Deleporte E (2010) ChemPhysChem 11:1667
141. Morozan A, Campidelli S, Filoramo A, Jousselme B, Palacin S (2011) Carbon 49:4839
142. D’Souza F, Das SK, Sandanayaka ASD, Subbaiyan NK, Gollapalli DR, Zandler ME, Wakahara T, Ito O (2012) Phys Chem Chem Phys 14:2940
143. Peng H, Qin H, Li L, Huang Y, Peng J, Cao Y, Komatsu N (2012) J Mater Chem 22:5764
144. Cheng F, Adronov A (2006) Chem Eur J 12:5053
145. Ozawa H, Yi X, Fujigaya T, Niidome Y, Asano T, Nakashima N (2011) J Am Chem Soc 133:14771
146. Sprafke JK, Stranks SD, Warner JH, Nicholas RJ, Anderson HL (2011) Angew Chem Int Ed 50:2313
147. Stranks SD, Sprafke JK, Anderson HL, Nicholas RJ (2011) ACS Nano 5:2307
148. Cheng F, Zhang S, Adronov A, Echegoyen L, Diederich F (2006) Chem Eur J 12:6062
149. Chen F, Zhu J, Adronov A (2011) Chem Mater 23:3188
150. Wang X, Liu Y, Qiu W, Zhu D (2002) J Mater Chem 12:1636
151. Ma A, Lu J, Yang S, Ng KM (2006) J Clust Sci 17:599
152. Wang J, Blau WJ (2008) Chem Phys Lett 465:265
153. Bartelmess J, Ehli C, Cid J-J, García-Iglesias M, Vázquez P, Torres T, Guldi DM (2011) Chem Sci 2:652
154. Chichak KS, Star A, Altoé MVP, Stoddart JF (2005) Small 4:452
155. Hecht DS, Ramirez RJA, Briman M, Artukovic E, Chichak KS, Stoddart JF, Grüner G (2006) Nano Lett 6:2031
156. Peng X, Komatsu N, Kimura T, Osuka A (2008) ACS Nano 2:2045
157. Wang F, Matsuda K, Rahman AFMM, Kimura T, Komatsu N (2011) Nanoscale 3:4117
158. Liu G, Yasumitsu T, Zhao L, Peng X, Wang F, Bauri AK, Aonuma S, Kimura T, Komatsu N (2012) Org Biomol Chem 10:5830
159. Wang F, Matsuda K, Rahman AFMM, Peng X, Kimura T, Komatsu N (2010) J Am Chem Soc 132:10876
160. Rahman AFMM, Wang F, Matsuda K, Kimura T, Komatsu N (2011) Chem Sci 2:862
161. Backes C, Schmidt CD, Hauke F, Hirsch A (2010) Chem Asian J 6:438
162. Wang RK, Chen W-C, Campos DS, Ziegler KJ (2008) J Am Chem Soc 130:16330
163. Chen W-C, Wang RK, Ziegler KJ (2009) ACS Appl Mater Interfaces 1:1821

164. Roquelet C, Garrot D, Lauret J-S, Voisin C, Alain-Rizzo V, Roussignol P, Delaire JA, Deleporte E (2010) Appl Phys Lett 97:141918
165. Garrot D, Langlois B, Roquelet C, Michel T, Roussignol P, Delalande C, Deleporte E, Lauret J-S, Voisin C (2011) J Phys Chem C 115:23283
166. Roquelet C, Vialla F, Diederichs C, Roussignol P, Delalande C, Deleporte E, Lauret J-S, Voisin C (2012) ACS Nano 6:8796
167. Roquelet C, Langlois B, Vialla F, Garrot D, Lauret J-S, Voisin C (2013) Chem Phys 413:45
168. Chae HG, Liu J, Kumar S (2006) Carbon nanotube-enabled materials. In: O'Connell MJ (ed) Carbon nanotubes properties and applications. CRC Taylor and Francis, Boca Raton, p 213
169. Spitalsky Z, Tasis D, Papagelis K, Galiotis C (2010) Prog Polym Sci 35:357
170. Coleman JN, Dalton AB, Curran S, Rubio A, Davey AP, Drury A, McCarthy B, Lahr B, Ajayan PM, Roth S, Barklie RC, Blau WJ (2000) Adv Mater 12:213
171. Curran SA, Ajayan PM, Blau WJ, Carroll DL, Coleman JN, Dalton AB, Davey AP, Drury A, McCarthy B, Maier S, Stevens A (1998) Adv Mater 10:1091
172. Star A, Stoddart JF, Steuerman D, Diehl M, Boukai A, Wong EW, Yang X, Chung S-W, Choi H, Heath JR (2001) Angew Chem Int Ed 40:1721
173. Curran S, Davey AP, Coleman JN, Dalton AB, McCarthy B, Maier S, Drury A, Gray D, Brennan M, Ryder K, de la Chapelle ML, Journet C, Bernier P, Byrne HJ, Carroll DL, Ajayan PM, Lefrant S, Blau W (1999) Synth Met 103:2559
174. Yi W, Malkovskiy A, Chu Q, Sokolov AP, Colon ML, Meador M, Pang Y (2008) J Phys Chem B 112:12263
175. Chen Y, Malkovskiy A, Wang X-Q, Lebron-Colon M, Sokolov AP, Perry K, More K, Pang Y (2012) ACS Macro Lett 1:246
176. Chen Y, Xu Y, Perry K, Sokolov AP, More K, Pang Y (2012) ACS Macro Lett 1:701
177. Steuerman DW, Star A, Narizzano R, Choi H, Ries RS, Nicolini C, Stoddart JF, Heath JR (2002) J Phys Chem B 106:3124
178. Star A, Liu Y, Grant K, Ridvan L, Stoddart JF, Steuerman DW, Diehl MR, Boukai A, Heath JR (2003) Macromolecules 36:553
179. Tang BZ, Xu HY (1999) Macromolecules 32:2569
180. Yuan WZ, Sun JZ, Dong YQ, Häussler M, Yang F, Xu HP, Qin AJ, Lam JWY, Zheng Q, Tang BZ (2006) Macromolecules 39:8011
181. Yuan WZ, Sun JZ, Liu JZ, Dong Y, Li Z, Xu HP, Qin A, Häussler M, Jin JK, Zheng Q, Tang BZ (2008) J Phys Chem B 112:8896
182. Zhao H, Yuan WZ, Mei J, Tang L, Liu XQ, Yan M, Shen XY, Sun JZ, Qin AJ, Tang BZ (2009) J Polym Sci Part A Polym Chem 47:4995
183. Ikeda A, Nobusawa K, Hamano T, Kikuchi K (2006) Org Lett 8:5489
184. Goh RGS, Motta N, Bell JM, Waclawik ER (2006) Appl Phys Lett 88:053101
185. Schuettfort T, Snaith HJ, Nish A, Nicholas RJ (2010) Nanotechnology 21:025201
186. Stranks SD, Weisspfennig C, Parkinson P, Jonston MB, Herz LM, Nicholas RJ (2011) Nano Lett 11:66
187. Caddeo C, Melis C, Colombo L, Mattoni A (2010) J Phys Chem C 114:21109
188. Lee HW, Yoon Y, Park S, Oh JH, Hong S, Liyanage LS, Wang H, Morishita S, Patil N, Park YJ, Park JJ, Spakowitz A, Galli G, Gygi F, Wong PHS, Tok JBH, Kim JM, Bao Z (2011) Nat Commun 2:541
189. Dabera GDMR, Jayawardena KDGI, Prabhath MRR, Yahya I, Tan YY, Nismy NA, Shiozawa H, Sauer M, Ruiz-Soria G, Ayala P, Stolojan V, Adikaari AADT, Jarowski PD, Pichler T, Silva SRP (2013) ACS Nano 7:556
190. Stranks SD, Yong C-K, Alexander-Webber JA, Weisspfennig C, Johnston MB, Herz L, Nicholas RJ (2012) ACS Nano 6:6058
191. Chen J, Liu HY, Weimer WA, Halls MD, Waldeck DH, Walker GC (2002) J Am Chem Soc 124:9034
192. Kang YK, Lee OS, Deria P, Kim SH, Park TH, Bonnell DA, Saven JG, Therien MJ (2009) Nano Lett 9:1414

193. Cheng F, Imin P, Maunders C, Botton G, Adronov A (2008) Macromolecules 41:2304
194. Deria P, Sinks LE, Park TH, Tomezsko DM, Brukman MJ, Bonnell DA, Therien MJ (2010) Nano Lett 10:4192
195. Rosario-Canales MR, Deria P, Therien MJ, Santiago-Avilés JJ (2012) ACS Appl Mater Interfaces 4:102
196. Liu XL, Ly J, Han S, Zhang DH, Requicha A, Thompson ME, Zhou CW (2005) Adv Mater 17:2727
197. Huang JE, Li XH, Xu JC, Li HL (2003) Carbon 41:2731
198. Jiménez P, Maser WK, Castell P, Martínez MT, Benito AM (2009) Macromol Rapid Commun 30:418
199. Sainz R, Small WR, Young NA, Valles C, Benito AM, Maser WK, in het Panhuis M (2006) Macromolecules 39:7324
200. Cochet M, Maser WK, Benito AM, Callejas MA, Martínez MT, Benoit JM, Schreiber J, Chauvet O (2001) Chem Commun 1451
201. Zengin H, Zhou WS, Jin JY, Czerw R, Smith DW, Echegoyen L, Carroll DL, Foulger SH, Ballato J (2002) Adv Mater 14:1480
202. Carroll DL, Czerw R, Webster S (2005) Synth Met 155:694
203. Kim D, Kim Y, Choi K, Grulan JC, Yu C (2010) ACS Nano 4:513
204. Li J, Liu J-C, Gao C-J (2010) J Polym Res 17:713
205. Moon JS, Park JH, Lee TY, Kim YW, Yoo JB, Park CY, Kim JM, Jin KW (2005) Diam Relat Mat 14:1882
206. Fan BH, Mei XG, Sun K, Ouyang JY (2008) Appl Phys Lett 93:143103
207. Jalili R, Razal JM, Wallace GG (2012) J Mater Chem 22:25174
208. Sim J-B, Yang HH, Lee M-J, Yoon J-B, Choi S-M (2012) Appl Phys A 108:305
209. Hwang J-Y, Nish A, Doig J, Douven S, Chen C-W, Chen L-C, Nicholas RJ (2008) J Am Chem Soc 130:3543
210. Nish A, Hwang J-Y, Doig J, Nicholas RJ (2008) Nanotechnology 19:095603
211. Gao J, Kwak M, Wildeman J, Herrmann A, Loi MA (2011) Carbon 49:333
212. Gao J, Annema R, Loi MA (2012) Eur Phys J B 85:246
213. Gao J, Loi MA, Figueiredo de Carvalho EJ, dos Santos MC (2011) ACS Nano 5:3993
214. Berton N, Lemasson F, Tittmann J, Stürzl N, Heinrich F, Kappes MM, Mayor M (2011) Chem Mater 23:2237
215. Ozawa H, Fujigaya T, Song S, Suh H, Nakashima N (2011) Chem Lett 40:470
216. Akazaki K, Toshimitsu F, Ozawa H, Fujigaya T, Nakashima N (2012) J Am Chem Soc 134:12700
217. Lemasson F, Berton N, Tittmann J, Hennrich F, Kappes MM, Mayor M (2012) Macromolecules 45:713
218. Gerstel P, Klumpp S, Hennrich F, Altintas O, Eaton TR, Mayor M, Barner-Kowollik C, Kappes MM (2012) Polym Chem 3:1966
219. Mistry KS, Larsen BA, Blackburn JL (2013) ACS Nano. 10.1021/nn305336x
220. Izard N, Kazaoui S, Hata K, Okazaki T, Saito T, Iijima S, Minami N (2008) Appl Phys Lett 92:243112
221. Bisri SZ, Gao J, Derenskyi V, Gomulya W, Iezhokin I, Gordiichuk P, Herrmann A, Loi MA (2012) Adv Mater 24:6147
222. Bindl DJ, Safron NS, Arnold MS (2010) ACS Nano 4:5657
223. Bindl DJ, Arnold MS (2013) J Phys Chem C 117:2390
224. Umeyama T, Kawabata K, Tezuka N, Matano Y, Miyato Y, Matsushige K, Tsujimoto M, Isoda S, Takano M, Imahori H (2010) Chem Commun 46:5969
225. Lemasson F, Tittmann J, Hennrich F, Stürzl N, Malik S, Kappes MM, Mayor M (2011) Chem Commun 47:7428
226. Wang WZ, Li WF, Pan XY, Li CM, Li L-J, Mu YG, Rogers JA, Chan-Park MB (2011) Adv Funct Mater 21:1643

Top Curr Chem (2014) 348: 127–138
DOI: 10.1007/128_2013_449

Fullerene-Stoppered Bistable Rotaxanes

Aurelio Mateo-Alonso

Abstract This chapter aims at giving an overview of the different types of fullerene-stoppered bistable rotaxanes, their switching mechanism and their potential applications with a special focus on fullerene-driven molecular shuttles.

Keywords Bistable rotaxanes · C_{60} · Fullerene · Mechanically interlocked architectures · Molecular machines · Molecular shuttles

Contents

1 Introduction

Bistable rotaxanes or molecular shuttles are mechanically interlocked components that present a ring component (or macrocycle) threaded by an axle (or thread). The presence of two bulky stoppers at both ends of the axle prevents dethreading and ensures that the macrocycle remains interlocked [1–4]. Since the macrocycle is only mechanically bonded to the thread, it can be positioned along different parts of

---

A. Mateo-Alonso (✉)
POLYMAT, University of the Basque Country UPV/EHU, Avenida de Tolosa 72, E-20018 Donostia-San Sebastian, Spain

Ikerbasque, Basque Foundation for Science, E-48011 Bilbao, Spain
e-mail: amateo@frias.uni-freiburg.de

the axle called stations. In the case of bistable rotaxanes the axle possess two different stations among which the macrocycle can switch.

C_{60} [5] has been introduced in this type of architecture as a stopper because of its large size. However, most importantly, C_{60} can also act as a photo/electroactive component since it possesses very useful properties with application in different fields such as photovoltaics, nonlinear optics, among many others. In fact, the relocation of the macrocycle has been applied to modulate the optoelectronic properties of fullerenes at the molecular-level. This implies that the relocation of the macrocycle can be used to design multiresponsive materials and also that such a response can be used to monitor and interface submolecular motion with the macroscopic world. Moreover, the C_{60} stopper has also been utilised as a unit able to monitor and induce simultaneously the position of the macrocycle. All these different applications of fullerene stoppers will be illustrated with specific examples below.

Overall, this chapter aims at giving an overview of the different types of fullerene-stoppered bistable rotaxanes, their switching mechanism and their potential applications with special focus on fullerene-driven molecular shuttles. The information in this chapter can be expanded in several reviews that cover the whole spectrum of fullerene interlocked architectures [6–8].

2 Solvent Switchable Rotaxanes

The first fullerene bistable rotaxane [9] was reported in 2003 and was based on the Leigh-type [2, 10] solvent switchable molecular shuttles (Scheme 1). The thread of rotaxane **1** possesses two stations: a diamide and an alkyl station. In solvents with a low hydrogen bond basicity such as $CHCl_3$, the macrocycle sits on top of the diamide by means of four hydrogen bonds between the amidic NH of the macrocycle and the carbonyls of the amides on the thread (**1A**). Conversely, in a solvent with a high hydrogen bond basicity such as dimethyl sulfoxide (DMSO), the solvent interacts more efficiently with the hydrogen bond binding sites of the macrocycle and the diamide and thus the macrocycle decomplexes from the hydrogen bond binding sites and switches in order to sit on top of the alkyl station (**1B**). An important characteristic of this type of bistable rotaxanes is that the position of the macrocycle along the thread can be distinguished by spectroscopy, in particular by looking at the triplet–triplet absorption characteristics of C_{60}, which appeared to be affected by the close proximity of the macrocycle (**1A**) and restored when located on top of the alkyl chain (**1B**).

In an attempt to synthesise a rotaxane with the switchable behaviour as rotaxane **1** but with higher yields, rotaxane **2** was designed and synthesised (Scheme 2) [11]. From the structural point of view rotaxane **2** possesses exactly the same features as rotaxane **1**: a C_{60} stopper, a diamide next to the fullerene, an alkyl station and a second stopper at the other end of the thread. In a similar fashion, in solvents with a low hydrogen bond basicity such as $CHCl_3$ the macrocycle sits on

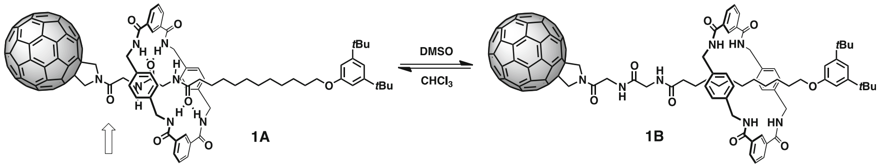

Scheme 1 Solvent switchable molecular shuttle

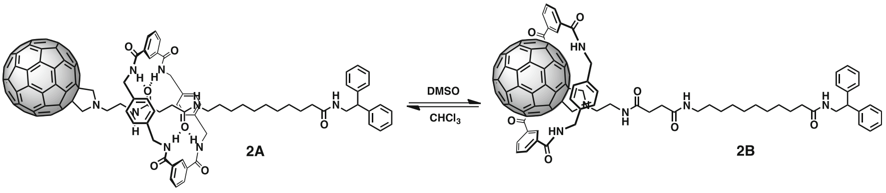

Scheme 2 "Reverse" shuttling

top of the diamide by hydrogen bond complementarity (**2A**). Most surprisingly, in solvents with a high hydrogen bond basicity such as DMSO the macrocycle switched in the opposite direction (**2B**). This "reverse" shuttling behaviour was attributed to the existence of an additional amide in between the diamide station and the macrocycle, which is indicated by an arrow in Scheme 1. This is explained in terms of solvation. In rotaxane **1**, the close proximity of the three consecutive solvated amides to C_{60} does not allow the macrocycle to get closer to the fullerene. In the case of rotaxane **2** that extra amide is missing. Hence the C_{60} stopper is accessible to the macrocycle because the pathway towards C_{60} is less solvated and thus accessible to the macrocycle. Therefore in this situation the macrocycle upon decomplexation can move forward or backwards but it prefers to switch towards C_{60} because it can interact with C_{60} by means of π-stacking interactions. This system had an important implication since the fullerene stopper could be used as a unit or station to induce the displacement of the macrocycle.

At this stage it was important to prove that fullerene could also be used to induce a large amplitude displacement of the macrocycle. A third generation of molecular shuttles was designed in which the diamide station was located at the other end of the thread, away from C_{60}, by means of a long triethylene glycol spacer (Scheme 3) [12]. In this new type of rotaxane the macrocycle is located near the biphenyl stopper at the other end by means of hydrogen bond recognition between the macrocycle and the diamide station in solvents with low hydrogen bond basicity (**3A**). However, in solvents that disturb hydrogen bonds such as DMSO the macrocycle relocated all along the tread to π-stack to the fullerene at the other end (**3B**). An additional asset of rotaxane **3** is the fact that the position of the macrocycle can be easily monitored by means of steady-state emission since the macrocycle interacts directly with the C_{60} stopper [12, 13]. The position of

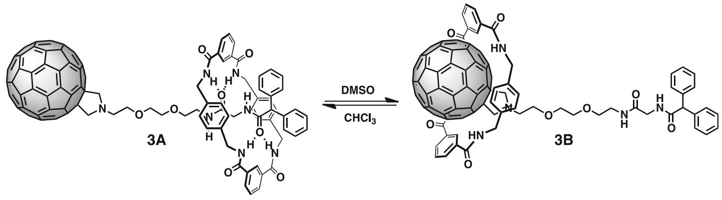

Scheme 3 Solvent switchable fullerene-driven molecular shuttle

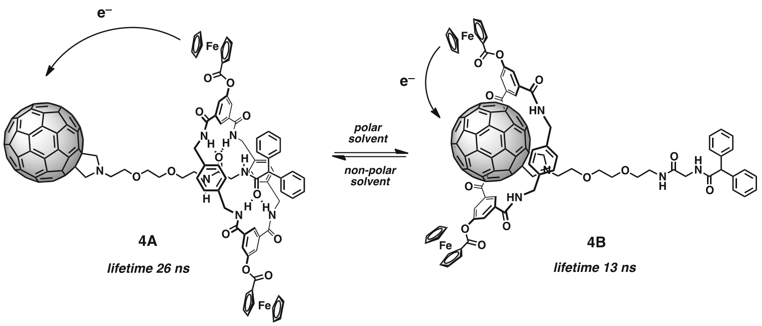

Scheme 4 Electron Donor-Acceptor molecular shuttles

the macrocycle can also be used to modulate the nonlinear optical response of the fullerene [14].

This large amplitude fullerene driven molecular shuttle has been used as a scaffold to prepare a donor–acceptor system [15–17]. As a matter of fact, two ferrocene electron donors have been introduced in the macrocycle giving rise to a tunable donor–acceptor system (Scheme 4) [15]. By changing the position of the macrocycle through a solvent change, the relative distance between the ferrocene electron donors and the C_{60} electron acceptors varies sufficiently to change the electron transfer kinetics upon irradiation, which is reflected by the different lifetimes of the photoinduced radical pairs in **4A** and **4B**.

3 Electrochemically Switchable Rotaxanes

Solvent switching is a very powerful approach since it ensures a complete structural characterisation of the two states in solution. However, it is not useful to develop practical applications of molecular shuttles. In a society powered by electricity, electrons appear as a much more practical stimulus that allows interfacing of the movement of such molecular components with current technologies. C_{60} is an excellent electron acceptor and it can be selectively reduced with up to six electrons and possesses easily accessible reduction potentials [18]. The stability of this

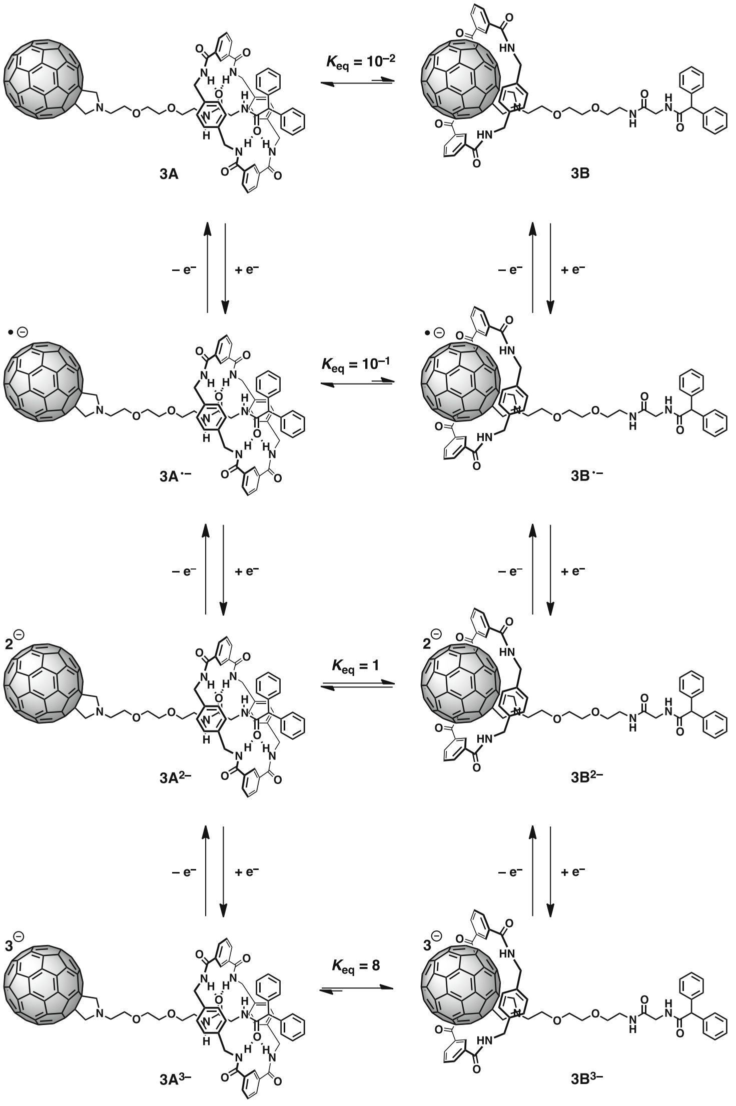

Scheme 5 Electrochemically switchable fullerene-driven molecular shuttle

negative charge species derives from the low reorganisation energy and the very large π-system that ensures a high delocalisation of the electrons [19].

Rotaxane **3** can also be switched electrochemically by exploiting the electrochemical properties of C_{60} (Scheme 5) [12]. This can be effected and monitored by means of cyclic voltammetry. The equilibrium constants between **3A** and **3B** at the different redox states were estimated by a combination of cyclic voltammetry and simulations of the corresponding voltammograms by using the square scheme mechanism set out in Scheme 5. In a solvent with low hydrogen bond basicity such as tetrahydrofuran (THF) the macrocycle is preferentially located on the diamide station by hydrogen bond recognition; this is reflected by $K_{eq} = 10^{-2}$ in the neutral state (**3A**). Upon the reduction of C_{60} with one electron to produce the radical-anion, the equilibrium is shifted towards **3B** but still the macrocycle is still preferentially located over the dipeptide station (**3A**) as reflected by $K_{eq} = 10^{-1}$. The reduction of the fullerene with a second electron provides the fullerene-dianion. In this redox state the equilibrium is more shifted towards **3B** and a $K_{eq} = 1$ was calculated. This implies that either the macrocycle is constantly switching between **3A** and **3B** or that there is 50% of **3A** and 50% of **3B**. The reduction of the C_{60} stopper with a third electron provides the trianion. In this redox state the equilibrium is completely shifted towards **3B** by a strong interaction between the macrocycle and the negatively charged fullerene that stabilises the negative charge present on the fullerene. This interaction is strong enough to overcome four hydrogen bonds as reflected by $K_{eq} = 8$.

The exchange of the isophthalamide-based macrocycle (**3**) for a dinicotinamide-based macrocycle (**5**) results in a much higher positional discrimination that was attributed to the polarisation of the macrocycle by the presence of an N atom (Scheme 6) [20]. In a similar fashion, the equilibrium constants of rotaxane **5** at the different redox states were estimated by a combination of cyclic voltammetry and simulations of the corresponding voltamograms by using the square scheme mechanism set out in Scheme 6. The first difference is clearly seen in the neutral state in which a tenfold difference in the equilibrium constant is observed when comparing rotaxane **5** with rotaxane **3**. Nevertheless the macrocycle is still residing preferentially on top of the diamide station (**5A**). When the fullerene is reduced to the radical-anion a $K_{eq} = 1$ was calculated, which corresponds to an equimolar distribution of **5A** and **5B**. The reduction of the fullerene to the dianion shifts the equilibrium completely towards **5B** ($K_{eq} = 10$). When the fullerene was reduced to the trianion a $K_{eq} = 80$ was obtained, the highest so far observed for fullerene-driven molecular shuttles.

Even if the positional discrimination between stations **5B** and **5A** is very large (80:1), a very high operation potential ($E_{1/2} = -1.743$ V vs decamethylferrocene) is necessary, which hinders the development of practical applications. For this reason, a new fullerene-stoppered molecular shuttle was synthesised with two positive charges on the macrocycle (Scheme 7) [20]. The presence of positive charges strengthens the existing π–π interactions between the macrocycle and the electrogenerated fullerene negatively charged species by means of an electrostatic component, which resulted in an excellent recognition motif for fullerene radical anions. Simulations were carried out only on the first redox state due to the simultaneous reduction of the macrocycle and the fullerene upon the formation of the dianion. As expected, simulations of the voltammogram of rotaxane **6** using the square scheme mechanism set out in Scheme 7 revealed that **6A** dominates in the neutral state ($K_{eq} = 10^{-1}$), but upon reduction of the fullerene stopper to the radical anion ($E_{1/2} = -0.580$ V vs decamethylferrocene), the equilibrium is completely dominated by **6B** ($K_{eq} = 5$). This illustrates the great affinity between the fullerene

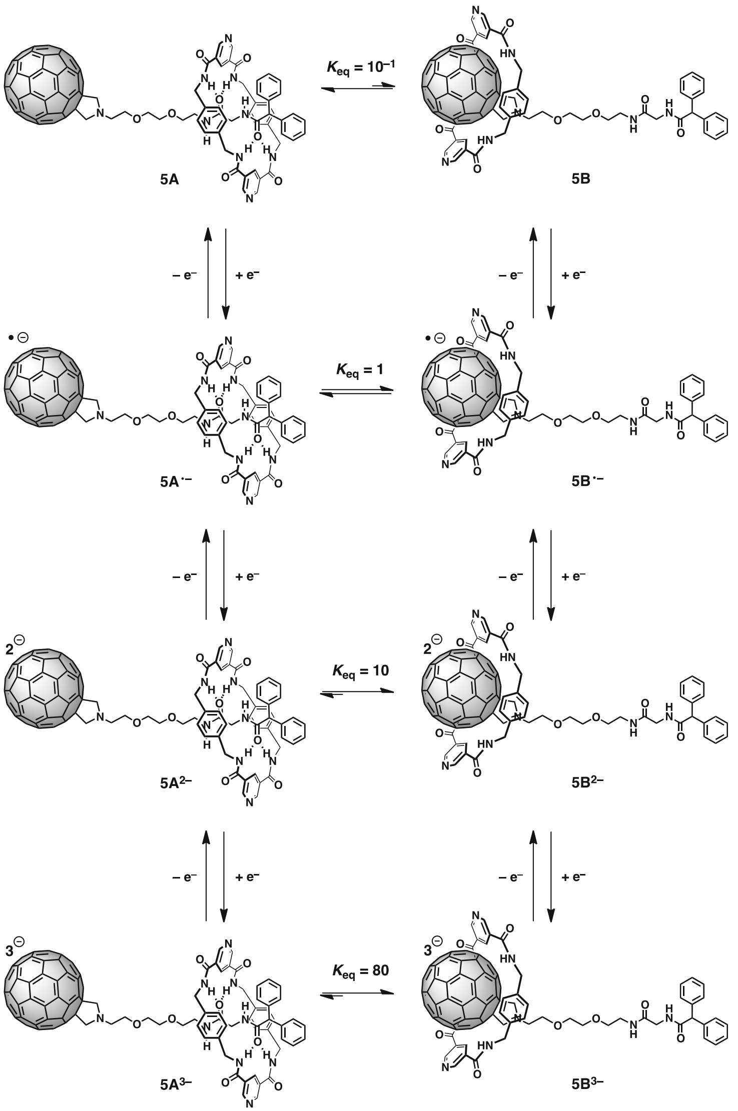

Scheme 6 A highly efficient electrochemically switchable fullerene-driven molecular shuttle

radical anion and the macrocycle, but most importantly that it is possible to switch the macrocycle efficiently by the reduction of only one electron and the application of a very small reduction potential.

A different type of electrochemically driven fullerene-stoppered molecular shuttle has been reported, in which the shuttling mechanism is based only on π–π interactions (Scheme 8) [21]. The thread of rotaxane **7** presents two electron-rich stations: a tetrathiafulvalene (TTF) and a 1,5-dihydroxynaphthalene (DNP).

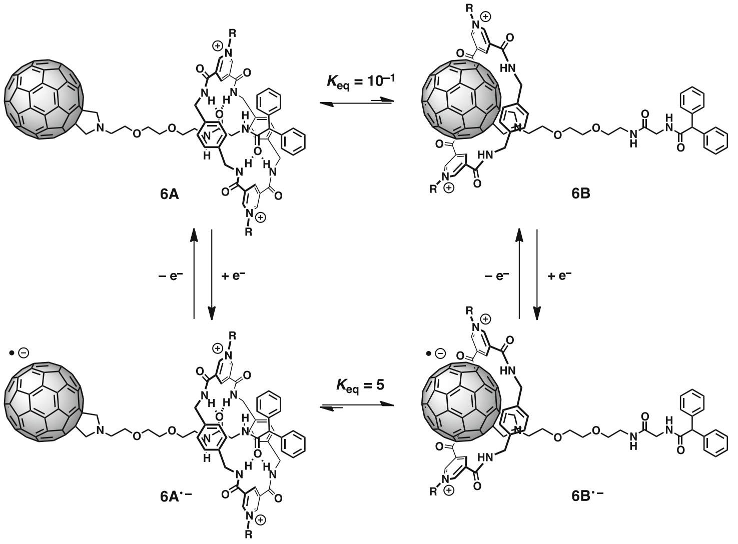

Scheme 7 Shuttling through fullerene radical-anion recognition

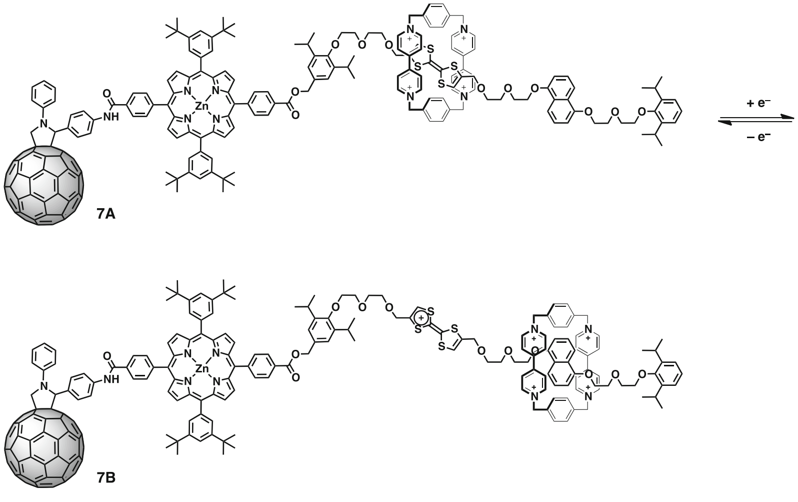

Scheme 8 Electrochemically switchable molecular shuttle

The electron-deficient tetracationic macrocycle sits on top the TTF station by π–π interactions, since it is more electron-rich than the DNP station. Upon electrochemical oxidation of the TTF, the tetracationic macrocycle leaves the positively charged TTF station by electrostatic repulsion to bind the DNP station, since it is more electron-rich than the oxidised TTF.

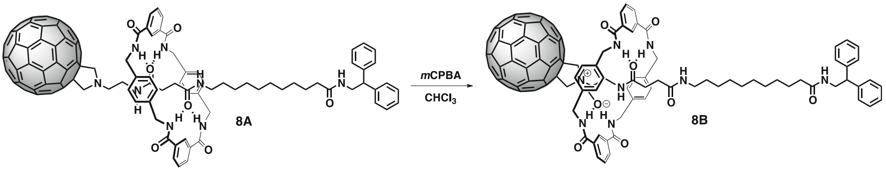

Scheme 9 Switching by oxidation of fulleropyrrolidines

4 Chemically Switchable Rotaxanes

In the same way as solvent switchable rotaxanes, in chemically switchable rotaxanes it is possible to freeze both translational isomers, which allows studying independently their differences in terms of reactivity and photophysical behaviour. Nevertheless, as illustrated below, the relocation of the ring component is not always reversible.

Fulleropyrrolidines can be oxidised to the corresponding fulleropyrrolidine *N*-oxide by addition of *m*-chloroperbenzoic acid (MCPBA) under high dilution conditions [22]. As mentioned above, in solvents with a low hydrogen bond basicity the macrocycle of rotaxane **8A** sits on the diamide station by hydrogen bonds. When rotaxane **8A** was *N*-oxidised, the macrocycle switches to bind preferentially the *N*-oxide and one of the amides of the diamide station (**8B**). This change of position takes place because of the higher hydrogen bond basicity of *N*-oxides vs amides, which is patent from the fact that even if **8B** is dissolved in solvents that disturb hydrogen bonds such as DMSO, the macrocycle does not move at all from that position. The encapsulation of the *N*-oxide by the macrocycle inhibits the known deoxygenation of fulleropyrrolidine *N*-oxide and thus the translocation could not be reversed (Scheme 9).

A different type of fullerene-stoppered bistable rotaxane is driven by exploiting the recognition between ammonium salts and crown ethers (Scheme 10) [23, 24]. Rotaxane **9** displays a fullerene-stoppered thread with an ammonium salt. In solvents with a low hydrogen bond basicity, the macrocycle sits on top of the ammonium salt by hydrogen bond recognition (**9A**). This promotes a π–π interaction between the porphyrin on the macrocycle and the fullerene stopper. The acetylation of the ammonium salt to provide an amide blocks that binding site and thus the macrocycle switches into a new co-conformation in which the macrocycle is positioned closer to the fullerene (**9B**) but that does not allow an interaction between the porphyrin and the fullerene. A detailed photophysical study revealed photoinduced electron transfer between the porphyrin and the C_{60} stopper with a lifetime of 180 ns in **9A** [24]. Acylation of the ammonium salt led to **9B** and to enhancement of the lifetime of the radical pair (560 ns). When **9A** was acylated with a ferrocene electron-donating unit a similar behaviour as in **9B** was observed [25]. However, when **9A** was acylated with a triphenylamine derivative a hole shift from the porphyrin to the triphenylamine unit became apparent [26, 27].

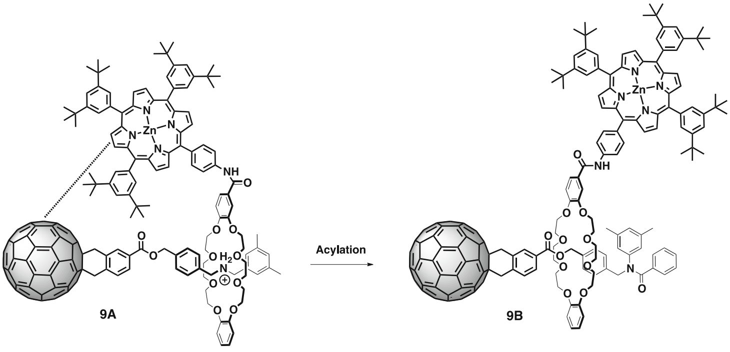

Scheme 10 Switching by acylation

5 Conclusions

This chapter illustrates that the design and the synthesis of fullerene-stoppered bistable rotaxanes are important and relevant topics of research. The synthesis of such molecular systems has been achieved by combining known methodologies to construct interlocked architectures with new molecular recognition concepts that involve the use of the fullerene stopper not only as a stopper but also as a unit able to induce submolecular displacement through stimuli of a different nature. The combination of bistable rotaxanes with fullerenes gives rise to a variety of new materials that combine the switchable properties of rotaxanes with the optoelectronic properties of fullerenes. This new generation of switchable materials have shown great promise in the modulation of some of the most characteristics properties of fullerenes such as emission, electron-accepting and nonlinear optical properties. The above-mentioned solvent-, electrochemical- and chemical-switchable bistable rotaxanes illustrate the current state-of-the-art of the field which clearly paves the way for the preparation of more efficient systems and also for the design of new bistable rotaxanes switchable by light.

References

1. Schill G (1971) Catenanes, rotaxanes and knots. Academic, New York
2. Kay ER, Leigh DA, Zerbetto F (2007) Angew Chem Int Ed 46:72–191
3. Balzani V, Credi A, Venturi M (2008) Molecular devices and machines: concepts and perspectives for the nanoworld. Wiley-VCH, Weinheim
4. Stoddart JF (2009) Chem Soc Rev 38:1802–1802
5. Kroto HW, Heath JR, O'Brien SC, Curl RF, Smalley RE (1985) Nature 318:162–163
6. Mateo-Alonso A (2010) Chem Commun 46:9089–9099
7. Mateo-Alonso A, Guldi DM, Paolucci F, Prato M (2007) Angew Chem Int Ed 46:8120–8126
8. Martin N, Nierengarten JF (2012) Supramolecular chemistry of fullerenes and carbon nanotubes. Wiley-VCH, Weinheim

9. Da Ros T, Guldi DM, Morales AF, Leigh DA, Prato M, Turco R (2003) Org Lett 5:689–691
10. Kelly T, Kay E, Leigh D (2005) Hydrogen bond-assembled synthetic molecular motors and machines. In: Kelly TR (ed) Molecular machines, vol 262. Springer, Berlin, pp 133–177
11. Mateo-Alonso A, Fioravanti G, Marcaccio M, Paolucci F, Jagesar DC, Brouwer AM, Prato M (2006) Org Lett 8:5173–5176
12. Mateo-Alonso A, Fioravanti G, Marcaccio M, Paolucci F, Rahman GMA, Ehli C, Guldi DM, Prato M (2007) Chem Commun 1945–1947
13. Mendoza SM, Berna J, Perez EM, Kay ER, Mateo-Alonso A, De Nadai C, Zhang S, Baggerman J, Wiering PG, Leigh DA, Prato M, Brouwer AM, Rudolf P (2008) J Electron Spectrosc 165:42–45
14. Mateo-Alonso A, Iliopoulos K, Couris S, Prato M (2008) J Am Chem Soc 130:1534–1535
15. Mateo-Alonso A, Ehli C, Rahman GMA, Guldi DM, Fioravanti G, Marcaccio M, Paolucci F, Prato M (2007) Angew Chem Int Ed 46:3521–3525
16. Mateo-Alonso A, Ehli C, Guldi DM, Prato M (2008) J Am Chem Soc 130:14938–14939
17. Mateo-Alonso A, Prato M (2010) Eur J Org Chem 1324–1332
18. Echegoyen L, Echegoyen LE (1998) Acc Chem Res 31:593–601
19. Guldi DM (2000) Chem Commun 321–327
20. Scarel F, Valenti G, Gaikwad S, Marcaccio M, Paolucci F, Mateo-Alonso A (2012) Chem Eur J 18:14063–14068
21. Saha S, Flood AH, Stoddart JF, Impellizzeri S, Silvi S, Venturi M, Credi A (2007) J Am Chem Soc 129:12159–12171
22. Mateo-Alonso A, Brough P, Prato M (2007) Chem Commun 1412–1414
23. Sasabe H, Kihara N, Furusho Y, Mizuno K, Ogawa A, Takata T (2004) Org Lett 6:3957–3960
24. Sasabe H, Sandanayaka ASD, Kihara N, Furusho Y, Takata T, Araki Y, Ito O (2009) Phys Chem Chem Phys 11:10908–10915
25. Maes M, Sasabe H, Kihara N, Araki Y, Furusho Y, Mizuno K, Takata T, Ito O (2005) J Porphyr Phthalocya 9:724–734
26. Sasabe H, Furusho Y, Sandanayaka ASD, Araki Y, Kihara N, Mizuno K, Ogawa A, Takata T, Ito O (2006) J Porphyr Phthalocya 10:1346–1359
27. Sandanayaka ASD, Sasabe H, Araki Y, Kihara N, Furusho Y, Takata T, Ito O (2010) J Phys Chem A 114:5242–5250

Top Curr Chem (2014) 348: 139–180
DOI: 10.1007/128_2013_475

Catalysis-Material Crosstalk at Tailored Nano-Carbon Interfaces

Michele Melchionna, Marcella Bonchio, Francesco Paolucci, Maurizio Prato, and Paolo Fornasiero

Abstract The use of carbon nanomaterials as supports for molecular and nanostructured catalysts is becoming a more and more popular strategy to improve heterogeneous catalysis. Their outstanding electronic and optical properties together with high surface area and thermal and mechanical stabilities make them ideal elements to provide catalysts with additional or improved characteristics. The role of the carbon nanostructures in the different types of catalysis is more intricate and often involves active and strong interactions between the support and the catalytic active species, creating a synergistic effect that in many cases leads to performance enhancement and an expanded range of possible applications. In particular, photocatalysis and electrocatalysis seem to benefit from the features of these types of carbon support, although applicability can be extended to more classic transformations of organic substrates.

Keywords Carbon nanohorns · Carbon nanostructures · Carbon nanotubes · Electrocatalysis · Fuel cells · Graphene · Heterogeneous catalysis · Lithium ion batteries · Metal nanoparticles · Photocatalysis · Water splitting

---

M. Melchionna, M. Prato and P. Fornasiero (✉)
Department of Chemical and Pharmaceutical Sciences, INSTM, Center of Excellence for Nanostructured Materials (CENMAT) University of Trieste, Via L. Giorgieri 1, 34127 Trieste, Italy
e-mail: pfornasiero@units.it

M. Bonchio
Department of Chemical Sciences and ITM-CNR, University of Padova, via F. Marzolo 1, 35131 Padova, Italy

F. Paolucci
G. Ciamician Chemistry Department, University of Bologna, via Selmi 2, 40126 Bologna, Italy

Contents

Abbreviations

AC	Amorphous carbon
Ar	Aryl
BFC	Biofuel cell
Bu	Butyl
cat	Catalyst
CB	Conduction band
cm	Centimeters
CNH	Carbon nanohorn
CNT	Carbon nanotube
ECSA	Electroactive surface area
equiv	Equivalent(s)
Et	Ethyl
FC	Fuel cell
G	Graphene
GO	Graphene oxide
GOD	Glucose oxidase
h	Hour(s)
HER	Hydrogen evolving reaction
i-Pr	Isopropyl
ITO	Indium tin oxide
L	Liter(s)
LIB	Lithium ion batteries
M	Metal
Me	Methyl
min	Minute(s)
mol	Mole(s)
MOR	Methanol oxidation reaction

MWCNT	Multi-walled carbon nanotube
NPs	Nanoparticles
Nu	Nucleophile
OAm	Oleylamine
ORR	Oxygen reduction reaction
PAMAM	Polyaminoamide
Ph	Phenyl
POM	Polyoxometalate
Pr	Propyl
py	Pyridine
QE	Quantum efficiency
rGO	Reduced graphene oxide
rt	Room temperature
s	Second(s)
SWCNT	Single-walled carbon nanotube
THF	Tetrahydrofuran
TOF	Turnover frequency
V	Volt
VB	Valence band
WOR	Water oxidation reaction

1 Introduction

Careful tuning of the nature of the supports used for dispersing the catalytic active phases has become an indispensable tool to obtain active and stable heterogeneous catalysts. The type of support used, its properties, and its interactions with the specific catalytic system are all important factors that influence the chemical reaction to be catalyzed.

In general terms, supports can be classified into two main groups:

1. Inert supports, meaning that they are inert under the reaction conditions and simply supply a better structural environment for the actual catalyst;
2. Active supports, when they play a more complex role to improve the catalysis very much or even allow new or alternative chemical transformations to take place.

The first class of supports comprises traditional inorganic materials such as SiO_2 and Al_2O_3, amorphous carbon, transition metal oxides such as ZrO_2, and various zeolites. The second group typically contains reducible oxides such as TiO_2, CeO_2, Fe_2O_3, etc., even if their classification as active supports also depends on the specific application. The major structural benefit offered by using supports is their ability to provide high dispersion of the active phase of the catalyst (supported molecular catalyst, metal nanoparticles, or metal oxides) as a consequence of the generally high and stable surface area that they possess. High dispersion of catalysts usually results in improved activities and stability, with influence also on the selectivity.

A second important parameter to be considered is the porosity of the material used as support. Although mass transfer processes can be neglected in homogenous systems, they become a serious limitation in reactions where reagents, products, and catalysts are present in different phases. In particular, the active species is usually located within confined zones (i.e., pores) of the catalyst. Since the reagent and the active species need to be in contact with each other for the chemical transformation to take place, the kinetics of the reaction are heavily dependent upon the diffusion rate of the reagents into the pores (as well as of the products out of the pores) to reach the active site. Such diffusion, in particular for liquid–solid phase catalysis, can be as slow as to constitute the rate-limiting step. Pores size can be fine-tuned to control the accessibility of reagents and, in turn, the chemical selectivity when two or more competing reactions take place. Appropriate choice of support allows for tailoring the porosity of the resulting catalytic systems and, in turn, the rate and selectivity of the catalytic process.

Where the structural role of catalytic supports has been well known and exploited for some time, in recent years the development of systems where the supports exert a more active function than simply being a structural scaffold has been the subject of extensive research. The discovery of systems where the active phase of the catalysts (a molecular entity, a metal oxide species, or a metal nanoparticle) and the supports interact in a more intimate manner has given rise to more complex mechanisms of action, which can lead to unseen chemical or physical behaviors and, in turn, to unexpected reactions. Often, the term *hybrid* is used to describe these functional materials where the properties of the support and those of the actual catalytically active center are merged to afford brand new properties not necessarily related to the two individual components.

The steady proliferation of reports on novel catalytic systems featuring such active supports keeps opening new dimensions, thus expanding the range of reactions that heterogeneous catalysis may offer. Whether or not we have just witnessed the dawn of a new era in catalysis-related materials chemistry, carbon nanostructures stand alone as the undoubted protagonists of the major recent breakthroughs in this field. Their high surface area, mechanical and thermal stability, and tunable topography, combined with their fascinating electronic properties, make them outstanding and often superior supports in heterogeneous catalysis. In particular, graphene (G) and carbon nanotubes (CNTs) are the two most investigated carbon nanostructures, although others such as carbon nanohorns (CNHs) and carbon nanofibers (CNFs) are gaining some popularity. All these nanomaterials share the common feature of a fused polyaromatic structure that is organized into different shapes and geometries at the macromolecular level.

The idea of using carbon-based supports for heterogeneous catalysis is not new, given the vast utilization of amorphous carbon (i.e., carbon black) to disperse the active species efficiently. However, as briefly mentioned earlier, the possibility of combining and merging the exceptional properties of these carbon nanomaterials with those of the catalysts has opened up a terrific range of new options. Moreover, tests have shown higher stability and longer term durability of carbon nanostructures under several catalytic conditions, such as in electrocatalysis for oxygen reduction in fuel cells, where instead carbon black tends to be subject to morphological changes, ultimately leading to catalyst aggregation [1].

One more promising asset of using carbon nanostructures in catalysis relates to their applicability as removable templates for the synthesis of metal particles. Carbon nanotubes have been predominantly scrutinized for this function; they can efficiently induce the growth of particles with selected size, morphology and porosity. As CNTs can oxidize below the melting points of many metals or metal oxides, they can in principle be removed by high temperature oxidation in case their presence is not desirable for the specific catalytic purpose. In this regard, a pioneering work described how to obtain nanotubes-vanadium oxide composites by annealing mixtures of partially oxidized carbon nanotubes and V_2O_5 powders in air. The vanadium oxides uniformly coated the external part of the tube, forming thin crystalline sheets, together with intercalation inside the tubes. The carbon component was then partially eliminated by oxidation, leaving behind layered oxide fibers of desired widths [2].

There is ample scope for reactions where carbon nanostructure-supported catalysts can be applied, ranging from standard organic hydrogenations/oxidations, or C–C cross-couplings (e.g., Suzuki–Miyaura and Heck reactions), to electrocatalysis for fuel cells or biomass conversions, or even photocatalytic processes (e.g., water splitting to generate hydrogen and oxygen or contaminant photodegradation in self-cleaning products).

The purpose of this chapter is to highlight the impact of this emerging new class of materials in the field of heterogeneous catalysis. In particular, current accessibility to carbon nanostructure-inorganic hybrids will be outlined, and their properties and catalytic performance discussed as a function of the carbon support/metal catalyst interaction. Due to the vast number of existing studies on this topic, this chapter is not meant to be an exhaustive list of all reported reactions. Our aim is rather to identify current and future trends for the use of these hybrid systems in chemical transformations, especially where prospects are more encouraging. Our discussion will be organized according to the specific carbon nanostructure used as catalytic support.

2 Graphene

Graphene (G) is a planar single sheet of graphite. It is currently seen as the new frontier of nanomaterials research, and its use in heterogeneous catalysis holds great promise. Electrocatalysis and photocatalysis seem to benefit particularly from the properties of this carbon support, and thus these two types of catalysis will be discussed in more detail herein.

It is common practice to consider as graphene even structures composed of a few carbon layers (maximum 10) stacked together, since they exhibit very similar properties to individual G sheets. However, the unique properties offered by G decline with the increase in the number of layers, as the structure approaches that of three-dimensional (3D) graphite.

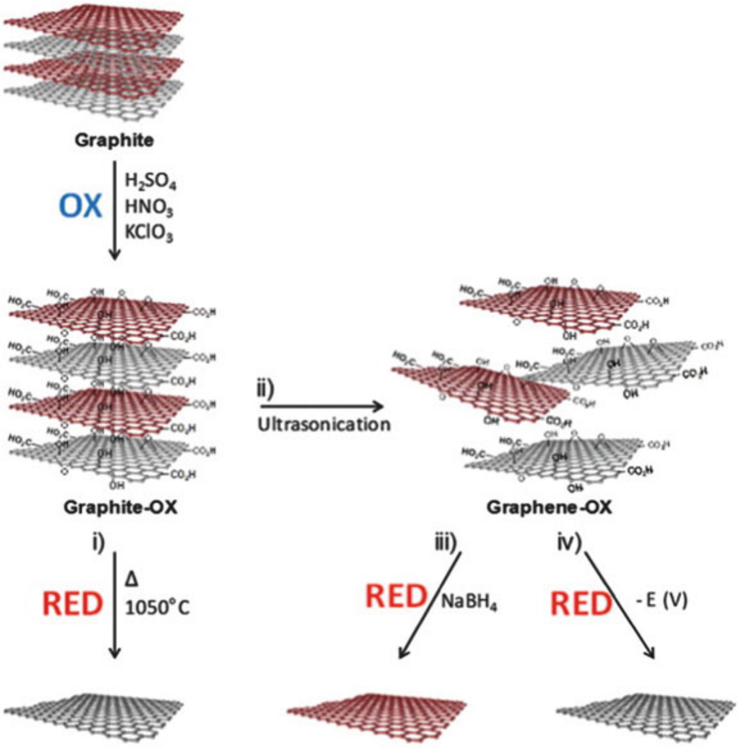

Fig. 1 Single sheets of graphene can be obtained from graphite via oxidation (OX), exfoliation (i.e., by ultrasonication), and reduction (RED). Reprinted from [124], Copyright (2012), with permission from Elsevier

Conductivity of graphene and its transparency are important attributes. Its electronic features are particularly fascinating, with graphene showing ambipolar electric field effects: depending on the applied electric field (i.e., positive or negative), charge carriers can be holes or electrons, with mobility that can exceed 15,000 $cm^2\ V^{-1}\ s^{-1}$ [3].

However, the great potential of graphene is counterbalanced by the challenges posed by its practical use. One serious limitation, for instance, is its strong tendency towards aggregation due to the very efficient π-stacking of graphene planes; as a result, its dispersibility in organic or aqueous solvents is dramatically reduced. There are a number of methods to afford isolation of a graphene single sheet (or a few G sheets). As of today's state-of-the-art, the simplest and most used method is chemical functionalization via graphite oxidation, followed by exfoliation (Fig. 1). Oxidation is usually performed with strong oxidants, such as HNO_3, $KMnO_4$ and H_2SO_4. Subsequent ultrasonication allows for exfoliation and gives access to graphene oxide (GO), a nanosheet of graphene containing a range of functionalities (e.g., carboxyl, epoxide, and hydroxyl groups). Finally, GO can be reduced by several species (e.g., $NaBH_4$, hydrazine, and hydroquinone) to afford graphene, with partial re-establishment of the original G structure, and its unique electronic and optical properties. The reason why oxidation is a convenient pre-step to preparing graphene is at least dual: first, introduction of functional groups disrupts the conjugated aromatic pattern, generates local sp^3 hybridized carbon atoms, and reduces π–π interactions, thus allowing for easier exfoliation and dispersion in liquid media; second, the so-introduced oxygen-containing functionalities are capable of binding cationic metal species, favoring nucleation and growth of metal nanoparticles on the G surface.

An interesting alternative is to use the metal precursor as both catalyst reagent and GO reductant in order to have a concerted single-step synthesis. For example, $SnCl_2$ and $TiCl_3$ were used as reducing agents to generate G from GO, while yielding G decoration with SnO_2 and TiO_2, respectively, for subsequent applications [4].

2.1 Electrochemical Reactions

Electrochemical catalysis is at present one of the two most explored areas for real graphene applications. In particular, reports are proliferating on the advantages of using G in the assembly of fuel cells and lithium ion batteries.

Fuel cells (FCs) are electricity-producing devices that exploit oxidation of fuel (generally methanol) at the anode and reduction of oxygen at the cathode. On account of the “greener” technology associated with FCs in comparison with conventional energy conversion systems, many attempts are being made to increase their performances for market development. Above all, sluggish kinetics of the oxygen reduction reaction (ORR) constitutes a major hurdle, especially when attempting to use in low operating temperatures.

ORR is generally catalyzed by platinum (Pt) or its alloys (Fig. 2), and additional drawbacks for fuel cells implementation relate to the high cost and relatively low availability of Pt and its relatively low durability under the conditions used in some types of FCs (poisoning due to CO chemisorption). For this reason, maximization of Pt nanoparticles active area and creation of more robust systems are both desirable avenues, since they ultimately lead to lower metal loading and longer durability. In particular, G has been extensively investigated as catalyst support, due to its robustness, relative chemical inertness, and a high theoretical specific surface area (~2,600 m^2/g) [5]. Furthermore, the etching off of the metal nanoparticles from the support does not seem to be a key issue with G; on the contrary, etching off often occurs under acidic conditions when employing conventional carbon supports, and this leads to catalyst deterioration. Preparation of 2-nm Pt NPs uniformly dispersed on G displayed higher activity and better stability than the commercially available *E*-TEK C/Pt catalyst [6].

One emerging option is to introduce another metal into the Pt-G system to achieve geometrical and electronic adjustment of Pt nanoparticles, yielding

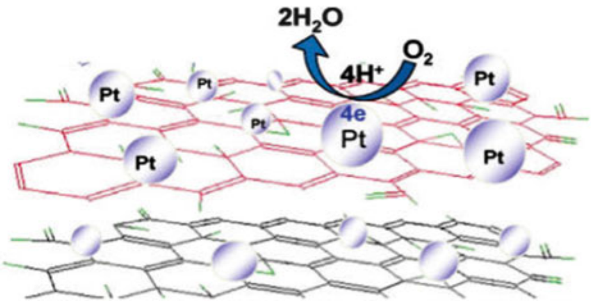

Fig. 2 Schematic representation of oxygen reduction reaction (ORR) catalyzed by platinum (Pt) nanoparticles supported on graphene sheets, the so-called Pt–G system. Reprinted with permission from [12]. Copyright 2009 American Chemical Society

enhanced catalytic activity. For example, solution phase self-assembly of bimetallic FePt NPs on graphene exhibited better performance both in terms of activity (1.6 mA/cm^2 at 0.512 V and 0.616 mA/cm^2 at 0.557 V) and stability (no change after 10,000 potential sweeps) for the ORR in 0.1 M $HClO_4$. The authors related the improved activity to the close contact between the FePt NPs and the graphene layers, as this promotes the polarization of the p-electrons and thus facilitates oxygen adsorption and activation on the bimetallic surface [7].

Liu and co-workers addressed some of the drawbacks associated with carbon-supported electrodes for the ORR in polymer electrolyte membrane (PEM) fuel cells. Such limitations include long term vulnerability to corrosion under oxidative conditions and the decrease of the active surface area of the catalyst following agglomeration of the metal nanoparticles on the carbon support. A possible solution to these existing issues is first to combine the G support with a transition metal oxide, for subsequent dispersion of nanoparticles made of a second metal. The authors carried out growth of indium tin oxide (ITO) nanocrystals on G sheets, and later used this hybrid system as a support for Pt NPs. The system takes advantage of both greater stability of the oxide and exceptional G surface area. It is not surprising that the combination of these two features yields excellent catalytic performance and durability. Moreover, the type of interaction between the three different species (i.e., ITO, G, and Pt NPs) was studied both experimentally and by modelling (DFT) showing an unprecedented triple junction structure, which endows the Pt nanoparticles with additional stabilization (Fig. 3) [8].

The strategy of assembling ternary materials of the type Pt-X-graphene (where X can be either an inorganic or an organic material) is expected to become more and more popular in the near future. A few systems of this kind have already been made, including Pt–TiO_2–G [9], Pt-lucigenin-G [10], and Pt-pyrogallol-G [11].

Kamat et al. assembled electrodes based on Pt nanoparticles deposited on GO and studied their electrocatalytic performance in proton exchange membrane (PEM)-based fuel cells. In this study they compared the GO-Pt catalyst with the same catalyst pre-treated with hydrazine (to allow for partial restoration of the sp^2 G network), followed by annealing at 300°C to remove the excess of hydrazine from the electrode surface. This treatment results in an 80% enhancement of the electroactive surface area (ECSA) as compared to untreated GO-Pt. ECSA is an important parameter to help evaluate the effectiveness of charge transfer onto and

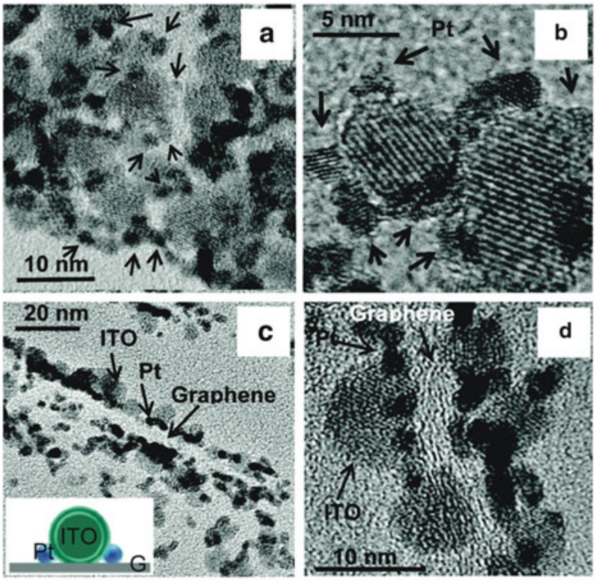

Fig. 3 TEM images showing the intimate contact between graphene (G), ITO, and Pt NPs (**a**, **b**), and the cross section TEM images of Pt–ITO–graphene (**c**, **d**). *Inset*: The schematic structure of Pt–ITO–graphene nanocomposite. Adapted with permission from [8]. Copyright 2011 American Chemical Society

from the electrode surface. The re-aggregation induced by the reduction process was to some extent minimized by the dispersed metal nanoparticles [12]. The experiment is somehow in agreement with the widespread view that regeneration of G skeletal polyaromaticity and therefore conductivity is of key importance to improve catalytic efficiency.

In light of the need for more cost-effective FCs, it is not surprising that catalytic systems based on cheaper transition metals are being highly sought after. At present, the use of alternative transition metals appears restricted to FCs working under alkaline conditions, where ORR is more facile and metal catalysts are more stable. Cobalt is one of the most promising candidates, particularly when used in the oxide form. Monodispersed Co/CoO core shell nanoparticles (where the CoO layer envelops a Co core) have been deposited on G through self-assembly, and the activity for the reduction of oxygen in alkaline conditions (0.1 M KOH) was shown to be high, and dependent on the interaction between the carbon surface and the Co/CoO NPs, as well as the tuning of the relative Co and CoO core-shell dimensions [13]. Co_3O_4, which by itself is a poor catalyst for ORR, when used as a hybrid with mildly oxidised G, reveals itself to be a high-performing bi-functional catalyst for both ORR and the reverse oxygen evolution reaction (OER). This is an important finding for the construction of self-regenerative FCs. When compared with Pt/C, this system is capable of holding stable currents for a longer time, and the decay was shown to be very little for over 2 weeks. Although the mechanism remains unclear, the active site is presumably the Co metal at the interface with graphene [14].

For other Co derivatives, such as sulfides or selenides, activities were generally reported to be much lower than Pt-based systems, and the reduction of oxygen has a preferential two-electron pathway, while for Pt and other metal catalysts the

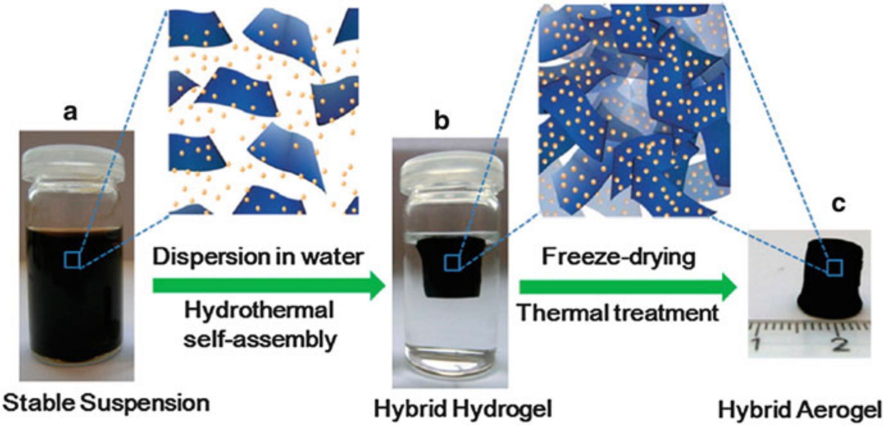

Fig. 4 Fabrication process for the 3D Fe_3O_4/N-GAs catalyst. (**a**) Stable suspension of GO, iron ions, and PPy dispersed in a vial. (**b**) Fe- and PPy-supporting graphene hybrid hydrogel prepared by hydrothermal self-assembly and floating on water in a vial, and its ideal assembled model. (**c**) Monolithic Fe_3O_4/N-GAs hybrid aerogel obtained after freeze-drying and thermal treatment. Reprinted with permission from [17]. Copyright 2012 American Chemical Society

reaction proceeds via a more efficient four-electron pathway. However, a $Co_{1-x}S$/graphene hybrid has been recently prepared through controlled synthesis, where the conductive G layer electrochemically couples the Co sulfide NPs and modulates their growth, resulting in a much enhanced activity [15]. This example reinforces the concept of G conductivity as key feature of efficient hybrid systems. In addition, a high surface area facilitates mass transfer into the catalysts, and thus the support helps with the collection and transfer of electrons to the electrode surface. Studies have shown that charge transfers across the interface between the metal and the G layer, and this occurs upon a certain range of G–metal spacings and of Fermi levels of the two individual moieties. In another instance, Au clusters were grown on reduced GO via a so-called "clean" method, which excludes the presence of additional protecting/reducing molecules; the final hybrids possess exceptional activity for the ORR [16].

Doping of G constitutes another tool to increase catalytic activity. For instance, N-doped G was used as a support for the deposition of Fe_3O_4 NPs. The synthetic method allowed for uniform deposition of the metal NPs, with an interconnected macroporous framework of G sheets. The crucial step is the hydrothermal self-assembly at 180°C, which yields to controlled nucleation and growth of the Fe_3O_4 NPs with simultaneous incorporation of polypyrrole species that causes the N-doping (Fig. 4) [17].

Because the electrocatalytic reduction of oxygen constitutes the bottleneck for the assembly of FCs, a great deal of research has focused on this reaction. However, enhancing catalytic activity for the methanol oxidation reaction (MOR) that occurs at the anode of FCs is equally desirable. The same considerations as in the ORR case are valid here, with the synergistic effects between metal catalyst and support affording

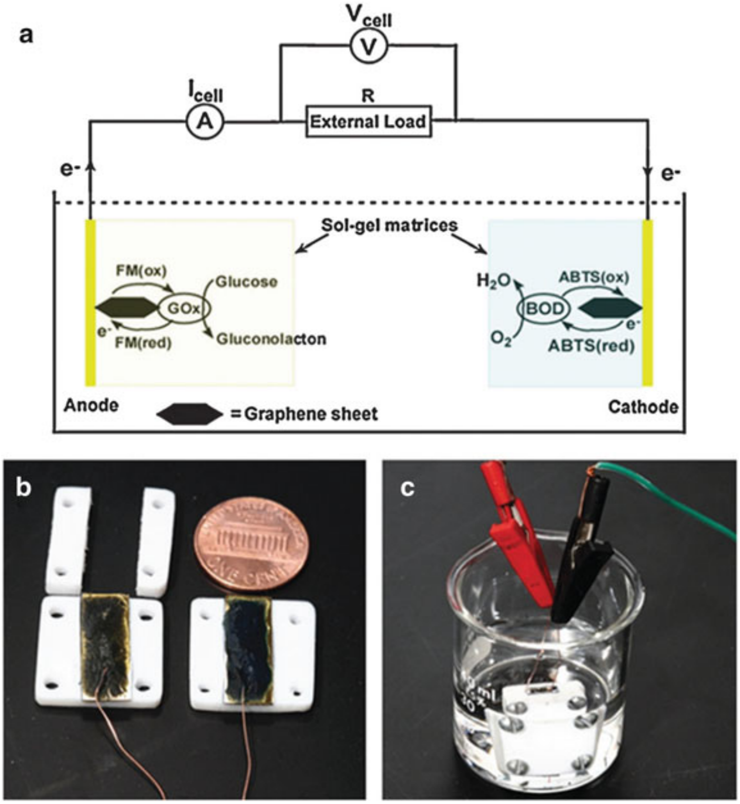

Fig. 5 (**a**) Membrane-less enzymatic BFCs (EBFCs) composed of glucose oxidase (GOD) and bilirubin oxidase (BOD) as anodyc and catodic enzymes, respectively, on a G support, (**b**) EBFC test setup, (**c**) schematic configuration of the membrane-less EBFC. Reprinted from [24], Copyright (2010), with permission from Elsevier

higher performances than commercial catalysts. Once again, Pt stands out as the most active and frequently used metal, and a number of research groups have devised synthetic strategies to prepare G–Pt hybrids to catalyse MOR [18–20]. Bimetallic systems have also been prepared featuring Pt–Ru [21] and Pt–Pd [22].

Systems using metals other than platinum have been used for FC applications for the hydrogen evolution reaction (HER). MoS_2 appears to be an excellent catalyst for this reaction; its combination with G supports has been studied, and the high activity of the resulting hybrid was attributed to the strong chemical and electronic coupling between the carbon support and the catalyst [23].

An intriguing opportunity arises from the use of G in biofuel cells (BFCs), where one of the two electrodes features an enzyme-based catalyst. BFCs are emerging as an intriguing power source for medical appliances, and their miniaturization to the nanoscale is a requirement for their in vivo use at cellular level. Li et al. used G as a support for the preparation of membrane-less enzymatic BFCs (EBFCs) composed of glucose oxidase (GOD) and bilirubin oxidase (BOD) as anodic and cathodic enzymes, respectively (Fig. 5). The catalytic efficiency of the system was compared to that of the hybrid which uses SWCNTs as a support (instead of G), showing a twice as high efficiency for the G-based cell [24]. Similarly, Zheng and co-workers used G matrices for the assembly of BFCs consisting of GOD and lactase as electrodes [25].

Improvement of the performance of lithium ion batteries (LIBs) represents the second realm of electrocatalysis where the use of G is being extensively explored. The challenges faced today for the assembly of efficient LIBs lie in the slow diffusion of the Li^+ ions and the low electron transport at the electrodes. Moreover, some of the electrodes suffer from the large volume change during Li^+ insertion and extraction, and this causes cracking or other physical damage, and ultimately the electrical disconnection of the catalyst from the collector. Finally, when the batteries work at high charge/discharge rates, the resistance at the interface between the electrode and the electrolyte is increased, with fewer and fewer available sites for entrance/exit of the Li^+ ions as the reaction proceeds.

Many electrodes are being designed (typically metal oxides such as TiO_2, SnO_2, metals, metal phosphides, etc) with the aim of overcoming these obstacles, in pursuit of a more efficient electron and Li-ion transport, and to alleviate volume changes and agglomeration by increasing the porosity of the electrode. Carbon materials, and graphene in particular, seem to fulfill this role very well, and efforts currently focus on the integration of G to form hybrid nanostructured electrodes. Several examples are already available in the literature, generally presenting G hybrids with metal oxides. For instance, a considerable enhancement of the Li insertion/extraction processes in LIBs takes place when using G as a conductive additive in combination with electrocatalytically active TiO_2 [26]. Similarly, preparation of SnO_2/G composites exhibited very high reversible specific capacity, possibly explained in terms of first, the high BET specific surface area that increases electrochemical activity and renders (1) partially reversible, second, the protection exerted by the intercalating G sheets that prevent direct contact and therefore agglomeration of SnO_2 during charge/discharge, third, the porous structure of G that acts as a buffer for the volume changes during Li insertion/extraction, and fourth, the conductivity of G that facilitates charge transport [27, 28]:

$$SnO_2 + 4Li^+ + 4e^- \rightarrow 2Li_2O + Sn \tag{1}$$

Synergistic effects between the conductive G support and the active metal oxide and maximization of the electrochemically active area were also invoked for the G/Co_3O_4 hybrid, which showed higher performance than the isolated G and Co_3O_4 in terms of charge/discharge capacities (Fig. 6) [29].

As for FCs, ternary systems represent one of the latest trends in research for the manufacture of LIBs electrodes. As a representative example, the preparation of Fe_3O_4–SnO_2–G hybrid is reported to have shown a higher performance than the binary systems composed of either Fe_3O_4–G or SnO_2–G. The results are explained by the authors as a consequence of the excess of Li_2O formed (see (2)) that helps

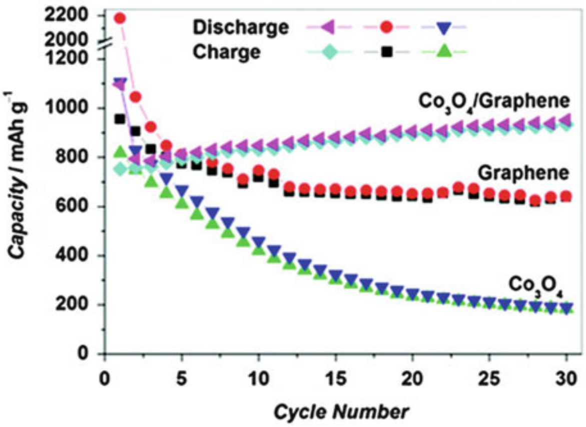

Fig. 6 G/Co_3O_4 hybrid showed higher performance than the isolated G and Co_3O_4 in terms of charge/discharge capacities. Adapted with permission from [29]. Copyright 2010 American Chemical Society

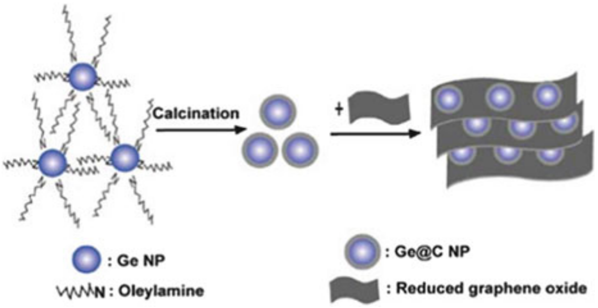

Fig. 7 Catalytic Ge NPs are protected from agglomeration by a shell of oleylamine prior to their dispersion on G sheets. Reprinted with permission from [31]. Copyright 2012 American Chemical Society

recovery of the Fe to improve the oxidation process (see (3)); introduction of the Fe_3O_4 seems to play a role in the decrease of the initial irreversibility of the capacity [30]:

$$SnO_2 + 4Li^+ + 4e^- \leftrightarrow 2Li_2O + Sn \quad (2)$$

$$3Fe + 4Li_2O \leftrightarrow 4Fe_3O_4 + 8Li^+ + 8e^- \quad (3)$$

Assembly of ternary systems has also been exploited to prevent agglomeration of the catalyst NPs by protection with appropriate shells before decoration on G sheets. Guo et al. reported the ingenious protection of germanium with carbon shells (C) from oleylamine and successive dispersion on G (Fig. 7) [31].

A similar strategy has been used for the preparation of other electrodes, such as SnO_2–C–G [32] and $LiFePO_4$–C–G [33]. An alternative approach uses the 3D hierarchical $LiFePO_4$–G hybrid prepared via a template-free sol–gel method; this system also showed improved kinetics for the insertion/extraction of Li-ions [34].

One final application worth mentioning relates to the possibility of employing G as a dynamic support for electrocatalytic water oxidation reaction (WOR). This reaction represents the half-reaction of a process called "water splitting" (see (4)), which is undoubtedly one of the most important reactions in modern applied chemistry:

$$2H_2O \rightarrow 2H_2 + O_2 \tag{4}$$

Water splitting is employed in photosynthesis, the light-induced conversion of carbon dioxide and water into sugar and dioxygen, as a renewable multi-electron source. Due to the multi-electron pathway, oxidation of water ($2H_2O \rightarrow O_2 + 4H^+ + 4e^-$; $E^0 = 1.23$ V vs NHE), is a thermodynamically and kinetically unfavored process, which poses severe challenges to its implementation. A great deal of effort is currently being made to develop electrocatalysts that can effect water oxidation smoothly, and carbon nanotubes come across as very promising components to enhance activity of the catalytic systems.

Electron transport and accumulation across the 2D π-conjugated framework has been shown to facilitate the WOR in a graphene-tetraruthenium polyoxometalate (Ru_4POM) hybrid. This catalyst features a ruthenium-oxo core, that mimics the natural oxygen evolving center of the photosynthetic II enzyme [35], since both cores are constituted by four redox active transition metals, connected through μ-oxo or μ-hydroxo bridges [36, 37]. Moreover, the tetraruthenium core can be considered as a fragment of ruthenium oxide, mounted into a molecular totally inorganic scaffold [38].

The assembly of the hybrid is particularly ingenious (Fig. 8), as it does not sacrifice the electronic properties of G by its prior oxidation; instead, it involves G covalent modification directly via 1,3-dipolar cycloaddition, followed by a two-step sequence to attach a first generation polyaminoamide (PAMAM) dendron. Finally, the Ru_4POM units are bound via a combination of electrostatic and hydrogen bond interactions. Confinement of the inorganic moieties into the flat zones of the G support, as well as the multilayered structure, results in the modulation of kinetics for the electron transfer process. Notably, the turnover frequency for the water oxidation electrocatalysis (WOC) is one order of magnitude higher than that for the bare catalyst [39].

2.2 *Photochemical Reactions*

The semiconductivity of G makes it a highly advantageous support for photocatalytic processes [40]. In recent years, emphasis has been placed on the use of such processes for solar energy and environment protection applications.

Photoactive materials include semiconducting metal oxides (e.g., TiO_2, ZnO, WO_3, Bi_2WO_4) or other metal derivatives (i.e., CdS) that have structures ensuring the presence of a filled valence band (VB) and an empty conduction band (CB). The general mechanism of action for photo-driven processes evolves from the generation of electron–hole pairs: following excitation by a photon $h\nu$ of appropriate energy that matches (or exceeds) that of the VB-CB band gap, the electron is moved into the conduction band, leaving a hole in the valence band. These charge carriers, however, are unstable, as the electron and the hole tend to recombine quickly and dissipate

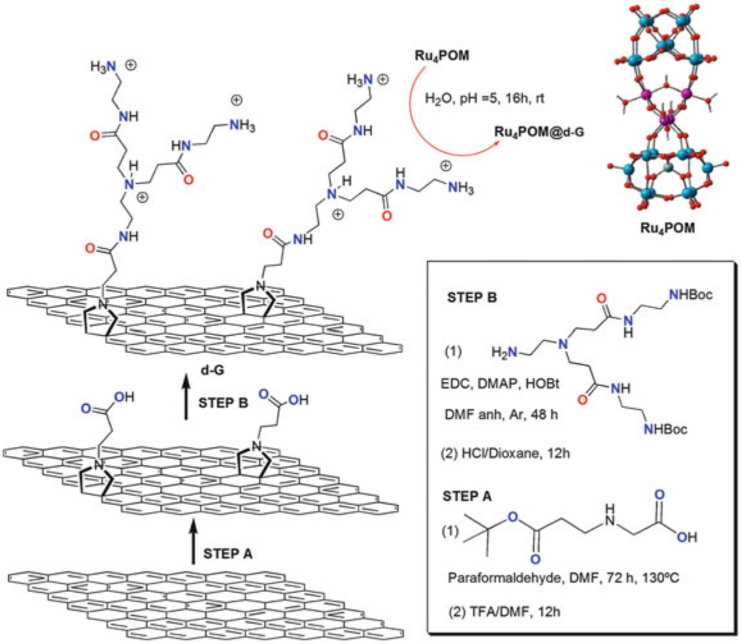

Fig. 8 Covalent modification of G via 1,3-dipolar cycloaddition allows for the supramolecular anchorage of the negatively charged water oxidation catalyst Ru4POM by electrostatic forces and hydrogen bonding provided by the positively charged PAMAM dendrons on the G surface. Reprinted with permission from [39]. Copyright 2013 American Chemical Society

heat, thus lowering the efficiency of the photocatalytic materials, posing a limit to their practical application. Hence, discovery of materials where the recombination of the charge carriers can be delayed (or even suppressed) has become a key objective for photo-catalysis, in particular concerning energy research.

One of the strategies commonly adopted to reach an efficient separation of the photo-induced electron–hole pair is to combine different materials, including other semiconductive metal oxides, or noble metal NPs, or nano-carbon conjugates. Indeed, carbon-based supports, typically carbon nanotubes, can be employed with this aim. In this case, the improvement in catalytic activity derives from the electronic properties of CNTs, in terms of light collection and conversion, high surface area or controlled functionalization, and finally their ability to tune the morphology of the photo-active material upon strategic assembly methods. For similar reasons, G has been extensively scrutinised, and its role in the functioning of photocatalytic systems has been the subject of many in-depth studies.

We mentioned in the previous section the importance of the water splitting reaction as a crucial step in artificial photosynthesis finalized to solar light storage, and how the water oxidation half-reaction constitutes the bottleneck for this process. However, considered in its entirety, water splitting is also one of the cleanest and most cost-effective methods of hydrogen production. There are massive expectations on

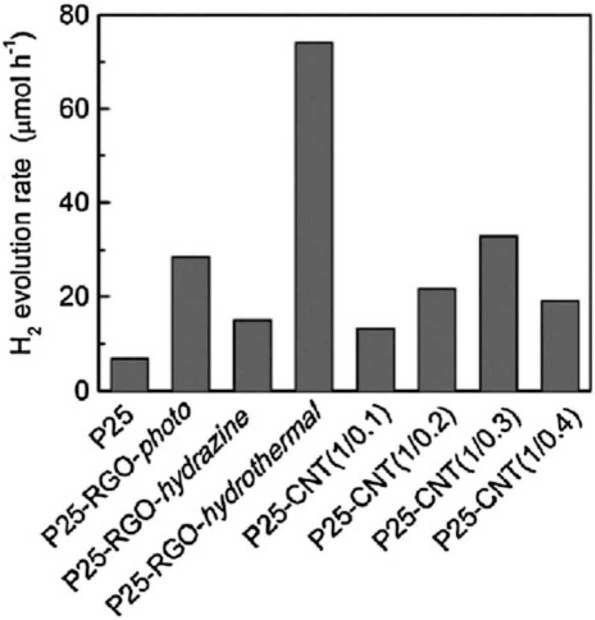

Fig. 9 Hydrogen evolution from methanol aqueous solutions catalyzed by TiO_2–GO composites, under different methods of GO reduction (i.e., hydrazine, UV-assisted, sol–gel, hydrothermal). Reprinted with permission from [42]. Copyright 2011 American Chemical Society

molecular hydrogen as a future alternative and environmentally friendly energy vector, so that photocatalytic hydrogen evolution reaction (HER) has naturally attracted much attention.

Typical semiconductor catalysts employed for this purpose are based on TiO_2 and their integration on G sheets has been studied to evaluate changes in catalytic performance. A series of TiO_2/G composites with varying G contents were prepared via sol–gel methods; in particular, samples with 5 wt% G content exhibited the highest activity for photocatalytic hydrogen evolution under visible light, exceeding that of the reference catalyst P25. Interestingly, higher G percentages produced detrimental effects, probably because electron/hole recombination centers were introduced into the composite. Moreover, the catalyst activity was sensitive to calcination conditions used to prepare the final catalyst, with better activities observed when calcination was carried out under nitrogen [41].

Another study (Fig. 9) tackled hydrogen evolution from methanol aqueous solutions, catalyzed by TiO_2–GO composites, under different methods of GO reduction (i.e., hydrazine, UV-assisted, sol–gel, hydrothermal). This study highlights the significance of restoring (at least partially) the original G conducting properties for photocatalytic purposes [42].

Integration of G was also attempted in the nitrogen-doped $Sr_2Ta_2O_7$, one of the catalysts with the highest performance known to date, and activity for HER turned out to be increased under solar radiation. When G was used to support a Pt co-catalyst, the evolution of hydrogen from water splitting with $Sr_2Ta_2O_{7-x}N$ reached an outstanding rate of 293 µmol/h with 280–550 nm radiation and a quantum efficiency (QE) of 6.45%. As a comparison, for the same system

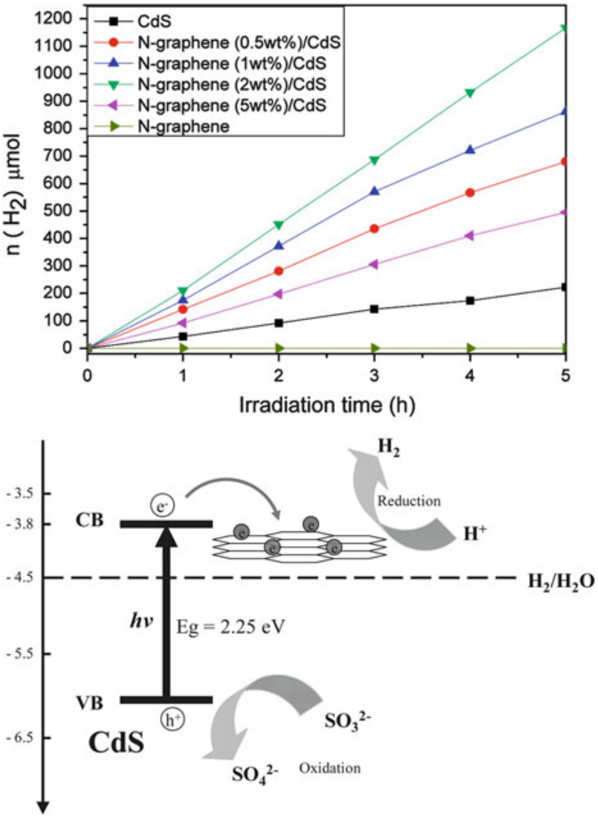

Fig. 10 H_2 evolution of CdS, *N*-graphene/CdS composites with different contents of *N*-graphene (*top*). The energy level diagram for *N*-graphene/CdS nanocomposites in relation to the redox potentials for water spitting process (*bottom*). Reprinted with permission from [44]. Copyright 2011 American Chemical Society

without G, values of 194 μmol/h with a QE of 4.26% were achieved under the same conditions [43]. Enhanced activities (fivefold) with respect to the isolated benchmark catalyst CdS were also observed with the addition of 2 wt% of N-doped G into the system (Fig. 10, top). The authors explained the increase in activity as a consequence of the G/G^{-} potential, being lower than the CB of CdS, but higher than the reduction potential of H^{+} (Fig. 10, bottom). This yields a more favoured electron transfer from the CdS conduction band into the G layer, and an easier reduction of H^{+}, leading to faster rates of H_2 evolution [44].

The electron transfer from semiconducting TiO_2 into reduced graphene oxide (rGO) after photoexcitation has been studied and it was demonstrated how the G layer can shuttle the electrons across the π network and converge them into a second catalyst (in the reported study Ag) to carry out a reduction reaction (Fig. 11) [45]. In practice, G acts as a two-dimensional conductive support that anchors two different catalyst particles and efficiently suppresses recombination of the charge carriers.

This scenario is of importance for several photocatalytic processes, especially for the assembly of ternary systems. For example, synthesis of TiO_2 NPs on a layered MoS_2–G hybrid gives rise to a TiO_2–MoS_2–G ternary system with exceptional photocatalytic activity for the water splitting reaction (Fig. 12). The

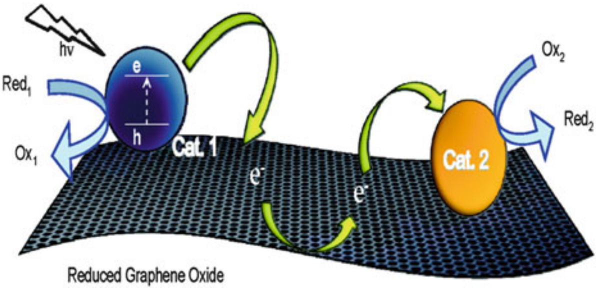

Fig. 11 After photoexcitation of TiO_2 (*blue*) on a graphene support (*gray mat*), electrons are shuttled across the π network from the TiO_2 catalyst onto a second catalyst (*yellow*) where they participate in a reduction reaction. Reprinted with permission from [45]. Copyright 2010 American Chemical Society

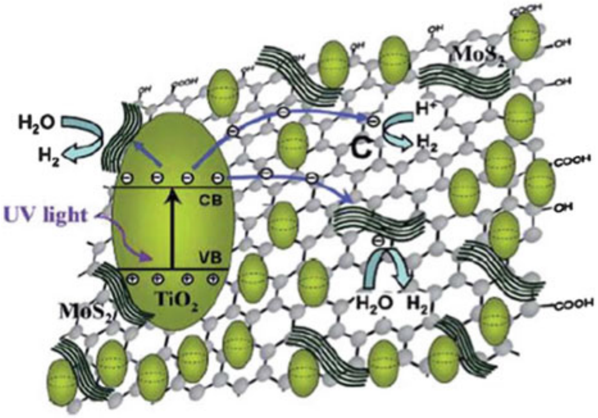

Fig. 12 TiO_2-MoS_2-G ternary system has exceptional photocatalytic activity for the water splitting reaction. Reprinted with permission from [46]. Copyright 2012 American Chemical Society

mechanism is based on the transfer of electrons from TiO_2 through the graphene planes into the MoS_2 nanosheets, where they react with the adsorbed H^+ cations to generate H_2 [46].

Photocatalysis is also becoming a more and more popular strategy for the degradation of air and water pollutants. As for the water splitting reaction, TiO_2 is one of the most studied catalysts for reasons related to its low toxicity and high photocatalytic activity. Its combination with other materials (e.g., noble metals, other metal oxides, and CNTs) has been under the research spotlight for some time. Synthesis of TiO_2-G hybrids is now emerging as an extremely promising material for the photocatalytic degradation of organic pollutants and water remediation.

Li et al. synthesised P25 TiO_2-G via hydrothermal methods and tested it in the degradation of methylene blue (MB). The system exhibited high adsorption of dyes due to the aromatic regions of G, which mediate favourable stacking interactions with MB; moreover, transparency of G and the Ti–O–C bonds translates into an extended light absorption range, with a more efficient light utilization by the catalyst; finally, the separation of the e^-/h^+ charge carriers is very efficient because of the excellent properties of G as charge acceptor. The combination of all these effects affords a considerable enhancement of the rate of degradation of MB as compared to the pristine material [47].

Suppression of charge recombination in MB degradation (catalyzed by TiO_2 nanorods-GO composites under UV irradiation) appears to be linked to the reaction between GO electrons and adsorbed O_2, with the pollutant being degraded by the produced hydroxyl radicals. The process is outlined in the equations below:

$$\mathrm{TiO_2} + hv \rightarrow \mathrm{TiO_2}(\mathrm{e}^- + h^+) \tag{5}$$

$$\mathrm{TiO_2}(\mathrm{e}^-) + \mathrm{Graphene} \rightarrow \mathrm{TiO_2} + \mathrm{Graphene}\ (\mathrm{e}^-) \tag{6}$$

$$\mathrm{Graphene}\ (\mathrm{e}^-) + \mathrm{O_2} \rightarrow \mathrm{Graphene} + \mathrm{O_2}^- \tag{7}$$

$$\mathrm{TiO_2}(h^+) + \mathrm{OH}^- \rightarrow \mathrm{TiO_2} + \cdot\mathrm{OH} \tag{8}$$

$$\cdot\mathrm{OH} + \mathrm{Pollutants} \rightarrow \mathrm{Degradation\ products} \tag{9}$$

Design of alternative synthetic methods led to the preparation of highly efficient TiO_2 nanorods-G systems. The synthesis addressed the formation of small size TiO_2 nanocrystals, which possess large surface area and high quantum size effect, on the entire G sheet, whereas previous syntheses could only deposit limited amounts of the titanium oxide NPs confined to the edges of G. The as-prepared composites showed significantly higher efficiency for MB degradation and their formation relied on a water/toluene two-phase self-assembly (Fig. 13), a process that the authors also claimed to be reproducible for other non-polar organic-soluble nanocrystals [48].

Although TiO_2 has been the most studied catalyst, other semiconductor oxides have been investigated in the formation of hybrids with G for the degradation of various organic pollutants. For example, the system SnO_2-G can even outperform the analogous system with TiO_2 in the degradation of rhodamine B (RhB) in water under visible light. This method exploits the thermodynamically more favoured electron transfer from RhB* to SnO_2, as a consequence of the large potential difference between the RhB* and SnO_2 [49]. The same reaction was studied for the Bi_2WO_6-G system (Fig. 14), and the authors attributed the enhanced activity to the interaction and charge equilibration between G and Bi_2WO_6; this leads to lowering of the Fermi level of G-BWO, and to a high migration efficiency of photoinduced electrons, and thus to effective suppression of charge recombination and in turn to oxygen reduction [50]. Other catalysts include ZnO–graphene [51], $InNbO_4$–graphene [52], and Ag/AgBr/GO [53].

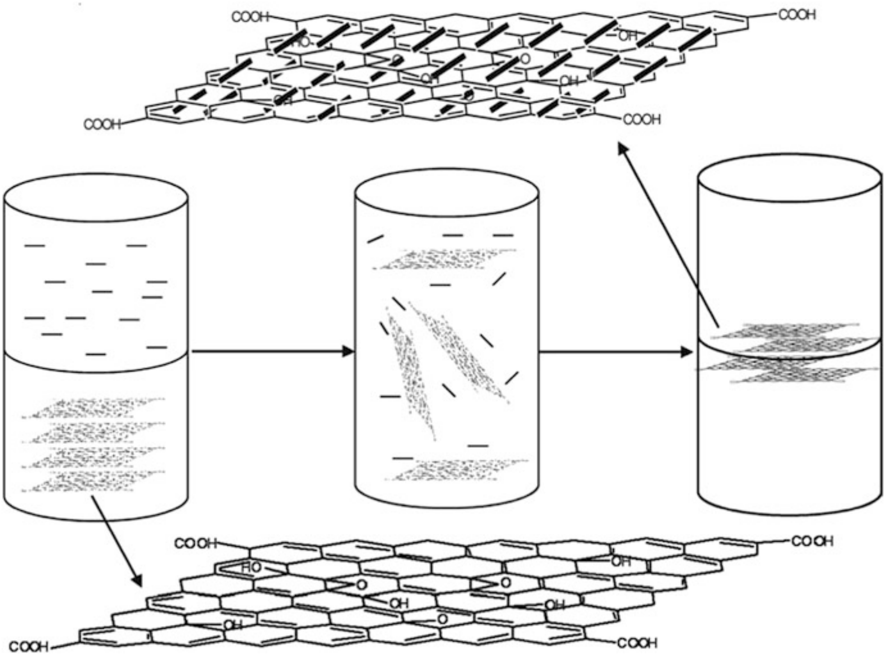

Fig. 13 TiO_2 nanorods-G system prepared via water/toluene two-phase self-assembly. Reprinted with permission of John Wiley and Sons, Inc. Copyright 2010 from [48]

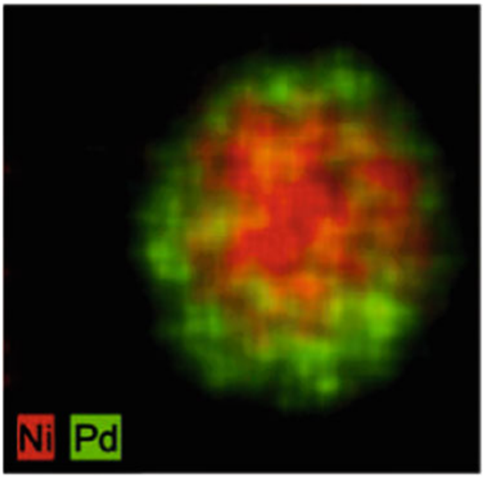

Fig. 14 Mapping TEM image in false colors of core-shell Ni/Pd NPs. Reprinted with kind permission from Springer Science + Business Media [55]

2.3 Organic Reactions

Heterogeneous catalysis based on G-supports has also been applied to organic transformations, although to a lesser extent. Examples include metal-mediated formation of carbon–carbon bonds, such as the Suzuki–Miyaura method. Palladium is the metal of choice for this type of reaction due to its fast rates and excellent selectivity. For example, facile access to palladium NPs–G hybrids was achieved, and the system proved to be very effective for Suzuki–Miyaura couplings [54].

Maximization of the catalyst active area is a key issue for reducing expensive metal usage while retaining high conversion rates. Preparation of core/shell systems, where metal NPs are enveloped in a shell made of a different metal, is often used as a strategy to increase the active area of the catalyst. As an example, oleylamine (OAm) has been used both as a solvent and as a surfactant; in the presence of Ni and Pd salts and trace amounts of trioctylphosphine (TOP) it led to monodisperse Ni(core)/Pd(shell) alloys (Fig. 14). These NPs were then deposited on G via a solution phase-based self-assembly method; they were then tested for Suzuki–Miyaura couplings of several arylboronic acids and aryl halides, and they displayed a very high activity. The role of G here was to foster the catalyst with a higher surface area, while providing the overall system with excellent stability [55].

Given the isoelectronic nature of Pd(0) and Au(I), efforts have been made to prepare analogous gold catalysts for the Suzuki reaction. Controlled-size Au NPs were deposited either on G or GO via easy and environmentally friendly routes; Suzuki coupling towards biphenyl derivatives was successfully accomplished. Moreover, the catalysts could easily be recovered by centrifugation and washing with water [56, 57].

Access to Pd NPs–G composites was also achieved via microwave irradiation, a method that has the advantage of providing uniform and rapid heat to the reaction mixture; in the presence of reducing agents such as hydrazine, this heat is exploited to reduce the precursor GO in situ during reaction with Pd NPs. In addition, better control of the deoxygenation of GO can be obtained. The catalyst thus prepared was not only active for Suzuki couplings but also for Heck reactions between aryl halides and substituted styrenes [58]. The same authors expanded the scope to Sonogashira C–C cross-couplings, using a Pd–G catalyst prepared by pulsed laser irradiation of aqueous solutions of GO and Pd ions, without using any chemical reducing agent [59].

Other than formation of C–C bonds, G-supported metals are widely used for the oxidation or reduction of organic substrates. In particular, turnover frequencies as high as 30,137 mol/h mol_{Pd} were reported for the solvent-free aerobic oxidation of benzyl alcohols to benzaldehydes using Pd/G prepared via wet impregnation. The oxidant species is molecular oxygen, revealing the promising potential of G-based catalysts towards utilization of O_2. In this case, the O_2-TPD (TPD = Temperature programmed desorption) profiles suggest that the adsorption of oxygen was facilitated by spill-over from palladium sites to the adjacent bridge sites of G [60]. Hydrogenation of alkenes and alkynes was also efficiently accomplished by supporting Fe NPs on G; the catalyst could easily be recovered by magnetic decantation [61].

Fig. 15 Helicity of CNTs. From *left* to *right*: armchair, chiral, zig-zag

3 Carbon Nanotubes

Today, carbon nanotubes (CNTs) can be considered as the core of what has been termed the “nanotechnology revolution.” They are versatile components in a variety of applications, and research articles that report their use in catalysis are available in very large numbers.

In general, CNTs can simply be described as G sheets rolled up in a cylindrical structure; depending on whether they are composed of a single sheet or multiple concentric rolled-up layers, they are respectively defined as single-walled (SWCNTs) or as multi-walled (MWCNTs) carbon nanotubes. As in graphene, the excellent conductivity properties relate to the extended π-conjugation, a consequence of the fused polyaromatic framework. One obvious but key difference between G and CNTs is the curvature introduced on the polyaromatic arrangement of the latter. Although loss of planarity results in a distortion from pure sp^2 hybridization of carbon atoms, significant Van der Waals forces are still exerted between individual tubes (in the order of 1,000 eV), due to the tubes’ large surface area [62]. As a result, CNTs tend to aggregate into bundles. This dramatically reduces the solubility of CNTs in most organic or aqueous solvents, and functionalization (either covalent or non-covalent) is generally required to disrupt the sp^2 pattern and to improve CNTs solubility and processability [63–65].

When unfunctionalized, CNTs display different electronic properties depending on the different helicity that they possess, the term helicity refers to the angle of the wrapping of the G sheet into a tubular geometry. Three types of structures are found: armchair, chiral, and zig-zag (Fig. 15), which exhibit different electronic properties as a consequence of the different π–π^* band gaps. Upon mathematical calculations based on specific geometrical parameters, it is possible to assign a specific electronic behavior to each structure. Hence, armchair tubes are always metallic, whereas zig-zag and chiral tubes can be either metallic or semiconductors.

In general, CNTs have so far been a more exploited material in catalysis compared to G or other carbon nanostructures, as their discovery dates back to almost 20 years earlier [66]. Therefore, the number and types of CNTs-catalyzed reactions is far larger too [67].

An advantage offered by CNTs is the possibility to dope the carbon framework with foreign atoms, typically nitrogen or boron. Insertion of a heteroatom offers a convenient path to adjust the tubes’ chemical and physical properties to fulfill catalytic requirements of different reactions [68].

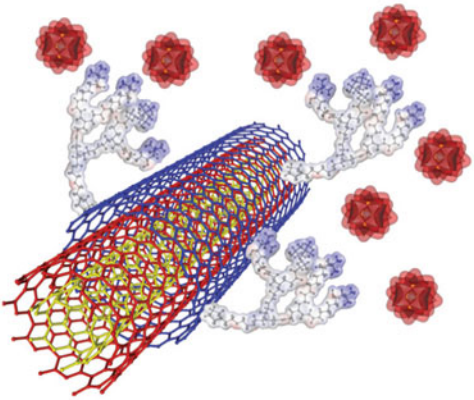

Fig. 16 POM@MWCNTs hybrid assembled via electrostatic interaction between MWCNTs functionalized with cationic PAMAM ammonium-dendrimers (*light blue*) and POMs (*red*). Reprinted by permission from Macmillan Publishers Ltd from [74]. Copyright 2010

3.1 Electrochemical Reactions

As described in the previous chapter, electrochemical transformations are a typical case where the exceptional conductivity of some carbon nanosupports can be exploited. In particular, CNTs have had a major role as a support for various electrocatalysts.

As outlined in Sect. 2.1, water oxidation constitutes the half-reaction of water splitting, and the discovery of processes that can facilitate this thermodynamically unfavoured reaction are highly desirable. A recent remarkable advance in this field is the assembly of MWCNTs decorated with the polyoxometalate (POM) $M_{10}[Ru_4(H_2O)4(\mu\text{-}O)_4(\mu\text{-}OH)_2\ (\gamma\text{-}SiW_{10}O_{36})_2]$ (M = Cs, Li) [69, 70]. The POM@MWCNTs hybrid (Fig. 16) was prepared by means of electrostatic scavenging at pH = 5 using the Li salt POM precursor, and the cationic PAMAM ammonium dendrimers-functionalised MWCNTs (PAMAM = polyamidoamine). The modification of MWCNTs with positively charged functional groups [71, 72] able to capture POM moieties has been further extended to alternative synthetic approaches. Examples include MW-irradiation, a solvent-free method that affords nanotubes bearing extended arrays of positive charges [73]. POM@MWCNTs exhibit extraordinary turnover frequencies (TOFs) for water oxidation (Fig. 17), reaching 300 cycles/h at low overpotentials of 0.35 V.

In this case, CNTs fulfill multiple tasks, as they control catalyst morphology, they provide a heterogeneous support, they increase surface area, and they channel the electrons to the electrode for better energy dispersion and relief of catalytic fatigue. Ultimately, MWCNTs act as a conductive scaffold to improve the electric contact between redox-active centers and the electrode surface [74].

Another class of ruthenium complexes that has shown good prospects for the electrocatalytic WOR is based on the use of bipyridine ligands. An interesting concept is the linkage of metal active species to CNTs via Van der Waals interactions, which are non-destructive towards the sp^2 hybridized aromatic pattern and thus allow preservation of their conductive properties. For example, binding of $Ru(bpa)(pic)_2$

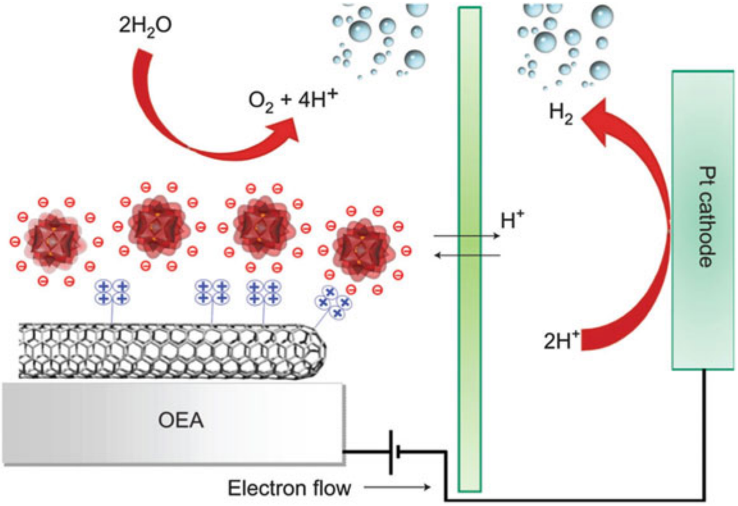

Fig. 17 Sketch of the POM@MWCNTs electrode for electrocatalytic water oxidation. Reprinted by permission from Macmillan Publishers Ltd from [74]. Copyright 2010

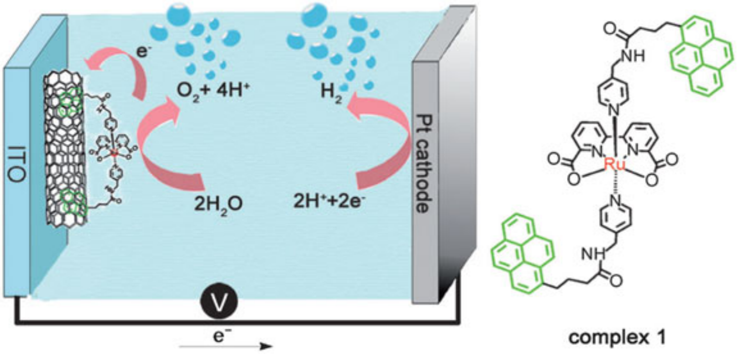

Fig. 18 Non-covalent interactions mediate the binding of Ru(bpa)(pic)$_2$ (i.e., complex 1) to CNTs for efficient electrocatalysis of water splitting. Reprinted with permission of John Wiley and Sons, Inc. Copyright 2013 from [75]

(i.e., 2,2-bipyridine-6,6-dicarboxylic acid, H_2bpa; 4-picoline, pic) takes advantage of the two pyrene groups to anchor to the nanotubes sidewalls (Fig. 18). The presence of the CNTs also guarantees a stronger attachment of the catalyst to the ITO electrode. Experiments of electrocatalysis at low potential highlighted the benefits of the assembly strategy, with reported TOFs exceeding 1,700 cycles/h [75].

The cathodic half-reaction of water splitting involves the generation of molecular hydrogen. Mimicking photosynthetic water splitting to generate H_2 could open the way to a new era in energy production, replacing carbon as fuel to establish greener power technologies. Hydrogen evolution is one of the desired electrochemical reactions for the manufacture of FCs, too.

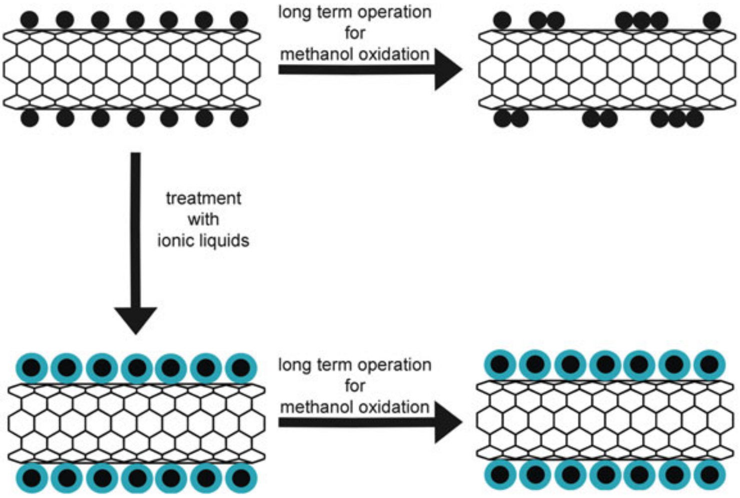

Fig. 19 Ionic liquid polymer thin films (*blue*) provide Pt-CNTs catalysts for MeOH oxidation with long-term operational stability, thanks to the inhibition of the migration and agglomeration of Pt NPs (*top*). This effect is achieved via mechanical isolation of PIL thin layers between Pt NPs (*bottom*)

In this regard, one of the most representative examples is given by the preparation of a bioinspired nickel bisdiphosphine covalently attached to MWCNTs to mimic the active sites of hydrogenase enzymes. These are metalloproteins capable of catalyzing interconversion between H_2 and pairs of electrons and protons. This is the process that takes place at one electrode in FCs too. In particular, the Ni-based catalyst anchored to CNTs has high catalytic activity under strong acidic conditions, which are those applied in proton-exchange-membrane FCs. The same catalyst can also conveniently catalyze the inverse reaction, hydrogen oxidation, with excellent turnover frequencies [76].

FCs that employ fuels other than H_2 are valuable alternatives, especially in view of safety and portability issues. For instance, methanol and formic acid can be employed in methanol fuel cells (DMFCs) and direct formic acid fuel cells (DFAFCs), respectively. The former follows a six electron/six proton anodic reaction:

$$CH_3OH + H_2O \rightarrow CO_2 + 6H^+ + 6e^- \tag{10}$$

To address durability problems in FC applications, stabilization of catalysts was achieved in different ways, including use of HF-treated CNTs [77] or protecting silica layers [78]. A more environmental-friendly approach makes use of ionic liquid polymer thin films (PILs). PILs provide Pt-CNTs catalysts for MeOH oxidation with long-term operational stability, thanks to the inhibition of the migration and agglomeration of Pt NPs. This effect is achieved via mechanical isolation of PIL thin layers between Pt NPs (Fig. 19) [79].

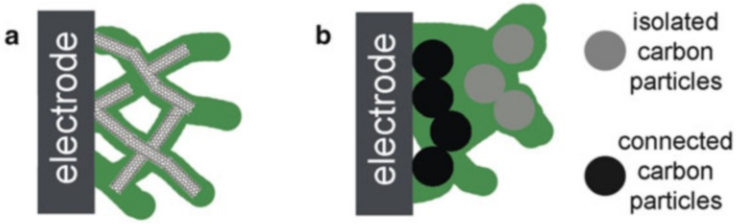

Fig. 20 CNTs morphology allows for better interconnection of metal particles with the electrode (**a**) compared with carbon black (**b**)

As for the case with graphene, development of an ever growing number of catalytic systems based on CNT supports for ORR is a prominent area of research. Similar systems to those described for G have been prepared with CNTs. These systems address the additional issues related to catalyst stability in strong acidic conditions, as used for most FC types.

Most common composites for ORR are CNTs decorated with Pt NPs. For example, spontaneous reduction of Pt^{4+} ions and growth of Pt NPs on functionalised MWCNTs allowed for the preparation of efficient catalysts with the use of platinum as high as 75%. In this study, the authors compared the system with commercial Pt/C, which exhibited a much lower use of the metal under the same operative conditions (39%). The tubular structure of CNTs in this case is able to provide an electron pathway for the metal to the Teflon-bond carbon electrode (Fig. 20a). In contrast, this does not occur with carbon black, where most of the particles are isolated by the dielectric organic polymer, resulting in less Pt particles being involved in the reaction (Fig. 20b) [80].

Combination of Pt with single-walled carbon nanotubes has also been studied for ORR. Films of Pt-SWCNTs hybrids were cast on a rotating disk electrode. Subsequent electrocatalytic tests underlined the improved stability provided by SWCNTs to the electrode, which did not display any significant oxygen reduction currents for over 36 h [1].

Research on the use of less precious metals for ORR electrocatalysis is another important aspect for FCs market development. For instance, synthesis of a system with cobalt, prepared by growth of Co_3O_4 nanocrystals on N-doped MWCNTs, has been shown to be a good candidate for the reduction of oxygen in alkaline conditions [81].

3.2 *Photochemical Reactions*

The theoretical discussion on the advantages of using carbon nanostructures as supports in photocatalytic processes has already been outlined in Sect. 2.2 when we introduced graphene supports. The same concepts apply to systems with carbon nanotubes.

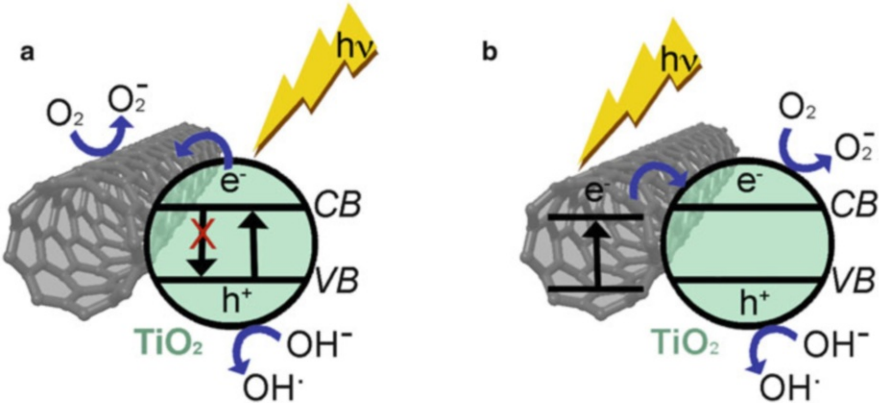

Fig. 21 Two proposed mechanisms for CNTs mediated synergistic effect in TiO_2 photocatalysis: CNTs may serve as electron sink (**a**) or photosensitizers (**b**)

Effective methods to increase recombination times include formation of a semiconductor–metal junction called a Schottky barrier, where there is a space-charge separation region, with electrons flowing from one material to the other at the interface of the two materials. In practice, CNTs would function as an electron sink, scavenging away the electrons and retarding recombination (Fig. 21a) [82].

An alternative mechanism has been proposed to explain the observed synergistic effects for the photo-catalytic activity in pollutants degradation. This hypothesis postulates a photosensitizer (rather than an adsorbant) role of CNTs. The tubes would inject excited electrons into the CB of the metal oxide forming superoxide radicals; the electrons would then be transferred back to the CNTs; as a result, holes would be present in the VB of the metal oxide, with generation of O_2^- or ·OH species (Fig. 21b) [83, 84].

Water splitting has frequently been mentioned in previous sections, with the half-reaction WOR being one of the most popular transformations in heterogeneous electrocatalysis. In addition to being theoretically the greenest way to produce molecular hydrogen, it is also involved in one of the most important processes in nature, i.e., photosynthesis by green plants. In fact, one of the most ambitious projects presently undergoing research is artificial replication of natural photosynthesis [69].

Photocatalytic hydrogen evolution of composites with CNTs has been reported, although this area is still relatively underexplored. In binary systems made of TiO_2/MWCNTs, CNTs help suppress charge pairs recombination, resulting in enhanced photoresponse by the catalyst for HER. Notably, hydrothermal direct growth of TiO_2 NPs on MWCNTs surface led to a binary composite of high activity under visible light. Moreover, enhancement of the absorption wavelength for TiO_2 above 400 nm was induced by $\pi \rightarrow \pi^*$ electronic transition of MWCNTs, and $n \rightarrow \pi^*$ between the n-orbit of the oxygen species of TiO_2 and MWCNTs. This process is fundamental for the formation of electron/hole pairs, and for their separation during photocatalysis under visible light. Remarkably, hydrogen evolution rates were reported to exceed 8,000 μmol g^{-1} h^{-1} [85].

Fig. 22 TiO_2/SWCNTs are efficient catalysts in phenol photo-oxidation. Reprinted with permission from [88]. Copyright 2008 American Chemical Society

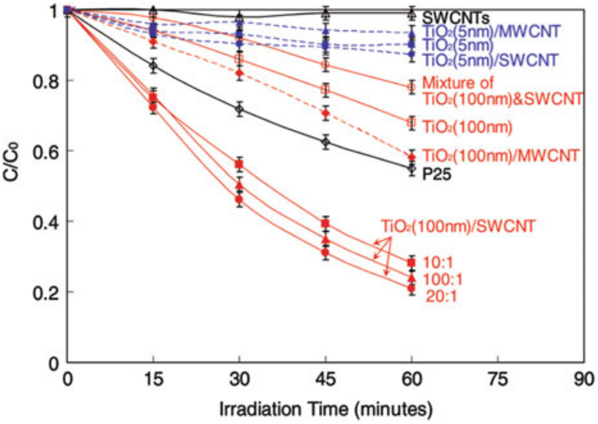

The same electronic transitions had been previously invoked to describe an MWCNT/TiO_2:Ni catalyst, where it was proposed that MWCNTs may act as photosensitizers, thus allowing absorption of the catalyst over the whole UV–Vis range. The catalyst, prepared by modified chemical vapor deposition (CVD) using a previously synthesised NiO–TiO_2 precursor, proved active for H_2 evolution from methanol–water solutions under visible light illumination [86].

TiO_2/CNTs hybrids appear to be amongst the most promising systems not only for HER but also for photocatalysis in general. For example, acid-catalyzed sol–gel synthesis of titania/MWCNTs composites was employed in the UV or visible light irradiation treatment of water for the removal of phenol contaminants. Best results were obtained with 20 wt% of MWCNTs, with the catalyst capable of completely degrading phenol within 4 h. Titania-MWCNTs synergy was more pronounced under visible light, confirming that increased catalyst absorption is observed in this wavelength range with consequent decrease of bandgap energy [87].

A more rigorous study that addressed structure and function of TiO_2/CNTs composites was conducted by Gray et al. The authors assessed previous speculations on the electron/hole pairs separation by means of electron transfer from the metal oxide to the CNTs. They prepared composites with three different types of TiO_2 (i.e., large or small anatase, and mixed-phase Degussa P25), and either MWCNTs or SWCNTs. Such materials were then tested in the photo-oxidation of phenols. As a result of the closer contact between SWCNTs-TiO_2 in comparison with MWCNTs-TiO_2, photo-oxidation turned out to be enhanced when the former was used (Fig. 22) [88].

Shuttling of photo-excited electrons along the SWCNTs was confirmed, as the relative position of the SWCNT CB edge permits the transfer of electrons from the anatase surface. Although similar behavior was observed for MWCNTs, reduced individual contact between MWCNTs and anatase enhanced photocatalytic activity of the metal oxide to a lesser extent (Fig. 23) [88].

Another semiconducting oxide that has been employed in combination with CNTs is ZnO. Attachment of ZnO to SWCNTs was achieved to study the photo-excited

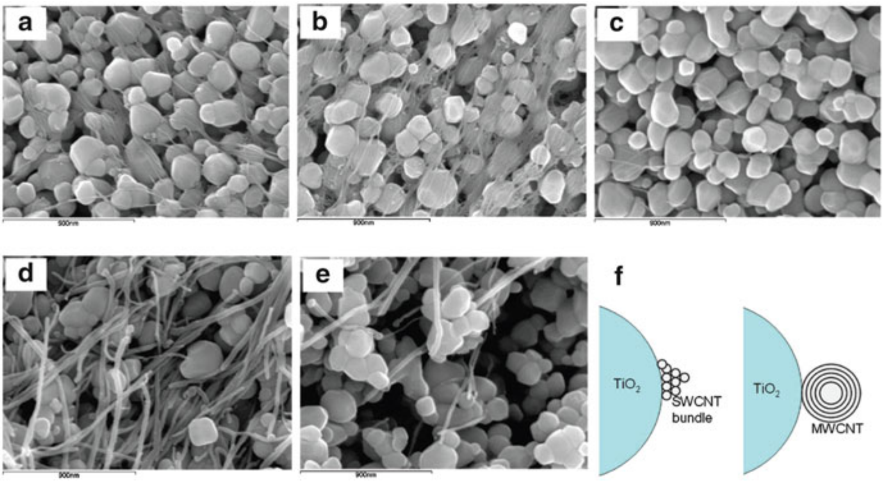

Fig. 23 TEM images (**a**–**e**) and a schematic representation (**f**) showing increased contact between TiO_2 and SWCNTs (**a**–**c**) compared to TiO_2 and SWCNTs (**d**, **e**). Reprinted with permission from [88]. Copyright 2008 American Chemical Society

state interaction between the two materials, when linked together. The experiment was conducted by means of photo-electrochemical measurements after deposition of the ZnO-SWCNTs hybrids on optically transparent electrodes. Although only a limited enhancement in the photoconversion efficiency was observed, the authors could demonstrate the charge transfer interaction between the photo-excited ZnO and the functionalized SWCNTs [89]. More recently, use of ZnO/CNTs has also been shown to be effective as photo-electrode both for the assembly of dye-sensitized solar cells [90] and for photo-catalytic water splitting [91].

A polyol method to support CdS on MWCNTs has also been employed to catalyze the visible light-induced photodegradation of the azo dye Brilliant Red X-3B, a wastewater contaminant. In this case, migration of photogenerated electrons onto the MWCNTs support was confirmed by detecting the intermediate H_2O_2 with the iodide method. Formation of hydrogen peroxide occurs during visible light catalysis and is indicative of a reduction in electron/hole recombination times:

$$\mathrm{CdS} + h\nu \rightarrow h_{\mathrm{VB}}{}^{+} + e_{\mathrm{CB}}{}^{-} \tag{11}$$

$$2e_{\mathrm{CB}}{}^{-} + \mathrm{O}_2 + 2\mathrm{H}^{+} \rightarrow \mathrm{H}_2\mathrm{O}_2 \tag{12}$$

The presence of MWCNTs indeed facilitates photocatalytic efficiency in comparison with AC-supported CdS and isolated CdS. In addition to longer term charge pairs separation, CNTs also favor adsorption of the dye and of O_2 [92]. Recently, covering of MWCNTs with core-shell systems (Fig. 24) composed of three different mesoporous oxides (i.e., CeO_2, TiO_2, and ZrO_2) embedding noble metals (i.e., Pd and Pt) was attained. These hybrids resulted in the assembly of versatile catalysts for

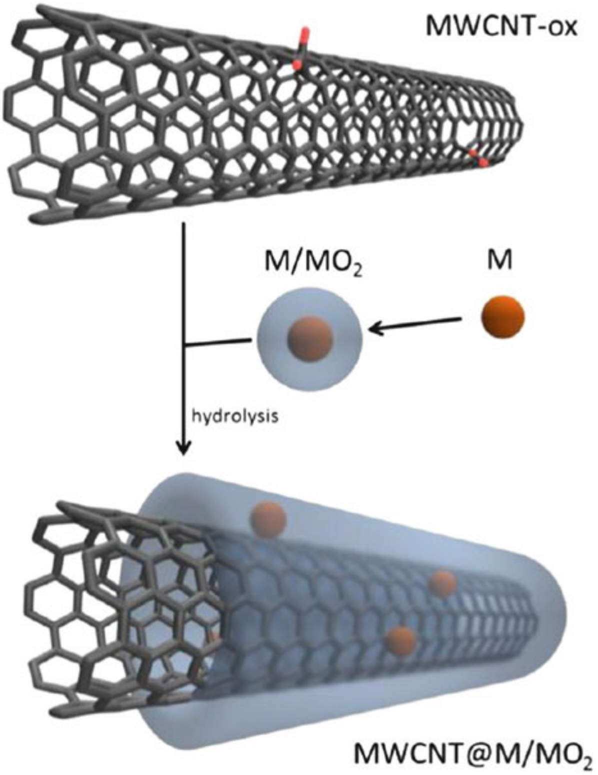

Fig. 24 Coverage of MWCNTs with core-shells of different metals and metal oxides is a recent approach for efficient photo-catalysed hydrogen evolution. Reprinted with permission from [93]. Copyright 2012 American Chemical Society

various reactions, including photocatalytic methanol reforming. The MWCNTs@M/M'O_2 catalysts were prepared via solution-based methods, which allow easy control of the oxide layer thickness by simple adjustment of the starting materials molar ratios. The outstanding activity for methanol reforming (i.e., four times higher than those of the reference catalysts Pd@TiO_2 and Pt@TiO_2) was attributed to efficient delocalization of photogenerated electrons. As a result, a longer lifetime of electron/hole pairs separation was achieved, and ultimately faster rates of H_2 evolution were recorded. Moreover, it has been proposed that MWCNTs may directly participate as photosensitizers in the light absorbance process, since H_2 evolution rate did not depend on the metal oxide layer thickness [93].

3.3 *Organic Reactions*

Probably the most striking difference in the number of reports concerning CNTs as catalytic supports in comparison with the other carbon nanostructures involves the transformation of organic substrates. There is a plethora of M/CNTs systems developed for hydrogenation, oxidation, and C–C cross coupling reactions. In most cases it is considered that the main role of the carbon nanotubes is to offer a better dispersion for the metal nanoparticles as a result of the CNTs high surface area, and provide superior thermal and structural stability to the catalyst. In some reports, higher catalytic activities are interpreted in terms of stabilization by the nanotubes of transient higher oxidation states of the metal particles.

Pioneering work by Planeix and co-workers described the preparation of RuNP/CNTs by reaction of ruthenium 2,5-pentanedionate with CNT and subsequent reduction with diluted H_2 streaming. Catalytic tests on the hydrogenation of cinnamaldehyde revealed an outstanding selectivity (up to 92%) towards the reduction of the C=O functionality together with an 80% conversion. The authors attributed the selectivity to CNT-induced specific interactions of the metal particles with the substrate. When they repeated the test using alumina or silica as supports, selectivity was dramatically reduced [94]. The finding is a milestone in CNT-based heterogeneous catalysis as it disclosed the role of nanotubes as active supports, capable of driving reactivity pathways.

A ruthenium/CNT catalyst active in the hydrogenation of *p*-chloronitrobenzene (*p*-CNB) to *p*-chloroaniline (*p*-CAN) was prepared under MW irradiation, using $RuCl_3 \cdot 3H_2O$ as metal precursor and low boiling point solvents. TOFs up to 370 per hour were observed for the formation of the amine, while the C–Cl bond remained intact [95].

Hydrogenation reactions catalyzed by Ru/CNTs hybrids were carried out on various other substrates with excellent activities, including complete reduction of benzene rings [96]. High conversions and selectivities for hydrogenation reactions have been achieved using M/CNTs catalysts featuring palladium, platinum, gold, rhodium, and iridium [97].

Oxidation, and particularly oxidation of alcohols, by means of several noble metal/CNTs systems has also been studied. Catalysts active in hydrogenation reactions are often also capable of performing oxidation. Ruthenium, for example, has been reported to catalyze oxidation of primary, secondary, and tertiary benzyl alcohols when combined with MWCNTs more efficiently than other Ru systems (RuNP/TiO_2, RuNP/AC, RuO_2). Moreover, the catalyst displayed sensitivity towards the alcohol of almost 100% when other potentially reactive groups such as sulfur, nitrogen, or C–C double bonds [98].

Selective oxidation of glycerol under alkaline conditions was achieved by MWCNTs-supported Au nanoparticles. The catalyst could perform the oxidation of the secondary hydroxyl functional group [99]. Several other noble metal catalysts supported on CNTs have been shown to possess good activities and selectivities for other biomass conversion reactions [100].

A fascinating prospect is to exploit the tubular structure of CNTs to confine catalysts inside the CNT channels, thus using the supports as nanoreactors. For example, ruthenium NPs were endohedrally inserted within the tubes and their activity in the oxidation of carbon monoxide was compared with that of the metal dispersed on the CNTs sidewalls; the confined catalyst showed a wider operating temperature window (60–120°C) and better stability (as long as 100 h at 100°C); evidently the micro-environment created by the nanotube cavities augments the density of the reacting CO molecules around the metal nanoparticles while protecting the catalyst itself, resulting in better performance for this oxidation [101].

C–C cross coupling reactions have been successfully accomplished via the best known metal-catalyzed couplings, with palladium obviously being the most used transition metal. Several Suzuki (see for example [102–104]), Sonogashira (see for example [105–107]), and Heck (see for example [108–110]) reactions were reported with activities almost invariably exceeding those of the metal supported on non-CNTs supports. In contrast with hydrogenation and oxidation reactions, the catalytic performance for C–C coupling seems to depend on the metal particle size; it is therefore important to consider the effects that CNTs have on the selection of the particles size range during the catalyst assembly stage.

The MWCNTs/core-shell system described in Sect. 3.1 active for the water gas shift reaction exhibits good activity for the Suzuki–Miyaura coupling; crucial for the catalysis is the templating ability of the MWCNTs, which can impart specific organization of the particles around the support. The activity does not seem to depend on the M@M'O_2 thickness, however, but rather on synergistic effects between the carbon support and the metal/metal oxide.

4 Other Carbon Nanostructures: Carbon Nanohorns and Carbon Nanofibers

The term carbon nanofibers (CNFs) more generally refers to CNT-types of structure where the rolled up graphene sheets are not necessarily cylindrical, with shapes varying from cones to cups or plates. As the name suggests, carbon nanohorns (CNHs) are horn-shaped graphene sheets [111] which aggregate in what are often referred to as "dahlia-like" and "bud-like" structures; they can also be either single-wall (SWCNHs) or multi-wall (MWCNHs).

These carbon nanostructures have been less explored in catalysis and the assessment of their potential in real application is still in its infancy, despite both CNHs and CNFs having been known for more than a decade.

The majority of papers on both types of carbon nanostructures regard their use as supports in electro-catalytic systems for applications in energy storage devices.

4.1 Carbon Nanohorns

One of the advantages related to carbon nanohorns is the more cost-effective method of preparation, which does not necessarily employ expensive metal catalysts. Very recently, arc evaporation of graphite in the atmosphere proved to be a very economical method for large scale production of CNHs (Fig. 25) [112].

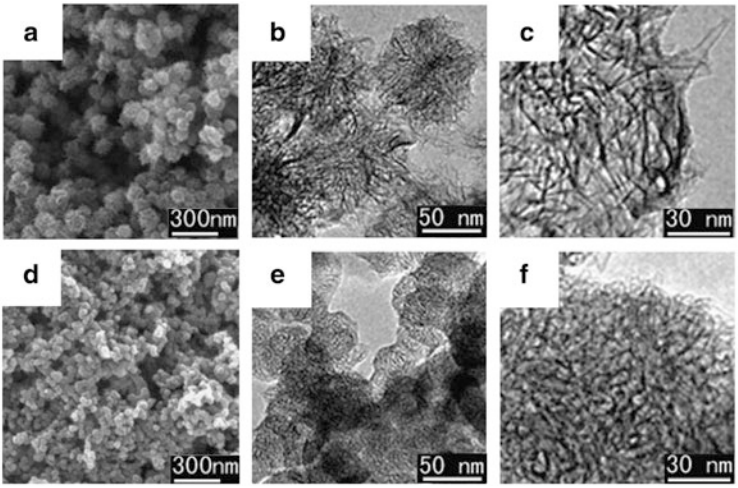

Fig. 25 SEM and TEM images of carbon nanohorns produced by arc-discharge in air (**a**–**c**) and carbon dioxide (**d**–**f**). Reprinted from [112], Copyright (2010), with permission from Elsevier

"Free standing" electrodes are based on CNHs laser-grown on a highly porous 3D network of carbon microfibers and decorated with either Ni/Co NPs or Pt NPs. The electrocatalysts were tested for the ORR and the MOR, showing large currents in both cases. The catalyst also has good potential for applications in lithium ion batteries, showing an unprecedented reversible Li^+ intercalation of 1,628 mA h g^{-1}) [113].

The same authors later provided a more comprehensive study of the electroanalytical features of the system with Pt. Optimized conditions revealed that CNHs supported Pt NPs could generate higher peak current densities than the analogous catalysts supported on CNTs and CNFs for the oxidation of potassium ferrocyanide. Moreover, in contrast with other carbon nanostructures where the charge transfer is governed by diffusion, in this case it occurs via surface confined processes. In-depth studies were conducted on the electrochemical activity towards ORR and MOR, showing that, when optimized, the catalysts are able to outperform other benchmark electrodes [114].

Doping of the carbon support has also been explored as a viable way to improve activity further. A method allowing anchoring of "unprotected" Pt nanoclusters on nitrogen-doped SWCNHs resulted in the assembly of a nanocomposite cathode catalyst for ORR. Performances of the catalyst were greatly enhanced both in terms of activity and durability [115].

The large specific surface area and the high electrical conductivity make CNHs promising candidates for lithium ion batteries. Fe_2O_3 coated with CNHs exhibited high rate and cycle stability at currents as high as 1,000 mA g^{-1} at the anode for LIBs. The synthesis was relatively simple, involving hydrothermal procedures and the use of metal-free SWCNHs starting material prepared by arc-discharge.

Fig. 26 Schematic representation of the structure and properties of TiO_2/carbon nanohorns composite. Reprinted from [117], Copyright (2013), with permission from Elsevier

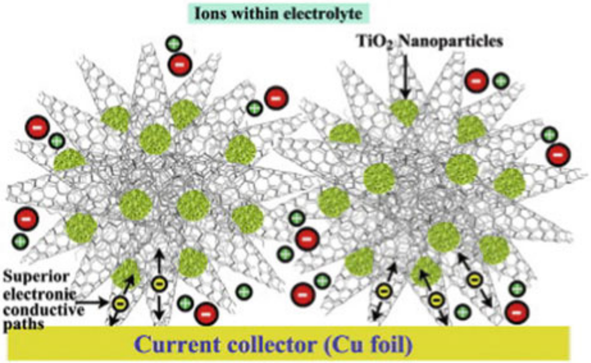

The excellent catalytic performance was attributed to a combination of factors: the increase of electronic conductivity by the SWCNHs, therefore hindering Fe_2O_3 aggregation during charge/discharge phases, and the high surface area of SWCNHs together with small size Fe_2O_3 particles that can provide large electrode/electrolyte contact area and short path length for Li^+ transport [116].

High charging/discharging rates were also reported for a SWCNHs/TiO_2 (nanoporous anatase) hybrid (Fig. 26), where the nanohorns assist storage by furnishing electrons, with capacities exceeding those for the analogous CNT-based hybrid [117].

As regards other reactions, C–C cross coupling via the Suzuki–Miyaura reaction was achieved by means of Pd-decorated SWCNHs. High TOFs were obtained for a series of aryl halides coupling with PhB $(OH)_2$, presumably as a consequence specific potential field of the intrahorn nanospaces [118].

4.2 *Carbon Nanofibers*

One of the first reports featuring CNFs as catalytic support was published in 1995. The authors prepared the CNFs by interaction of iron powder with a mixture of CO_2/H_2 at 600°C, and, after deposition of Fe/Cu (7:3), studied their catalytic behavior towards the hydrogenation of ethylene to ethane. The investigation also evaluated the particle size distribution as a comparison with AC and γ-alumina supports, showing a broader distribution for particles grown on CNFs (Fig. 27) [119].

The catalytic activity of the CNF-supported catalysts was considerably higher than with the other two supports. The authors recognized that activity was not dependent upon the particle size distribution, but rather upon electron-transfer processes occuring between support and metal; this results in electronic perturbation of the catalysts and consequently different adsorption and reactivity characteristics. Furthermore, they hypothesized a preferred crystallographic orientation of the metals induced by the crystallinity of the CNF graphitic skeleton [119].

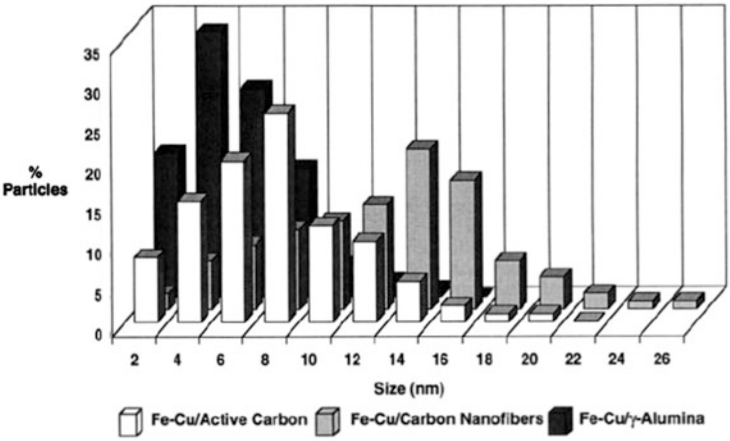

Fig. 27 Particle size distribution for Fe–Cu catalysts grown on different supports. Reprinted with permission from [119]. Copyright 1994 American Chemical Society

Since those days, more studies have been conducted, mostly highlighting the excellent catalytic properties of CNF-supported metal nanoparticles, particularly for hydrogenation and oxidation of organic substrates, or for application in electrocatalytic processes, with emphasis on FCs assembly.

Hydrogenation of α,β-unsaturated molecules was studied to assess the activity and selectivity of a Pd/CNFs system prepared by wet impregnation. When compared with the commercially available charcoal-supported Pd catalyst, the superiority of the CNF-based system was exceptionally pronounced in terms of activity and selectivity. The high surface area of the nano-structured support reduces mass transfer limitations of the reagents to the catalytically active species [120].

An interesting investigation established that different CNF platelets orientation (Fig. 28) used as supports for nickel nanoparticles can impact on the activity and selectivity of hydrogenation of simple α,β-unsaturated compounds such as 1,3-butadiene. The authors invoked the CNF-templated growth of the Ni NPs into specific and diverse orientations as the main factor responsible for catalytic differences. The example is important in that it proves the option of tailoring the morphology metal particles in order to attain desired catalytic performances [121].

Several other examples are available in the literature on the utilization of CNFs as supports in hydrogenation and oxidation reactions. More recently, carbon nanofibers have been combined with noble metals to improve ORR activity. With an eye to applications in fuel cells, CNFs were studied as electrode metal supports for ORR and MOR.

For instance, a MW-assisted polyol method afforded CNF/PtRu NPs with the carbon nanostructures displaying platelet, herringbone, and tubular geometries. Activities towards methanol oxidation outperformed in all cases those of commercial PtRu loaded on Vulcan XC72R carbon black. Order of activities for the three

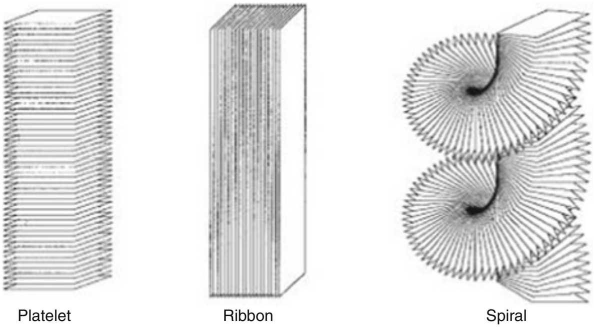

Fig. 28 Schematic representation of the three unique conformations of graphite nanofibers used as a catalyst support material. Reprinted with permission from [121]. Copyright 1998 American Chemical Society

supports was shown to be platelet > tubular ~ herringbone CNFs; however, the Brunauer–Emmett–Teller (BET) surface areas was in the order herringbone > tubular ~ platelet, thus indicating that other factors in additions to the surface areas need to be taken into account to explain catalytic characteristics [122].

Finally, it is worth mentioning that the use of CNFs in C–C cross coupling reactions has been reported. One of the pioneer examples is the synthesis of a CNFs/Pd hybrid that showed good activity in Heck couplings of a series of aryl halides and olefins. In addition to good activities, other advantages were spotted such as the stability of the system at relatively high temperatures, recyclability of the catalyst, and its insensitivity to oxygen contamination [123].

5 Conclusions

Effective heterogeneous catalysis is crucially dependent upon the appropriate support. Carbon nanostructures have proved to fulfill this role with outstanding efficiency. Carbon nanotubes and graphene appear to be versatile materials that can be combined with virtually any transition metal to afford preparation of hybrid catalysts with improved activity and stability. Currently, graphene and carbon nanotubes represent the focus of research and reports are exponentially proliferating. Applications in electrocatalysis, with a view to energy saving applications (fuel cells and lithium ion batteries), and in photocatalysis, through the efficient achievement of important processes such as water splitting and contaminant degradations, seem to be particularly promising. Conductivity properties and the ability to disperse catalyst nanoparticles through intrinsically high surface areas are key features of both carbon nanostructures. Carbon nanotubes are also being widely employed as supports in organic transformations, where they can induce chemoselectivity in processes such as hydrogenations and oxygenations and in metal-catalyzed C–C cross coupling reactions, aiding adsorption of reagents and placing them in closer proximity with the active species. Carbon nanohorns and carbon nanofibers present similar characteristics, and although they have not enjoyed thus far the same popularity of G and CNTs, they constitute valuable variants and their use in heterogeneous catalysis has already been highlighted. An important additional possibility that carbon nanostructures have opened is the control over morphology and pore size distribution of metal nanoparticles during the growth stage; they can basically act as templates, removable if necessary, and tailor the properties and performances of the particular catalyst.

Carbon nanostructures are an integral part of today's nanotechnology revolution, and their application in the most diverse fields is holding immense prospects. Heterogeneous catalysis is one such field, and one of the biggest challenges faced today is the implementation of these systems into real life applications.

Acknowledgements This work was supported by the FP7-NMP-2012-SMALL-6 (project ID 310651) and by HI-PHUTURE (protocol 2010N3T9M4).

References

1. Kongkanand A, Kuwabata S, Girishkumar G, Kamat P (2006) Single wall carbon nanotubes supported platinum nanoparticles with improved electrocatalytic activity for oxygen reduction reaction. Langmuir 22:2392–2396
2. Ajayan PM, Stephan O, Redlich P, Colliex C (1995) Carbon nanotubes as removable templates for metal oxide nanocomposites and nanostructures. Nature 375:564–567
3. Geim AK, Novoselov KS (2007) The rise of graphene. Nat Mater 6:183
4. Zhang J, Xiong Z, Zhao XS (2011) Graphene–metal–oxide composites for the degradation of dyes under visible light irradiation. J Mater Chem 21:3634–3640
5. Stoller MD, Park S, Zhu Y, An J, Ruoff RS (2008) Nano Lett 8:3498
6. Kou R, Shao Y, Wang D, Engelhard MH, Kwak JH, Wang J, Viswanathan VV, Wang C, Lin Y, Wang Y, Aksay IA, Liu J (2009) Electrochem Commun 11:954–957
7. Guo S, Sun S (2012) FePt nanoparticles assembled on graphene as enhanced catalyst for oxygen reduction reaction. J Am Chem Soc 134:2492
8. Kou R, Shao Y, Mei D, Nie Z, Wang D, Wang C, Viswanathan VV, Park S, Aksay IA, Lin Y, Wang Y, Liu J (2011) Stabilization of electrocatalytic metal nanoparticles at metal–metal oxide–graphene triple junction points. J Am Chem Soc 133:2541
9. Neppolian B, Bruno A, Bianchi CL, Ashokkuma M (2012) Ultrasonic Sonochem 19:9
10. He Y, Cui H (2012) Chem Eur J 18:4823
11. Shi Q, Mu S (2012) J Power Sources 203:48
12. Seger B, Kamat PV (2009) Electrocatalytically active graphene–platinum nanocomposites. Role of 2-D carbon support in PEM fuel cells. J Phys Chem C 113:7990–7995
13. Guo S, Zhang S, Wu L, Sun S (2012) Co/CoO nanoparticles assembled on graphene for electrochemical reduction of oxygen. Angew Chem Int Ed 51:1170
14. Liang Y, Li Y, Wang H, Zhou J, Wang J, Regier T, Dai H (2011) Co_3O_4 nanocrystals on graphene as a synergistic catalyst for oxygen reduction reaction. Nat Mater 10:180
15. Wang H, Liang Y, Li Y, Dai H (2011) $Co_{1-x}S$–Graphene hybrid: a high-performance metal chalcogenide electrocatalyst for oxygen reduction. Angew Chem Int Ed 50:10969
16. Yin H, Tang H, Wang D, Gao Y, Tang Z (2012) Facile synthesis of surfactant-free Au cluster/graphene hybrids for high-performance oxygen reduction reaction. ACS Nano 6:8288

17. Wu Z-S, Yang S, Sun Y, Parvez K, Feng X, Müllen K (2012) 3D nitrogen-doped graphene aerogel-supported Fe_3O_4 nanoparticles as efficient electrocatalysts for the oxygen reduction reaction. J Am Chem Soc 134:9082
18. Li Y, Gao W, Ci L, Wang C, Ajayan PM (2010) Carbon 48:1124
19. Guo S, Dong S (2011) Graphene nanosheet: synthesis, molecular engineering, thin film, hybrids, and energy and analytical applications. Chem Soc Rev 40:2644
20. Yoo E, Okata T, Akita T, Kohyama M, Nakamura J, Honma I (2009) Nano Lett 9:2255
21. Bong S, Kim Y-R, Kim I, Woo S, Uhm S, Lee J, Kim H (2010) Electrochem Commun 12:129
22. Guo S, Dong S, Wang E (2010) Three-dimensional Pt-on-Pd bimetallic nanodendrites supported on graphene nanosheet: facile synthesis and used as an advanced nanoelectrocatalyst for methanol oxidation. ACS Nano 4(1):547
23. Li Y, Wang H, Xie L, Liang Y, Hong G, Dai H (2011) MoS_2 nanoparticles grown on graphene: an advanced catalyst for the hydrogen evolution reaction. J Am Chem Soc 133:7296
24. Liu C, Alwarappan S, Chen Z, Kong X, Li C-Z (2010) Membraneless enzymatic biofuel cells based on graphene nanosheets. Biosens Bioelectron 25:1829
25. Zheng W, Zhao HY, Zhang JX, Zhou HM, Xu XX, Zheng YF, Wang YB, Cheng Y, Jang BZ (2010) A glucose/O_2 biofuel cell base on nanographene platelet-modified electrodes. Electrochem Commun 12:869
26. Wang D, Choi D, Li J, Yang Z, Nie Z, Kou R, Hu D, Wang C, Saraf LV, Zhang J, Aksay IA, Liu J (2009) Self-assembled TiO_2–graphene hybrid nanostructures for enhanced Li-ion insertion. ACS Nano 3:907
27. Paek SM, Yoo E, Honma I (2009) Nano Lett 9:72
28. Liana P, Zhub X, Lianga S, Li Z, Yangb W, Wanga H (2011) High reversible capacity of SnO_2/graphene nanocomposite as an anode material for lithium-ion batteries. Electrochim Acta 56:4532
29. Wu Z-S, Ren W, Wen L, Gao L, Zhao J, Chen Z, Zhou G, Li F, Cheng H-M (2010) ACS Nano 4:3187
30. Lian P, Liang S, Zhu X, Yang W, Wang H (2011) A novel Fe_3O_4–SnO_2-graphene ternary nanocomposite as an anode material for lithium-ion batteries. Electrochim Acta 58:81
31. Xue D, Xin S, Yan Y, Jiang K, Yin Y, Guo Y, Wan L (2012) Improving the electrode performance of Ge through Ge@C core-shell nanoparticles and graphene networks. J Am Chem Soc 134:2512
32. Zhang C, Peng X, Guo Z, Cai C, Chen Z, Wexler D, Li S, Liu H (2012) Carbon 50:1897
33. Su C, Bu X, Xu L, Liu J, Zhang C (2012) Electrochim Acta 64:190
34. Yanga J, Wanga J, Wanga D, Li X, Genga D, Liangb G, Gauthierb M, Li R, Suna X (2012) 3D porous $LiFePO_4$/graphene hybrid cathodes with enhanced performance for Li-ion batteries. J Power Sources 208:340–344
35. Sartorel A, Carraro M, Maria Toma F, Prato M, Bonchio M (2012) Shaping the beating heart of artificial photosynthesis: oxygenic metal oxide nanoclusters. Energy Environ Sci 5:5592–5603
36. Sartorel A, Carraro M, Scorrano G, De Zorzi R, Geremia S, McDaniel ND, Bernhard S, Bonchio M (2008) Polyoxometalate embedding of a catalytically active tetra-ruthenium(IV)-oxo-core by template directed metalation of $[\gamma\text{-SiW}_{10}O_{36}]^{8-}$. J Am Chem Soc 130:5006–5007
37. Sartorel A, Miró P, Salvadori E, Romain S, Carraro M, Scorrano G, Di Valentin M, Llobet A, Bo C, Bonchio M (2009) Water oxidation at a tetraruthenate core stabilized by polyoxometalate ligands: experimental and computational evidence to trace the competent intermediates. J Am Chem Soc 131:16051
38. Piccinin S, Sartorel A, Aquilanti G, Goldoni A, Bonchio M, Fabris S (2013) Water oxidation surface mechanisms replicated by a totally inorganic tetraruthenium-oxo molecular complex. PNAS. doi:10.1073/pnas.12134 86110
39. Quintana M, Montellano Lopez A, Rapino S, Toma FM, Iurlo M, Carraro M, Sartorel A, Maccato C, Ke X, Bittencourt C, Da Ros T, Van Tendeloo G, Marcaccio M, Paolucci F, Prato M, Bonchio M (2013) Knitting the catalytic pattern of artificial photosynthesis to a hybrid graphene nanotexture. ACS Nano 7:811

40. Xiang Q, Yu J, Jaroniec M (2012) Graphene-based semiconductor photocatalysts. Chem Soc Rev 41:782
41. Zhang X-Y, Li H-P, Cui X-L, Lin Y (2010) Graphene/TiO_2 nanocomposites: synthesis, characterization and application in hydrogen evolution from water photocatalytic splitting. J Mater Chem 20:2801–2806
42. Fan W, Lai Q, Zhang Q, Wang Y (2011) Nanocomposites of TiO_2 and reduced graphene oxide as efficient photocatalysts for hydrogen evolution. J Phys Chem C 115:10694
43. Mukherji A, Seger B, Lu GQ, Wang LZ (2011) Nitrogen doped $Sr_2Ta_2O_7$ coupled with graphene sheets as photocatalysts for increased photocatalytic hydrogen production. ACS Nano 5:3483
44. Jia L, Wang DH, Huang YX, Xu AW, Yu HQ (2011) Highly durable N-doped Graphene/CdS nanocomposites with enhanced photocatalytic hydrogen evolution from water under visible light irradiation. J Phys Chem C 115:11466
45. Lightcap IV, Kosel TH, Kamat PV (2010) Anchoring semiconductor and metal nanoparticles on a two-dimensional catalyst mat. Storing and shuttling electrons with reduced graphene oxide. Nano Lett 10:577
46. Xiang Q, Yu J, Jaroniec M (2012) Synergetic effect of MoS_2 and graphene as cocatalysts for enhanced photocatalytic H_2 production activity of TiO_2 nanoparticles. J Am Chem Soc 134:6575–6578
47. Zhang H, Lv X, Li Y, Wang Y, Li J (2010) P25-graphene composite as a high performance photocatalyst. ACS Nano 4:380
48. Liu J, Bai H, Wang Y, Liu Z, Zhang X, Sun DD (2010) Self-assembling TiO_2 nanorods on large graphene oxide sheets at a two-phase interface and their anti-recombination in photocatalytic applications. Adv Funct Mater 20:105
49. Zhang JT, Xiong ZG, Zhao XS (2011) J Mater Chem 21:3634
50. Gao E, Wang W, Shang M, Xu J (2011) Synthesis and enhanced photocatalytic performance of graphene-Bi_2WO_6 composite. Phys Chem Chem Phys 13:2887
51. Li BJ, Cao HQ (2011) J Mater Chem 21:3346
52. Zhang XF, Quan X, Chen S, Yu HT (2011) Appl Catal B 105:237
53. Zhu MS, Chen PL, Liu MH (2011) ACS Nano 5:4529
54. Li Y, Fan X, Qi J, Ji J, Wang S, Zhang G, Zhang F (2010) Palladium nanoparticle–graphene hybrids as active catalysts for the Suzuki reaction. Nano Research 3:429
55. Metin Ö, Ho SF, Alp C, Can H, Mankin MN, Gültekin MS, Chi M, Sun S (2013) Ni/Pd core/shell nanoparticles supported on graphene as a highly active and reusable catalyst for Suzuki–Miyaura cross-coupling reaction. Nano Res 6:10
56. Li Y, Fan X, Qi J, Ji J, Wang S, Zhang G, Zhang F (2010) Gold nanoparticles graphene hybrids as active catalysts for Suzuki reaction. Mater Res Bull 45:1413
57. Zhang N, Qiu H, Liu Y, Wang W, Li Y, Wanga X, Gao J (2011) Fabrication of gold nanoparticle/graphene oxide nanocomposites and their excellent catalytic performance. J Mater Chem 21:11080
58. Siamaki AR, El Rahman A, Khder S, Abdelsayed V, El-Shall MS, Gupton BF (2011) Microwave-assisted synthesis of palladium nanoparticles supported on graphene: a highly active and recyclable catalyst for carbon–carbon cross-coupling reactions. J Catal 279:1
59. Moussa S, Siamaki AR, Gupton BF, El-Shall MS (2012) Pd-partially reduced graphene oxide catalysts (Pd/PRGO): laser synthesis of Pd Nanoparticles supported on PRGO nanosheets for carbon–carbon cross coupling reactions. ACS Catal 2:145
60. Wu G, Wang X, Guan N, Li L (2013) Palladium on graphene as efficient catalyst for solvent-free aerobic oxidation of aromatic alcohols: role of graphene support. Appl Catal Environ 136–137:177
61. Stein M, Wieland J, Steurer P, Tölle F, Mülhaupt R, Breit B (2011) Iron nanoparticles supported on chemically-derived graphene: catalytic hydrogenation with magnetic catalyst separation. Adv Synt Catal 353:253
62. Coleman JN, Fleming A, Maier S, O'Flaherty S, Minett AI, Ferreira MS, Hutzler S, Blau WJ (2004) J Phys Chem B 108(11):3446–3450

63. Melchionna M, Prato M (2013) Functionalizing carbon nanotubes: an indispensible step towards applications. ECS J Solid State Sci Technol 2:M3040–M3045
64. Singh P, Campidelli S, Giordani S, Bonifazi D, Bianco A, Prato M (2009) Organic functionalisation and characterisation of single-walled carbon nanotubes. Chem Soc Rev 38:2214–2230
65. Tasis D, Tagmatarchis N, Bianco A, Prato M (2006) Chemistry of carbon nanotubes. Chem Rev 106:1105–1136
66. Iijima S (1991) Helical microtubules of graphitic carbon. Nature 354:56
67. Wu B, Kuang Y, Zhang X, Chen J (2011) Noble metal nanoparticles/carbon nanotubes nanohybrids: synthesis and applications. Nano Today 6:75–90
68. Mabena LF, Ray SS, Mhlanga SD, Coville NJ (2011) Nitrogen-doped carbon nanotubes as a metal catalyst support. Appl Nanosci 1:67–77
69. Carraro M, Sartorel A, Toma F, Puntoriero F, Scandola F, Campagna S, Prato M, Bonchio M (2011) Artificial photosynthesis challenges: water oxidation at nanostructures interfaces. Top Curr Chem 303:121–150
70. Sartorel A, Truccolo M, Berardi S, Gardan M, Carraro M, Toma FM, Scorrano G, Prato M, Bonchio M (2011) Oxygenic polyoxometalates: a new class of molecular propellers. Chem Commun 47:1716–1718
71. Herrero MA, Toma FM, Al-Jamal KT, Kostarelos K, Bianco A, Da Ros T, Bano F, Casalis L, Scoles G, Prato M (2009) Synthesis and characterization of a carbon nanotube-dendron series for efficient siRNA delivery. J Am Chem Soc 131:9843–9848
72. Campidelli S, Sooambar C, Lozano Diz E, Elhi C, Guldi DM, Prato M (2006) Dendrimer-functionalized single-wall carbon nanotubes: synthesis, characterization and photoinduced electron transfer. J Am Chem Soc 128:12544–12552
73. Toma FM, Sartorel A, Iurlo M, Carraro M, Rapino S, Hoober-Burkhardt L, Da Ros T, Marcaccio M, Scorrano G, Paolucci F, Bonchio M, Prato M (2011) Tailored functionalization of carbon nanotubes for electrocatalytic water splitting and sustainable energy applications. ChemSusChem 4:1447
74. Toma FM, Sartorel A, Iurlo M, Carraro M, Parisse P, Maccato C, Rapino S, Rodriguez Gonzalez B, Amenitsch H, Da Ros T, Casalis L, Goldoni A, Marcaccio M, Scorrano G, Scoles G, Paolucci F, Prato M, Bonchio M (2010) Efficient water oxidation at carbon nanotube–polyoxometalate electrocatalytic interfaces. Nat Chem 826
75. Li F, Zhang B, Li X, Jiang Y, Chen L, Li Y, Sun L (2013) Highly efficient oxidation of water by a molecular catalyst immobilized on carbon nanotubes. Angew Chem Int Ed 50:12276
76. Le Goff A, Artero V, Jousselme B, Tran PD, Guillet N, Métayé R, Fihri A, Palacin S, Fontecave M (2009) From hydrogenases to noble metal–free catalytic nanomaterials for H_2 production and uptake. Science 326:1384
77. Li YL, Hu FP, Wang X, Shen PK (2008) Electrochem Commun 10:1101
78. Matsumori H, Takenaka S, Mastune H, Kishida M (2010) Appl Catal A 373:176
79. Wu BH, Hu D, Yu YM, Kuang YJ, Zhang XH, Chen JH (2010) Chem Commun 46:7954
80. Wei ZD, Yan C, Tan Y, Li L, Sun CX, Shao ZG, Shen PK, Dong HW (2008) Spontaneous reduction of Pt(IV) onto the sidewalls of functionalized multiwalled carbon nanotubes as catalysts for oxygen reduction reaction in PEMFCs. J Phys Chem C 112:2671–2677
81. Liang Y, Wang HD, Peng D, Chang W, Hong G, Li Y, Gong M, Xie L, Zhou J, Wang J, Regier TZ, Wei F, Dai H (2012) Oxygen reduction electrocatalyst based on strongly coupled cobalt oxide nanocrystals and carbon nanotubes. J Am Chem Soc 134:15849–15857
82. Zhang WD, Jiang LC, Ye JS (2009) J Phys Chem C 113:16247
83. Wang W, Serp P, Kalck P, Faria JL (2005) Visible light photodegradation of phenol on MWNT-TiO_2 composite catalysts prepared by a modified sol–gel method. J Mol Catal A Chem 235:194–199
84. Zhang W-D, Xu B, Jiang L-C (2010) Functional hybrid materials based on carbon nanotubes and metal oxides. J Mater Chem 20:6383–6391
85. Dai K, Peng T, Ke D, Wei B (2009) Photocatalytic hydrogen generation using a nanocomposite of multi-walled carbon nanotubes and TiO_2 nanoparticles under visible light irradiation. Nanotechnology 20:125603

86. Ou Y, Lin J, Fang S, Liao D (2006) MWNT–TiO_2:Ni composite catalyst: a new class of catalyst for photocatalytic H_2 evolution from water under visible light illumination. Chem Phys Lett 429:199–203
87. Wang W, Serp P, Kalck P, Gomes Silva C, Faria JL (2008) Preparation and characterization of nanostructured MWCNT-TiO_2 composite materials for photocatalytic water treatment applications. Mater Res Bull 43:958–967
88. Yao Y, Li G, Ciston S, Lueptow RM, Gray KA (2008) Photoreactive TiO_2/carbon nanotube composites: synthesis and reactivity. Environ Sci Technol 42:4952–4957
89. Vietmeyer F, Seger B, Kamat PV (2007) Anchoring ZnO particles on functionalized single wall carbon nanotubes. excited state interactions and charge collection. Adv Mater 19:2935–2940
90. Chang W-C, Cheng Y-Y, Yu W-C, Yao Y-C, Lee C-H, Ko H-H (2012) Enhancing performance of ZnO dye-sensitized solar cells by incorporation of multiwalled carbon nanotubes. Nanoscale Res Lett 7:166
91. Xie S, Lu X, Zhai T, Li W, Yu M, Liang C, Tong Y (2012) Enhanced photoactivity and stability of carbon and nitrogen co-treated ZnO nanorod arrays for photoelectrochemical water splitting. J Mater Chem 22:14272–14275
92. Ma L-L, Sun H-Z, Zhang Y-G, Lin Y-L, Li J-L, Wang E, Yu Y, Tan M, Wang J-B (2008) Preparation, characterization and photocatalytic properties of CdS nanoparticles dotted on the surface of carbon nanotubes. Nanotechnology 19:115709
93. Cargnello M, Grzelczak M, Rodríguez-González B, Syrgiannis Z, Bakhmutsky K, La Parola V, Liz-Marzán LM, Gorte RJ, Prato M, Fornasiero P (2012) Multiwalled carbon nanotubes drive the activity of metal@oxide core–shell catalysts in modular nanocomposites. J Am Chem Soc 134:11760–11766
94. Planeix JM, Coustel N, Coq B, Bretons V, Kumbhar PS, Dutartre R, Geneste P, Bernier P, Ajayan PM (1994) Application of carbon nanotubes as supports in heterogeneous catalysis. J Am Chem Soc 116:7935–7936
95. Antonetti C, Oubenali M, Raspolli Galletti AM, Serp P, Vannucci G (2012) Novel microwave synthesis of ruthenium nanoparticles supported on carbon nanotubes active in the selective hydrogenation of *p*-chloronitrobenzene to *p*-chloroaniline. Appl Catal Gen 421:99–107
96. Jahjah M, Kihn Y, Teuma E, Gómez M (2010) Ruthenium nanoparticles supported on multiwalled carbon nanotubes: highly effective catalytic system for hydrogenation processes. J Mol Catal A Chem 332:106–112
97. John J, Gravel E, Namboothiri INN, Doris E (2012) Advances in carbon nanotube-noble metal catalyzed organic transformations. Nanotech Rev 1:515–539
98. Yanga X, Wanga X, Qiu J (2010) Aerobic oxidation of alcohols over carbon nanotube-supported Ru catalysts assembled at the interfaces of emulsion droplets. Appl Catal Gen 382:131–137
99. Rodrigues EG, Carabineiro SAC, Delgado JJ, Chen X, Pereira MFR, Orfao JJM (2012) J Catal 285:83–91
100. Zhu J, Holmen A, Chen D (2013) Carbon nanomaterials in catalysis: proton affinity, chemical and electronic properties, and their catalytic consequences. ChemCatChem 5:378–401
101. Li B, Wang C, Yi G, Lin H, Yuan Y (2011) Enhanced performance of Ru nanoparticles confined in carbon nanotubes for CO preferential oxidation in a H2-rich stream. Catal Today 164:74–79
102. Pan HB, Yen CH, Yoon B, Sato M, Wai CM (2006) Recyclable and ligandless Suzuki coupling catalyzed by carbon nanotube-supported palladium nanoparticles synthesized in supercritical fluid. Synt Commun 36:3473–3478
103. Chen X, Hou Y, Wang H, Cao Y, He J (2008) Facile deposition of Pd nanoparticles on carbon nanotube microparticles and their catalytic activity for Suzuki coupling reactions. J Phys Chem C 112:8172–8176
104. Sullivan JA, Flanagan KA, Hain H (2009) Suzuki coupling activity of an aqueous phase Pd nanoparticle dispersion and a carbon nanotube/Pd nanoparticle composite. Catal Today 145:108–113

105. Olivier JH, Camerel F, Ziessel R, Retailleau P, Amadouc J, Pham-Huu C (2008) Microwave-promoted hydrogenation and alkynylation reactions with palladium-loaded multi-walled carbon nanotubes. New J Chem 32:920–924
106. Sokolov VI, Rakov EG, Bumagin NA, Vinogradov MG (2010) New method to prepare nanopalladium clusters immobilized on carbon nanotubes: a very efficient catalyst for forming carbon-carbon bonds and hydrogenation. Fullerenes Nanotubes Carbon Nanostruct 18:558–563
107. Santra S, Ranjan P, Bera P, Ghosh P, Mandal SK (2012) Anchored palladium nanoparticles onto single walled carbon nanotubes: efficient recyclable catalyst for N-containing heterocycles. RSC Adv 2:7523–7533
108. Yoon B, Wai CM (2005) Microemulsion-templated synthesis of carbon nanotube-supported Pd and Rh nanoparticles for catalytic applications. J Am Chem Soc 127:17174–17175
109. Corma A, Garcia H, Leyva A (2005) Catalytic activity of palladium supported on single wall carbon nanotubes compared to palladium supported on activated carbon: study of the Heck and Suzuki couplings, aerobic alcohol oxidation and selective hydrogenation. J Mol Catal A Chem 230:97–105
110. Rodríguez-Pérez L, Pradel C, Serp P, Gomez M, Teuma E (2011) Supported ionic liquid phase containing palladium nanoparticles on functionalized multiwalled carbon nanotubes: catalytic materials for sequential Heck coupling/hydrogenation process. ChemCatChem 3:749–754
111. Iijima S, Yudasaka M, Yamada R, Bandow S, Suenaga K, Kokai F, Takahashi K (1999) Nano-aggregates of single-walled graphitic carbon nano-horns. Chem Phys Lett 309:165–170
112. Li N, Wang Z, Zhao K, Shi Z, Gu Z, Xu S (2010) Carbon 48:1580–1585
113. Brahim A, Hamoudi Z, Takahashi H, Tohji K, Mohamedi M, Khakani MAE (2009) Carbon nanohorns-coated microfibers for use as free-standing electrodes for electrochemical power sources. Electrochem Commun 11:862–866
114. Hamoudi Z, Brahim A, Khakani MAE, Mohamedi M (2013) Electroanalytical study of methanol oxidation and oxygen reduction at carbon nanohorns-Pt nanostructured electrodes. Electroanalysis 25:538–545
115. Zhang L, Zheng N, Gao A, Zhu C, Wang Z, Wang Y, Shi Z, Liu Y (2012) A robust fuel cell cathode catalyst assembled with nitrogen-doped carbon nanohorn and platinum nanoclusters. J Power Sources 220:449–454
116. Zhao Y, Li J, Ding Y, Guan L (2011) Single-walled carbon nanohorns coated with Fe_2O_3 as a superior anode material for lithium ion batteries. Chem Commun 47:7416–7418
117. Xu W, Wang Z, Guo Z, Liu Y, Zhou N, Niu B, Shi Z, Zhang H (2013) Nanoporous anatase TiO2/single-wall carbon composite as superior anode for lithium ion batteries. J Power Sources 232:193–198
118. Itoh T, Danjo H, Sasaki W, Urita K, Bekyarova E, Arai M, Imamoto T, Yudasaka M, Iijima S, Kanoh H, Kaneko K (2008) Catalytic activities of Pd-tailored single wall carbon nanohorns. Carbon 46:172–175
119. Rodriguez NM, Kim M-S, Baker RTK (1994) Carbon nanofibers: a unique catalyst support medium. J Phys Chem 98:13108–13111
120. Pham-Huu C, Keller N, Charbonniere LJ, Ziessel R, Ledoux MJ (2000) Carbon nanofiber supported palladium catalyst for liquid-phase reactions. An active and selective catalyst for hydrogenation of CNC bonds. Chem Commun 1871–1872
121. Park C, Baker RTK (1998) Catalytic behavior of graphite nanofiber supported nickel particles. 2. The influence of the nanofiber structure. J Phys Chem B 102:5168–5177
122. Tsuji M, Kubokawa M, Yano R, Miyamae N, Tsuji T, Jun M-S, Hong S, Lim S, Yoon S-H, Mochida I (2007) Fast preparation of PtRu catalysts supported on carbon nanofibers by the microwave-polyol method and their application to fuel cells. Langmuir 23:387–390
123. Zhu J, Zhou J, Zhao T, Zhou X, Chen D, Yuan W (2009) Carbon nanofiber-supported palladium nanoparticles as potential recyclable catalysts for the Heck reaction. Appl Catal Gen 352:243–250
124. Bonanni A, Huiling Loo A, Pumera M (2012) Graphene for impedimetric biosensing. Trends Anal Chem 37:12–21

Top Curr Chem (2014) 348: 181–204
DOI: 10.1007/128_2013_474

Carbon Nanotubes in Tissue Engineering

Susanna Bosi, Laura Ballerini, and Maurizio Prato

Abstract As a result of their peculiar features, carbon nanotubes (CNTs) are emerging in many areas of nanotechnology applications. CNT-based technology has been increasingly proposed for biomedical applications, to develop biomolecule nanocarriers, bionanosensors and smart material for tissue engineering purposes. In the following chapter this latter application will be explored, describing why CNTs can be considered an ideal material able to support and boost the growth and the proliferation of many kinds of tissues.

Keyword Bone replacement · Carbon nanotubes · Cardiac tissue engineering · Neural regeneration · Tissue engineering

Contents

S. Bosi (✉) and M. Prato
Department of Chemical and Pharmaceutical Sciences, University of Trieste, Address Via Licio Giorgieri, 1 Trieste, Italy
e-mail: prato@units.it

L. Ballerini
Department of Life Sciences, University of Trieste, Address Via Licio Giorgieri, 1 Trieste, Italy

Abbreviations

BMP	Bone morphogenetic protein
BP	Bucky paper
CNFs	Carbon nanofibres
CNT	Carbon nanotube
DNA	Deoxyribonucleic acid
DRG	Dorsal root ganglia
ECM	Extracellular matrix
Hap	Hydroxyapatite
HIV	Human immunodeficiency virus
MEA	Multielectrode array
MWNT	Multiwalled carbon nanotube
NT-3	Neurotrophin3
PLCL	Poly (lactide-*co*-ε-caprolactone)
PLGA	Poly (lactic-*co*-glycolic acid)
rhBMP-2	Recombinant human bone morphogenetic protein-2
RNA	Ribonucleic acid
SWNT	Single walled carbon nanotube

1 Introduction

At a time when the nanotechnologies are dominating the scene in almost all branches of sciences, and even invading our daily life, the search for nanostructurable materials able to provide active support and effective interactions with biosystems at the molecular and submolecular level is very active. In this scenario, in recent years carbon nanotubes (CNTs) are certainly numbered among the most interesting, fascinating and studied nanomaterials for a variety of applications. This particular allotropic form of carbon has, in fact, such peculiar and unique properties that it is potentially exploitable in many application areas of the nanosciences.

The need for materials able to interface with biological systems at the nanoscale is a very hot topic in modern medicine. Carbon nanotubes have found many possible applications not only as promising materials for technological purposes and industrial applications but also in the biomedical field. There is a wide range of possible biological applications of CNTs reported in the literature and therefore a complete review of this topic is a titanic job. We will only refer to representative examples, which can provide the reader with a flavour of the potential of CNTs in this exciting area.

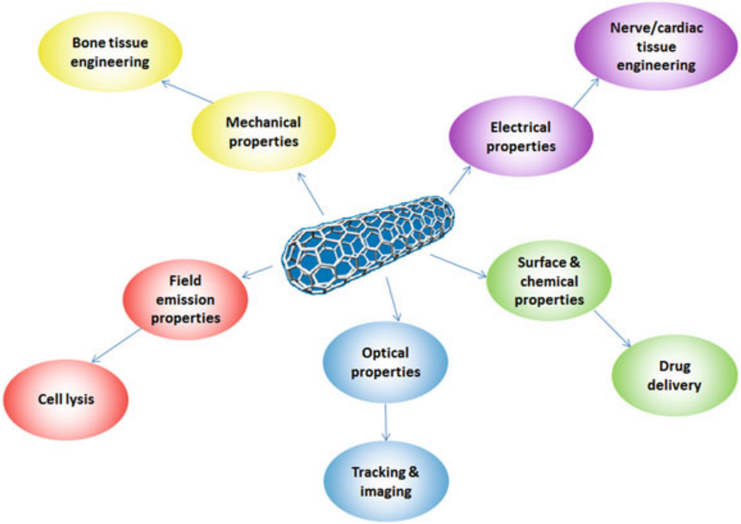

Fig. 1 CNT features and their possible biomedical fields of application

1.1 Biomedical Applications of Carbon Nanotubes

Motivated by the peculiar features of CNTs, research towards their biomedical applications has been progressing rapidly (Fig. 1).

Due to their ability to cross biological membranes and to bear multiple functionalization on their backbones, CNTs have been studied as vectors for many different classes of therapeutic agents. Even though the specific mechanism of internalisation (endocytosis or needle-like penetration) is still not completely clear, it is generally recognised that CNTs are able to enter cells, regardless of cell type and functional groups on their surface [1, 2]. In addition, their high surface area provides attachment sites for molecules, allowing for multiple derivatisation. Moreover, several in vitro and in vivo studies have shown, so far, that many types of chemically functionalised CNTs are biocompatible with the biological milieu, demonstrating how the in vivo behaviour of this material can be modulated by the degree and type of functionalisation, both critical aspects that need to be tuned accurately [3–6]. For these reasons, CNTs have been used as molecular carriers for a variety of therapeutic agents as antitumor drugs [7], antigens for an immunotherapeutic approach [8], targeting moieties (antibodies or peptides) [9] and liposomes that can in turn act as vectors of molecules [10]. CNTs can be used as non-viral molecular transporters for the delivery of short interfering RNA (siRNA) into human T cells and primary cells. The delivery ability and RNA interference efficiency of nanotubes far exceed those of several existing non-viral transfection agents, including various formulations of liposomes. It was suggested that nanotubes could be used as generic molecular transporters for various types of biologically important cells, from cancer cells to T cells and primary cells, with superior silencing effects over conventional liposome-based non-viral agents [11, 12]. CNT-mediated nucleic acid transport has also been studied to deliver antisense oligonucleotides with proapoptotic activity [13, 14] to achieve gene transfer, or to combine a nucleic acid delivery system with photodynamic therapy [15].

The possibility of hosting small molecules inside the cavity of the nanotube has also been explored, allowing the depiction of CNTs as nanocapsules, a role that may realize the "magic bullet" concept of a molecule capable of detecting and selectively destroying a cancer cell [16].

The transporter properties of CNTs can also be exploited for in vivo imaging application, for example, conjugating CNTs with traceable radionuclides or fluorescent probes [17, 18]. Nanotube-based optical biosensors may be used to detect specific targets inside the human body, e.g. tumour cells, wrapping the tubes by a protein that can link only to the targeted cells [19]. For example, a coordinated biosensor made of Au nanoparticles and SWNTs [20] has been studied for detecting HIV-1 PR, an aspartic protease responsible for virion assembly and maturation, on the nanomolar scale [21]. The realization of highly sensitive detection of this protease was promising to expedite development of effective HIV-1 PR inhibitors. Another example in viral disease diagnosis is the electrical detection of hepatitis C virus RNA [22]. A large surface-to-volume ratio and unique electronic properties made CNTs an optimal component for fabricating high-sensitive biodetectors, which were crucially needed in the diagnosis of viral diseases and the development of new anti-viral drugs. It was predictable, therefore, that CNTs might contribute considerably to the treatment of infectious diseases in the future.

Due to their ability to interact with infrared radiation, CNTs can be used for hyperthermal therapy of tumours. In fact, biological tissues are known to be transparent to 700- to 1,100-nm near-infrared light where CNTs show a strong optical absorbance. Appropriately functionalized CNTs with targeting moieties can reach the desired site (tumour) and release locally therapeutic molecules or cause an excessive local heating, leading in both cases to cell death [9].

A few studies have also described CNT antimicrobial activity: Kang et al. have demonstrated that highly purified pristine SWNTs with a narrow diameter distribution, coming in direct contact with cells, can cause severe membrane damage and subsequent cell inactivation [23]. The same authors investigated the antimicrobial potential of SWNTs incorporated within the biomedical polymer poly(lactic-*co*-glycolic acid) (PLGA). They found that *Escherichia coli* and *Staphylococcus epidermidis* viability and metabolic activity were significantly diminished in the presence of SWNT–PLGA, and this effect was correlated with SWNT length and concentration [24].

Finally, and perhaps more importantly, the branch of biomedical sciences where CNTs are finding the widest variety of applications is represented by tissue engineering. This discipline studies the possibilities of replacing damaged, non-functional or degenerated biological tissues by means of artificial (bio)materials able to mimic as much as possible the natural environment.

For their peculiar features of high mechanical strength, elasticity and good thermal and electrical conductivity, CNTs are largely studied as key components for innovative materials in tissue engineering. They have been shown, in many cases, to be biocompatible and to support the growth and the proliferation of many classes of cells. However, as we will discuss in more in detail in the following chapters, the toxicity of this carbon form is still an issue to be clarified.

2 CNTs for Bone Tissue Engineering

Treatment of bone defects in humans, including those associated with the removal of tumours, trauma and abnormal bone development, faces important limitations. Current therapies such as autografts, allographs and metal prostheses do not generally favour bone regeneration in itself. Instead, they replace the lost bone by an artificial material. One novel aspect of modern tissue engineering is the attempt to create tissue replacement by culturing bone cells on synthetic 3D scaffolds or live prosthesis. An ideal scaffold for bone tissue regeneration should possess mechanical properties similar to the bone tissue being replaced, good biocompatibility with surrounding tissue, large degree of porosity and high pore size and high pore interconnectivity for bone tissue ingrowth. The synthetic scaffold material can be either biodegradable, disappearing as the new bone grows, or non-biodegradable. In the latter case, the non-biodegradable material behaves as an inert matrix on which cells proliferate and deposit new live matrix, which must become functional, normal bone. Despite extensive research, no existing man-made scaffold can meet all these requirements. Hence the development of novel biomaterials and scaffold fabrication techniques is critical for the success of bone tissue engineering.

Bone structure and function depend intimately on the arrangement of cellular and noncellular components at the micro- and nanoscale level [25]. These include cell types such as osteoblasts, osteoclasts and osteocytes embedded in a mineralized extracellular matrix consisting of collagen and a number of noncollagenous proteins [25].

The nanocomposite films or materials are expected to support the colonization with cells by some necessary requirements as nanoscale surface roughness, i.e., the presence of irregularities smaller than 100 nm, peculiar morphology or specific characteristics such as hydrophilicity or conducibility.

The surface nano-roughness of the substrates to be colonized should mimic, as much as possible, the nanoarchitecture of the natural extracellular matrix (ECM) as well as of the cell membrane, such as the size of some ECM molecules, their folding and branching. The nanostructure of a material also improves the adsorption of cell adhesion-mediating ECM molecules, present in biological fluids or synthesized and deposited by cells contacting the material. On nanostructured materials the cell adhesion-mediating molecules are adsorbed in advantageous geometrical conformations, allowing for good accessibility of their active sites by the cell adhesion receptors [26, 27].

In comparison with hydrophobic surfaces, wettable surfaces adsorb a lower amount of albumin, i.e. a non-adhesive protein for cells. However, the cell adhesion is optimal only on moderately wettable surfaces. Another property that can be very important is the electroactivity, as electrical charge, electrical potential and electrical conductivity, which could enable the electrical stimulation of cells [28]. Interestingly, the adhesion, growth, maturation and function of cells on electroactive surfaces are improved even without active stimulation of cells with an electrical current. The underlying mechanism probably includes enhanced adsorption of cell adhesion-mediating proteins, a more advantageous geometrical conformation of these proteins for their accessibility by cell adhesion receptors and facilitation of cellular processes, such as activation of ion channels in the cell membrane, movement of charged molecules inside and outside the cell, up-regulated mitochondrial activity and enhanced proteosynthesis (for a review see [29]). Furthermore, electroactive substrates can significantly increase the mechanical and chemical resistance of the implant surface, preventing the release of ions and material particles from the bulk material.

All these special requirements for optimal bone-compatible scaffolds can be met by carbon-based materials and composites as demonstrated by an increasing number of scientific publications. Indeed, the tensile strength of SWNTs is about 100 times higher than that of steel, while their specific weight is about 6 times lower [30–32]. Thus, CNTs could find ideal applications in hard tissue surgery, e.g. to reinforce artificial bone implants, particularly scaffolds for bone tissue engineering made of relatively soft synthetic or natural polymers.

CNTs have been shown to be fully biocompatible with osteocytes and bone cells [33]. MWNTs adjoining bone induce little local inflammatory reaction, show high bone-tissue compatibility, permit bone repair, become integrated into new bone and accelerate bone formation stimulated by recombinant human bone morphogenetic protein-2 (rhBMP-2) [34]. CNTs have been shown to support nucleation of hydroxyapatite (Hap) in correspondence of their defect sites [35]. Moreover, CNTs can also inhibit osteoclastic bone resorption in vivo as reported by Narita and coworkers [36].

Osteosarcoma cells were cultured on chemically modified single-walled carbon nanotubes and MWNTs [33]. CNTs carrying neutral electrical charge (PEG functionalized) sustained the highest cell growth and production of plate-shaped crystals of mineralized bone matrix. There was a dramatic change in cell morphology in osteoblasts cultured on MWNTs, which corresponded with changes in plasma membrane functions.

As a consequence of these encouraging preliminary results, the number of studies on CNTs or CNT composite-based scaffolds for the replacement of defective bone tissue has increased dramatically.

Many naturally occurring biopolymers have been studies in hard tissue engineering to replace bone tissue. Their major problem lies essentially in their low mechanical strength and CNTs have been considered the perfect material to reinforce three-dimensional structures formed by natural polymers. Many bionanocomposites containing SWNTs or MWNTs have been developed with biopolymers like chitosan [37], alginate [38], hyaluronate [39, 40], collagen [41] and polylactic acid (PLA) [42]. All these composites have demonstrated lack of cytotoxicity, more stability and more mechanically resistance with respect to their homologs without CNTs (Fig. 2).

Synthetic polymers have also been utilized together in an attempt to reduce biodegradation rates, although maintaining the tissue requirements, such as poly

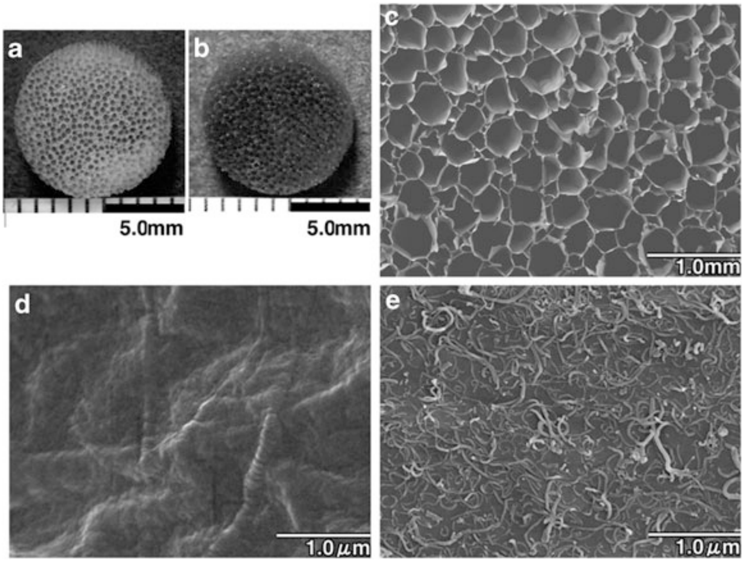

Fig. 2 The whole shape of the uncoated collagen sponge honeycomb (**a**) and MWNT-coated sponge (**b**). (**c**) SEM image of an MWNT-coated sponge. (**d**) SEM image of the inside surface of an uncoated sponge. (**e**) SEM image of the inside surface of the MWNT-coated sponge. Reprinted with permission of [40]

(lactide-*co*-glycolide) (PLGA) [42], polymethyl methacrylate [43], polypropyl fumarate [44, 45], polyurethanes [46] and polycarbosilane [47].

Hydroxyapatite, the inorganic calcium-containing constituent of bone matrix and teeth, has been integrated in CNT-based structures to create a CNT-reinforced brittle HAp bioceramic [48]. In order to make them more "bone-friendly" unfunctionalized CNTs have simply been mixed in HAp matrices but they have shown better results on the spontaneous mineralization of HAp crystals when functionalized. Functionalized CNTs have been also further derivatized by in situ deposition of HAp providing a good biocompatibility with osteoblasts [49].

Another strategy to improve the performances of CNT-based implants as replacement of bone tissue provides for a scaffold designed to deliver useful molecules such as bone trophic factors, immobilized and with reproducible gradients, or that can be further structured to incorporate cell transplants. In a recent study neurotrophin-3 (NT-3) was incorporated in a chitosan-SWCNT hydrogel and, under electrically simulated conditions, a steady release of the agent (NT-3) was observed, suggesting an electrically controlled factor delivery. The presence of CNTs in the biohydrogel composite facilitated the electron transfer more efficiently [50]. A similar strategy can be adopted for releasing bone specific factors from functionalized CNT dispersed polymer scaffolds for effective bone tissue engineering as already done in the case of bone morphogenetic protein (BMP) adsorbed on MWNT-chitosan scaffolds [51].

Electrical stimulation of osteoblast cells may not seem intuitive for any practical advantage, but exposure to alternating currents increased bone cell proliferation and extracellular calcium production of osteoblasts grown on CNT-polylactic acid composites, demonstrating an application for accelerated bone repair [28].

Some in vivo studies have been conducted in animals, implanting CNT composites in defecting bones: COOH-functionalized MWNTs reinforced with polymethyl methacrylate/HAp have been implanted in some holes of a sheep tibia and the cellular response has been examined [43]. The authors have found that this novel composite accelerates cell maturation by providing a mechanically competent bone matrix; this likely facilitates osteointegration in vivo. In another study hyaluronic acid functionalized SWNTs were injected in rat tooth sockets under conditions in which bone formation is compromised (diabetic rats) [52]: results indicate that the bone repair process in the tooth sockets in diabetic rats was significantly restored 14 days after first molar extraction, suggesting that these materials can potentially be useful in therapies for bone tissue reconstruction in normal and adverse metabolic states.

In conclusion, CNTs could be a very good choice as structural and functional constituents of 3D scaffolds for bone tissue engineering. Probably the best solution consists of a complex composite of nanocarbon materials, biopolymers and biominerals enriched with bone growth factors to take advantage of all the positive features typical of each class of materials. An important issue is that so far no sufficient pre-clinical or clinical studies with nanomaterials for bone repair have been conducted while exhaustive toxicological studies on these materials have to be performed.

3 CNTs for Neural Tissue Engineering

Due to the complexity of the nervous system anatomy and function, repairing damaged nerves as well as recovering full function of injured nerves have been particularly challenging when compared to other tissue repairs (such as bone repair). Traditional neural implantation and surgery (such as using autografts, allografts, xenografts and silicon probes for the continuous diagnosis and treatment of neural tissue or other biomaterial nerve graft devices) have posed a variety of problems such as rejection, immune response, incomplete functional recovery and instability of the materials. For these reasons the demand for new biocompatible and long-term stable materials for neural regeneration and total functional recovery is very urgent. Current strategies to approach neuronal regeneration use nerve conduits and synthetic guidance devices, made of degradable or non-degradable compounds that can guide and facilitate peripheral nerve regeneration. Various conduits have been fabricated for bridging nerve gaps after injury, and both natural and synthetic materials have been used [53]. The main characteristic of these materials is a longitudinal organization mimicking the natural structure of the nerve pathway within the brain and spinal cord. They are designed to serve as conduits for axonal elongation and to constrain the direction of regenerative outgrowth. Moreover, they should be able to direct regenerating axons to reconnect with their target neurons and enhance functional restoration of the nerve [54]. Many experiments have been performed to study functional recovery after injury in animal models. A promising strategy for treatment of neuronal injuries is to support and promote axonal growth by the use of nanometer-scale materials, especially nanotubes and nanofibres. They mimic tubular structures that appear in nature, such as microtubules, ion channels and axons. Nanotubes can be produced from various materials, such as carbon, synthetic polymers, DNA, proteins, lipids, silicon and glass. With their exceptional properties of small size, flexibility, strength, inertness, electrical conductivity and ease of combination with various biological compounds they are the perfect candidates for interfacing successfully with damaged neuronal tissues.

Since 2000 when Mattson and colleagues found that CNTs deposited on functionalized CNTs were not only surviving but also elongating their neurites in all directions [55], the study of these materials as functional components of composites for the support of the regeneration of neural tissue has been set up by many research groups.

CNTs seem to be particularly appealing in these applications for all their physical features but above all for their relatively high conductivity, useful to sustain the electrical communication between neuronal cells. Moreover, as in the case of bone regeneration, they can be functionalized with chemical groups or molecules able to improve the growth and the survival of cells. It has also been demonstrated that the charge surface on the CNT wall is crucial for cell wellbeing as indicated by the presence of increased growth cones, longer average neurite length and more elaborated neurite branching. These boosting effects are mainly achieved when positive charges are exposed on CNT surfaces [56].

Neurons and several other cell types appear to adhere and grow extremely well on surfaces with topography on the nanoscale [57]. Just by varying its degree of roughness, a substrate can be cell adhesive or non-adhesive depending exclusively on the surface roughness (as observed for rough or smooth SiO_2). CNTs can be deposited to form bidimensional films or can give the formation of 3D structures in such a way as to control their surface roughness. It was shown that neuronal cells are able to grow and elongate their neurites onto CNT-based substrates with a precise nanotopography [58]. Conductive CNTs have been shown to modulate the growth and the morphology of neuronal cells in a narrow range of conductivity, promoting the outgrowth of neurites with a decrease in the number of growth cones as well as an increase in cell body area [59]. Furthermore, the orientation of CNTs can be controlled and is able to affect the direction of neurites outgrowth [60] and accordingly it should be possible for them to drive the direction of the electric signal propagation. CNTs deposited via a combination of microlithography and chemical vapour deposition supported the growth of neurons, affecting their capability of extending neurites and guiding these cell processes along their length. Surface topography in terms of length of nanotubes was observed to play an important role in process guidance [61]. Neurite processes showed preferential adhesion to the edges of long CNT patterns whereas no selectivity was observed in the short CNT patterns. This behaviour could also be due to the rigidity of CNTs: short CNTs do not

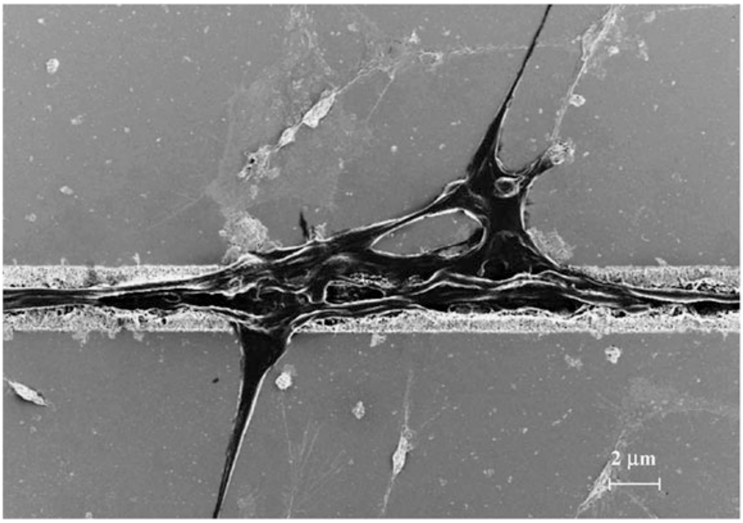

Fig. 3 Scanning electron micrograph demonstrating guided neurite growth along an MWNT array pattern. The extending neurite is shown interacting with the edges of the pattern. This morphology is observed 24 h after initial seeding of the cells. Reprinted with the permission of Zhang et al. [61]

offer the motile growth cone with a suitable surface for process development. The long CNTs in comparison are flexible and undergo deformation to accommodate the proliferating neurite (Fig. 3).

In order to improve further the biocompatibility of unconstrained CNTs and to produce 3D structures able to be colonized by neuronal cells and to foster communication between them, many research groups have tried to incorporate CNTs in polymeric scaffolds where they can play a strengthening and electrically functional role. CNTs have been integrated into various biopolymer-based hydrogels such as collagen [62], chitosan [63] and agarose [64]. In general, all these substrates are very good supports for neuronal cells, able to sustain their growth and their ability to extend neurites and growth cones without much toxicity. However, none of these scaffolds has yet been tested in vivo.

Similar results have been achieved by CNT composites based on synthetic polymers, mostly polyester polymers such as electrospun fibres of poly(D,L-lactic-*co*-glycolic acid (PLGA) [65] and of poly (L-lactic acid-*co*-caprolactone) (PLCL) [66].

The most outstanding results concerning the interface between CNTs and neurons are related to the effects on the electrical activity of neuronal networks. In a study performed in 2005, we compared the electrical activity of hippocampal neuronal networks directly grown on this MWNT mat with that of control networks grown on pure glass by means of the patch-clamp technique [67]. The frequency of spontaneous events (postsynaptic currents, PSCs) in networks cultured on CNTs was strongly boosted and increased (approximately sixfold) compared with controls. Moreover, the balance between inhibitory and excitatory components in the neuronal network was not affected. By means of single-cell electrophysiology techniques, electron microscopy analysis and theoretical modelling, it has been hypothesized that CNTs can provide a kind of shortcut between the proximal and distal compartments of the neuron [68]. This theory, supported by the observation that neuronal membranes establish a tight but discontinuous contact with the CNT substrate, was further corroborated by other experiments where, when cells were forced to fire trains of action potentials, the presence of extra-membrane after depolarization potentials was detected, and this was much more frequent on CNT deposited cells compared to those grown on an inert glassy support. This kind of backpropagating action potentials represents a regenerative ability that neurons exhibit in cellular processes such as the tuning of synaptic activity, the expression of spike timing-dependent plasticity, the release of modulatory messengers and the modulation of synaptic plasticity [69]. Another interesting observation concerns the impact of CNTs on the synaptic activity of neuronal networks: the probability of finding synaptically connected pairs of neurons is almost doubled in the presence of the CNT substrate. Moreover, the synaptic plasticity was also affected because cells grown on CNTs demonstrate a potentiated short-term synaptic condition instead of a normal depression after a presynaptic spike train. All these impressive effects are entirely attributable to the peculiar features of conductivity and physical chemical properties of CNTs that impact on the network activity and spike propagation.

Not only cells but also more complex neuronal systems have been tested on CNTs: embryonic spinal cord and dorsal root ganglia (DRG) explants have been interfaced to a film of purified MWNTs [70]. With respect to the controls, DRG cultured on CNTs displayed a higher number of longer neuronal processes growing in tight contact with the substrate bearing a higher number of growth cones at their tips. These neuronal processes seemed to loosen on the CNT carpet, increasing their contact surface, and were less stiff than in the control. The overall interaction of the DRG with the substrate appears to be very intimate and similar to that reported for cell cultures. DRGs were stimulated and the response to an afferent stimulation was registered by single neurons located in a portion of the slice that was not in contact with the CNTs layer. We found that the amplitude of the response to DRG stimulation was strongly increased in both its excitatory and inhibitory components but the ability to integrate repetitive stimulations was preserved. In addition, the spontaneous activity was also preserved.

CNT coated surfaces can potentially be used for a wide variety of applications such as retinal implants, network repair and neuro-welding.

Recently many research groups have dedicated their attention to the production and the study of neuronal performances. One of the first contributions in this field was that of Khraiche et al. (2009). The authors cultured rat hippocampal neurons on multi-arrayed electrodes (MEAs), whose tips were covered with CNTs (SWNTs). They observed that the electrical activity of the neuronal networks was detectable 4 days after seeding and continued to grow until day 7, while neurons developed on control (bare gold) electrodes showed no electrical activity until day 7. The hypothesis is that the rough SWNT surface provides cells with a larger surface area to adhere to, leading to an increased activation of adhesion molecules (such as integrins), which might in turn promote a faster neuronal differentiation [71]. In this direction, Shein and coworkers coated MEA electrodes with CNTs, obtaining islands with a conductive, three-dimensional, exceptionally high surface area [72]. Dissociated cortical neurons cultured on these electrodes adhered only and directly to these islands, and self-assembled in neuronal networks patterned on the CNT neurochip. Once the neurons had adhered and self-organized, the CNT–MEA allowed very high fidelity, direct recording of neuronal activity, and an effective electrical stimulation of neurons at the electrode sites. An interesting application of this kind of devices was explored by Shoval et al.: they investigated the use of MWNT coated microelectrodes as an interface for retinal recording and stimulation applications [73]. Whole-mount retinas isolated from neonatal mice were placed on the electrodes, allowing electrical recordings of the spontaneous, typical, propagating retinal waves. With respect to commercially available electrodes, recordings from MWNT–MEAs showed a consistently higher signal-to-noise ratio, and a relevant increase in the amplitude of the recorded spikes over a period of minutes to hours was observed. The proposed hypothesis is that a dynamic interaction between MWNTs and neurons produces an improvement in cell–electrode coupling, resulting in the phenomena detected. Finally the authors validated the suitability of their MWNT electrodes for sustained neuronal stimulation.

In another paper, where SWNTs were deposited directly on standard platinum electrodes to fabricate MEAs for electrophysiological recordings, the advantages of CNT–MEAs over metal electrodes in neuronal recordings were further confirmed [74]. In this report, the application of SWNT-modified MEAs to record electrical activity from whole-mount rabbit to standard, platinum electrode-based MEAs was discussed.

Although production of a functionally efficient neural prosthesis is still a long way off, there are some promising nanomaterials that would seem to be very useful for this purpose and CNTs are definitely among them. Their good conductivity and efficient supporting ability together with a confirmed biocompatibility with neuronal cells make CNTs particularly interesting as constituents in biomimetic scaffolds to guide axon regeneration and improve neural activities.

4 Carbon Nanotubes for Cardiac Tissue Engineering

Another tissue in which electrical signals are propagated that can potentially be successfully interfaced with an electroconductive material like CNTs is cardiac tissue. As for the neuronal system, the possibility to have a bi- or three-dimensional substrate able to reinforce and regenerate cardiac functionality could represent incredible progress in many heart pathologies, including heart failure (myocardial infarction) and congenital cardiovascular defects.

Cardiac tissue engineering aims for the development of a bioengineered construct that can provide physical support to the damaged cardiac tissue by replacing certain functions of the damaged extracellular matrix and prevent adverse cardiac remodelling and dysfunction after myocardial infarction. Cardiovascular biomaterials can be based on either biodegradable or non-biodegradable materials. Within this matrix of conductive vs non-conductive and biodegradable vs non-biodegradable materials lie the most commonly studied materials and techniques used to promote heart health. Synthetic polymers offer advantages in their ability to tailor the mechanical properties, and natural polymers offer cell recognition sites necessary for cell, adhesion and proliferation. Most of the injectable scaffolds developed for myocardial applications are, however, non-conductive, lack nanofibrous architectures on the submicrometer scale (10–100 nm in diameter) and are typically mechanically weaker than native heart tissues. For these reasons, CNTs seem to be theoretically the ideal material for a successful biomaterial for cardiac applications.

The first study of biocompatibility of CNTs with cardiac cells has been performed with rat cardiac cells cultured onto a suspension of SWNTs [75]. Within a short time (3 days) CNTs did not display significant toxicity while for longer time the toxic effects have been ascribed to physical interactions. These long-term negative effects have been evidenced after reseeding the cardiac cells: non-viable cells coming from SWNT-treated samples increased by 25%, when compared to reseeded cells not treated with SWNTs.

We discovered outstanding effects on cardiac cells cultured on CNTs substrates. Neonatal rat ventricular myocytes (NRVM) were able to interact with non-functionalized CNT (MWNT) deposited glass coverslips by forming tight contacts with the material (Fig. 4) [76]. Cardiac myocytes modify their viability, proliferation, growth, maturation and electrophysiological properties when interacting with CNT scaffolds. CNTs appear to have two opposing effects on the development: they prolong the proliferative state, which maintains some cells in an undifferentiated state, and they accelerate the maturation of the differentiated cardiac myocytes in terms of a more negative NRVM resting potential compared to control, indication of the fact that the cells become more adult-like. The mechanism that regulates these effects is not clear yet but we have observed by TEM microscopy that CNTs develop irregular tight contacts with the membranes, contacts that are morphologically similar to those seen in neurons cultured on MWNTs [67]. Moreover, it is not excluded that other modifications, indirectly brought about by MWNTs, such as the deposition of the extracellular matrix or the cell contact driven cytoskeletal dynamics, are ultimately responsible for the detected positive effects.

The development of three-dimensional architectures of cardiac cells at the nanoscale able to improve next generation transplantable cell-enriched devices for tissue implants is the main requirement for progress towards a practical application of these materials for heart regenerative medicine [77]. Carbon nanomaterials in the form of carbon nanofibres (CNFs) have been integrated in composites in order to achieve conductive matrices able to accommodate myocardial cells. Carbon nanofibres have been added to biodegradable PLGA to increase the conductivity and cytocompatibility of pure PLGA [78]. Human cardiomiocytes proliferated on the different PLGA:CNF ratios; an increase in proliferation density from 530% on day 1 to 700% on day 5 resulted between the 100:0 and 25:75 (PLGA:CNF wt%) ratio. CNFs are characterized by a structure called stacked-cup carbon nanotubes (the overall structure appears like concentric cylinders) and hence CNFs possess

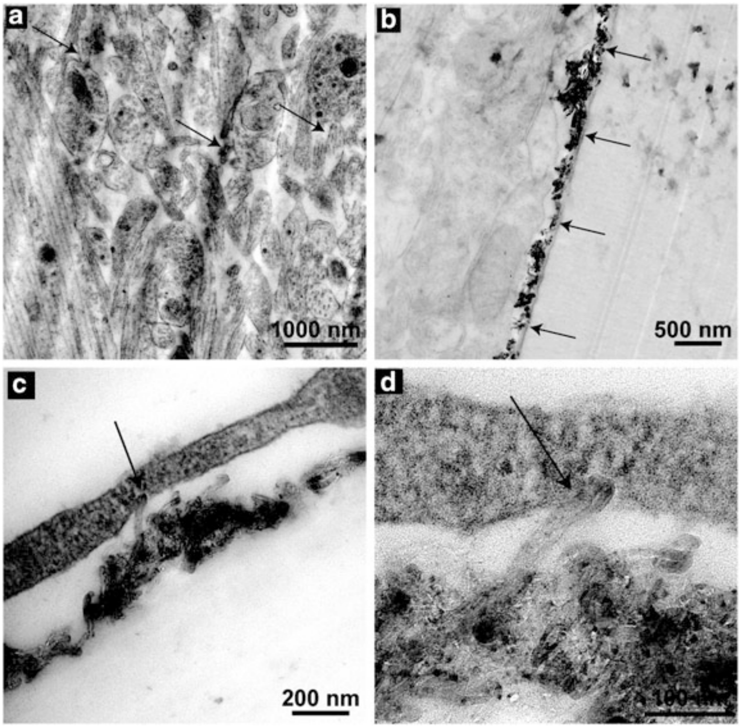

Fig. 4 Characterization of MWNT substrates and ultrastructural interaction between MWNTs and cultured cardiac myocytes. TEM planar section (**a**) of NRVM grown on carbon nanotube layer reveals a healthy organization of cardiac myocyte networks, accompanied by the presence of desmosome-like contacts (*arrows*). TEM sagittal sections (**b**–**d**) illustrate nanotube–membrane contacts. In (**b**), it is possible to appreciate the continuous layer of MWNTs interacting with cells (*arrowheads*); (**c**, **d**) are a series of further high-magnification micrographs from the same section. Note how nanotubes are "pinching" cell membranes (*arrows*). Reprinted with the permission of [67]

nanoscale geometries which imitate the extracellular matrix of various tissues (such as the heart), potentially leading to improved cytocompatibility of these materials [79]. Although requiring further study, CNFs can play a similar important role in promoting cardiomyocyte by increasing victronectin and laminin adsorption, two adhesion glycoproteins of the extracellular matrix that in turn will induce cell adhesion and proliferation. While the mechanism of enhanced cardiomyocyte density is not clearly detailed at this time, it could have to do with the topography of PLGA-CNF composites and/or the increased presence of CNF on PLGA surfaces, which can control initial protein adsorption through altered surface energetics. Pedrotty et al. showed that numerous cardiac cell functions (including adhesion, proliferation and migration) might be modulated by electrical stimulation [80], hence requiring the use of a conductive material in cardiac applications. Also, Mihardjo et al. demonstrated that enhanced myocardial repair following ischemic injury could be achieved using conductive polymers, such as polypyrrole [81]. The conductivity values measured for PLGA-CNF substrates were lower than those of heart tissue (ranging from 0.16 longitudinally to 0.005 S m^{-1} transversely) [82], but future techniques (such as CNF or CNT alignment) may increase the anisotropic conductivity to match that of heart tissue [83]. It is also important not to exceed the stimulatory conductivity of the cells, avoiding a possible decreased cell function.

In terms of carbon nanomaterial-based devices for functional regenerative purposes, an interesting cardiac construct has been produced by Shin and colleagues [84]: CNTs were embedded into photo-crosslinkable gelatin methacrylate (GelMA) hydrogels, resulting in ultra-thin 2D patches where neonatal rat cardiomyocytes were seeded. These cells showed strong spontaneous and stimulated synchronous beating. In addition, a protective effect against doxorubicin (cardio-toxic) and heptanol (cardio-inhibitor) was observed. When released from glass substrates, the 2D cardiac patches (centimetre size) formed 3D soft actuators with controllable linear contractile, pumping and swimming actuation behaviours. CNT concentration of 3 mg/mL led to tissues with optimal electrophysiological functions, while 5 mg/mL showed the maximal protective effect. CNTs formed electrically conductive and collagen fibril-like nanofibres bridging pores, which mechanically strengthened the gel, promoted cardiac cell adhesion and maturation, and improved cell-cell electrical coupling. Compared to existing scaffold materials, CNT-GelMA seems to be a very promising multifunctional cardiac scaffold.

5 Other Tissue Engineering Possibilities for CNTs

Some recent papers describe attempts to explore CNTs as substrates for a variety of different tissues.

Rat hepatocytes have been seeded onto CNT-coated surfaces and their morphological and their functional behaviour has been studied [85]. Primary hepatocytes exhibit different morphological and functional characteristics depending on the surface properties on which they are deposited. Hepatocytes in a serum-containing medium adhered on the CNT surface and formed monolayer configuration in the form of spheroids. This peculiar shape seems to be due to the hydrophobic features of the CNT substrate. Furthermore the expression levels of connexin-32 (a molecule that forms gap junctions for cell–cell communication) were higher on the CNT-coated than on the collagen- and CNT/collagen-coated surfaces used as controls, indicating the development of intracellular communication between cells under those conditions. This study is a very preliminary exploration of CNT-based substrates for hepatocyte cultures that needs further data to verify the real efficacy.

Another interesting practical application of CNT-based composite materials involves the regeneration of dermal tissue in wound healing. From the combination of SWNTs and polyvinylpyrrolidone in aqueous media, Simmons and coworkers have produced a highly pure microporous film that, due to the iodine non-covalently linked to SWNTs, have antiseptic properties and can be used as an antiseptic bandage. Electrical pulses sent through the composite may allow for enhanced cell growth and faster reconstitution of the damaged tissue [86].

Lima and coauthors described a faster and longer-stroke artificial muscle based on yarns made from sheets of CNTs with a solid guest or filler material such as wax; melting and solidifying the wax twists or untwists the yarn and generates motion [87]. Other guest materials are activated by chemical absorption or illumination by light. The new artificial muscle outperforms existing artificial muscles, allowing possible applications such as linear and rotary motors, and might replace biological muscle tissue if biocompatibility can be established.

The so-called bucky paper (BP), a macroscopic assembly of entangled carbon nanotubes, is a relatively new material that can be formed by single, double or multiwalled CNTs with different lengths, diameters or aspect ratios. BP has been proposed for the encapsulation of islet cells for diabetes treatment, as an artificial membrane for retinal and iris pigment epithelial transplantation, as a flexible antiseptic bandage, as immune shielding for cells and tissues, as a carrier for gene or drug delivery and as a scaffold for tissue engineering. BP was recently shown to be non-toxic and not to affect the in vitro proliferation and viability of both normal human arterial smooth muscle cells and human dermal fibroblasts. Martinelli et al. have studied the adhesive properties of BP on a wet compliant substrate [88]. By means of shear and peeling adhesion tests they have shown that BP readily and strongly adheres to a trimmed muscular fascia of a rabbit abdominal wall, chosen as the model substrate. The material has been compared to commercially available prosthetic materials and it was demonstrated to possess superior properties of adhesion and stability. BP could find applications in abdominal prosthetic surgery or for wound closure, thus allowing not only easier surgery procedures but also reduction in the use of conventional perforating fixation, to which serious postoperative complications are usually associated.

6 Toxicity of CNTs

The main bar to the use of CNT-based materials in a biological environment is the controversial question of their potential toxicity. In the literature there are a number of conflicting reports concerning this issue: some investigations have reported toxic effects following the exposure of several cell types to both SWNTs and MWNTs, while others demonstrate very low or insignificant cellular responses. This debate is mainly due to the fact that toxicity depends on factors like purity (metal content), surface modification (charge), dimensions (aspect ratio <3), layer number and degree of dispersion (aggregate formation) [89] (see Table 1).

Metal impurities, especially catalyst metal contaminants, such as Fe, Y, Ni, Mo, and Co coming from production methods are the most important factor in CNT cytotoxicity. Even if it is almost impossible to remove all the impurities completely because they are entrapped in graphitic shells, they can be released in the biological medium causing negative effects [90]. However, acid treated SWNTs and MWNTs

Table 1 Basis of CNT toxicity

	Cell types/ animals	Type of CNTs	CNT toxicity
Metal impurities	H460	SWCNTs containing 19.4%Ni/5.49%Y; 14.3%Ni/2.09%Y; 3.15%Ni/9.21%Co; 22.8%Ni/4.79%Y; 24.1%Ni/4.17%Y; 3.3%Co/1.27%Mo	Nickel is bioavailable at toxicologically significant concentrations
	NR8383; A549	Purified SWCNTs; SWCNTs containing 0.009%Fe/ 2.8%Co/4.2%Mo; purified MWNTs; MWNTs containing Ni	Dose- and time-dependent increase of intracellular ROS; decrease of mitochondrial membrane potential
	RAW264.7	SWCNTs containing 26% Fe or 0.23% Fe	Hydroxyl radical generation: loss of intracellular low molecular weight thiols; accumulation of lipid hydroperoxides
	HaCaT	SWCNTs containing 30% Fe	Formation of free radicals; accumulation of peroxidative product; antioxidant depletion; loss of cell viability
Surface charge and modification	HMMs	Acid-treated, water-soluble SWCNTs	Acid-treated SWCNTs are less aggregated within lysosomes and cytoplasm and cause no significant changes in cell viability or structure
Shape	HUVEC	Pristine SWCNTs; oxidized SWCNTs	Functionalized and pristine SWCNTs have limited cytotoxicity
	Normal mice	MWNTs 1,520 μm or longer	Length-dependent inflammation and formation of granulomas
	Human primary macrophages	Short CNTs; long, tangled CNTs; Long, needle-like CNTs	Tangled CNTs are swallowed into cells; long, needle-like CNTs activate secretion of IL-1α and IL-1β
Length	Normal mice	MWNTs 15–20 μm or longer	Long MWNTs cause inflammation and granulomas
	Human primary macrophages	Short CNTs; long, tangled CNTs; long, needle-like CNTs	Long, needle-like CNTs activate secretion of IL-1α and IL-1β

(continued)

Table 1 (continued)

	Cell types/ animals	Type of CNTs	CNT toxicity
	THP-1; rat	MWNTs 500 nm to 5 μm	MWNTs with an average length of 825 nm induce higher inflammation than those with an average length of 220 nm
	A549; THP-1; Normal mice	MWNTs: length 5–15 μm, diameter 20–60 nm; length 1–2 μm, diameter 60–100 nm; length 1–2 μm, diameter <10 nm	Long and thick MWNTs induce the strongest DNA damage and increase the total cell number in abdominal lavage fluid while similar SWCNTs caused little effect
	P53+/−mice	long MWNTs 1–20 μm	Long MWNTs (short not included) can form fibrous or rod-shaped particles of length around 10–20 micrometer (μm) and induce mesothelioma
Agglomeration	SPC; DRG	Agglomerated SWCNTs; better dispersed SWCNT bundles	Highly agglomerated SWCNTs significantly decrease the overall DNA content
	MSTO-211H	CNT agglomerates; CNT bundles	Suspended CNT-bundles are less cytotoxic than asbestos, rope-like agglomerates
Layer number	RAW 264.7	Pristine graphene	Depletion of the mitochondrial membrane potential and increase of intracellular ROS and apoptosis
	Alveolar macrophage	SWCNTs; MWNTs (diameters 10–20 nm)	SWCNTs > MWNTs

Reprinted with permission of [89]

with a very small metal content are commercially available. The functionalization of CNT surface is determinant to reduce the toxicity: indeed, it has been demonstrated in vitro that appropriately functionalized CNTs are taken up and methabolized by immunoregulatory cells as B and T lymphocytes as well as macrophages, without affecting cell viability. [91]. Furthermore, the functionalization and the surface charge affect the binding of blood proteins and this could greatly alter their cellular interaction pathways and their metabolic fate and can reduce the cytotoxicity [92]. We have demonstrated that chemical functionalization reactions and appended functionalities that lead to shortening or untangling/debundling of aqueous dispersions of f-MWNTs will help to resolve toxicological risks associated with long-fibre exposure [93]. Another important aspect to take into consideration is the administration route used combined with the dose. In general it is very difficult to evaluate the toxicity of CNTs because of the extreme heterogeneity of samples described through the literature. To make experimental results comparable, it is necessary to establish recognized standard CNT samples in toxicity testing and also to establish standardized and reliable methods for evaluating CNT toxicity.

7 Summary and Conclusions

Among the different possible application of CNTs for biomedical purposes, tissue engineering can be acknowledged as one of the more interesting. Thanks to their physical and chemical features, CNTs can provide the final composite with those biomimetic requirements that are fundamental for a full biocompatibility and a functional efficiency. In general the research in this field is still at an early stage and there is still much to do in order to improve the interaction between tissues and materials at cellular and sub-cellular levels and to clarify all doubts regarding toxicity issues but, as reported in this overview, preliminary results are very promising, indicating CNTs as ideal support for tissue growth and recovery.

Acknowledgments This work was supported by the Italian Ministry of Education MIUR (cofin Prot. 2010N3T9M4 and Firb RBAP11C58Y), the European Union through the ERC Advanced Grant "Carbonanobridge".

References

1. Kam NWS, Liu Z, Dai H (2006) Carbon nanotubes as intracellular transporters for proteins and DNA: an investigation of the uptake mechanism and pathway. Angew Chem Int Ed Engl 45: 577–581
2. Kostarelos K, Lacerda L, Pastorin G, Wu W, Wieckowski S, Luangsivilay J, Godefroy S, Pantarotto D, Briand JP, Muller S, Prato M, Bianco A (2007) Cellular uptake of functionalized carbon nanotubes is independent of functional group and cell type. Nat Nanotechnol 2: 108–113

3. Singh R, Pantarotto D, Lacerda L, Pastorin G, Klumpp C, Prato M, Bianco A, Kostarelos K (2006) Tissue biodistribution and blood clearance rates of intravenously administered carbon nanotube radiotracers. Proc Natl Acad Sci 103(9):3357–3362
4. Lacerda L, Ali-Boucetta H, Herrero MA, Pastorin G, Bianco A, Prato M, Kostarelos K (2008) Tissue histology and physiology following intravenous administration of different types of functionalized multiwalled carbon nanotubes. Nanomedicine 3(2):149–161
5. Lacerda L, Herrero MA, Venner K, Bianco A, Prato M, Kostarelos K (2008) Carbon-nanotube shape and individualization critical for renal excretion. Small 4(8):1130–1132
6. Kostarelos K, Bianco A, Prato M (2009) Promises, facts and challenges for carbon nanotubes in imaging and therapeutics. Nat Nanotechnol 4(10):627–633
7. Madani SY, Naderi N, Dissanayake O, Tan A, Seifalian AM (2011) A new era of cancer treatment: carbon nanotubes as drug delivery tools. Int J Nanomedicine 6:2963–2979
8. Fan H, Zhang I, Chen X, Zhang L, Wang H, Da Fonseca A, Manuel ER, Diamond DJ, Raubitschek A, Badie B (2012) Intracerebral CpG immunotherapy with carbon nanotubes abrogates growth of subcutaneous melanomas in mice. Clin Cancer Res 18(20):5628–5638
9. Chakravarty P, Marches R, Zimmerman NS, Swafford AD, Bajaj P, Musselman IH, Pantano P, Draper RK, Vitetta ES (2008) Thermal ablation of tumor cells with carbon nanotubes. Proc Natl Acad Sci 105(25):8697–8702
10. Karchemski F, Zucker D, Barenholz Y, Regev O (2012) Carbon nanotubes-liposomes conjugate as a platform for drug delivery into cells. J Control Release 160(2):339–345
11. Liu Z, Winters M, Holodniy M, Dai H (2007) siRNA delivery into human T cells and primary cells with carbon-nanotube transporters. Angew Chem Int Ed Engl 46(12):2023–2027
12. Herrero MA, Toma FM, Al-Jamal KT, Kostarelos K, Bianco A, Da Ros T, Bano F, Casalis L, Scoles G, Prato M (2009) Synthesis and characterization of a carbon nanotube-dendron series for efficient siRNA delivery. J Am Chem Soc 131(28):9843–9848
13. Jia N, Lian Q, Shen H, Wang C, Li X, Yang Z (2007) Intracellular delivery of quantum dots tagged antisense oligodeoxynucleotides by functionalized multiwalled carbon nanotubes. Nano Lett 7(10):2976–2980
14. Liu M, Chen B, Xue Y, Huang J, Zhang L, Huang S, Li Q, Zhang Z (2011) Polyamidoamine-grafted multiwalled carbon nanotubes for gene delivery: synthesis, transfection and intracellular trafficking. Bioconjug Chem 22(11):2237–2243
15. Zhu Z, Tang Z, Phillips JA, Yang R, Wang H, Tan W (2008) Regulation of singlet oxygen generation using single-walled carbon nanotubes. J Am Chem Soc 130(33):10856–10857
16. Hilder TA, Hill JM (2008) Carbon nanotubes as drug delivery nanocapsules. Curr Appl Phys 8 (3–4):258–261
17. McDevitt MR, Chattopadhyay D, Kappel BJ, Jaggi JS, Schiffman SR, Antczak C, Njardarson JT, Brentjens R, Scheinberg DA (2007) Tumor targeting with antibody-functionalized, radiolabeled carbon nanotubes. J Nucl Med 48(7):1180–1189
18. Ruggiero A, Villa CH, Holland JP, Sprinkle SR, May C, Lewis JS, Scheinberg DA, McDevitt MR (2010) Imaging and treating tumor vasculature with targeted radiolabeled carbon nanotubes. Int J Nanomedicine 5:783–802
19. Agüí L, Yáñez-Sedeño P, Pingarrón JM (2008) Role of carbon nanotubes in electroanalytical chemistry: a review. Anal Chim Acta 622(1–2):11–47
20. ShiH XT, Nel AE, Yeh JI (2007) Coordinated biosensors – development of enhanced nanobiosensors for biological and medical applications. Nanomedicine 2(5):599–614
21. Mahmoud KA, Luong JHT (2008) Impedance method for detecting HIV-1 protease and screening for its inhibitors using ferrocene-peptide conjugate/Au nanoparticle/single-walled carbon nanotube modified electrode. Anal Chem 80(18):7056–7062
22. Dastagir T, Forzani ES, Zhang R, Amlani I, Nagahara LA, Tsui R, Tao N (2007) Electrical detection of hepatitis C virus RNA on single wall carbon nanotube-field effect transistors. Analyst 132(8):738–740
23. Kang S, Pinault M, Pfefferle LD, Elimelech M (2007) Single-walled carbon nanotubes exhibit strong antimicrobial activity. Langmuir 23:8670–8673

24. Aslan S, Loebick CZ, Kang S, Elimelech M, Pfefferle LD, Van Tassel PR (2010) Antimicrobial biomaterials based on carbon nanotubes dispersed in poly(lactic-co-glycolic acid). Nanoscale 2(9): 1789–1794
25. Taton TA (2001) Nanotechnology: boning up on biology. Nature 412:491
26. Webster TJ, Ergun C, Doremus RH, Siegel RW, Bizios R (2000) Specific proteins mediate enhanced osteoblast adhesion on nanophase ceramics. J Biomed Mater Res A 51:475–483
27. Price RL, Ellison K, Haberstroh KM, Webster TJ (2004) Nanometer surface roughness increases select osteoblast adhesion on carbon nanofiber compacts. J Biomed Mater Res A 70: 129–138
28. Supronowicz PR, Ajayan PM, Ullmann KR, Arulanandam BP, Metzger DW, Bizios R (2001) Novel current-conducting composite substrates for exposing osteoblasts to alternating current stimulation. J Biomed Mater Res A 59(3):499–506
29. Shi G, Rouabhia M, Meng S, Zhang Z (2008) Electrical stimulation enhances viability of human cutaneous fibroblasts on conductive biodegradable substrates. J Biomed Mater Res A 84(4): 1026–1037
30. Iijima S, Hichihashi T (1993) Single-shell carbon nanotubes of 1-nm diameter. Nature 363: 603–605
31. Yakobson B, Smalley R (1997) Fullerene nanotubes: C 1,000,000 and beyond some unusual new molecules—long, hollow fibers with tantalizing electronic and mechanical properties—have joined diamonds and graphite in the carbon family. Am Scientist 1997(85):324–337
32. Iijima S (2002) Carbon nanotubes: past, present, and future. Physica B 323(1–4):1–5
33. Zanello LP, Zhao B, Hu H, Haddon RC (2006) Bone cell proliferation on carbon nanotubes. Nano Lett 6(3):562–567
34. Usui Y, Aoki K, Narita N et al (2008) Carbon nanotubes with high bone-tissue compatibility and bone-formation acceleration effects. Small 4(2):240–246
35. Liao S, Xu G, Wang W, Watari F, Cui F, Ramakrishna S, Chan CK (2007) Self-assembly of nano-hydroxyapatite on multi-walled carbon nanotubes. Acta Biomater 3(5):669–675
36. Narita N, Kobayashi Y, Nakamura H et al (2009) Multiwalled carbon nanotubes specifically inhibit osteoclast differentiation and function. Nano Lett 9(4):1406–1413
37. Venkatesan J, Ryu B, Sudha PN, Kim S-K (2012) Preparation and characterization of chitosan-carbon nanotube scaffolds for bone tissue engineering. Int J Biol Macromol 50(2):393–402
38. Yildirim ED, Yin X, Nair K, Sun W (2008) Fabrication, characterization, and biocompatibility of single-walled carbon nanotube-reinforced alginate composite scaffolds manufactured using freeform fabrication technique. J Biomed Mater Res B Appl Biomater 87(2):406–414
39. Sá M, Andrade V, Mendes R, Caliari M, Ladeira L, Silva E, Silva G, Corrêa-Júnior J, Ferreira A (2012) Carbon nanotubes functionalized with sodium hyaluronate restore bone repair in diabetic rat sockets. Oral Dis. doi:10.1111/odi.12030
40. Mendes RM, Silva GA, Caliari MV, Silva EE, Ladeira LO, Ferreira AJ (2010) Effects of single wall carbon nanotubes and its functionalization with sodium hyaluronate on bone repair. Life Sci 87(7–8):215–222
41. Hirata E, Uo M, Takita H, Akasaka T, Watari F, Yokoyama A (2011) Multiwalled carbon nanotube-coating of 3D collagen scaffolds for bone tissue engineering. Carbon 49(10): 3284–3291
42. Hirata E, Uo M, Nodasaka Y, Takita H, Ushijima N, Akasaka T, Watari F, Yokoyama A (2010) 3D collagen scaffolds coated with multiwalled carbon nanotubes: initial cell attachment to internal surface. J Biomed Mater Res B Appl Biomater 93(2):544–550
43. Cheng Q, Rutledge K, Jabbarzadeh E (2013) Carbon nanotube-poly(lactide-co-glycolide) composite scaffolds for bone tissue engineering applications. Ann Biomed Eng 41(5): 904–916. doi:10.1007/s10439-012-0728-8
44. Singh MK, Gracio J, LeDuc P et al (2010) Integrated biomimetic carbon nanotube composites for in vivo systems. Nanoscale 2(12):2855–2863
45. Shi X, Sitharaman B, Pham QP, Liang F, Wu K, Edward Billups W, Wilson LJ, Mikos AG (2007) Fabrication of porous ultra-short single-walled carbon nanotube nanocomposite scaffolds for bone tissue engineering. Biomaterials 28(28):4078–4090

46. Verdejo R, Jell G, Safinia L, Bismarck A, Stevens MM, Shaffer MSP (2009) Reactive polyurethane carbon nanotube foams and their interactions with osteoblasts. J Biomed Mater Res A 88(1):65–73
47. Wang W, Watari F, Omori M, Liao S, Zhu Y, Yokoyama A, Uo M, Kimura H, Ohkubo A (2006) Mechanical properties and biological behavior of carbon nanotube/polycarbosilane composites for implant materials. J Biomed Mater Res B Appl Biomater 82B(1):223–230
48. Shin US, Yoon IK, Lee GS, Jang WC, Knowles JC, Kim HW (2011) Carbon nanotubes in nanocomposites and hybrids with hydroxyapatite for bone replacements. J Tissue Eng 674287
49. Xiao Y, Gong T, Zhou S (2010) The functionalization of multi-walled carbon nanotubes by in situ deposition of hydroxyapatite. Biomaterials 31(19):5182–5190
50. Thompson BC, Moulton SE, Gilmore KJ, Higgins MJ, Whitten PG, Wallace GG (2009) Carbon nanotube biogels. Carbon 47(5):1282–1291
51. Abarrategi A, Gutiérrez MC, Moreno-Vicente C, Hortigüela MJ, Ramos V, López-Lacomba JL, Ferrer ML, del Monte F (2008) Multiwall carbon nanotube scaffolds for tissue engineering purposes. Biomaterials 29(1):94–102
52. Sá M, Andrade V, Mendes R, Caliari M, Ladeira L, Silva E, Silva G, Corrêa-Júnior J, Ferreira A (2012) Carbon nanotubes functionalized with sodium hyaluronate restore bone repair in diabetic rat sockets. Oral Dis. doi:10.1111/odi.12030
53. Panseri S, Cuhna C, Lowery J, Del Carro U, Taraballi F, Amadio S, Vescovi A, Gelain F (2008) Electrospun micro-and nanofiber tubes for functional nervous regeneration in sciatic nerve transections. BMC Biotechnol 8:39–51
54. Bradbury EJ, McMahon SB (2006) Spinal cord repair strategies: why do they work? Nature 7: 644–653
55. Mattson MP, Haddon RC, Rao AM (2000) Molecular functionalization of carbon nanotubes and use as substrates for neuronal growth. J Mol Neurosci 14(3):175–182
56. Hu H, Ni Y, Mandal SK, Montana V, Zhao B, Haddon RC, Parpura V (2005) Polyethyleneimine functionalized single-walled carbon nanotubes as a substrate for neuronal growth. J Phys Chem B 109(10):4285–4289
57. Berry CC, Campbell G, Spadiccino A, Robertson M, Curtis ASG (2004) The influence of microscale topography on fibroblast attachment and motility. Biomaterials 25:5781–5788
58. Sorkin R, Greenbaum A, David-Pur M, Anava S, Ayali A, Ben-Jacob E, Hanein Y (2009) Process entanglement as a neuronal anchorage mechanism to rough surfaces. Nanotechnology 20(1): 015101
59. Malarkey EB, Fisher KA, Bekyarova E, Liu W, Haddon RC, Parpura V (2009) Conductive single-walled carbon nanotube substrates modulate neuronal growth 2009. Nano Lett 9(1): 264–268
60. Galvan-Garcia P, Keefer EW, Yang F, Zhang M, Fang S, Zakhidov AA, Baughman RH, Romero MI (2007) Robust cell migration and neuronal growth on pristine carbon nanotube sheets and yarns. J Biomater Sci Polym Ed 18(10):1245–1261
61. Zhang X, Prasad S, Niyogi S, Morgan A, Ozkan M, Ozkan CS (2005) Guided neurite growth on patterned carbon nanotubes. Sens Actuators B Chem 106:843–850
62. Cho Y, Borgens RB (2010) The effect of an electrically conductive carbon nanotube/collagen composite on neurite outgrowth of PC12 cells. J Biomed Mater Res A 95(2):510–517
63. Huang Y-C, Hsu S-H, Kuo W-C, Chang-Chien C-L, Cheng H, Huang Y-Y (2011) Effects of laminin-coated carbon nanotube chitosan fibers on guided neurite growth. J Biomed Mater Res A 99A(1):86–93
64. Lewitus DY, Landers J, Branch JR, Smith KL, Callegari G, Kohn J, Neimark AV (2011) Biohybrid carbon nanotube/agarose fibers for neural tissue engineering. Adv Funct Mater 21: 2624–2632
65. Lee HJ, Yoon OJ, Kim DH, Jang YM, Kim HW, Lee WB, Lee NE, Sung S (2010) Neurite outgrowth on nanocomposite scaffolds synthesized from PLGA and carboxylated carbon nanotubes. Adv Eng Mater 11:B261–B266

66. Jin GZ, Kim M, Shin US, Kim HW (2011) Neurite outgrowth of dorsal root ganglia neurons is enhanced on aligned nanofibrous biopolymer scaffold with carbon nanotube coating. Neurosci Lett 501:10–14
67. Lovat V, Pantarotto D, Lagostena L, Cacciari B, Grandolfo M, Righi M, Spalluto G, Prato M, Ballerini L (2005) Carbon nanotube substrates boost neuronal electrical signaling. Nano Lett 5(6): 1107–1110
68. Cellot G, Cilia E, Cipollone S et al (2009) Carbon nanotubes might improve neuronal performance by favouring electrical shortcuts. Nat Nanotechnol 4:126–133
69. Waters J, Schaefer A, Sakmann B (2005) Backpropagating action potentials in neurones: measurement, mechanisms and potential functions. Prog Biophys Mol Biol 87:145–170
70. Fabbro A, Villari A, Laishram J, Scaini D, Toma FM, Turco A, Prato M, Ballerini L (2012) Spinal cord explants use carbon nanotube interfaces to enhance neurite outgrowth and to fortify synaptic inputs. ACS Nano 6(3):2041–2055
71. Khraiche ML, Jackson N, Muthuswamy J (2009) Early onset of electrical activity in developing neurons cultured on carbon nanotube immobilized microelectrodes. In: Conference proceedings: annual international conference of the IEEE engineering in medicine and biology, Minneapolis (MN, US), pp 777–780
72. Shein M, Greenbaum A, Gabay T, Sorkin R, David-Pur M, Ben-Jacob E, Hanein Y (2009) Engineered neuronal circuits shaped and interfaced with carbon nanotube microelectrode arrays. Biomed Microdevices 11(2):495–501
73. Shoval A, Adams C, David-Pur M, Shein M, Hanein Y, Sernagor E (2009) Carbon nanotube electrodes for effective interfacing with retinal tissue. Front Neuroeng 2:4
74. Fabbro A, Cellot G, Prato M, Ballerini L (2011) Interfacing neurons with carbon nanotubes: (re)engineering neuronal signaling. Prog Brain Res 194:241–252
75. Garibaldi S, Brunelli C, Bavastrello V, Ghigliotti G, Nicolini C (2006) Carbon nanotube biocompatibility with cardiac muscle cells. Nanotechnology 17(2):391–397
76. Martinelli V, Cellot G, Toma FM et al (2012) Carbon nanotubes promote growth and spontaneous electrical activity in cultured cardiac myocytes. Nano Lett 12(4):1831–1838
77. Dvir T, Timko BP, Kohane DS, Langer R (2011) Nanotechnological strategies for engineering complex tissues. Nat Nanotechnol 6(1):13–22
78. Stout D, Basu B, Webster TJ (2011) Poly(lactic-co-glycolic acid): carbon nanofiber composites for myocardial tissue engineering applications. Acta Biomater 7(8):3101–3112
79. Tran PA, Zhang L, Webster TJ (2009) Carbon nanofibers and carbon nanotubes in regenerative medicine. Adv Drug Deliv Rev 61:1097–1114
80. Pedrotty DM, Koh J, Davis BH, Taylor DA, Wolf P, Niklason LE (2005) Engineering skeletal myoblasts: roles of three-dimensional culture and electrical stimulation. Am J Physiol Heart Circ Physiol 288:H1620–H1626
81. Mihardja SS, Sievers RE, Lee RJ (2008) The effect of polypyrrole on arteriogenesis in an acute rat infarct model. Biomaterials 29:4205–4210
82. Roberts-Thomson KC, Kistler PM, Sanders P, Morton JB, Haqqani HM, Stevenson I, Vohra JK, Sparks PB, Kalman JM (2009) Fractionated atrial electrograms during sinus rhythm: relationship to age, voltage, and conduction velocity. Heart Rhythm 6:587–591
83. Bal S (2010) Experimental study of mechanical and electrical properties of carbon nanofiber/epoxy composites. Mater Design 31:2406–2413
84. Shin SR, Jung SM, Zalabany M, Kim K, Zorlutuna P, Kim SB, Nikkhah M, Khabiry M, Azize M, Kong J, Wan KT, Palacios T, Dokmeci MR, Bae H, Tang X, Khademhosseini A (2013) Carbon nanotube embedded hydrogel sheets for engineering cardiac constructs and bioactuators. ACS Nano 7(3):2369–2380
85. Koga H, Fujigaya T, Nakashima N, Nakazawa K (2011) Morphological and functional behaviors of rat hepatocytes cultured on single-walled carbon nanotubes. J Mater Sci Mater Med 22(9):2071–2078
86. Simmons TJ, Rivet CJ, Singh G, Beaudet J, Sterner E, Guzman D, Hashim DP, Lee SH, QianG, Lewis KM, Karande P, Ajayan PM, Gilbert RJ, Dordick JS (2012) Application of CNT

to wound healing biotechnologies. Nanomaterials for Biomedicine. ACS Symposium Series, pp 155–174

87. Lima MD, Li N, De Andrade MJ et al (2012) Electrically, chemically, and photonically powered torsional and tensile actuation of hybrid carbon nanotube yarn muscles. Science 338: 928–932
88. Martinelli A, Carru GA, D'Ilario L, Caprioli F, Chiaretti M, Crisante F, Francolini I, Piozzi A (2013) Wet adhesion of buckypaper produced from oxidized multiwalled carbon nanotubes on soft animal tissue. ACS Appl Mater Interfaces 5(10):4340–4349. doi:10.1021/am400543s
89. Liu Y, Zhao Y, Sun B, Chen C (2013) Understanding the toxicity of carbon. Acc Chem Res 46(3): 702–713
90. Liu X, Gurel V, Morris D, Murray DW, Zhitkovich A, Kane AB, Hurt RH (2007) Bioavailability of nickel in single-wall carbon nanotubes. Adv Mater 19(19):2790–2796
91. Dumortier H, Lacotte S, Pastorin G, Marega R, Wu W, Bonifazi D, Briand JP, Prato M, Muller S, Bianco A (2006) Functionalized carbon nanotubes are non-cytotoxic and preserve the functionality of primary immune cells. Nano Lett 6:1522–1528
92. Salvador-Morales C, Basiuk EV, Basiuk VA, Green MLH (2007) Effects of covalent functionalisation on the biocompatibility characteristics of multi-walled carbon nanotubes. J Nanosci Nanotechnol 8:1–10
93. Ali-Boucetta H, Nunes A, Sainz R, Herrero MA, Tian B, Prato M, Bianco A, Kostarelos K (2013) Asbestos-like pathogenicity of long carbon nanotubes alleviated by chemical functionalization. Angew Chem Int Ed Engl 52(8):2274–2278

Top Curr Chem (2014) 348: 205–236
DOI: 10.1007/128_2013_451

Folds and Buckles at the Nanoscale: Experimental and Theoretical Investigation of the Bending Properties of Graphene Membranes

Vittorio Morandi, Luca Ortolani, Andrea Migliori, Cristian Degli Esposti Boschi, Emiliano Cadelano, and Luciano Colombo

Abstract The elastic properties of graphene crystals have been extensively investigated, revealing unique properties in the linear and nonlinear regimes, when the membranes are under either stretching or bending loading conditions. Nevertheless less knowledge has been developed so far on folded graphene membranes and ribbons. It has been recently suggested that fold-induced curvatures, without in-plane strain, can affect the local chemical reactivity, the mechanical properties, and the electron transfer in graphene membranes. This intriguing perspective envisages a materials-by-design approach through the engineering of folding and bending to develop enhanced nano-resonators or nano-electro-mechanical devices. Here we present a novel methodology to investigate the mechanical properties of folded and wrinkled graphene crystals, combining transmission electron microscopy mapping of 3D curvatures and theoretical modeling based on continuum elasticity theory and tight-binding atomistic simulations.

Keywords 3D reconstruction · Bending rigidity · Geometric phase analysis · Graphene · Tight binding · Transmission electron microscopy

---

V. Morandi (✉), L. Ortolani, A. Migliori and C. Degli Esposti Boschi
CNR-IMM Bologna, via Gobetti 101, I-40129 Bologna, Italy
e-mail: morandi@bo.imm.cnr.it

E. Cadelano and L. Colombo
Department of Physics, University of Cagliari, Cittadella Universitaria,
I-09042 Monserrato (Ca), Italy

Contents

Abbreviations

BLE	Bilayered edged graphene
CNT	Carbon nanotube
CVD	Chemical vapor deposition
DP	Diffraction pattern
FFT	Fast Fourier transform
GPA	Geometric phase analysis
HRTEM	High resolution transmission electron microscopy
STEM	Scanning transmission electron microscope
TB	Tight-binding
TEM	Transmission electron microscope

1 Introduction

The capabilities of modern low-voltage aberration-corrected TEMs and STEMs, in terms of resolution in imaging and associated spectroscopies, enable the investigation of a wide range of properties of graphene-based materials, with atomic sensitivity and resolution. Among these investigations we can find the morphological aspects (shape, dimensions, thickness), as well as the structural ones (crystalline habits, edges, defects, strain), to the physical and chemical properties (doping, functionalization) of the systems under analysis, [1–5], using these instruments and the related techniques as fundamental tools for the investigation of graphene-based materials [6, 7].

In this work we will focus on the structural properties of graphene membranes and, in more detail, on their 3D structure, showing how this can be reconstructed through a combined experimental–theoretical approach taking into account, on one side, geometric phase analysis (GPA) of HREM [8, 9] images, and, on the other, a combination of continuum elasticity theory and atomistic TB simulations.

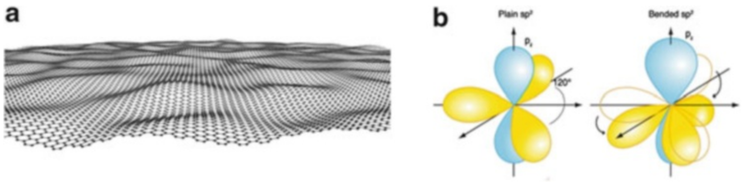

Fig. 1 (**a**) 3D sketch of an intrinsically bent free-standing graphene flake; (**b**) graphical representation of the bent sp^2 orbitals

2 Mapping Curvature at the Nanoscale

The stability of 2D crystals was debated for decades since, according to the so-called Mermin–Wagner theorem, in 2D lattices thermal agitation will induce long wavelength fluctuations which will destroy the long-range crystalline order [10]. The existence of graphene was then debated until the discovery of a full set of 2D crystals in 2005 [11].

Since the beginning it was clear that the structure of graphene was not perfectly flat; nevertheless nowadays not so much is known on the precise 3D structure of free-standing membranes. Indeed, free-standing graphene exists as a crumpled sheet stabilized by its intrinsic corrugations [12]. Ripples and folds induce curvatures in the 2D carbon lattice, bending the sp^2 sigma bonds and locally modifying the electronic properties of the materials (see Fig. 1).

Graphene membranes, when not supported or suspended, folds, realizing complex structures [13–15]. It is worth noting that whenever the honeycomb lattice bends, its electronic transport properties change, and interesting edge conduction states can be obtained over micrometric lengths. This suggested the possibility to engineer the transport properties of this material by modifying its 3D structure, and strain and bending have been the subject of intense theoretical and experimental studies [16–19]. Recent results indicate that the curvature induced by folding can be at the origin of significant changes of chemical reactivity [20, 21] and of the mechanical [22] and charge transport properties [23, 24] of graphene membranes.

The folding of graphene membranes depends on several factors, like lattice orientations, crystal defects, and possibly adsorbed molecules, as well as on the surrounding environment [25–28]. A deeper understanding of the mechanism leading to the bending and the folding of the membranes is still an issue and a deeper understanding of the curvature mechanics in graphene is essential to understand the profound relations between its 3D structure and its properties. In this framework there are two methodologies typically adopted to recover 3D structures at the nanoscale, i.e., electron tomography in the TEM and scanning probe microscopy (SPM).

Unfortunately, neither of these techniques work properly for suspended graphene membranes. Indeed, electron tomography needs to acquire more than 100 images of the same region in different projections to reconstruct its 3D structure successfully [29], a requirement that hardly matches with the high electron beam damage

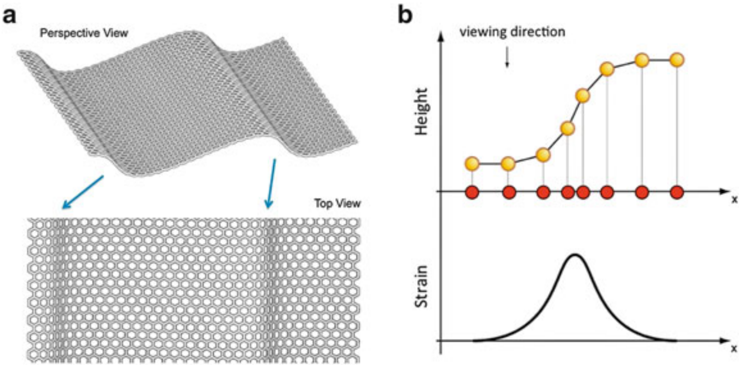

Fig. 2 (**a**) Schematics of the perspective view and the top view of a bent 2D crystal; (**b**) 1D sloped atomic chains (*yellow circles*) with the corresponding projected image on the x-axis (*red circles*) (*top*) and calculated apparent strain along the x-axis (*bottom*)

sensitivity, even at low energies, of graphene membranes [30]. On the other hand, SPM typically needs supported samples to accomplish the interaction between the probe and the membranes and to avoid, or at least minimize, artifacts due to modification of the structure of the membrane [31].

Here we present a novel method to map 3D deformations in suspended graphene membrane, requiring only one micrograph, and based on the so-called GPA that will be discussed in detail in the following.

The idea behind this is indeed very simple. If we observe in the TEM a wrinkled two-dimensional crystal like that depicted in Fig. 2a, the microscope will provide us with a projected image of the crystal lattice in the direction of the beam. The effect of this projection is that regions of the membrane not perpendicular to the electron beam will appear as compressed. Therefore, from the measurements of these apparent strains in the image of the lattice, in principle one can calculate back the local slope of the flake with respect to the electron beam.

To focus this approach, we can consider a simplified model, such as that represented in Fig. 2b, where, on the top, a one-dimensional chain of atoms showing a height variation is depicted. Despite interatomic distances being kept fixed, in the TEM image we will see the atomic positions projected in the direction of the beam over the x-axis, indicated by the red circles. It is worth noting that the distances between the projected positions in the image varies in accordance with the slope of the undulated atomic chain. At the bottom of Fig. 2b is shown a profile of the local strain as it would be calculated from the projected atomic positions. Using simple geometry, it is clear that a measure of this *apparent strain* in the image will provide an immediate measure of the local slope of the undulated chain, thereby providing a complete reconstruction of its two-dimensional structure.

Let us introduce in more detail the principles of image formation in the TEM, as this will be the basis for a complete understanding of the strain recovery techniques. If we consider a crystal illuminated by an electron beam, as in the TEM, each of the

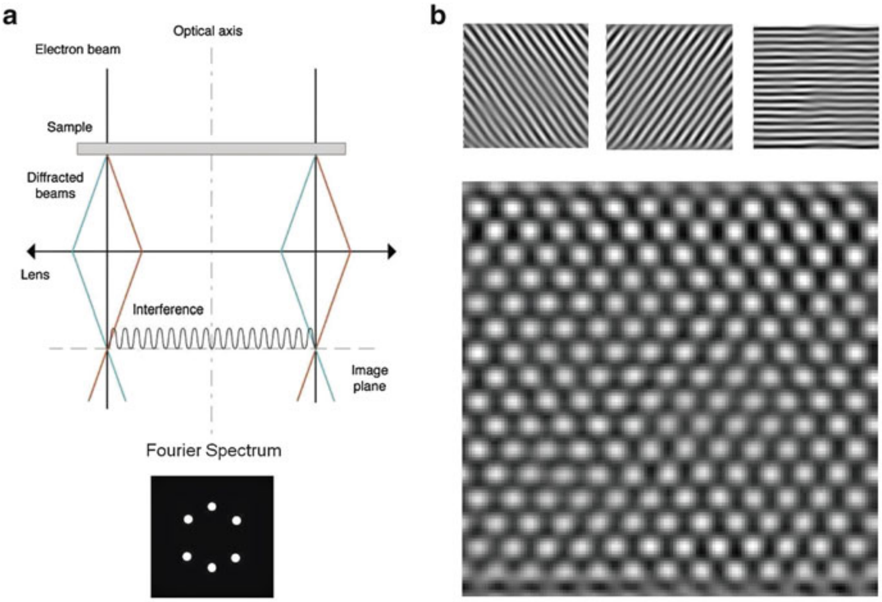

Fig. 3 (**a**) Schematics of the interference pattern generation on the image plane and typical hexagonal direction pattern of a honeycomb crystal lattice; (**b**) HREM image formation by the superposition of three interference patterns generated by three different families of planes

crystal planes forming the structure will split the electron beam into multiple beams, the unscattered beam and several diffracted beams, as shown at the top of Fig. 3a. The objective lens of the TEM at high magnification, i.e., in the *high resolution* imaging mode, is set to bring those diffracted beams to superimpose on the image plane, resulting in an interference pattern, where the fringes follow the direction of the original crystal planes. At the top of Fig. 3b there are reported, as an example, three sets of diffracted wavefronts representing three independent sets of crystal planes.

The results of the superposition of these diffracted wavefronts is shown at the bottom. The interference pattern represents the so-called high resolution electron microscopy image (HREM). In the reciprocal space, like in a diffraction pattern, the fringes appear as couples of symmetric spots, indicating a precise frequency corresponding to the spacing of the fringes, as shown at the bottom of Fig. 3a. A real as well as an apparent deformation of the crystal plane periodicities, like those highlighted in Fig. 2, will result in a deformation of the fringes in the image, and the corresponding information in the reciprocal space will be encoded in the region around the corresponding spot. Therefore, once taking into account the ability to separate the contribution to the modulation of the fringe spacing in an HREM image of the real and of the apparent deformations of the crystal, the problem of mapping undulations and bending of a graphene membrane can be reduced to recovering the strain out of the HREM image.

2.1 Geometric Phase Analysis

GPA is a technique that analyzes the geometric distortions in the HREM image of a crystal lattice by means of Fourier analysis. The reconstructed phase is called *geometric* to avoid confusion with the electronic phase of the electron wavefront: its meaning and the information it contains on the geometric distortions of the image will be explained and discussed in the following. It is appropriate at this point to introduce some formalism that will facilitate understanding of the underlying mechanism of GPA strain reconstruction.

An HREM micrograph is a 2D image and a vector $\boldsymbol{r}$ can be defined in order to indicate the position of a point. The intensity $I(\boldsymbol{r})$ of the HREM image, as discussed in the previous section, is represented by the superposition of interference fringes created by the various beams diffracted by the sample. We can identify the direction of these beams, and the direction of the relative system of fringes in the image, with the wave-vectors $\boldsymbol{g}$ of the reciprocal space. If we consider the image of a perfect crystal, free from any deformation, its intensity $I(\boldsymbol{r})$ can be expressed as a Fourier series over the frequencies $\boldsymbol{g}$, as

$$I(\boldsymbol{r}) = \sum_{\boldsymbol{g}} I_{\boldsymbol{g}} \mathrm{e}^{2\pi i\, \boldsymbol{g}\cdot\boldsymbol{r}}, \tag{1}$$

where $I_{\boldsymbol{g}}$ is a coefficient representing the *intensity* of the fringe system originating from that particular $\boldsymbol{g}$. In the reciprocal space the Fourier transform of (1) becomes:

$$\tilde{I}(\boldsymbol{k}) = \sum_{\boldsymbol{g}} I_{\boldsymbol{g}} \delta(\boldsymbol{k} - \boldsymbol{g}), \tag{2}$$

where δ is the Dirac delta function. For a perfect crystal, the reciprocal space is non-zero only at the positions of the $\boldsymbol{g}$ vectors.

Deformations in the specimen lattice can be introduced using the displacement field $\boldsymbol{u}(\boldsymbol{r})$ with the following transformation [32]:

$$\boldsymbol{r} \mapsto \boldsymbol{r} - \boldsymbol{u}(\boldsymbol{r}). \tag{3}$$

The effect of this displacement vector field is that the reciprocal lattice directions $\boldsymbol{g}$ are not defined globally for the crystal; instead they are local, depending on the position $\boldsymbol{g}(\boldsymbol{r})$. Then for a deformed crystal (1) becomes

$$I(\boldsymbol{r}) = \sum_{\boldsymbol{g}} I_{\boldsymbol{g}}\, \mathrm{e}^{2\pi i\, \boldsymbol{g}\cdot\boldsymbol{r}} \mathrm{e}^{-2\pi i\, \boldsymbol{g}\cdot\boldsymbol{u}(\boldsymbol{r})}. \tag{4}$$

In real crystals lattice distortions are not the only imperfections present, since we need to take into account thickness variations and, as in the case of graphene membranes, possible undulations. All these effects require one to consider the intensity coefficients $I_{\boldsymbol{g}}$ to be the local function $I_{\boldsymbol{g}}(\boldsymbol{r})$ of the position [8]. If we define the complex functions $H_{\boldsymbol{g}}(\boldsymbol{r})$ as

$$H_{\boldsymbol{g}}(\boldsymbol{r}) = I_{\boldsymbol{g}}(\boldsymbol{r})\mathrm{e}^{-2\pi i\,\boldsymbol{g}\cdot\boldsymbol{u}(\boldsymbol{r})}. \tag{5}$$

then the Fourier transform of (4) becomes

$$\tilde{I}(\boldsymbol{k}) = \sum_{\boldsymbol{g}} \tilde{H}_{\boldsymbol{g}}(\boldsymbol{k}) \otimes \delta(\boldsymbol{k}-\boldsymbol{g}). \tag{6}$$

In the case of a deformed crystal, in the reciprocal space there is now some dispersion of the intensity around the positions of the reciprocal vectors $\boldsymbol{g}$. The information about the deformations in the sample is encoded in the $\tilde{H}_{\boldsymbol{g}}(\boldsymbol{k})$ functions. The amplitude term of these functions will give the modulation in intensity of the interference fringes in the direction of each $\boldsymbol{g}$, while the phase term describes the variations in the inter-fringe spacing around the image area. As already mentioned, this phase term is called *geometric phase*.

The original HREM digital image is transformed by FFT to its frequency spectrum and the pixels close to a specific $\boldsymbol{g}$ vector are selected using a circular mask. The distance between two nearby $\boldsymbol{g}$s limit the diameter of the mask, and therefore it limits the resolution of the reconstructed maps, which is usually of the order of a nanometer. The effect of the shape of the mask is beyond the scope of this manuscript and the explicit expression of the mask will be omitted in the following calculations (see [33] for details).

Selecting the region of the reciprocal space around a particular $\boldsymbol{g}$ we are selecting one specific $\tilde{H}_{\boldsymbol{g}}(\boldsymbol{k})$ and setting the origin of the Cartesian reference system to the position of $\boldsymbol{g}$. Inverse FFT will give back the complex image:

$$\mathrm{FFT}\big(\tilde{H}_{\boldsymbol{g}}(\boldsymbol{k})\big) = H_{\boldsymbol{g}}(\boldsymbol{r}) = I_{\boldsymbol{g}}(\boldsymbol{r})\mathrm{e}^{-2\pi i\,\boldsymbol{g}\cdot\boldsymbol{u}(\boldsymbol{r})+\phi_g}. \tag{7}$$

When transforming back an additional phase constant, ϕ_g emerges. Mathematically the process should recover H back without any additional term, but the pixel nature of the image makes it impossible to determine exactly the position of the $\boldsymbol{g}$, which often lies in a sub-pixel position. This error in the re-centering of the reciprocal space means that a δ-like component is still present and will transform back to a constant phase in real space. The constant phase term $\phi_{\boldsymbol{g}}$ is removed from the reconstructed phase by re-normalizing the background over a reference area of the map [8].

The result of the reconstruction procedure is a complex image corresponding to one $H_{\boldsymbol{g}}(\boldsymbol{r})$. Amplitude and phase terms will be calculated according to the equations

$$\begin{array}{rcl} I_g(\boldsymbol{r}) & = & \Re\big(H_{\boldsymbol{g}}(\boldsymbol{r})\big) \\ P_{\boldsymbol{g}}(\boldsymbol{r}) & = & \Im\big(H_{\boldsymbol{g}}(\boldsymbol{r})\big) - \phi_{\boldsymbol{g}} \end{array}, \tag{8}$$

where $\Re$ and $\Im$ stands respectively for real and imaginary parts. The displacement field $\boldsymbol{u}(\boldsymbol{r})$, is a two-dimensional vector field, and to recover it in every direction it is necessary to reconstruct the $H_{\boldsymbol{g}}$ of two non-collinear $\boldsymbol{g}_1$ and $\boldsymbol{g}_2$. Mathematically we need to find two vectors $\boldsymbol{a}_1$ and $\boldsymbol{a}_2$, in the real space, solving the equation

$$\boldsymbol{u}(\boldsymbol{r}) = -\frac{1}{2\pi}\left[P_{\boldsymbol{g}_1}\boldsymbol{a}_1(\boldsymbol{r}) + P_{\boldsymbol{g}_2}\boldsymbol{a}_2(\boldsymbol{r})\right]. \tag{9}$$

From the displacement field $\boldsymbol{u}(\boldsymbol{r})$ it is finally possible to calculate the strain tensor ϵ [8]:

$$\epsilon = \begin{pmatrix} \varepsilon_{xx} & \varepsilon_{xy} \\ \varepsilon_{yx} & \varepsilon_{yy} \end{pmatrix} = \begin{pmatrix} \frac{\partial u_x}{\partial x} & \frac{\partial u_x}{\partial y} \\ \frac{\partial u_y}{\partial x} & \frac{\partial u_y}{\partial y} \end{pmatrix}. \tag{10}$$

All these procedure are available as a series of script implementing numerically GPA reconstructions and strain calculations. The software gives the strain tensor as separated components expressed as follows [8]:

$$\begin{array}{lcll} \varepsilon_{xx} & = & \frac{\partial u_x}{\partial x} & \text{Symmetric strain } E_x \\ \varepsilon_{yy} & = & \frac{\partial u_y}{\partial y} & \text{Symmetric strain } E_y \\ \varepsilon_{xy} & = & \frac{1}{2}\left(\frac{\partial u_x}{\partial y} + \frac{\partial u_y}{\partial x}\right) & \text{Symmetric strain } E_{xy}. \\ \Delta_{xy} & = & \frac{1}{2}\left(\frac{\partial u_x}{\partial x} + \frac{\partial u_y}{\partial y}\right) & \text{Mean dilatation } D_{xy} \\ \omega_{xy} & = & \frac{1}{2}\left(\frac{\partial u_y}{\partial x} - \frac{\partial u_x}{\partial y}\right) & \quad \text{Rotation } R_{xy} \end{array} \tag{11}$$

The definition of the x and y reference axis are chosen by the user at his own convenience.

GPA provides the instruments to reconstruct lattice deformations starting from the HREM image of a crystalline sample. All the limits of the technique are due to this specific image-based approach. As already stated, the image is representative of the lattice structure of the sample. Intensity features in the image, however, will be directly connected to the arrangement of planes in the sample only under restrictive conditions. A set of constraints is imposed by the HREM technique itself and others lie in the sample structure. It is beyond the scope of this manuscript to examine all the parameters determining the limits and the precision of the reconstructed strain maps [33]. Here it is important to note that the objective lens, and other imaging parameters, can strongly affect the result of the analysis. Most of the problems arising from the way the microscope transfers the spatial information from the specimen to the imaging plane can be minimized by using the latest generation aberration-corrected microscopes. The aberration-corrected microscope transfer function provides a faithful transfer of spatial frequency over a large range. The remaining geometric distortions induced by the lenses are removed by subtracting from the resulting phase images a reference deformation map specific to the microscope used.

The sample itself can present some important problems in the analysis of the HREM images. Variations in the thickness of the sample in the area under investigation induce an additional geometric phase displacements that will be impossible to distinguish from those induced by changes in the interatomic distances. Strong intensity variations of the interference fringes and, in the limiting case, a contrast inversion, will be interpreted by the numerical routine as an additional phase displacement not related to any physical strain.

Graphene membranes resolve or minimize many of the above-mentioned problems. The most important limitation in TEM sample preparation is the control over the thickness of the specimen. In the case of FGC membranes the thickness is ideally uniform, and it can be experimentally determined at atomic level without error and is normally constant over a large area. In our analysis we will concentrate on the determination of the apparent compression induced by the vertical geometrical projection of the bent membrane. We thus have a quasi-perfect sample to investigate with the GPA technique.

2.2 Experimental Reconstruction of Bent Graphene Membranes

Particular care was taken in setting up the experimental conditions for HREM imaging. The experiments were performed using the aberration-corrected Tecnai F20 TEM available at the CNRS-CEMES of Toulouse (http://www.cemes.fr), operated at an acceleration voltage of 100 kV to avoid structural damage to the carbon lattice. The sample was chosen according to the following criteria: it must have an explicit geometrical distortion, where the effect of projection induced apparent strain and real mechanical strain could be easily separated. Two kinds of sample were analyzed. The first were mechanically exfoliated graphite flakes, where thin electron transparent flakes can be easily obtained with thin borders composed of few-layers, typically folded over themselves. Natural graphite powder was exfoliated using a mortar and pestle and successively sonicated in isopropanol for additional exfoliation and dispersion. The resulting solution was drop-cast over standard 3 mm TEM holey carbon grids. The second kind of sample were graphene crystals grown by CVD on copper substrate and then transferred on a 3-mm TEM grid.

In Fig. 4 is shown the HREM image of a graphene flake prepared as highlighted before. The flake is folded over itself along two borders. From an analysis of the borders (0002) fringes it is possible to state that the flake is composed of three superimposed graphene layers (six total layers). By looking closer at the edges, as in inset (a) of Fig. 4, it is possible to determine the stacking order of the composing graphene sheets. The series of intensity peaks corresponding to the position of benzene rings in the stacked layers is highlighted by red circles. Their alignment along lines not perpendicular to the flake edge is characteristic of ABAB stacking.

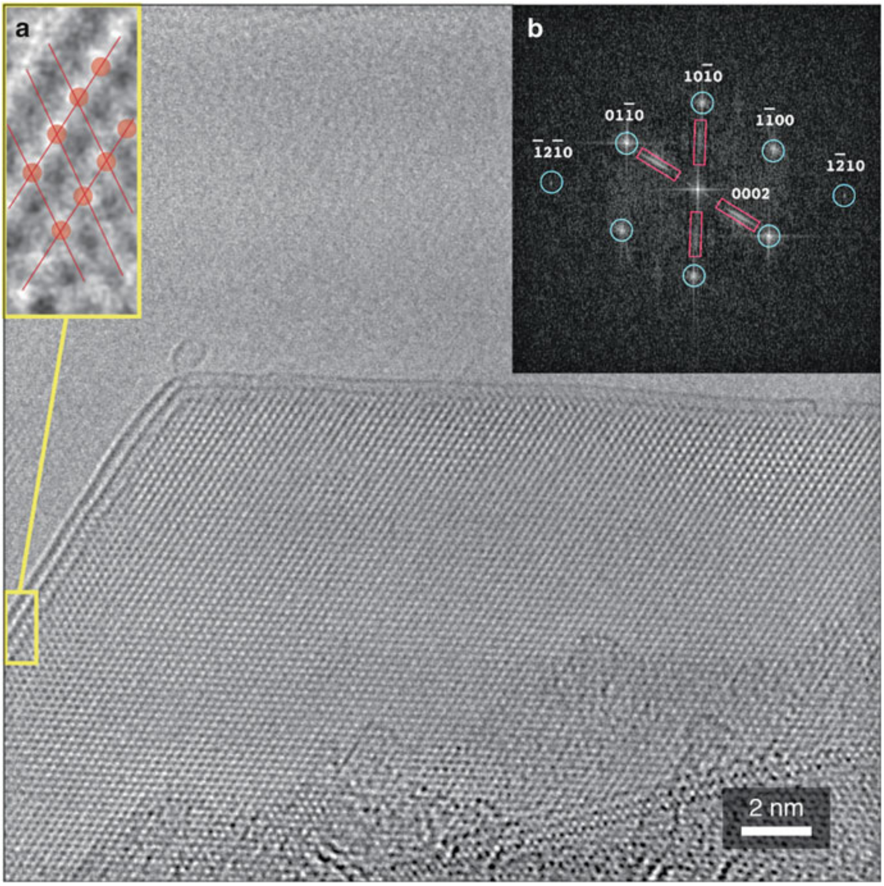

Fig. 4 HREM image of the border of an FGC flake. The membrane is folded over itself on two sides, exposing (0002) fringes, which makes possible to determine the number of layers in the membrane as 3. The inset (*a*) shows a close-up of the (0002) folded zone in the *yellow rectangle*. From the disposition of the intensity peaks it is possible do determine that the flake has *ABA* staking sequence. The inset (*b*) shows the FFT of the HREM image. Graphite reflections are marked for easier view (*blue circles*) and (0,0,0,2) reflections of the two borders are clearly visible (*red rectangles*)

Inset (b) of the same figure shows the FFT spectrum of the image. Graphite principal reflections are highlighted (blue circles) along with folded borders (0002) reflections (red rectangles).

An important feature of the image is the defocus difference which is apparent between the left-side and upper borders. The left border shows some evident Fresnel fringes due to under-focus, while the upper border is almost at focus, with no Fresnel fringe visible. This suggest that there is some height difference between the two regions, leading to the hypothesis that the membrane bends near the border, inducing a compression of the projected atomic positions.

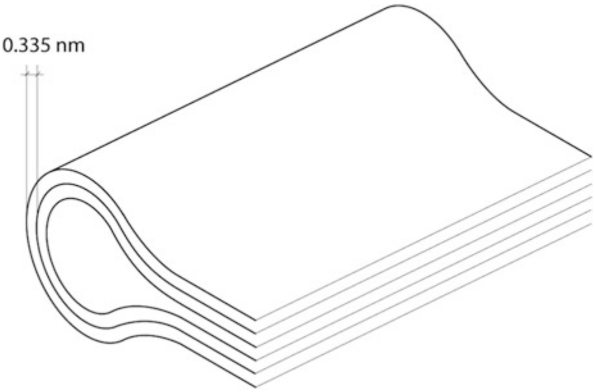

Fig. 5 Proposed schematics for the structure of the folded flake under investigation

Following this hypothesis, it is possible to make a model of the 3D structure of the folded border of the graphene flake, as reported in Fig. 5. The three-layers flake starts to bend, makes a curve, and folds over itself forming six stacked layers.

Looking back to the experimental image, it is worth noting that this flake is folded along particular directions. Indeed, looking at the FFT spectrum of the image we note that the upper and left border are folded respectively perpendicularly to $(01\bar{1}0)$ and $(10\bar{1}0)$ lattice direction. This means that when the three layers superimpose after the border bending they will stack over the original three matching lattice positions and, eventually, preserving the overall ABAB stacking.

What is important to note is that in this case the bending, and therefore the apparent strain in the projected lattice image, will be only in one direction. The sample is therefore in a suitably simple configuration to test GPA 3D reconstruction. It is important to stress here that a hypothesis of 3D structure of the flake, as shown in the schematics of Fig. 5, can be made from basic knowledge of the material and from a careful inspection of the HREM image itself (geometry, defocus variations, etc.). However, it is not possible in any way to *quantify* the surface height variation from a standard analysis of the HREM image. We will show that this can be obtained by GPA.

The first step in GPA is the reconstruction of the phase displacement maps relative to at least two non collinear $\boldsymbol{g}$ vectors. In the case of the flake under investigation we selected $(01\bar{1}0)$, $(10\bar{1}0)$, and $(1\bar{1}00)$ reflections of the reciprocal lattice. Figure 6 shows the results of the reconstruction. To select the $\tilde{H}_g(\boldsymbol{k})$ coefficients a numerical mask has been used, with an aperture corresponding to a final resolution of about 0.5 nm in the reconstructed phase maps.

The first noticeable feature of the phase maps of Fig. 6 is that large phase displacements can be seen in the $(10\bar{1}0)$ direction, near the upper border. Figure 7 shows the phase map for the $(10\bar{1}0)$ direction. Three triangular regions of significant phase displacement are aligned over the border and are indicated by white arrows. The right one is the larger and the most intense. A slight phase displacement is noticeable corresponding to these regions in the $(1\bar{1}00)$ direction, while in the $(01\bar{1}0)$ direction the phase is almost flat all over the flake.

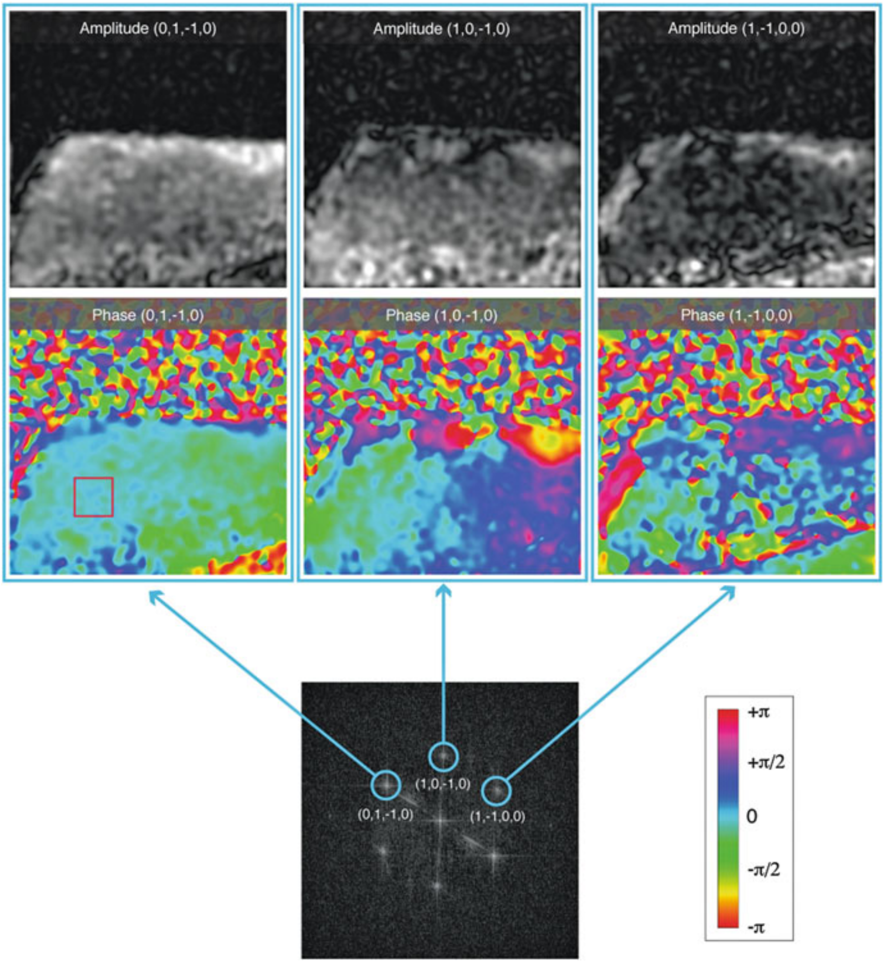

Fig. 6 Reconstructed amplitude and phase maps for the graphite reflections indicated by *blue circles* in the FFT of the image of Fig. 4. Variations in the phase values are mapped with a color scale. Large phase variations are visible near the upper border in the reconstructed phase map from the $(1, 0, \bar{1}, 0)$ ***g*** vector. Reference areas to re-normalize the phase backgrounds were taken in the regions corresponding to that marked by the *red rectangle* in the $(0, 1, \bar{1}, 0)$ phase map. The lateral dimension of the reconstructed phase maps is identical to that of the original HREM image (27.60 nm)

The apparent compression we are looking for is therefore acting displacing $(10\bar{1}0)$ and $(1\bar{1}00)$ fringes, leaving almost unmodified the $(01\bar{1}0)$ direction. To calculate strain maps we need to define a reference axis to project their components. A possible choice is the direction $(2\bar{1}\bar{1}0)$, assuming the flake is bent with a slope in that direction.

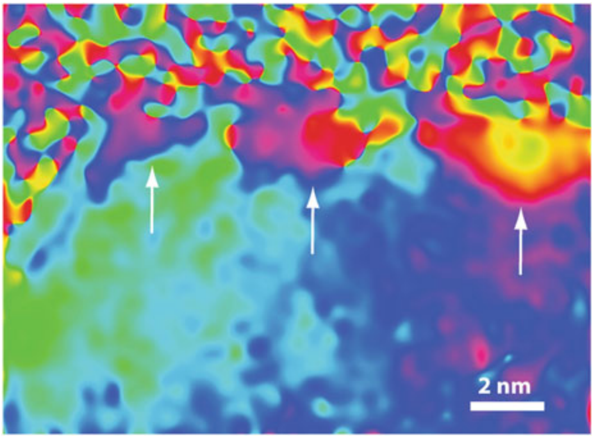

Fig. 7 Phase map reconstructed for the $(10\bar{1}0)$ direction. *Arrows* indicate large phase variations at the border of the flake

Figure 8 shows a close-up of the border region in HREM imaging and in the $(10\bar{1}0)$ phase map. The plot of Fig. 8c is taken in the marked region and shows that a large phase variation is local along the direction of the $(2\bar{1}\bar{1}0)$ lattice planes. We can form a hypothesis for the model of the atomic structure of the flake in this region as shown in Fig. 8d. According to the scheme in Fig. 5, three layers bend in the positive z direction while the other three bend in the opposite direction, creating a hollow space near the border curvature.

The calculated amplitude maps are generally slowly varying, except for some localized regions for $(1\bar{1}00)$ and $(01\bar{1}0)$. Between the large phase bumps of the $(1\bar{1}00)$ map, localized contrast inversions will be likely to generate artifacts during strain calculations [33]. The same problem is present in the marked region of the $(01\bar{1}0)$ amplitude map, near the left border. We will avoid these regions during analysis of the calculated strain maps.

This structural hypothesis will be verified by calculating the strain field map when choosing the Cartesian reference system indicated in Fig. 8a, i.e., with the x-axis in the $(2\bar{1}\bar{1}0)$ direction. As already discussed, we need two phase maps calculated for two non-collinear directions to recover the 2D strain field. Every couple of $\boldsymbol{g}$ vectors is mathematically equivalent, so a good criterion will be to choose the couple resulting in the higher signal-to-noise ratio. We checked different combinations and all the results were consistent. In the end, the best results have been obtained using the $(01\bar{1}0)$ and $(10\bar{1}0)$ directions.

Figure 9 shows the results for the strain maps ε_{xx} and ε_{yy}. They are significantly more affected by noise than the phase images because of the numerical process of calculating the derivative of the phase [34]. Nevertheless, the main features of the maps can be easily identified.

The central part of the flake is almost strain free in both the x and y components. Along the x-direction we recognize some strain change associated with the borders of the three regions already noted near the upper border. Consistent with the choice of axes, the largest strain variation is associated with the zone highlighted in Fig. 8a, b).

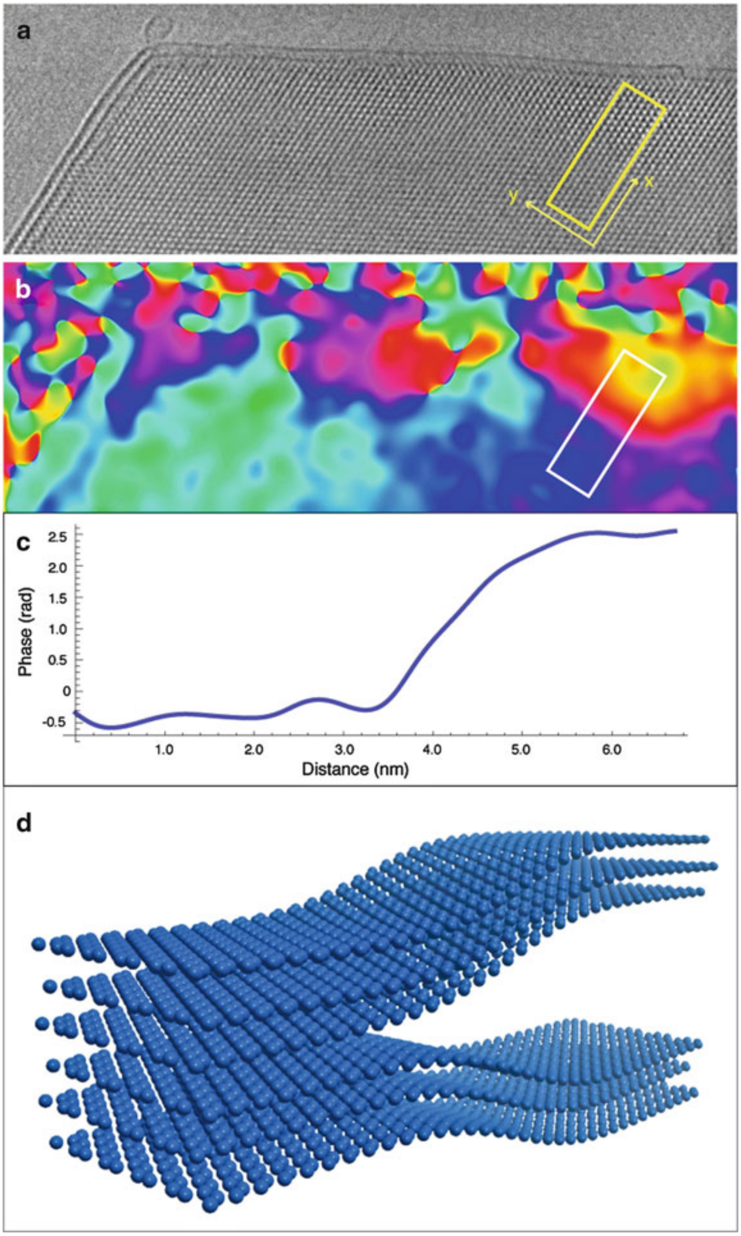

Fig. 8 (**a**) HREM image of the flake near the upper border. The region of interest (ROI) is marked by the rectangle and the Cartesian reference system for further analysis is indicated. (**b**) Corresponding region of the $(01\bar{1}0)$ phase map. The same ROI of (**a**) is reported. (**c**) Plot of the phase profile along the x-axis in the region of interest. (**d**) Schematics of the atomic structure of the flake in the ROI

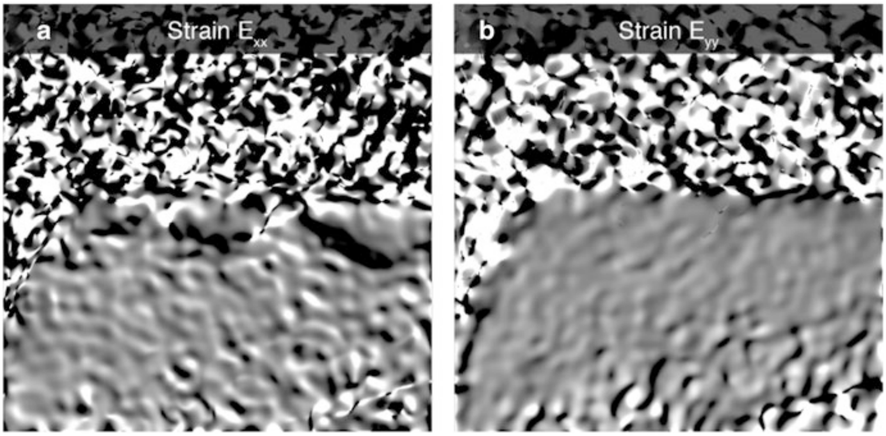

Fig. 9 Calculated strain field maps. (**a**) Components of the strain field along the $(2\bar{1}\bar{1}0)$ x-direction and (**b**) along the $(01\bar{1}0)$ perpendicular y-direction

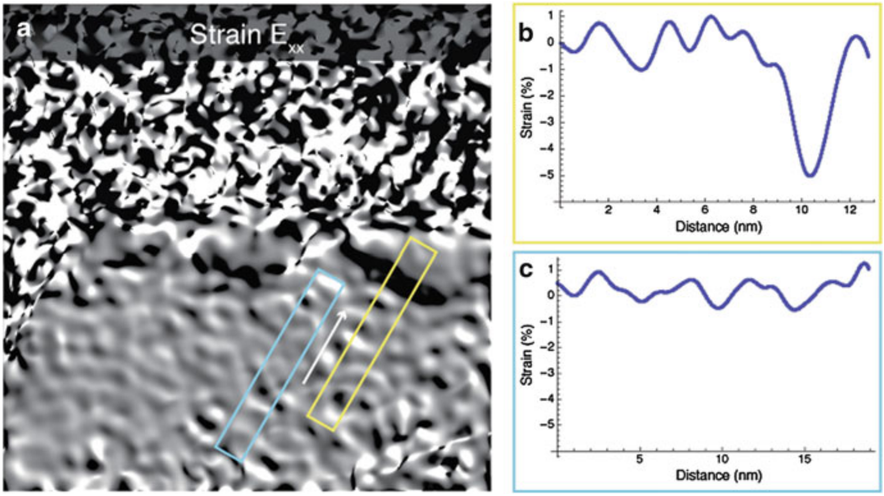

Fig. 10 (**a**) Calculated strain map E_{xx} in the $(2\bar{1}\bar{1}0)$ direction. (**b**) Profile of the strain intensity along the *yellow* ROI. (**c**) Profile of the strain intensity for the *blue* ROI. Profiles are acquired in the direction indicated by the *white arrow*

To recover the local deformation of the membranes from the strain maps we should retrieve the local slope value from the measured strain. For this purpose we need to find a zone were the apparent compression can be assumed to be along one direction only.

Recalling Fig. 8, it is possible to identify a region showing local uniaxial strain due to the geometric projection of the bent 3D atomic structure. The zone corresponds to the region marked with the yellow rectangle in Fig. 10a. According to the one-dimensional model previously discussed, we should find the peak of the compression associated to the position of the curvature inversion point in the bent flake.

Figure 10b shows the profile of the strain along the yellow rectangle. The plot indeed shows a localized peak in the strain corresponding to the middle region of the phase ramp of Fig. 8c. The measured compression is about 5%. Such a value is extremely high for a pure mechanical in-plane compression of the crystal lattice.

Taking into account that graphene has a Young's modulus of about 1 Tpa, a 5% compression implies a stress of about 10^{28} N/nm^2. Even if graphene should resist such a force without breaking the interatomic bonds, a compression like this would result in a 3D deformation. Thus, once more, we consider that such a strain is apparent, and due to the effect of projection of the bent flake on the *xy*-plane.

The profile of the unstrained central area (blue rectangle of Fig. 10c) enables analysis of the noise of the image. The two plots of Fig. 10 are obtained using the same intensity scale to visualize background oscillations easily. An average of the strain free area background shows noise oscillations of about 0.6%. Such oscillations are mainly due to the poor contrast of the graphite fringes in the HREM image. This noise is amplified by the numerical calculations performed by the GPA to obtain the derivative maps, and it is the first limitation of this technique. Nevertheless, in this case, a relatively good signal-to-noise ratio, with a few percent strain, is still present.

For each value of the position of the map, a value for the slope of the surface of the flake can be calculated, by means of simple trigonometry, that it is able to define immediately the local angle α between the flake surface and the *xy*-plane in terms of the strain ε as

$$\cos(\alpha) = (1 - \varepsilon). \tag{12}$$

From the value of α it is straightforward to calculate its tangent for each value of the strain. Then, the reconstruction of the 3D atomic structure of the graphite flake can be calculated from the fit of the local slope, which is the first derivative of the height displacement of the flake surface. A straight integration can give directly the atomic positions.

Figure 11 shows the results of the structure simulation. In the inset of Fig. 11a the integrated height as a function of the distance is plotted, and the three dimensional model is calculated accordingly. Each stacked layer change its z position of about 0.8 nm, as indicated in the lateral projection of Fig. 11b. It is almost certain that the bent structure of the three-layers graphene flakes can be reconstructed only from the analysis of the apparent strain in the HREM image.

The same method can be applied to a single graphene layer as that reported in Fig. 12 [35]. The membrane was grown by chemical vapor deposition (CVD) on a copper substrate and transferred on a TEM grid. The HREM image shows the folded edge of a monolayer membrane; the border is visible by the (0002) graphite lattice fringe and the two layers in the stacked regions are rotated by an angle $\theta = 21.7°$, as shown by the fast Fourier transform (FFT) in the bottom left corner inset.

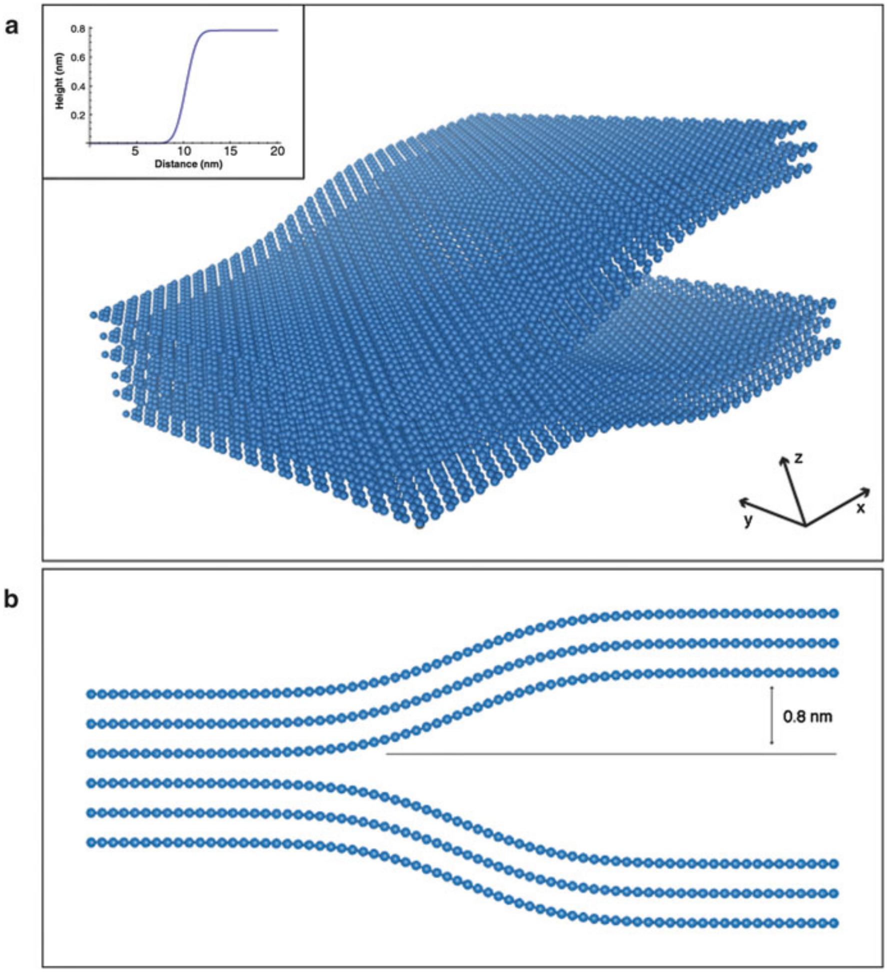

Fig. 11 Schematics of the reconstructed structure of the flake. (**a**) Perspective view. In the *inset* a plot of the elevation of each graphene layer. (**b**) Lateral view of the structure

In the top right corner a schematics of the superimposed lattices as they appear projected in the image is given. In addition it is clearly shown that the membranes are not atomically clean and adsorbates or residues from the growth are either on top or in between the membranes, changing its three dimensional configuration.

Figure 13 reports the resulting strain map in the direction perpendicular to the folded border. In the map a compression running along the border is clearly visible, close to a relaxed central area, where the two lattices are in contact and a strained internal region, parallel to the border. Analyzing the deformation in the two compressed region along the border, marked with 1 and 2 (see the profiles on the right of Fig. 13), and following the same procedure described before, it is possible

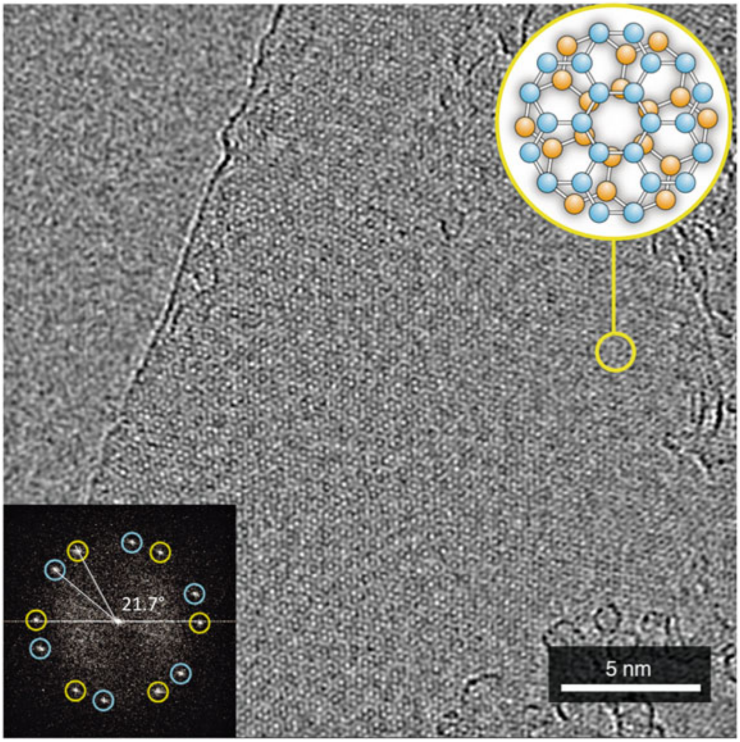

Fig. 12 HREM image of a single layer graphene flake folded edge. *Bottom left corner*: FFT of the image, showing the stacking orientation of the two lattices. *Top right corner*: schematics of the folded lattice

to interpret the strain as apparent and induced by the curvature of the fold, and therefore to estimate a maximum slope of 16° over a length of 3 nm in both regions, corresponding to a height variation of 0.8 nm.

Another example of a graphene flake showing a more pronounced 3D structure is reported in Fig. 14, where a different region of the same border of the flake shown in Fig. 12 is reported. The HREM image in Fig. 14a clearly shows an isolated defect on the folded border, indicated by the white circle, and two lines of compression joining at the defect site at the border, highlighted with the white lines. These curved compressed regions are clearly shown in the strain map in Fig. 14b. As before, we can analyze the strain along the two regions marked with (1) and (2), therefore measuring a height variation of about 1 nm over a length of 4 nm with a slope of 16° in region 1, and of 0.9 nm over a length of 2 nm and a slope of 27° in region 2. Therefore we can interpret the observed compression lines as a curved wrinkle induced in the folded edge by the defect, and the two membranes are wrapping in their interior the carbonaceous contaminants shown in the HREM micrograph.

It is worth noting that in all the reconstructed structures, close to the fold the curvature of the membrane is expected to increase up to 90°, and this is not

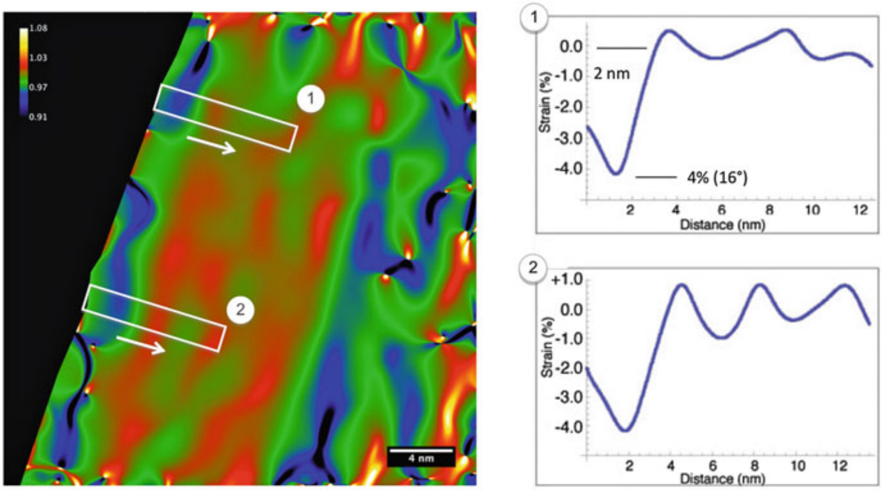

Fig. 13 Map of the strain component in the direction perpendicular to the edge of the fold. The internal part of the flake shows no significant strain, while parallel to the border we can observe compressed regions. (1, 2). On the right are reported the strain profiles acquired, respectively, over regions (1) and (2)

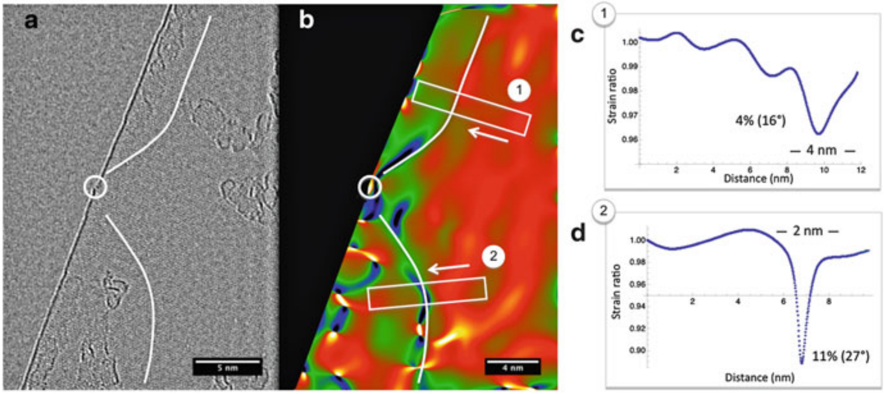

Fig. 14 (**a**) HREM image of a single graphene layer folded over itself. A point defect, highlighted by the *white circle*, is visible on the border; (**b**) map of the strain component in the direction perpendicular to the edge of the fold. *Two compressed lines*, highlighted with *white lines* in (**a**), are clearly visible; (**c**, **d**) strain profiles acquired, respectively, over regions (1) and (2)

highlighted in the apparent strain maps. In fact, this fold corresponds to an infinite apparent compression in the imaged lattice, and in the strain profiles it is hidden by geometric phase artifacts arising from the phase discontinuity at the interface between the flake and the vacuum. In addition, the spatial resolution achieved in the GPA reconstruction is 0.5 nm, which is the same order of the estimated fold curvature radius, making it impossible to map such a large and rapid variation of the crystal slope.

Nevertheless, in all the reported cases the method demonstrated effective in the reconstruction of the 3D structure of the graphene membranes, at least far from the region close to the folded edge. To validate the proposed methodology, the further step is to compare the experimental results with a model of the 3D structure of graphene flakes. This will be the subject of the next section.

3 Modeling the Bending Properties of Graphene Membranes: Conceptual Framework

In order to obtain trustworthy HRTEM simulated images addressed at validating the experimental results, the actual 3D atomic structure of folded graphene membranes is needed. With this aim, we proceed through a multi-step protocol, obtained by blending together atomistic and continuum modeling:

- The shape of a folded two-dimensional continuum membrane is at first predicted according to continuum elasticity.
- The shape corresponding to the minimum elastic energy configuration is then decorated by a carbon honeycomb lattice.
- Careful lattice relaxation follows, eventually driving to the actual atomistic configuration of a folded graphene sample.

A key-feature underlying the above protocol is that, while the bending processes of a two-dimensional continuum membrane involves only out-of-plane deformations, in a two-dimensional atomic lattice such a deformation pattern cannot be achieved without introducing bond strain [18]. This is mainly due to the distortion and mutual interaction between neighboring p_z orbitals. Thus, there is always interplay between real bond-length variations and the apparent strain observed by projection of a bent structure onto a plane. Taking into account properly the bond strain induced by bending is, in turn, a tough problem owing to the peculiar nature of the carbon–carbon interactions which can only be quantitatively modeled by quantum mechanics. Therefore, the atomistic relaxation outlined above is performed by tight-binding molecular dynamics, making use of the representation by Xu et al. [36].

4 Simulation Protocol

4.1 Step 1: Predicting the Shape of a Folded Continuum Membrane

From the continuum elasticity theory point of view, the equilibrium shape of a folded graphene (also known as BLE, Bilayered Edged Graphene) is the same as that of any other 2D solid membrane and, hence, can be predicted by solving

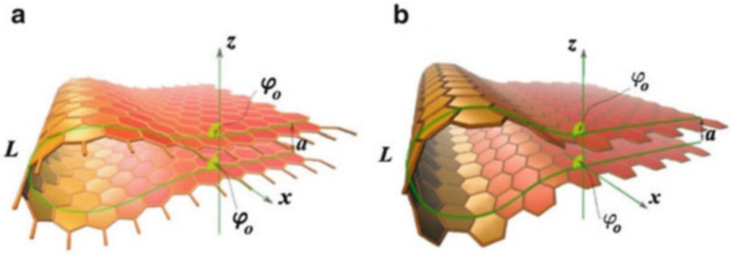

Fig. 15 3D rendering of the TB simulated graphene folds. (**a**) Armchair fold. (**b**) Zig–zag fold

the Euler–Poisson problem, just providing the correct geometrical boundary conditions.

The geometrical features of the specific configuration of a BLE graphene is achievable by imposing the correct length (L) of the bent carbon ribbon (i.e., as shown in Fig. 15, one can recognize two different regions, the inner one that is almost a flat bilayer of graphene and the bent closed edges), the attack angle (φ_o) (i.e., the angle obtained between the tangent plane at the folded region and the flat one where they match together), and the (almost) constant distance (a) between the two parallel layers along the flat region (see Fig. 15).

The length of the folded region in graphene results from the competition between the bending momentum (i.e., the bending moduli of graphene, the bending rigidity, and the Gaussian bending stiffness, depending on the mean and Gaussian curvatures, respectively) and the attractive Van der Waals potential, which engender the opening and the adhesion of the graphene sheet, respectively. In the matter of the geometric features, the generic cylindrical configuration observed in BLE involves only the mean curvature on the surface, and therefore the elastic energy stored by the curvature at certain conditions depends just on the bending rigidity (see Sect. 4.2).

The bending energy density $\mathcal{U}_b$ of a generic surface can be written as $\mathcal{U}_b = 2\kappa\mathcal{H}^2 - \bar{\kappa}\mathcal{K}$, where the mean curvature is $\mathcal{H} = \frac{1}{2}(k_1 + k_2)$ and the Gaussian curvature is defined as $\mathcal{K} = k_1 k_2$, $k_1 = R_1^{-1}$ and $k_2 = R_2^{-1}$ are the principal curvatures, while R_1 and R_2 are the local principal radii of curvature. Due to the Gaussian curvature being null, $\mathcal{K} = 0$, in the case of cylindrical geometry, the bending energy density $\mathcal{U}_b$ is given by $\mathcal{U}_b = \frac{1}{2}\kappa\, k_1^2$.

The corresponding problem consists in finding the curve $z = z(x)$ by minimizing the bending energy $U_b = \int\int \mathcal{U}_b \, d\sigma$ under the given boundary conditions that consist in fixing the positions of the two parallel edges (with length l) at a given distance a (i.e., the equilibrium distance of a bilayered graphene, $a = 1.41$ Å), a constrained width L (i.e., enforcing the absence of any in-plane stretching), and the attack angles are fixed for continuity reasons by the bilayer flat region.

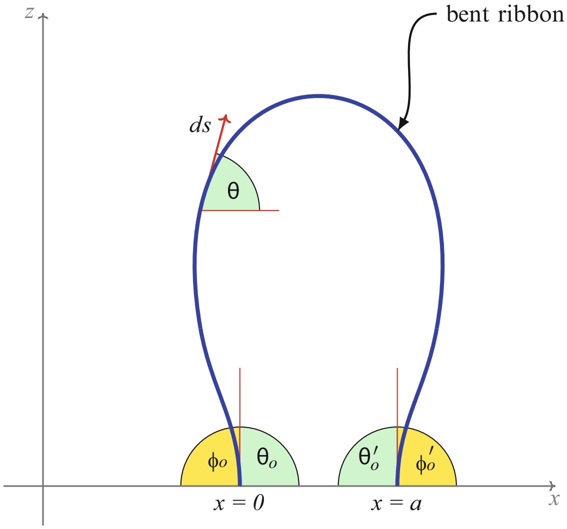

Fig. 16 A cross-section of a bent ribbon (*blue curve*) with parallel edges at fixed distance $a = 3.4$ Å, i.e., the equilibrium distance between two graphene layers. The ribbon width L and the edges distance a are taken as constant, and the attack angles θ_o and $\theta'_o = -\theta_o$ (or ϕ and ϕ') are fixed at $\pi/2$

In Fig. 16 the cross section of the bent graphene ribbon is sketched as a line with width L. Hence, by imposing the method of Lagrange multipliers:

$$U_b = \frac{1}{2}\kappa l \int_0^a \mathrm{d}x \left(\frac{\ddot{z}^2}{(1+\dot{z}^2)^{\frac{5}{2}}} + \lambda\sqrt{1+\dot{z}^2} \right). \tag{13}$$

The above integral can be written in the general form $G(z) = \int_0^a \mathrm{d}x\, \mathcal{F}(z, \dot{z}, \ddot{z}, x)$, which is the solution of the Euler–Poisson differential equation $\frac{\partial \mathcal{F}}{\partial z} - \frac{d}{\mathrm{d}x}\frac{\partial \mathcal{F}}{\partial \dot{z}} + \frac{d^2}{\mathrm{d}x^2}\frac{\partial \mathcal{F}}{\partial \ddot{z}} = 0$.

By the application of constrained variational calculus we eventually obtain the final geometry in parametric representation $[x(s), z(s)]$ with the given boundary conditions. First of all, by the angle definition we get $\dot{z} = \tan\theta$, and $\ddot{z} = \frac{1}{\cos^2\theta}\frac{\partial\theta}{\partial x}$. Introducing the arc length $s = \int_0^x \mathrm{d}x\sqrt{1+\dot{z}^2}$, the Euler–Poisson differential equation can be written as

$$\left(\frac{d\theta}{\mathrm{d}s}\right)^2 = +\lambda + C_{\mathbf{1}}\sin\theta + C_{\mathbf{2}}\cos\theta. \tag{14}$$

By imposing the fixed attack angle condition, i.e., $\theta(0) = \theta_o = \pi/2$ and $\theta(L) = -\theta_o$, as shown in Fig. 16, (14) leads to $\boldsymbol{C}_1 = 0$, and can be simplified as $\frac{d\theta}{\mathrm{d}s} = -\sqrt{\lambda + C\cos\theta}$, where $\boldsymbol{C} \equiv \boldsymbol{C}_2$ as well as in the following.

Finally, by using the length $L = \int_0^a \mathrm{d}x\sqrt{1+\dot{z}^2}$ and the distance a to obtain the parameters $\boldsymbol{C}$ and λ it follows that

$$\begin{aligned} L &= \int_{-\theta_o}^{\theta_o} \frac{d\theta}{\sqrt{\lambda + C\cos\theta}} \\ a &= \int_{-\theta_o}^{\theta_o} \frac{\cos\theta d\theta}{\sqrt{\lambda + C\cos\theta}} \end{aligned}.$$

Turning back in Cartesian coordinates,[1] we have obtained the parametric form of the minimized surface:

$$\begin{aligned} x &= L\frac{\int_{\theta(s)}^{\theta_o} \frac{\cos\theta d\theta}{\sqrt{(\lambda + C\cos\theta)}}}{\int_{-\theta_o}^{\theta_o} \frac{d\theta}{\sqrt{(\lambda + C\cos\theta)}}} \\ z &= L\frac{\int_{\theta(s)}^{\theta_o} \frac{\sin\theta d\theta}{\sqrt{(\lambda + C\cos\theta)}}}{\int_{-\theta_o}^{\theta_o} \frac{d\theta}{\sqrt{(\lambda + C\cos\theta)}}} \end{aligned}. \tag{15}$$

4.2 The Bending Rigidity of Graphene

The bending rigidity of graphene ($\kappa = 1.40$ eV), including relaxation effects, can be evaluated using carbon nanotubes instead of nanoribbons. Nanotubes, of course, do not show any edge effects, but the bending rigidity depends on the mean curvature, which in nanotubes is a geometric constant (the cylindrical geometry of a nanotube imposes the Gaussian curvature null, $\mathcal{K} = 0$). Including relaxation effects in the function of the nanotube radius R it possible to extract the pure bending energy term by comparing the radius variation between the reference starting tube, which has all bonds equal to the perfect graphene, namely 1.41 Å, and the fully relaxed one. In fact, bond stretching is observed down to (15,0) nanotubes [37–39]

The elastic energy density $\mathcal{U}$ [eVÅ^{-2}] of a nanotube can be written as the sum of the strain energy density and the bending energy density:

$$\mathcal{U} = \mathcal{U}_s + \mathcal{U}_b. \tag{16}$$

---

[1] We observe that $\frac{\mathrm{d}x}{\mathrm{d}s} = \cos\theta$, and $\frac{\mathrm{d}z}{\mathrm{d}s} = \frac{\mathrm{d}z}{\mathrm{d}x}\frac{\mathrm{d}x}{\mathrm{d}s} = \sin\theta$.

The bending energy density $\mathcal{U}_b$ of a general given surface can be written as

$$\mathcal{U}_b = 2\kappa\mathcal{H}^2 - \bar{\kappa}\mathcal{K}, \tag{17}$$

where the mean curvature is $\mathcal{H} = \frac{1}{2}(k_1 + k_2)$ and the Gaussian curvature is defined as $\mathcal{K} = k_1 k_2$, $k_1 = R_1^{-1}$ and $k_2 = R_2^{-1}$ are the principal curvatures, while R_1 and R_2 are the local principal radii of curvature. Choosing a cylindrical configuration that involves only one curvature (i.e., $k_1 = R_1^{-1}$ and $k_2 = 0$), the mean curvature is $\mathcal{H} = \frac{1}{2}k_1$, while the Gaussian curvature is null, $\mathcal{K} = 0$.

Thus in the case of cylindrical geometry, the bending energy density $\mathcal{U}_b$ is given by

$$\mathcal{U}_b = \frac{1}{2}\kappa\, k_1^2. \tag{18}$$

The total bending energy U_b can be calculated by performing the integral of the bending energy density $\mathcal{U}_b$ on the reference surface Σ_o, i.e., $U_b = \int\int_{\Sigma_o} \mathcal{U} d\sigma = 1/2\kappa l \int_{\gamma_o} k_1^2 \mathrm{d}s$, where $\Sigma_o = L_o l$ is the total area of the reference system, $\gamma_o = 2\pi R_o$ is the circumference of the cylinder with radius R_o, and s is the arc length ($0 < s < L_o$). Note that the reference surface Σ_o is defined as the surface of the corresponding rectangular flat slice which has been rolled to build the nanotubes, i.e., the unstrained graphene nanoribbon wherein all the bond length are equal to the equilibrium distance $d_{\text{C–C}} = 1.41$ Å between a pair of neighbor carbon atoms.

The solution of the integral is as follows:

$$U_b = \frac{1}{2}\kappa l \frac{2\pi R_o}{R^2}. \tag{19}$$

If the bending does not involve stretching, the radius R after the relaxation of the nanotube has to be equal to the reference cylinder radius R_o. Therefore the bending energy can be simplified as

$$U_b = \lim_{R \to R_o} \frac{1}{2}\kappa l \frac{2\pi R_o}{R^2} = \frac{\pi\kappa l}{R_o}. \tag{20}$$

Because the bending energy can be computed by atomistic simulation as the difference between the total energy of the nanotube E_o^{tube} and the corresponding reference flat system E_o^{flat}, namely $U_b = E_o^{\text{tube}} - E_o^{\text{flat}}$, the bending rigidity κ of a nanotube with radius R_o is given by

$$\kappa = \frac{R_o U_b}{\pi l}, \tag{21}$$

in the absence of stretching on the surface (Fig. 17).

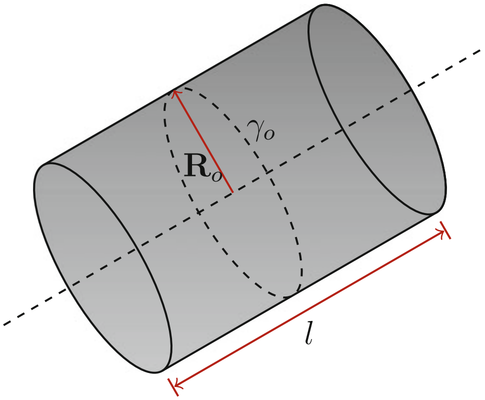

Fig. 17 A nanotube can be sketched as a simple cylinder. Here the radius R_o and circumference γ_o are referred to the reference configuration (i.e., without bond stretching), while the length l is fixed by imposing the periodic boundary condition along the cylinder axis (*dashed line*)

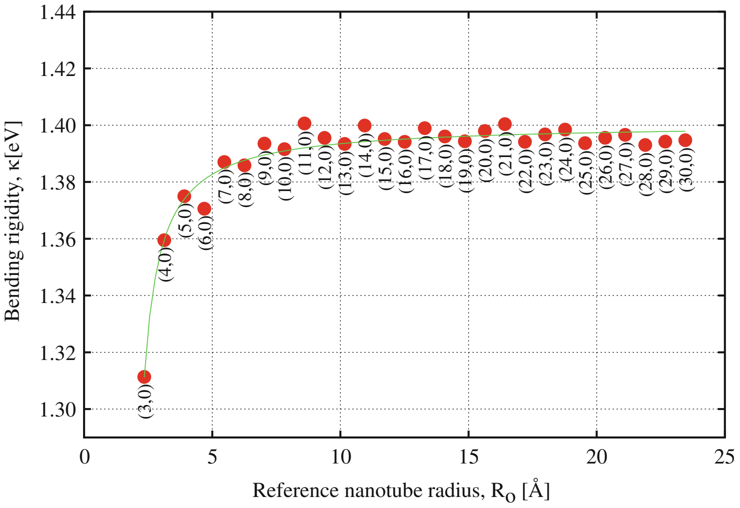

Fig. 18 Bending rigidity κ in function of the radius of a set of zig–zag nanotubes in the range of (3,0)–(30,0). The *symbols* show the value of the bending rigidity, as defined in (20), obtained by tight-binding simulations. Note that down to (15,0) a deviation from the constant value is observed. This fact is due to the rising of stretching bond effects due to the curvature. The asymptotic value is $\kappa = 1.40$ eV

However, if the nanotube dimension is down to a certain radius (see Fig. 18), the relaxation of the structure allows a variation of radius R. In these cases with $R \neq R_o$, it needs to take in account the non-negligible stretching term in (16). Thus, the stretching energy density $\mathcal{U}_s$ has to be integrated as follows:

$$U_s = \frac{1}{2}\frac{E}{1+\nu}\iint_{\Sigma_o}\left(\mathrm{Tr}\left(\hat{\varepsilon}^2\right) + \frac{\nu}{1-\nu}[\mathrm{Tr}(\hat{\varepsilon})]^2\right)d\sigma.$$

Here the nanotube length l is constant due to the periodic boundary condition imposed along the axis of the cylinder; hence, we can consider only the strain tensor $\hat{\varepsilon} = \begin{pmatrix} \zeta & 0 \\ 0 & 0 \end{pmatrix}$ along the circumference. So considering that $\zeta = \frac{\gamma - \gamma_o}{\gamma_o} = \frac{R - R_o}{R_o}$:

$$U_s = \frac{\pi R_o E l}{1-\nu^2}\left(\frac{R - R_o}{R_o}\right)^2. \tag{22}$$

Obviously, when $R \to R_o$, the stretching energy goes to zero, $U_s = 0$.

4.3 Step 2: Predicting the Actual Atomistic Structure of a Folded Graphene Membrane

Tight binding (TB) atomistic simulations have been performed making use of the sp^3, orthogonal, and next-neighbors tight-binding representation by Xu et al. [40] The present TB total energy model has been implemented within the scheme given by Goodwin et al. [41] for the dependence of the TB hopping integrals and the pairwise potential on the interatomic separation.

The following continuum analysis is useful to create reasonable input configurations for atomistic calculations, mainly with the aim of starting the relaxation routine from a configuration as close as possible to equilibrium. The investigated system consists in a squeezed nanotube formed by a perfect hexagonal carbon lattice, having circumference L and length l, corresponding to a simulation box containing ~900 carbon atoms. Moreover, periodic boundary conditions are assumed along the direction of the length l. The length (width) is developed along the armchair (zig–zag) direction of the honeycomb lattice.

Although reassuring, the above picture must be refined in order to take properly into account atomic-scale features. Full relaxation of the internal degrees of freedom of the systems is performed by zero temperature damped dynamics until interatomic forces result as not larger than ~10^{-5} eV/Å. We have so generated a set of configurations, where bending and stretching features are entangled, in order to simulate the HRTEM images.

Summarizing, we started from a configuration made by a hexagonal configuration mapped on the predicted shape with the desired chirality, then we obtained the correct values for the geometrical parameters using zero-temperature atomistic relaxation simulations adopting a TB semi-empirical scheme [31] plus a van der Waals interaction [42]. If the central region, where the layers remain parallel, is large enough, as shown in Fig. 15, any further constraint is not needed. The atomic

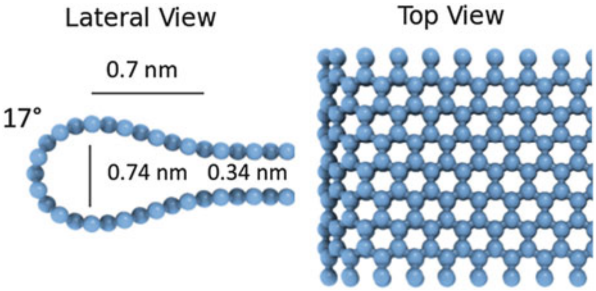

Fig. 19 *Lateral*, *left*, and *top* view, *right*, of the half-portion of the armchair tubular lattice structure

coordinates calculated so far allow us to simulate HREM images. It is important to note that in two-dimensional out-of-plane deformations it is impossible to achieve bending without introducing strain [18], and there is always interplay between real bond-length variations and the apparent strains due to the effect of projection of a bent structure. However, atomistic simulations performed on folded monolayer structures show that bond-length variations in the folded regions are <0.1% in the direction perpendicular to the edge [18]. This indicates that graphene stiffness ensures that changes in the interatomic distances are small compared to the effect of projection on the measured strain in the image.

5 Validation of the Experimental Procedure

As highlighted in the previous section, the modeling of the structure started from tubular lattices, imposing the structure to collapse at the center in order to simulate the two superimposed graphenes near a folded edge, as reported in Fig. 19. In this case one half of the structure of an armchair tube has been taken into account prolonged with flat graphenes, obtaining a folded monolayer edge, with a loop of 0.74 nm in diameter. The height variation with respect to the center of 0.2 nm is accommodated over a length of 0.7 nm with a slope angle of 17°. It is important to note that variations of the interatomic distances in the curved part result in being <1%, and therefore all the strain in a TEM image of such a structure should come from the effect of the projection of the atomic positions in the lattice.

The atomic position of the lattice obtained in this way has then been used as input to simulate HREM images, in exactly in the same experimental conditions shown before, using the JEMS package [43]. In Fig. 20a the top view of the folded armchair structure is given, while in Fig. 20b the corresponding simulated HREM image is shown for an energy of 100 keV and a small positive defocus and slightly positive spherical aberration. Then we applied the GPA to the simulated image to calculate the strain in the direction parallel to the border and perpendicular to it, as reported in Fig. 20c, d, respectively. In the direction parallel to the border there is no variation in the lattice, as we expect from the folding, where all the compression in the sloped region is along the perpendicular direction.

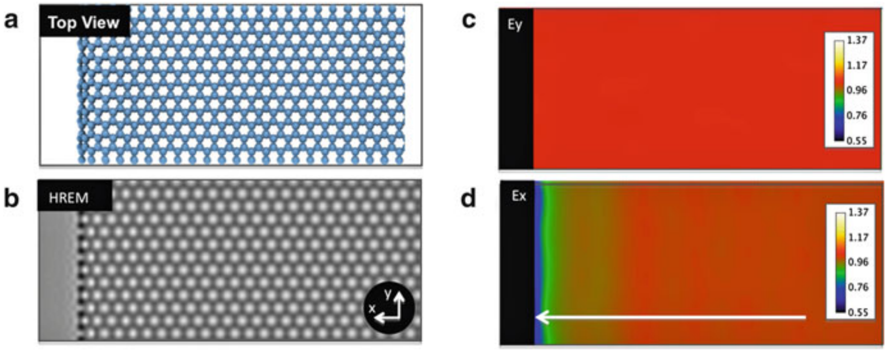

Fig. 20 (**a**) *Top view* of the simulated atomic position; (**b**) simulated HREM image from (**a**); (**c**) strain map along the direction parallel to the border; (**d**) strain map along the direction perpendicular to the border

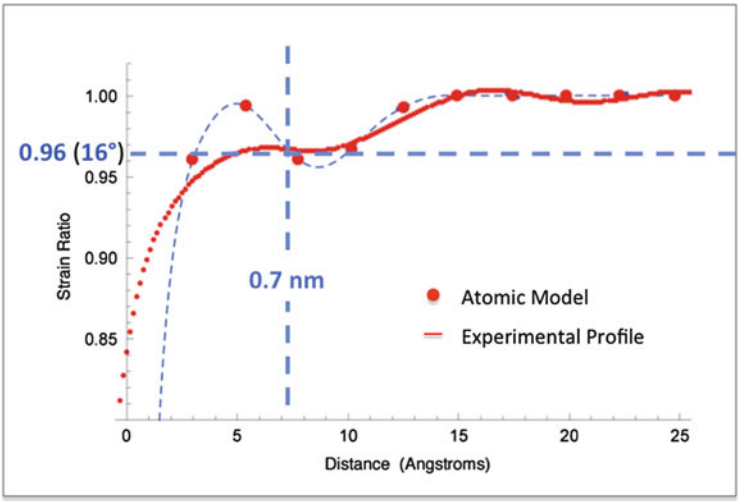

Fig. 21 Strain profile (*red line*) along the *white line* in Fig. 20d and compression values (*big red dots*) calculated from the projected atomic position of the simulated structure of Fig. 19

In Fig. 21 the line scan taken in the direction perpendicular to the folded border, along the white line in Fig. 20d, is shown. Moving from the flat region towards the border, we can measure a compression of about 4%, followed by a rapid increase of the strain as we approach the border where the crystal is almost parallel to the beam direction.

The large red dots in the profile are the compression values calculated from the projected atomic positions in the structure of Fig. 20d. The profile maps very well the compression corresponding to the inner curvature but, due to intrinsic resolution problems in the recovered strain map, it fails to map the rapid curve of the outer

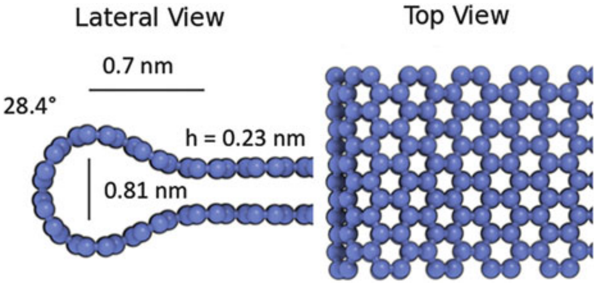

Fig. 22 *Lateral*, *left*, and *top* view, *right*, of the half-portion of the zig–zag tubular lattice structure

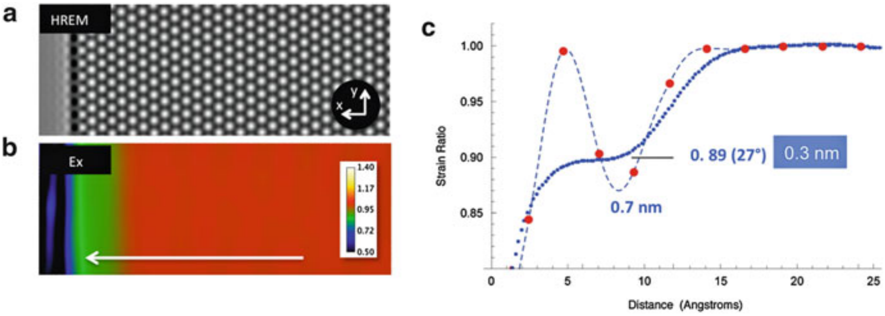

Fig. 23 (**a**) Simulated HREM image from the simulated atomic positions of Fig. 22; (**b**) strain map along the direction parallel to the border; (**c**) strain profile (*blue line*) along the *white line* in (**b**) and compression values (*big red dots*) calculated from the projected atomic position of the simulated structure of Fig. 22

part. Nevertheless, as in the experimental case, the intensity of the compression can be used to measure the local maximum slope, about 16°, and to measure the length of the curved region, estimated as 0.7 nm. Therefore it is possible to estimate a height variation of 0.2 nm, which is almost identical to the real height variation in the simulated structure.

To confirm further the capabilities of the method, following the very same approach, one half of the structure of a zig–zag tube has been taken into account, as reported in Fig. 22. In this case the modeled structure shows a loop of 0.81 nm in diameter, and thus a height variation with respect to the center of 0.23 nm accommodated over a length of 0.7 nm with a slope angle of about 28°. Again we can use the modeled atomic position as input for HREM image simulation to apply the GPA strain analysis to recover the 3D modeled structure. The results are reported in Fig. 23. Even in this case the spatial resolution of the map fails to show the rapid curvature at the outer edge, but at the same time it is possible to measure with great precision the structure of the internal region, with a slope of 27°, over a length of 0.7 nm, therefore estimating a height variation of 0.3 nm, close to the 0.23 expected from the model.

6 Conclusions

In this chapter we have presented a novel approach to study the mechanical properties of wrinkles and fold in graphene membrane, using a combination of TEM-based 3D mapping and blended continuum-atomistic modeling. The experimental results show that the apparent strain in the HREM images on graphene membranes provides precise information about the 3D sub-nanometer height and spatial resolution, in excellent agreement with predictions by atomistic tight-binding simulations.

Combining information from electron diffraction and HREM with the possibility of mapping the 3D membrane morphology is successful in characterizing freely suspended graphene crystals. In this work we have focused on the investigation of graphene folded edges, but the same methodology can be applied to investigate the elastic properties and 3D structure of complex folds and wrinkle geometries. In addition, the proposed approach is general and can be easily extended to other two-dimensional crystal like BN or MoS_2 membranes, as well as to hybrid multilayer thin-films composed of these materials.

Acknowledgement One of us (L.C.) acknowledges financial support under project PRIN 2010–2011 “GRAF”.

References

1. Krivanek OL, Dellby N, Murfitt MF, Chisholm MF, Pennycook TJ, Suenaga K, Nicolosi V (2010) Gentle STEM: ADF imaging and EELS at low primary energies. Ultramicroscopy 110:935–945
2. Warner JH, Roxana Margine E, Mukai M, Robertson AW, Giustino F, Kirkland AI (2012) Dislocation-driven deformations in graphene. Science 337:209–212
3. Meyer JC, Eder F, Kurasch S, Skakalova V, Kotakoski J, Jin Park H, Roth S, Chuvilin A, Eyhusen S, Benner G, Krasheninnikov AV, Kaiser U (2012) Accurate measurement of electron beam induced displacement cross sections for single-layer graphene. Phys Rev Lett 108:196102
4. Zan R, Bangert U, Ramasse Q, Novoselov KS (2011) Metal–graphene interaction studied via atomic resolution scanning transmission electron microscopy. Nano Lett 11:1087–1092
5. Zhou W, Kapetanakis MD, Prange MP, Pantelides ST, Pennycook SJ, Idrobo JC (2012) Phys Rev Lett 109:206803
6. Williams DB, Carter CB (2009) Transmission electron microscopy: a textbook for materials science. Springer, New York
7. Pennycook SJ, Nellist PD (2011) Scanning transmission electron microscopy. Springer, New York
8. Hytch M, Snoeck E, Kilaas R (1998) Quantitative measurement of displacement and strain fields from HREM micrographs. Ultramicroscopy 74:131–146
9. Grillo V, Rossi F (2013) Stem cell: a software tool for electron microscopy. Part 2. Analysis of crystalline materials. Ultramicroscopy, advanced online publication 125:112–129
10. Mermin N (1968) Crystalline order in two dimensions. Phys Rev 176:250–254
11. Novoselov K, Jiang D, Schedin F, Booth T, Khotkevich V, Morozov S, Geim A (2005) Two-dimensional atomic crystals. Proc Nat Acad Sci USA 102:10451–10453

12. Meyer JC, Geim AK, Katsnelson MI, Novoselov KS, Booth TJ, Roth S (2007) The structure of suspended graphene sheets. Nature 446:60–63
13. Bao W, Miao F, Chen Z, Zhang H, Jang W, Dames C, Lau CN (2009) Controlled ripple texturing of suspended graphene and ultrathin graphite membranes. Nat Nanotech 4:562–566
14. Vandeparre H, Pineirua M, Brau F, Roman B, Bico J, Gay C, Bao W, Lau CN, Reis PM, Damman P (2011) Wrinkling hierarchy in constrained thin sheets from suspended graphene to curtains. Phys Rev Lett 106:224301
15. Kim K, Lee Z, Malone BD, Chan KT, Aleman B, Regan W, Gannett W, Crommie MF, Cohen ML, Zettl A (2011) Multiply folded graphene. Phys Rev B 83:245433
16. Topsakal M, Bagci VMK, Ciraci S (2010) Current–voltage (I–V) characteristics of armchair graphene nanoribbons under uniaxial strain. Phys Rev B 81:205437
17. Cadelano E, Palla P, Giordano S, Colombo L (2009) Nonlinear elasticity of monolayer graphene. Phys Rev Lett 102:235502
18. Cadelano E, Giordano S, Colombo L (2010) Interplay between bending and stretching in carbon nanoribbons. Phys Rev B 81:144105
19. Poetschke M, Rocha CG, Foa Torres LEF, Roche S, Cuniberti G (2010) Modeling graphene-based nanoelectromechanical devices. Phys Rev B 81:193404
20. Feng J, Qi L, Huang J, Li J (2009) Geometric and electronic structure of graphene bilayer edges. Phys Rev B 80:165407
21. Tozzini V, Pellegrini V (2011) Reversible hydrogen storage by controlled buckling of graphene layers. J Phys Chem C 115:25523–25528
22. Zheng Y, Wei N, Fan Z, Xu L, Huang Z (2011) Mechanical properties of grafold: a demonstration of strengthened graphene. Nanotechnology 22:405701
23. Prada E, San-Jose P, Brey L (2010) Zero landau level in folded graphene nanoribbons. Phys Rev Lett 105:106802
24. Zhu W (2012) Structure and electronic transport in graphene wrinkles. Nano Lett 12:3431–3436
25. Pang ALJ, Sorkin V, Zhang Y-W, Srolovitz DJ (2012) Self assembly of free-standing graphene nano-ribbons. Phys Lett A 376:973–977
26. Qi L, Huang JY, Feng J, Li J (2010) In situ observations of the nucleation and growth of atomically sharp graphene bilayer edges. Carbon 48:2354–2360
27. Patra N, Wang B, Kral P (2009) Nanodroplet activated and guided folding of graphene nanostructures. Nano Lett 9:3766–3771
28. Catheline A, Ortolani L, Morandi V, Melle-Franco M, Drummond C, Zakri C, Penicaud A (2012) Solutions of fully exfoliated individual graphene flakes in low boiling points solvents. Soft Matter 8:7882–7887
29. Midgley P, Weyland M, Yates T, Tong J, Dunin-Borkowsky R (2004) Stem electron tomography for nanoscale materials science. Microsc Microanal 10:148–149
30. Molhave K, Gudnason SB, Pedersen AT, Clausen CH, Horsewell A, Boggild P (2007) Electron irradiation-induced destruction of carbon nanotubes in electron microscopes. Ultramicroscopy 108:52–57
31. Barboza APM, Chacham H, Oliveira CK, Fernandes TFD, Martins Ferreira EH, Archanjo BS, Batista RJC, de Oliveira AB, Neves BRA (2012) Dynamic negative compressibility of few-layer graphene, h-BN, and MoS_2. Nano Lett 12:2313–2317
32. Hytch M (1997) Analysis of variations in structure from high resolution electron microscope images by combining real space and Fourier space information. Microsc Microanal 8:41–57
33. Hytch M, Plamann T (2001) Imaging conditions for reliable measurement of displacement and strain in high-resolution electron microscopy. Ultramicroscopy 87:199–212
34. Snoeck E, Warot B, Ardhuin H, Rocher A, Casanove M, Kilaas R, Hytch M (1998) Quantitative analysis of strain field in thin films from HRTEM micrographs. Thin Solid Films 319:157–162
35. Ortolani L, Cadelano E, Veronese GP, Degli Esposti Boschi C, Snoeck E, Colombo L, Morandi V (2012) Folded graphene membranes: mapping curvature at the nanoscale. Nano Lett 12:5207–5212

36. Xu CH, Wang CZ, Chan CT, Ho KM (1992) A transferable tight-binding potential for carbon. J Phys Cond Matt 4:6047–6054
37. Dresselhaus G, Saito R, Dresselhaus MS (1998) Physical properties of carbon nanotubes. Imperial College, London
38. Shen L, Li J (2005) Equilibrium structure and strain energy of single-walled carbon nanotubes. Phys Rev B 71:165427
39. Chang T, Gao H (2003) Size-dependent elastic properties of a single-walled carbon nanotube via a molecular mechanics model. J Mech Phys Sol 51:1059
40. Xu Y, Gao H, Lil M, Guo Z, Chen H, Jin Z, Yu B (2011) Electronic transport in monolayer graphene with extreme physical deformation: ab initio density functional calculation. Nanotechnology 22:365202
41. Goodwin L, Skinner AJ, Pettifor DG (1989) Generating transferable tight-binding parameters: application to silicon. Europhys Lett 9:701–706
42. Rappe AK, Casewit CJ, Colwell KS, Goddard WA III, Skiff WM (1992) UFF, a full periodic table force field for molecular mechanics and molecular dynamics simulations. J Am Chem Soc 114:10024–10035
43. JEMS P Stadelmann, CIME-EPFL, Laudanne, Switzerland. http://cimewww.epfl.ch/people/stadelmann/jemsWebSite/jems.html. Accessed online 2013

Top Curr Chem (2014) 348: 237–266
DOI: 10.1007/128_2013_448

Graphene and Graphene Oxide Materials for Chemo- and Biosensing of Chemical and Biochemical Hazards

Piyush Sindhu Sharma, Francis D'Souza, and Wlodzimierz Kutner

Abstract Graphene, a new member of the carbon family, has attracted enormous attention due to its very peculiar properties like high surface area, mechanical strength, and conductivity. Moreover, graphene is exceptionally biocompatible if used as a substrate for immobilization of enzymes, bioreceptor molecules, or whole cells. Although it was isolated on a mass scale quite recently (in 2004), its use as a signal enhancing material in chemo- and biosensors has already seen a rapid growth. The aim of the present review is to bring out important advances of graphene-based sensing and, particularly, those related to rapid detection and quantization of the toxin, explosive, pesticide, pathogen, and microbe analytes. These analytes are important hazardous determinants of a safe living environment. This chapter therefore summarizes selected key strategies developed toward devising sensing systems with graphene and derivatives of graphene to detect and determine these hazards to safe living.

Keywords Biohazards · Biomarkers · Chemosensing · Explosives · Graphene · Graphene oxide · Pesticides · Toxins

---

P.S. Sharma
Department of Physical Chemistry of Supramolecular Complexes, Institute of Physical Chemistry, Polish Academy of Sciences, Kasprzaka 44/52, 01-224 Warsaw, Poland

F. D'Souza (✉)
Department of Chemistry, University of North Texas, Denton, 1155, Union Circle, #305070, TX 76203-5017, USA
e-mail: Francis.Dsouza@unt.edu

W. Kutner (✉)
Department of Physical Chemistry of Supramolecular Complexes, Institute of Physical Chemistry, Polish Academy of Sciences, Kasprzaka 44/52, 01-224 Warsaw, Poland

Faculty of Mathematics and Natural Sciences, School of Sciences, Cardinal Stefan Wyszynski University in Warsaw, Wóycickiego 1/3, 01-938 Warsaw, Poland
e-mail: wkutner@ichf.edu.pl

Contents

Abbreviations

Ab_1	Primary antibody
Ab_2	Secondary antibody
AChE	Acetylcholinesterase
Anti-IgG	Anti-immunoglobulin-G
ASV	Adsorptive stripping voltammetry
ATCl	Acetylthiocholine chloride
AuNP	Gold nanoparticle
CEA	Carcinoembryonic antigen
cfu	Colony-forming unit
chemFET	Chemical field-effect transistor
CNT	Carbon nanotube
CPBA	3-Carboxyphenylboronic acid
CR-GO	Chemically reduced graphene oxide
CVD	Chemical vapor deposition
DA	Dopamine
dc	Direct current
DMMP	Dimethylmethyl phosphonate
DPV	Differential pulse voltammetry
EDC	*N*-(3-Dimethylaminopropyl)-*N*′-ethylcarbodiimide
EGFR	Epidermal growth factor receptor
ER-GO	Electrochemically reduced graphene oxide
FCA	Ferrocenecarboxylic acid
FET	Field-effect transistor
GBP	Gold binding polypeptide
GCE	Glassy carbon electrode
GFET	Graphene field-effect transistor
GO	Graphene oxide
HER2	Human epidermal growth factor receptor 2
HOPG	Highly ordered pyrolytic graphite
IgG	Immunoglobulin
IL	Ionic liquid

LbL	Layer-by-layer
LOD	Limit of detection
LSV	Linear scan voltammetry
MC-LR	Microcystin-LR
MWCNT	Multi-wall carbon nanotube
NG	Nitrogen doped graphene
NHS	*N*-Hydroxysuccinimide
NP	Nanoparticle
OP	Organophosphate
OPH	Organophosphorus hydrolase
OPP	Organophosphorus pesticide
PB	Prussian blue
PDDA	Poly(diallyldimethylammonium chloride)
PSA	Prostate specific antigen
PSS	Polystyrene sulfonate
PtNP	Platinum nanoparticle
RSH	Thiocholine
RS-SR	Thiocholine(ox) (dimeric)
SAM	Self-assembled monolayer
SRB	Sulfur reducing bacteria
SWCNT	Single-wall carbon nanotube
SWV	Square wave voltammetry
TEM	Transmission electron spectroscopy
TNT	2,4,6-Trinitrotoluene
TR-GO	Thermally reduced graphene oxide
β-CD	β-Cyclodextrin

Symbols

E	Electrode potential
I	Current
I_{ds}	Drain-source current
V_{ds}	Drain-source voltage
V_{g}	Solution-gate voltage

1 Introduction

Carbon is present in all known forms of life. In fact, it is the most abundant element in the human body. Most of the biomacromolecules, such as enzymes, sugars, or nucleotides, contain carbon, which makes this element the chemical basis of all life known. In nature, several allotropes of carbon are encountered, namely, graphite, diamond, fullerenes, and carbon nanotubes (CNTs). Dimensionality of the carbon

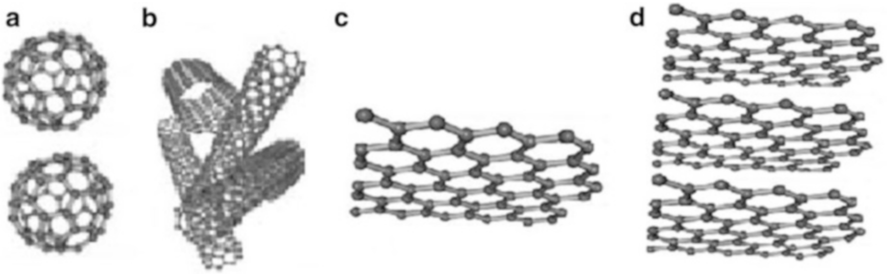

Scheme 1 Carbon allotropes of different dimensionality: (**a**) 0-D fullerene, (**b**) 1-D CNTs, (**c**) 2-D graphene, and (**d**) 3-D graphite

family starts with 0-D fullerene (Scheme 1a), through 1-D CNT (Scheme 1b), 2-D graphene (Scheme 1c), and ends with 3-D graphite (Scheme 1d) and diamond. Interestingly, these dimensionalities result from the different physical properties of the carbon forming these materials. For instance, graphite, CNTs, and fullerene consist of sp^2 hybridized carbon atoms. Therefore, they form π-bonds and can conduct electricity due to mobile π electrons delocalized above and below the planes of the hexagonal net of carbon atoms. However, in diamond all four outer-shell electrons of each carbon atom are “localized” between the atoms within σ-bonds. This localization restricts the movement of electrons. Hence, diamond does not conduct electric current.

In this carbon family, graphene appears as a new member; however, it is isolated from the already existing graphite allotrope (Scheme 1d) [1]. A single layer of graphite is called graphene. It is comprised of sp^2 hybridized carbon atoms π-bonded to form a 2-D hexagonal lattice (Scheme 1c). Due to its unique chemical and physical properties as well as its electronic configuration, this material is now in great demand to devise, among others, sensitive electrochemical chemo- and biosensors [2–8].

The first report on the graphene preparation on mass scale is dated 2004 [1], i.e., after centuries of preparation of graphite. It describes the preparation of graphene by mechanical exfoliation of a single layer of graphene from highly oriented pyrolytic graphite (HOPG). This approach is very reliable, allowing for preparation of graphene films up to 10 μm in size with thickness >3 nm. This report classifies graphene as the best possible material for metallic transistor applications. This is because of graphene scalability to nanometer sizes, which is the most important criterion for devising microtransistors. Additionally, graphene offers ballistic electron transport, linear current–voltage characteristics, and huge sustainable current densities ($<10^8$ A cm^{-2}). Besides, it is a zero-gap semiconductor of unparalleled strength (breaking strength ~40 N m^{-1}, Young’s modulus ~1.0 TPa) and record thermal conductivity. All of these parameters are achieved with a very low electronic noise of external origin, which is increasingly important as the size of microelectronic devices continues to shrink substantially. Therefore, this new carbon allotrope has received a warm welcome from all research groups active in this field, evidenced by the growing applications of graphene across many disciplines, including nanoelectronics [9], high-frequency electronics [10, 11], energy storage and conversion devices [12, 13], field-emission displays [14, 15], and transparent conductors [16]. However, in the present review we only focus on the applications of different forms of graphene in devising chemo- and biosensors for hazardous toxins.

Even before the discovery of graphene, other carbon materials, such as carbon nanofibers, fullerenes, and CNTs, have extensively been used for fabricating different electrochemical devices for sensing applications [17, 18]. Particularly, the CNTs were most studied for devising chemosensors [19]. After finding graphene, however, several reports demonstrated that, electroanalytically, graphene performs better than the extensively used CNTs [20, 21]. In comparison to one-dimensional CNTs, graphene offers a large detection area as well as exceptional and unique electronic properties, such as ultra-high electron mobility and ambipolar field effects [22].

2 Synthesis and Properties of Graphene

Nowadays, different synthesis routes are available to prepare graphene as either a single sheet or few-layer sheets. However, most of the procedures leads to graphene in the latter form. Mechanical peeling of HOPG is prevailingly used to produce over 3-nm thick graphene sheets up to 10 μm in size [1]. Typically, bulk quantities of graphene are prepared by preliminary chemical oxidation of graphite to graphite oxide with strong oxidants, such as $KMnO_4$, $KClO_3$, H_2O_2, etc. [23], followed by exfoliation/reduction through different chemical, thermal, or electrochemical treatments. Another interesting procedure, i.e., chemical vapor deposition (CVD), using a transition metal as the catalyst, produces bulk quantities of graphene [24]. However, this procedure always results in multi-layered graphene. Moreover, oxidative unzipping of single-wall (SWCNTs) or multi-wall (MWCNTs) carbon nanotubes is an efficient procedure of choice for graphene preparation (Scheme 2) [25, 26]. Notably, the successful application of graphene in sensing depends upon the procedure used for its preparation [27]. For instance, graphene produced by oxidative cleavage of CNTs or by CVD may contain metallic impurities. Hence, results obtained using these graphene materials and that obtained from graphite may differ. Therefore, only graphene of high purity is recommended for sensing applications.

Some synthetic methods produce graphene sheets with defects. Introduction of these defects results in a material of quite different, sometimes desired, properties than those of genuine graphene. One way to produce these defects in graphene is its chemical oxidation leading to graphene oxide (GO) (Scheme 3). Sheets of oxidized and, therefore, defective GO contain abundant epoxide and hydroxy groups in their central parts, and carboxy groups at edges [28]. Introduction of these defects, and thus varying functionalization appeared useful for stabilizing the GO solutions with respect to flocculation. This functionalization makes GO more hydrophilic, thus helping its easy dispersion in polar solvents and because of that its long-term stabilization. Both graphene and GO can be processed to form different novel materials with distinctly different morphological features. In these materials, carbon nanosheets can serve as either thin films or fillers in polymer nanocomposites.

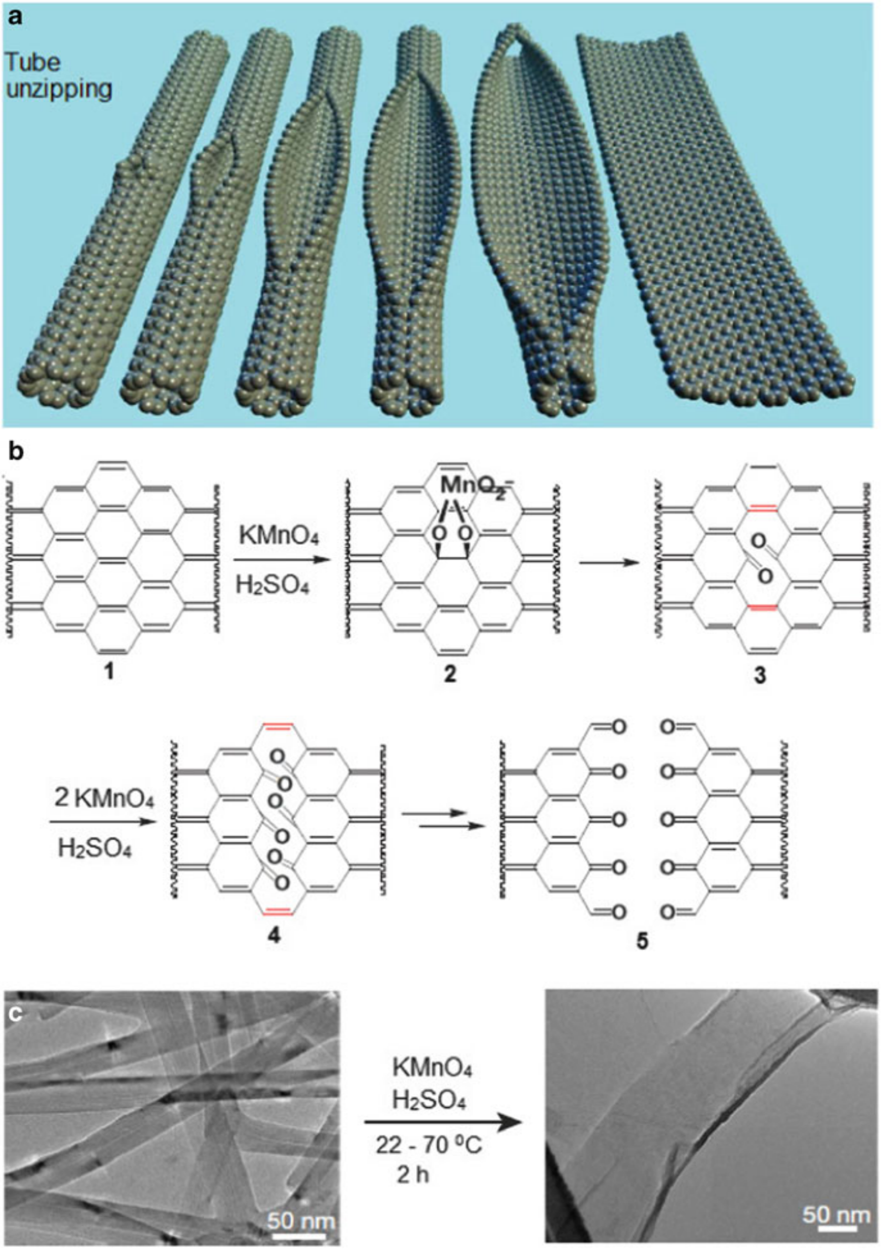

Scheme 2 (**a**) Representation of the gradual unzipping of the wall of SWCNT to form a nanoribbon. (**b**) The proposed chemical mechanism of nanotube unzipping. (**c**) The TEM images depicting transformation of SWCNTs into graphene oxide. Adapted from [25]

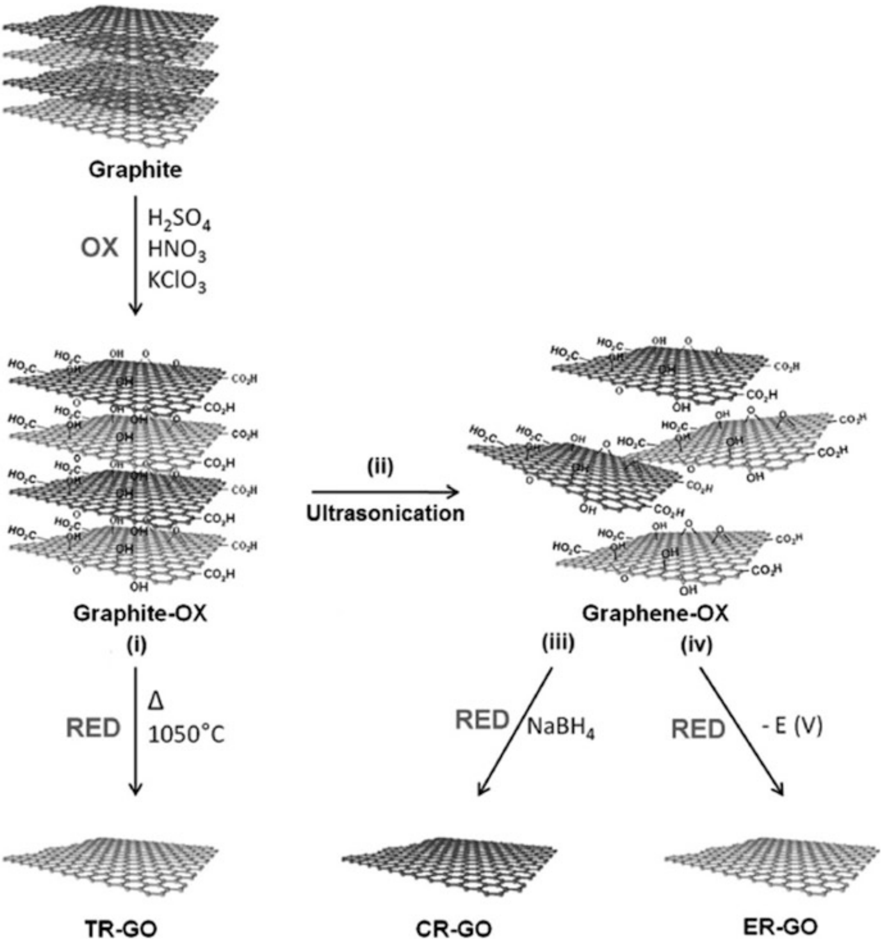

Scheme 3 Production of chemically modified graphenes using graphite as the starting material. Initially, graphite is oxidatively treated to generate graphite oxide. This treatment is followed by: (*i*) thermal reduction/exfoliation of graphite oxide to produce thermally reduced graphene oxide, TR-GO; (ii) exfoliation by ultrasonication generating graphene oxide, GO; (*iii*) chemical reduction of graphene oxide by using $NaBH_4$, which results in chemically reduced graphene oxide, CR-GO; (*iv*) electrochemical reduction of graphene oxide producing electrochemically reduced graphene oxide, ER-GO. OX and RED stand for oxidation and reduction, respectively. Adapted from [28]

Nevertheless, the most attractive GO feature is that it can partially be reduced back to the original graphene-like sheets. This can be accomplished by removing the oxygen-containing groups, thus recovering the original conjugated carbon structure.

Chemical reduction produces chemically reduced GO (CR-GO). Mostly the CR-GO sheets are considered as another kind of chemically derivatized graphene. Thermal and electrochemical reduction leads to thermally (TR-GO) and electrochemically (ER-GO) reduced graphene oxide, respectively. All these three materials represent different types of reduced GO [28] with their functionalization and structure profoundly different compared to those of pristine graphene. Interestingly, all these reduced GO forms are structurally different among themselves as well. For instance, TR-GO contains a large number of structural defects including holes, ad-atoms, pentagon–heptagon defects, and bond rotations or dislocation cores. However, its number of oxygen-containing functional groups is relatively lower than that of the other forms of reduced GO [28]. Therefore, one can expect a dramatic difference in electrochemical behavior of these reduced GOs.

Due to the presence of the abundant epoxide and hydroxy groups in their central parts and carboxy groups at their edges, the GO sheets readily lend themselves to further chemical functionalization either by covalent or non-covalent bonding. This functionalization is used to cross-link the adjacent layers and improve mechanical interactions between individual sheets, thus tailoring physical properties of GO [29]. Several reviews summarize the reports of covalent functionalization of the epoxy group decorated basal plane and the carboxylic acid modified edges of GO [30–32]. Moreover, there are reports on non-covalent functionalization of reduced GO on their basal planes via π–π-stacking or van der Waals interactions [32–34]. There are only a few examples of covalent functionalization of reduced GO [35]. These, with their 2-D structure, proved to be particularly useful for reinforcing different composites.

3 Graphene for Sensing

Carbon-based electrodes are efficiently being used as electrode materials in energy storage devices [36–38], as electrocatalysts [18], and, more importantly, to fabricate electrochemical sensing devices [5, 6, 8, 39]. These materials reveal several advantages for a wide range of possible applications including inertness and high electrocatalytic activity towards many redox processes. Compared to the noble metal (Au and Pt)-based electrode materials, carbon-based materials show some additional advantages. That is, the presence of the sp^2 hybridized carbon atom center in their structural backbone provides a route for surface modification. Sensing devices produced with the bare-carbon-based materials were able to determine analytes down to trace levels. Selective electrochemical determination of several biorelevant analytes in mixtures, e.g., ascorbic acid, dopamine, and uric acid, on traditional carbon-based electrodes is difficult because oxidation potentials of these analytes are similar [40]. Therefore, traditional carbon electrodes were unable to generate a separate signal for each of these analytes. Moreover, determination of analytes at an ultra-trace level, and mostly even below this level, is required. Unfortunately, carbon-based electrodes are unable to reach this level.

Apparently, “Necessity is the Mother of Invention.” The necessity to determine analytes below ultra-trace levels inspired the search for replacement of carbon-based electrodes or a method to modify these already existing carbon-based materials to reach the desired detectability and selectivity goals. The idea was to produce new materials with the help of already available materials.

So far, this search has resulted in fabrication of CNTs and graphene [1]. These single-nanometer-size carbon allotropes provide fascinating opportunities for devising chemosensors with detectability below the ultra-trace level. This ultrahigh detectability could be attained because of their unique structure and properties. Hence, the advancement of research in nanomaterials was essential to inventing ultrasensitive chemosensors. Impressively, analytes are now being determined down to a single-molecule level with these nanomaterials. The higher chemosensor detectability due to application of these nanomaterials can be explained by planarity of conventional electrodes. Therefore their active surface area is low. However, after coating these electrodes with films of nanomaterials this area is much higher.

3.1 Determination of Explosives

Nowadays, world-wide terrorism poses severe threat to the safety of human life. Moreover, the wide use of explosives for civil purposes causes heavy environmental pollution. Therefore low-cost sensing systems with high detectability and selectivity, combined with ease of use, are essential for the determination of these explosives. Advantageously, a sensing electrode material with a large surface area, such as graphene and CNTs, plays a crucial role in increasing detectability of nitroaromatic explosives.

Due to their extraordinarily high surface area, graphene-based nanomaterials have large accumulation capability, especially with respect to analytes with the π-electron structure. For instance, nitroaromatic compounds with their sp^2 hybridized carbon atoms are expected to adhere well, via π–π interactions, to graphene sheets. Therefore various chemosensors were devised using accumulation as a way of amplification of the analytical signal [41, 42]. In that direction, a glassy carbon electrode (GCE) was coated with the GO film and used for determination of nitroaromatic compounds [41]. The presence of the –OH and –COOH groups on the GO sheet helped to form strong hydrogen bonds with the –OH and $–NO_2$ groups of the nitroaromatic compounds. Additionally, the aromatic ring structure of the nitroaromatic compounds facilitates π-stacking. The partially positively charged nitrogen atom in the nitroaromatic compounds generates electrostatic interactions. Concertedly, these interactions promote high loading of the nitroaromatic analyte on GO (Table 1). Moreover, electrocatalytic activity of the CR-GO modified electrode is lower than that of GO with respect to reduction of nitroaromatic compounds because of lower density of oxygen-containing groups left on CR-GO. Furthermore, adsorption capacity of CR-GO is lower than that of GO (Fig. 1). For similar reasons, porphyrin functionalized graphene was used for the determination of explosives [43] (Table 1).

A comparative study highlighted the difference in 2,4,6-trinitrotoluene (TNT) detectability with the single-, few-, and multilayer graphene modified electrodes [44]. Surprisingly, there were no significant differences in reduction potentials, currents, pH dependence, and detectability of these nanomaterials (Table 1).

Table 1 Analytical parameters of graphene-based electrochemical sensors for nitroaromatic explosives

Analyte	Transduction method	Electrode material	Linear dynamic concentration range	LOD	References
4-Nitrophenol	LSV	GCE/GO	0.1–120 μM	0.02 μM	[41]
2,4,6-Trinitrotoluene	DPV	GCE/CR-GO	1–200 ng mL^{-1}	0.2 ng mL^{-1}	[42]
2,4-Dinitrotoluene	ASV	GCE/Porphyrin functionalized graphene	Up to 250 ng mL^{-1}	1 ng mL^{-1}	[43]
2,4,6-Trinitrotoluene				0.5 ng mL^{-1}	
1,3,5-Trinitrobenzene				1 ng mL^{-1}	
1,3-Dinitrobenzene				2 ng mL^{-1}	
2,4,6-Trinitrotoluene	DPV	GCE/single layer graphene GCE/few layer graphene GCE/multi layer graphene GCE/graphite	1–19 μg mL^{-1}	1 μg mL^{-1}	[44]
2,4,6-Trinitrotoluene	ASV	IL–graphene paste electrode	Up to 1,000 ng mL^{-1}	0.5 ng mL^{-1}	[45]
2,4,6-Trinitrotoluene	ASV	GCE/IL–graphene	0.03–1.5 μg mL^{-1}	4 ng mL^{-1}	[46]
2,4,6-Trinitrotoluene	LSV	GCE/N-doped graphene	0.5–8.8 μM	0.13 μM	[47]

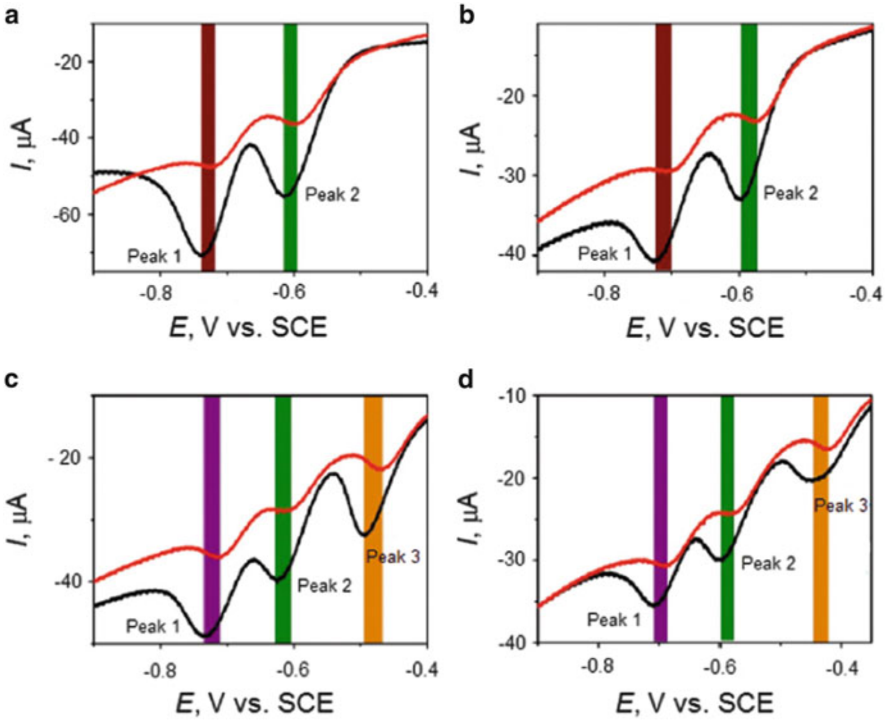

Fig. 1 Linear sweep adsorptive stripping voltammograms for the TR-GO (*black curves*) and NG (*red curves*) modified GCEs in deoxygenated 0.5 M NaCl solutions of different nitroaromatic compounds. (**a**) 11 μM 2,4-dinitrotoluene. (**b**) 12 μM 1,3-dinitrobenzene. (**c**) 8.8 μM 2,4,6-trinitrotoluene. (**d**) 9.38 μM 1,3,5-trinitrobenzene. The potential scan rate 0.1 V s^{-1}, accumulation time 120 s, accumulation potential 0.0 V. Adapted from [47]

However, the TNT accumulation on the graphite electrode bearing a few layers of graphene was by 20% higher than that of the graphite electrode.

Ionic liquids (ILs) provide high conductivity, chemical and thermal stability, and a wide potential range of electrode polarization. Therefore composites of different ILs and graphene were used to prepare an electrode material for TNT determination [45, 46]. Paste electrodes of the IL–graphene composite with a large specific surface area and pronounced mesoporosity provided higher electroactive surface area and lower charge transfer resistance than those of the IL–CNT and IL–graphite composites. Background current of the devised electrochemical chemosensor was low, its sensitivity (1.65 μA cm^{-2} ppb) was high, and limit of detection (LOD) of 0.5 ppb was much lower than those of the IL–CNT and IL–graphite composite electrodes (Table 1) [45]. Moreover, graphene covalently functionalized with IL was used for determination of TNT [46]. However, detectability of the resulting chemosensor did not exceed that of the IL–graphene composite (Table 1) [45].

In order to modulate electronic properties of graphene intrinsically, graphene was doped with a foreign element, e.g., nitrogen (NG) [47]. This doping resulted in an n-type semiconductor. Electrocatalytic activity of this semiconductor towards reduction of nitroaromatic compounds in alkaline solutions was higher than that of the parent graphene. Overpotential (~20 mV) was decreased in comparison to that of the TR-GO modified electrode. For doping, graphene was thermally annealed with melamine used as the nitrogen source. This approach avoided contamination of the semiconductor with the transition metal catalysts. Therefore the intrinsic catalytic performance was solely due to the nitrogen doping of graphene. The level of this doping in a graphene layer did not exceed 10.1%. The XPS high-resolution N 1s spectra revealed that the as-made NG mainly contained pyridine-like nitrogen atoms. When this NG was applied to modify the GCE surface for determination of nitroaromatic compounds, potentials of the linear sweep voltammetry (LSV) cathodic peaks corresponding to reduction of the four nitroaromatic compounds (Table 1) were shifted positively compared to those at the TR-GO modified GCE. Apparently, overpotential of the NG modified GCE was decreased owing to the nitrogen doping. However, cathodic peak currents at the NG modified GCE for the nitroaromatic compounds of the same concentrations were smaller than those at the TR-GO modified GCE. This result was due to the different specific surface areas of these two electrodes; the area-to-mass ratio for TR-GO was ~47 times higher than that for NG.

3.2 Determination of Toxins

Prevention of aggregation of graphene sheets is crucial in graphene sensing applications because most of its unique properties are revealed if graphene is present in the form of separate sheets. Therefore various efforts have been made to increase the graphene dispersibility or solubility. These include covalent or noncovalent functionalization, and particularly the use of polyelectrolytes as functionalizing agents [48]. For instance, poly(diallyldimethylammonium chloride) (PDDA), a linear positively charged polyelectrolyte, was used to non-covalently functionalize graphene sheets. These nanosheets were then further decorated with Pd nanoparticles (NPs) to increase the surface area of the graphene. An electrochemical sensor for chlorophenols was constructed based on this nanocomposite. Its electrocatalytic activity with respect to oxidation of chlorophenol was high (Table 2).

For increasing detectability of the chemosensor for bisphenol A, another procedure of GO doping with nitrogen was developed. It involved chemical reduction of graphene using hydrazine and ammonia as reducing agents [49]. Structure and surface chemistry of the resulting sheets of modified graphene strongly depended on the hydrothermal temperature. That is, for up to 5% nitrogen-doped, slightly wrinkled graphene sheets were obtained at 80°C. The response signal towards bisphenol A at this NG modified GCE was remarkably enhanced (Table 2).

In its hydrophobic molecular cavity, the β-cyclodextrin (β-CD) host compound can highly pre-concentrate different hydrophobic guest compounds. In two

Table 2 Analytical parameters of graphene-based electrochemical sensors for common toxins

Analyte	Transduction method	Electrode material	Linear dynamic concentration range	LOD	References
2-Chlorophenol	DPV	GCE/CR-GO-PDDA-IL-PdNPs-Nafion	4–800 μM	1.5 μM	[48]
Bisphenol A	Chronoamperometry at 0.54 V vs. SCE	GCE/NG-chitosan	10 nM–1.3 μM	5 nM	[49]
2-Nitrophenol	CV	GCE/CR-GO-hydroxypropyl-β-CD	50 nM–0.1 mM	10 nM	[50]
Microcystin-LR	Chronoamperometry at −0.4 V vs. Ag/AgCl	GCE/TR-GO-MC-LR-Ab_1-PtRu NPs-Ab_2	0.01–28 ng mL^{-1}	9.6 pg mL^{-1}	[52]
DMMP	Conductance	ChemFET/CR-GO	–	5 ng mL^{-1}	[59]

DMMP Dimethylmethylphosphonate

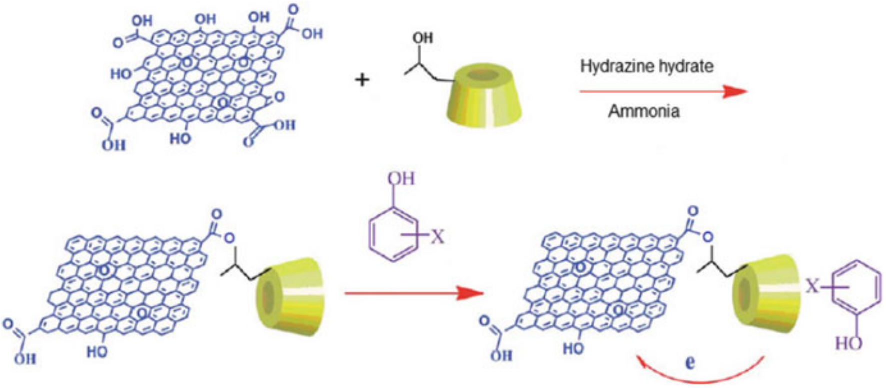

Scheme 4 Sketch of the procedure of covalent modification of CR-GO with the CD host for preconcentration of the nitrophenol analyte guests. Adapted from [50]

different studies, graphene was covalently (Scheme 4) [50] and non-covalently [51] modified with β-CD for determination of a nitrophenol pollutant and pesticide. Advantageously, neither of these modifications affected conductivity of the graphene sheets (Tables 2 and 3).

Electrochemical immunosensors are widely used as bioanalytical tools featuring the possibility of mass production, cost-effectiveness, feasible miniaturization, and, hence, portability. Among different types of immunosensors, a sandwich-type immunosensor is very common. In this immunosensor, generally, an immobilized antigen selectively binds to its corresponding antibody, Ab_1. Then this Ab_1 reacts with a secondary antibody, Ab_2, which labels a probe, such as enzymes, fluorescent dyes, and NPs. Stable immobilization of Ab_1 on an electrode surface is a prerequisite for devising reliable immunosensors. It means that these biosensors totally rely on the rate of reaction between the immobilized antibodies and substrates. Hence, they are inherently sensitive to factors that influence activity of the antibody. In addition, a limited stability of the immobilized Ab_1 can restrict the shelf life of the immunosensor. Therefore, an alternative enzyme-less immunosensor was fabricated (Scheme 5) using a graphene platform combined with the mesoporous Pt-Ru alloy for sensitive determination of microcystin-LR (MC-LR) [52]. MC-LR is the most toxic among cyclic heptapeptide hepatotoxins produced by freshwater species of cyanobacteria. Contamination with MC-LR and other microcystins is among the main causes of water pollution and outbreaks of mass biological poisoning. To construct an immunosensor, a primary antibody of MC-LR (Ab_1) was first immobilized on the GO sheets through amidation of the carboxy groups of GO and the available amine groups of Ab_1. A mesoporous Pt-Ru alloy was employed as a label of immobilization of the secondary antibody (Ab_2). The resulting (Pt-Ru)-Ab_2 was used as the label for immunosensing of MC-LR (Table 2).

Chemical weapons are classified according to their mechanism of action on humans. For instance, sarin and *O*-ethyl *S*-[2-(diisopropylamino)ethyl]

Table 3 Analytical parameters of graphene-based electrochemical sensors for pesticides

Analyte	Transduction method	Electrode material	Linear dynamic concentration range	LOD	References
Carbendazim	DPV	GCE/GO-β-CD	5–450 nM	2 nM	[51]
Chloropyrifos	Chronoamperometry at 0.06 V vs. SCE	GCE/GO-PtNPs-Cysteamine-Tyrosinase	0.25–10 ng mL^{-1}	0.2 ng mL^{-1}	[65]
Profenofos			1–10 ng mL^{-1}	0.8 ng mL^{-1}	
Malathion			5–30 ng mL^{-1}	3 ng mL^{-1}	
Paraoxon	Chronoamperometry at 0.4 V vs. Ag/AgCl	GCE/CR-GO-AuNPs-PDDA-AChE	0.1 pM–5 nM	0.1 pM	[66]
Paraoxon	Chronoamperometry at 0.85 V vs. Ag/AgCl	GCE/CR-GO-AuNPs-GBP-OPH	2–20 μM	95 nM	[68]
Monocrotophos	SWV	SPE/CR-GO-Prussian blue-Chitosan-AChE	1–600 ng mL^{-1}	0.1 ng mL^{-1}	[70]
Chloropyrifos	Chronoamperometry at 0.7 V vs. SCE	GCE/CR-GO-AuNPs-Cysteamine-CPBA-AChE	0.5–100 ng mL^{-1}	0.1 ng mL^{-1}	[71]
Malathion			0.5–100 ng mL^{-1}	0.5 ng mL^{-1}	
Carbofuran			0.1–100 ng mL^{-1}	0.05 ng mL^{-1}	
Isoprocarb					
Carbaryl	Chronoamperometry at 0.7 V vs. SCE	GCE/CR-GO-TiO_2-AChE	1 ng mL^{-1}–2 μg mL^{-1}	0.3 ng mL^{-1}	[72]
Methyl parathion	DPV	GCE/ER-GO-β-CD	0.3–500 ng mL^{-1}	0.05 ng mL^{-1}	[73]
Methyl parathion	SWV	GCE/GO-Chitosan-AuNPs	1–1,000 ng mL^{-1}	0.6 ng mL^{-1}	[67]
Paraoxon	Chronoamperometry at 0.85 V vs. Ag/AgCl	CR-GO-Nafion-OPH	Up to 20 μM	0.13 μM	[74]

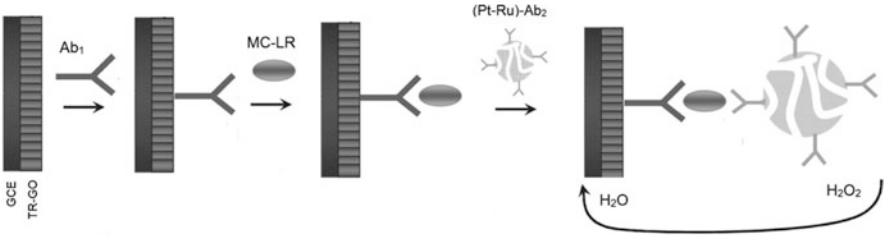

Scheme 5 The procedure of preparation of the microcystin-LR (MC-LR) immunosensor. (Pt-Ru)-Ab_2 stands for a particle of the Pt–Ru alloy with a second antibody, Ab_2, immobilized. Adapted from [52]

methylphosphonothioate (VX) are nerve agents. Among them, many toxic chemicals, including organophosphorus compounds – typical members of the nerve agent family, are considered to be one of the most toxic groups of warfare agents. In view of high sarin toxicity, dimethyl methylphosphonate (DMMP) is widely used in laboratory studies as its substitute because of similar chemical structure but much lower toxicity.

Toxin detection at a molecular level was attained with the carbon-based nanomaterials because every atom in these materials is a surface atom. Therefore, electron transport through these materials is highly sensitive to the presence of the adsorbed molecules. Based on this phenomenon, sorption-based sensors capable of detecting trace levels of toxic vapors using conventional low-power electronics have recently been fabricated. To date, the most successful effort in this direction involves chemosensors built with the use of SWCNTs where the mechanism of transduction of a recognition signal is based upon the conductance, resistance, or capacitance change [53–58]. Apparently, molecular interactions of the analyte with defect sites of the SWCNT sidewalls dominate the electrical response. This is because interactions of an analyte molecule with an sp^2-hybridized carbon atom site of SWCNT dramatically differ from those with a high-energy defect site. Therefore, detectability and selectivity of the chemosensor could be increased by a controllable increase of the defect density. Toward this end, a GO sheet decorated with the oxygen functional groups and defects were used to replace CNTs. For that, a resistance-based chemFET detection system using CR-GO was devised for determination of DMMP [59]. It was possible to control the resistance response of this system by suitably adjusting the reduction of GO. Moreover, time of exposure to hydrazine hydrate for reduction of GO and film thickness were controlled to optimize the low-frequency noise. These optimizations helped to detect DMMP at concentration as low as 5 ppb (Table 2).

Another study compared electrochemical performance of the GO, CR-GO, and GCE in determination of ractopamine and clenbuterol [60]. Both these compounds are illegally used as nutrient repartitioning agents. The differential pulse voltammetry (DPV) signals of ractopamine and clenbuterol at the GO modified GCE were much higher than those at the CR-GO modified GCE, or bare GCE. Moreover, the GO modified GCE showed separate oxidation signals for each analyte.

3.3 Determination of Pesticides

In analytical procedures of pesticide determination involving biosensors, different enzymes are used. The use of enzymes significantly amplifies detection signals. In these procedures, interaction of a pesticide with an immobilized enzyme inhibits the enzyme's specific activity towards its substrate to the extent depending on the pesticide type and concentration. For instance, acetylcholinesterase (AChE) [61], organophosphorus hydrolase (OPH) [62, 63], and tyrosinase [64] in particular, are widely used for determination of organophosphorus pesticides (OPPs) [17]. Enzymatic activity can be determined using different transduction techniques, including voltammetry, chronoamperometry, and potentiometry [17]. For devising a well functioning enzymatic biosensor, proper enzyme immobilization is critical. This is because the enzyme must remain active after the immobilization in order to catalyze transformation of the substrate efficiently. To this end, much effort has been paid to develop strategies of stable and functional enzyme immobilization onto different conducting solid supports. These include physical and/or chemical attachment, entrapment, and cross-linking. Moreover, a transducer on the surface of which the enzyme is to be immobilized should carefully be selected. That is, it has to allow for the fast charge transfer to ensure a rapid and sensitive response.

Graphene can be used as a conducting transducer support for electrochemical deposition of metal NPs. Metal NPs can readily be electrochemically deposited on defects of graphene sheets because of preferred nucleation of the NPs at vacancies along the edges of intact, nanometer-sized graphene sheets. The electrochemical route for synthesis of catalytic NPs is very attractive because they nucleate at electroactive sites of graphene sheets. Moreover, the 2-D structure of graphene affords a vast platform for loading various noble metal NPs. There are several excellent examples of application of graphene decorated with catalytic metal NPs for electrochemical determination of pesticides [65, 66]. For instance, platinum nanoparticles (PtNPs) were integrated with graphene for preparation of a biosensor for pesticides [65]. Electrostatic interactions between the tyrosinase molecules and a positively charged cysteamine self-assembled monolayer (SAM), pre-deposited on the surface of PtNPs, helped to immobilize this enzyme. Under optimum conditions, chronoamperometric response of this biosensor reached 95% of the steady-state current within less than 10 s, indicating fast electron transfer (Table 3). This fast response was attributed to the ability of graphene and PtNPs to increase the electron transfer rate.

Moreover, in addition to electrochemical deposition of NPs on graphene [67], other methods, such as preparation of a composite of NPs with a polyelectrolyte, was used to fabricate a chemosensor for OPP [66]. For that, CR-GO was decorated with gold nanoparticles (AuNPs) through a long-chain polyelectrolyte, such as PDDA. The polyelectrolyte presence prevented aggregation of NPs. Additionally, PDDA played the role of a linker for enzyme immobilization on the AuNPs–CR-GO composite. This combination significantly enhanced the enzyme loading and activity (Table 3).

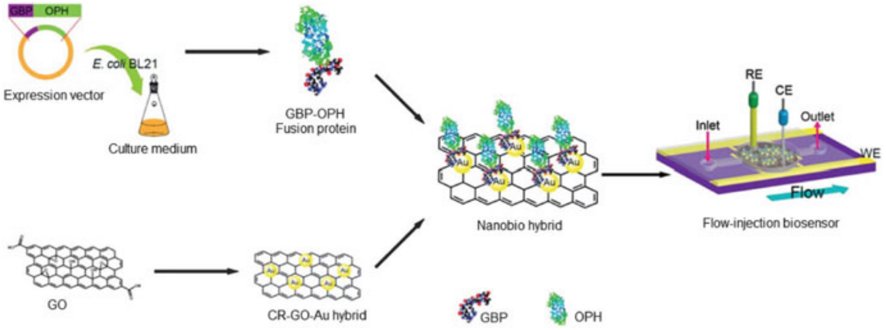

Scheme 6 Sketch of the procedure of fabrication of the GBP-OPH/Au-GO flow-injection analysis biosensor. *GBP* gold binding polypeptide, *OPH* organophosphorus hydrolase. Adapted from [68]

Furthermore, another approach to immobilization of an enzyme on AuNPs was quite recently proposed (Scheme 6) [68]. For that, a fusion protein was constructed by genetically fusing gold binding polypeptides (GBPs) to the OPH enzyme for its effective immobilization. The resulting GBP-OPH was self-immobilized directly to AuNPs immobilized onto the graphene surface via the GBP part. The OPH triggers enzymatic hydrolysis of pesticides and releases an electrooxidation product, whose anodic current response corresponds to the pesticide concentration (Table 3).

Prussian blue (PB) materials have been used extensively to fabricate biosensors for H_2O_2 and glucose determination because of their high electrocatalytic activity [69]. This property was exploited to prepare an AChE biosensor for determination of OPPs by using a nanocomposite of PB nanocubes and CR-GO [70]. Introduction of PB to the graphene matrix improved the electronic and ionic transport capability as well as electron self exchange within the matrix. Moreover, CR-GO presence in the nanocomposite increased both the electronic and potassium ion transport capability, resulting in the enhancement of the electrocatalytic activity (Table 3).

Boronic acid chemistry has been widely used to capture selectively and separate *cis*-diol containing biomolecules, such as glycoproteins. Because AChE is a glycoprotein, this chemistry was exploited to immobilize AChE on an electrode surface to fabricate a chronoamperometric biosensor for determination of the OP and carbamate pesticides (Scheme 7) [71]. For that, a GCE surface was modified consecutively with TR-GO and AuNPs. Then a cysteamine layer was immobilized on the AuNPs by self-assembly. Subsequently, a film was drop coated from a 3-carboxyphenylboronic acid (CPBA) solution containing *N*-(3-dimethylaminopropyl)-*N*′-ethylcarbodiimide (EDC) and *N*-hydroxysuccinimide (NHS). The carboxy groups of CPBA were activated by EDC and NHS to form reactive NHS esters. These esters were then reacted with amine groups of cysteamine to form covalent bonds. Next, the outermost exposed boronic acid groups served to immobilize AChE for final preparation of the biosensor (Table 3). However, this biosensor strongly suffered from low selectivity because both the OP and carbamate pesticides inhibit the AChE activity.

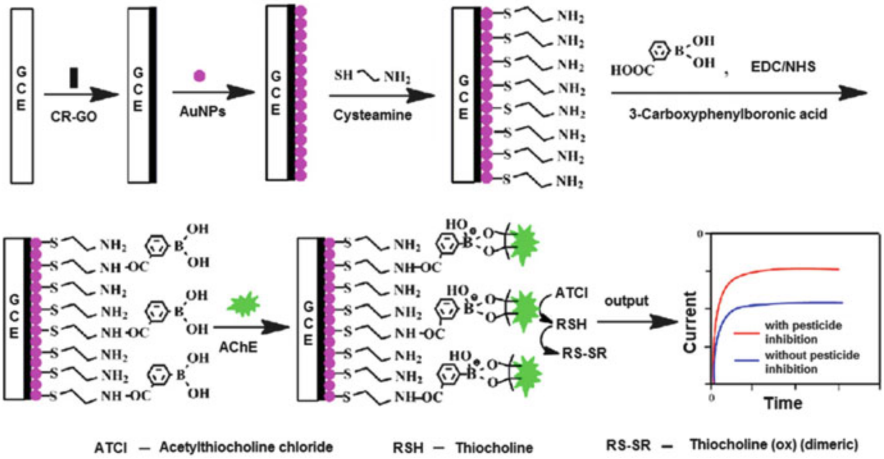

Scheme 7 Illustration of the procedure of fabrication of the GCE/CR-GO-AuNPs-cysteamine-CPBA-AChE biosensor. Adapted from [71]

Recently another metal oxide NP, namely TiO_2 [72], has been introduced into graphene to increase detectability of the biosensors fabricated. That was because the resulting nanocomposite films synergistically enhanced the detectability (Table 3).

Undoubtedly the enzyme-based biosensors are advantageously specific but their operational conditions are mostly limited by random orientation, uncontrolled conformation, and easy denaturation of the enzyme molecules. To overcome these deficiencies, various catalytic non-enzymatic graphene-based chemosensors were devised for the OP determination (Table 3) [51, 67, 73].

Flexible electrodes are expected to play an important role in portable electronic devices. To that end, free-standing conducting polymer films were doped with graphene for determination of OPP [74]. A (CR-GO)–Nafion® composite film was prepared by self-assembly (Scheme 8). The hydrophobic backbone of Nafion® provided a well-defined integrated structure on both the micro- and macroscale for fabrication of hybrid materials. Moreover, hydrophilic sulfonate groups of Nafion® enabled high (~0.5 mg mL^{-1}) and stable dispersion and long-term stability (up to 2 months) of a graphene suspension. The geometrically interlocked morphology of the (CR-GO)–Nafion® composite was highly integrated mechanically in the hybrid films while interpenetrating the CR-GO and Nafion® networks offered favorable conduction pathways for the charge transport. Importantly, this synergistic electrochemical characteristic of the (CR-GO)–Nafion® composite resulted in high conductivity (1,176 S m^{-1}), fast electron transfer, and low interfacial resistance of the composite. Consequently, the (CR-GO)–Nafion® composite reached an impressive LOD of OPP (Table 3).

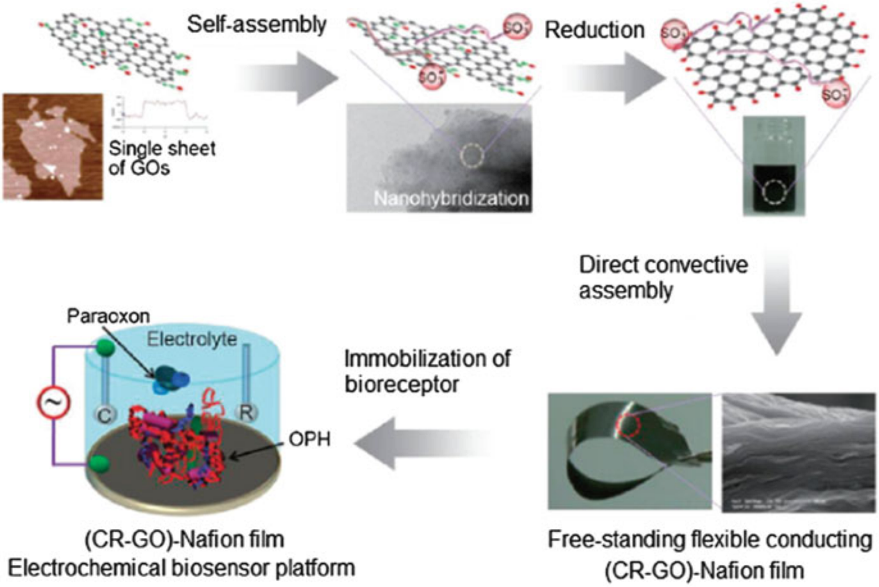

Scheme 8 Illustration of the procedure of preparation of the free-standing GO-Nafion® composite film. Adapted from [74]

3.4 Determination of Biomarkers

The use of graphene in FET-based sensors is becoming increasingly popular. Electrical properties of graphene are sensitive to its surface conditions. Based on this feature, several gas sensors using graphene field-effect transistors (GFETs) were fabricated. Moreover, this approach was recently applied for preparation of sensing devices for different biomarkers. A biomarker, i.e., biological marker, is in general a substance used as an indicator of a state of a biological system. Characteristically, it is objectively determined as an indicator of advances in normal or pathogenic biological processes or pharmacologic responses to a therapeutic treatment. Similarly to adsorption of gas molecules, adsorption of biomacromolecules on a graphene sheet results in a change of the graphene electronic properties, such as conductance and resistance. This change was used to determine concentration or quantity of a biomarker. Adjustable chemistry of a 2-D surface of graphene provided strong interface for adsorption of the biomacromolecule systems without any geometric restrictions and without compromising integrity of attachment of the biomacromolecules. To fabricate these GFET-based sensors, however, it is important to investigate changes of electronic properties of graphene under low electrical field to avoid oxidation of the biomolecules. GFETs were attempted to apply for biomacromolecule sensing by measuring the resistance or conductance change, or the drain current [75, 76].

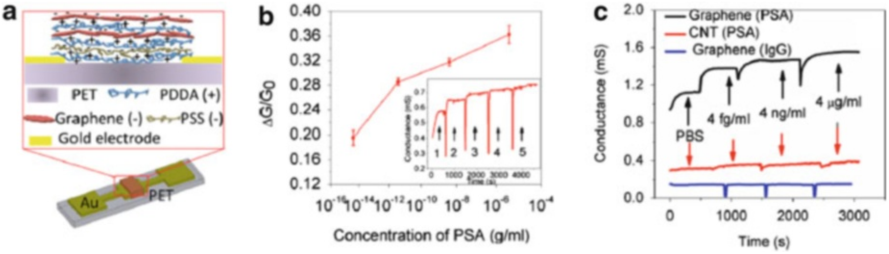

Scheme 9 (**a**) Illustration of layer-by-layer (LbL) self-assembly of graphene on surface of the gate of FET using polyelectrolytes. (**b**) Dependence of normalized conductance on concentration of PSA of a label-free graphene biosensor. *Inset*: the conductance vs time plot constructed for consecutive delivery of PSA of the following concentrations: (*1*) no PSA, (*2*) 4 fg mL^{-1}, (*3*) 4 pg mL^{-1}, (*4*) 4 ng mL^{-1}, and (*5*) 4 μg mL^{-1}. (**c**) Comparative and specificity measurements at the graphene and CNT chemFET. Adapted from [77]

Among others, a self-assembly approach was utilized for preparation of a label-free FET chemosensor for the PSA cancer biomarker [77]. For that, graphene was immobilized on the gate surface of FET using PDDA and the polystyrene sulfonate polyelectrolytes (Scheme 9). The concentration range of the PSA determination was relatively wide with this chemosensor. Advantageously, detectability of this chemosensor was higher than that of a similar CNT-based chemosensor, proving superiority of graphene over CNT for sensing applications (Table 4).

Favorably, the above GFETs are non-labeled sensing devices. However, their selectivity is low. For selectivity improvement, appropriate antibodies were immobilized on surface of gates of GFETs. But direct adsorption of any protein onto the GO surface is labile; the attached proteins can readily be removed just through washing – a common step in biosensor conditioning. This instability introduces low reproducibility of the device. To overcome this drawback, in one approach a graphene surface was decorated with AuNPs for stable protein immobilization [78]. For that, first, the TR-GO sheet was suspended above the gate surface. Next, anti-immunoglobulin-G (anti-IgG) was anchored to the TR-GO surface through AuNPs and this combined system functioned as a specific receptor for the IgG binding. This and other bindings were investigated by direct current (dc) measurements.

Moreover, a quite different strategy was adopted to increase detectability of a chemFET. In this strategy, the surface-to-volume ratio of the sensing film was increased. For that, GO-encapsulated silica nanoparticles were immobilized on the surface of the gate of FET, instead of metal NPs, for determination of the biomarker proteins for breast cancer [79]. This high surface-to-volume ratio of the GO-encapsulated NPs generated electrical surfaces that significantly increased LODs (Table 4).

In order to meet an increasing demand for ultrasensitive detection of cancer biomarkers, other different transduction techniques were implemented [80–82]. In one report, graphene decorated with (Fe_2O_3)NPs was used as a carrier to load a

Table 4 Analytical parameter of graphene-based electrochemical sensors for biomarkers

Biomarker	Transduction method	Electrode material	Linear dynamic concentration range	LOD	References
PSA	Conductance	ChemFET/G-PSS-PDDA	4 fg mL^{-1}–4 μg mL^{-1}	4 fg mL^{-1}	[77]
			0.4 pg mL^{-1}–4 μg mL^{-1}	0.4 pg mL^{-1}	
HER2	Conductance	ChemFET/Monoclonal Ab against HER2 or EGFR-CR-GO-SiNPs	1 pM–1 μM	1 pM	[79]
EGFR			100 pM–1 μM	100 pM	
PSA	Resistance	Polycarbonate film-GO-Ab PSA	0.1–1,000 ng mL^{-1}	0.08 ng mL^{-1}	[80]
CEA	DPV	GCE/CR-GO-Thionine-AuNPs-CEA Ab	10–500 pg mL^{-1}	4 pg mL^{-1}	[81]
PSA	SWV	GCE/GO-Ab$_1$-PSA-DA-F_3O_4-FCA-Ab$_2$	0.01–40 ng mL^{-1}	2 pg mL^{-1}	[82]

PSA prostate specific antigen, *CEA* carcinoembryonic antigen, *HER2* human epidermal growth factor receptor 2, *EGFR* epidermal growth factor receptor, *DA* dopamine, *FCA* Ferrocenecarboxylic acid

Table 5 Analytical parameters of graphene-based electrochemical sensors for pathogens

Pathogen	Transduction method	Electrode material	Linear dynamic concentration range	LOD	References
Rotavirus	Fluorescence	GO-EDC-SulfoNHS-Ab	11,000–10^5 pfu mL^{-1}	–	[83]
Sulfur reducing bacteria	Impedance	GCE/ER-GO-Chitosan-SRB Ab	10–10^7 cfu mL^{-1}	10 cfu mL^{-1}	[85]
E. coli	Conductance	ChemFET/GO-1-pyrenebutanoic acid succinimidyl ester-*E. coli* Ab	10–10^5 cfu mL^{-1}	10 cfu mL^{-1}	[86]

large amount of an electroactive compound, such as ferrocenecarboxylic acid (FCA) [82]. FCA accumulation helped to immobilize Ab_2 better, which in turn increased immunosensor detectability with respect to the PSA biomarker (Table 4).

3.5 Determination of Whole Cells

As described in Sect. 3.4, graphene provides a highly developed surface for adsorption of biomacromolecular systems. Hence, a large contact area of the solution–graphene interface available for adsorption of microbes and mammalian cells enabled the fabrication of sensing devices for pathogens [83], bacteria [84–86], and even infected red blood cells (Table 5) [87].

Microscale areas, sensitive to electrical properties incurred by surface modification, including modifiable chemical functionalization, make graphene nanostructures excellent candidates for devising sensing biodevices. For instance, attachment of a single bacterium generated ~1,400 charge carriers in a p-type graphene of a graphene-based single-bacterium sensing biodevice [84]. Although this proof-of-concept study demonstrated an impressive ability of GFET to detect a single bacterium, this sensing device was not specific because its detection signal relied on non-specific electrostatic adhesion of bacteria without discrimination with respect to the bacteria species. Therefore, an anti-*Escherichia coli* antibody-modified graphene was immobilized on the gate surface of FET to prepare a specific biosensor for *E. coli* (Scheme 10) [86]. The biosensor prepared that way did not respond to other different bacteria species, e.g., *Pseudomonas aeruginosa*, indicating specificity to *E. coli* (Table 5).

With a very similar approach, an impedimetric biosensor for determination of pathogenic sulfate reducing bacteria was devised. To afford high selectivity, appropriate antibody was immobilized on the surface of the electrodeposited composite of chitosan and graphene (Table 5) [85].

4 Conclusions and Perspectives

Integration of the graphene or graphene derivative matrices as recognition units with different transduction platforms triggered the burst of fabrication of sensing systems with high detectability and selectivity. That was possible because of high effective surface area, facile mass transport, and effective electrocatalytic properties of the graphene materials. However, pristine graphene is difficult to process because of its intrinsic insolubility. This drawback was circumvented by both its covalent and noncovalent derivatization. Through chemical reduction of GO or thermal treatment, graphene was covalently functionalized. This derivatization resulted in much higher dispersibility of the resulting material in both water and organic solvents. Moreover, some small molecules [43, 50] and polymers [48]

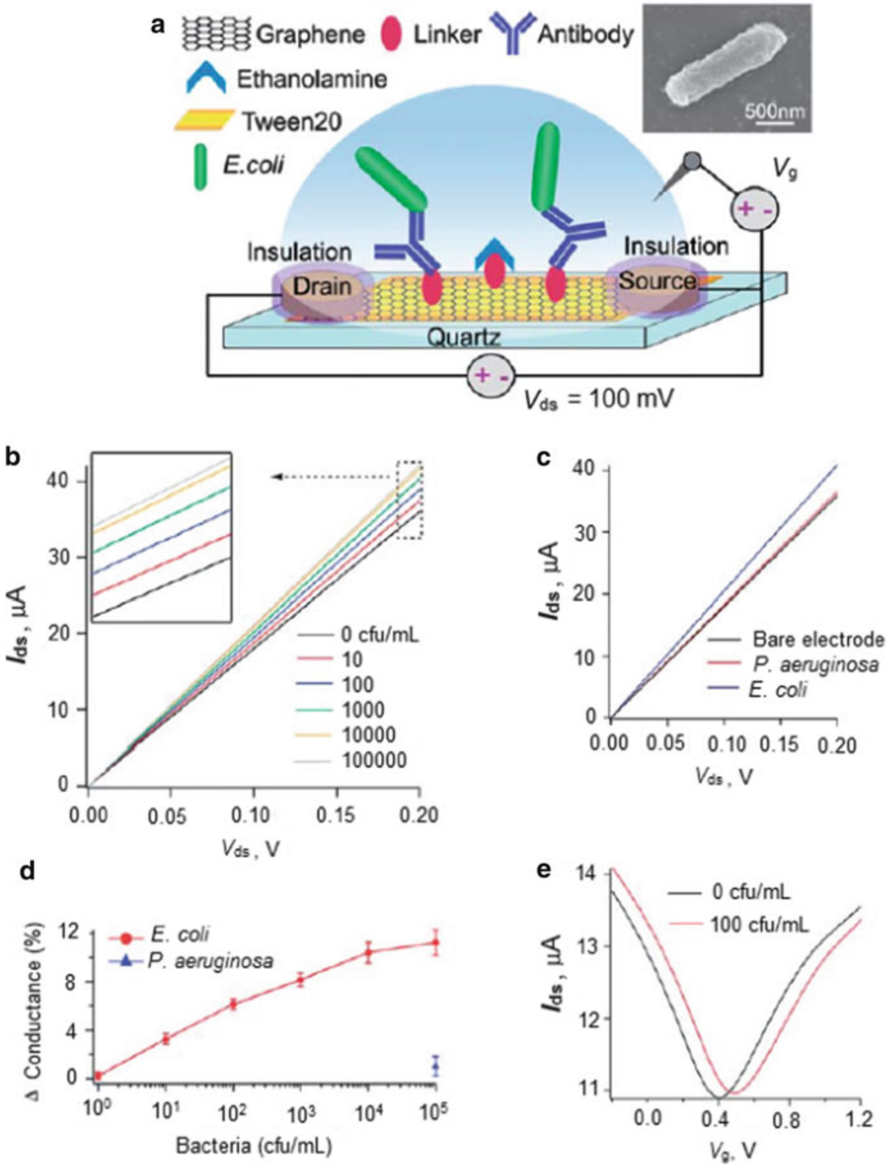

Scheme 10 (**a**) Sketch of anti-*E. coli* antibody functionalization of GFET for determination of *E. coli*. (**b**) I_{ds} vs V_{ds} curves for the anti-*E. coli* antibody functionalized graphene device after incubation with *E. coli* of different concentrations, $V_g = 0$ V. (**c**) I_{ds} vs V_{ds} curves for the antibody functionalized graphene device before and after incubation of *P. aeruginosa* and *E. coli* (both 10^5 cfu mL^{-1}). $V_g = 0$ V. (**d**) Percentage change of graphene conductance caused by *P. aeruginosa* (*triangles*) and *E. coli* (*circles*) of different concentrations. (**e**) Transfer curves of the antibody functionalized GFET before and after incubation with *E. coli* (100 cfu mL^{-1}). I_{ds} drain source current, V_g solution-gate voltage, V_{ds} drain-source voltage. Adapted from [86]

were introduced onto the graphene surface. This graphene decoration resulted in its much higher dispersibility in different solvents. Furthermore, graphene was non-covalently functionalized by van der Waals forces or π-stacking.

Generally, non-covalent functionalization has little effect on the original properties of graphene. Mostly biopolymers, such as chitosan, and β-CD were used for non-covalent derivatization of graphene [51, 88]. They adsorb on graphene by hydrophobic interactions and π-stacking.

Electrochemical reduction is effective in depositing metal NPs directly on graphene. Because these NPs nucleate and grow on the graphene conducting surface during electrolysis, this procedure affords smooth conducting communication between the graphene and the NPs. However, the electrolysis must be carefully controlled for preparation of the graphene–(metal NPs) composites of high size uniformity and density of NPs. Surprisingly, this direction of modification of graphene with NPs is not much explored [67]. Instead, another approach to assemble metal NPs on graphene appeared to be more attractive [66, 81, 89]. In this approach, NPs are chemically reduced in the presence of graphene sheets with no linking molecules being involved. Moreover, the GO sheets with high surface area and abundance of functional groups, such as carboxy, keto, hydroxy, and epoxide group, facilitated nucleation of the metal NPs. Although the graphene-based 2-D surface enables even distribution of NPs on an individual sheet, the graphene–NPs hybrid sheets are randomly stacked if used for electrode modification. This stacking inevitably leads to aggregation of these sheets. Therefore graphene-encapsulated (metal oxide)NPs have been produced to decrease further aggregation of graphene sheets [79].

Pristine graphene behaves like a zero-band-gap semiconductor. In this direction, doping appeared to be a powerful route to tailor its electronic properties. The heteroatom doping on the graphene edge served this purpose effectively. For that, mostly, the nitrogen heteroatom was used.

Because of this zero-band gap semiconductor nature and surface tunability, graphene appeared to be a primary candidate for devising different chemFET-based sensing systems. Combination of the chemFET transduction with the graphene-based recognition results in highly sensitive chemo- and biosensors for different analytes including biomolecules, biomarker proteins, and various strains of bacteria (Tables 1, 2, 3, 4, and 5). Moreover, analyte determination at a molecular level is possible [84]. Furthermore, selectivity of the chemFET sensing systems was improved by graphene functionalization with specific receptors, like antibodies.

As outlined in this chapter, integration of graphene or nanomaterials-based graphene derivatives with transducer surface has prompted rapid development of electrochemical sensors for toxins, explosives, pesticides, pathogens, and even microbes (Tables 1, 2, 3, 4, and 5). Additionally, an integration of metal NPs or polymers and graphene improved performance of these sensors. Besides, biocompatibility of graphene provided a suitable surface for immobilization of biomolecules.

Still, the design and synthesis of new carbon allotropes with well defined structures and properties is a significant and ongoing challenge within the new materials science and technology and there is a large number of new forms of

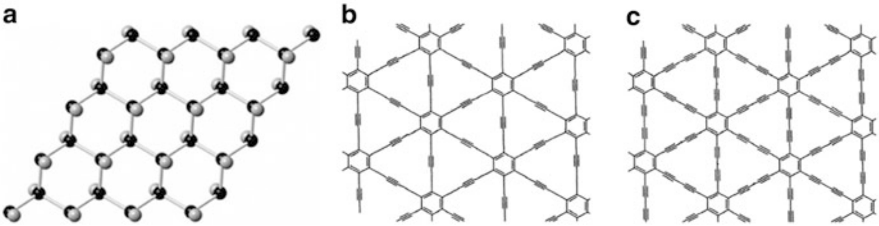

Scheme 11 Different allotropes of graphene: (**a**) graphane, (**b**) graphyene, and (**c**) graphdiyne

graphene to be discovered [90]. Recently, three allotropes of graphene were proposed, namely graphane (Scheme 11a) [91, 92], graphyene (Scheme 11b) [93–95], and graphdiyne (Scheme 11c) [96–99]. The latter, with its unique structure, was predicted to be the most stable among diacetylenic synthetic carbon allotropes [96]. These allotropes are expected to be semiconductors [91, 96]. Because of their structure and low dimensionality, they can provide a fertile playground for fundamental research and technological applications.

In conclusion, graphene and its derivatives are highly advantageous for determination of biocompounds. However, their sensing superiority over CNTs is still not much emphasized. In fact, very few reports provide graphene vs CNT comparative studies. Therefore much work is needed in this direction. Undoubtedly, the cost-effective syntheses and purification procedures for these nanostructured materials will further increase possibilities of their applicability for fabrication of chemosensors in general and electrochemical sensors in particular.

Acknowledgements PSS and WK thank the European Regional Development Fund (Project ERDF (POIG.01.01.02-00-008/08 2007–2013)). The work of WK was partially realized within the International PhD projects Program of the Foundation for Polish Science (MPD/2009/1/styp19) co-financed from European Regional Development Fund within Innovative Economy Operational Program “Grant for innovation”. FD thanks the US National Science Foundation for their financial support.

References

1. Novoselov KS, Geim AK, Morozov SV, Jiang D, Zhang Y, Dubonos SV, Grigorieva IV, Firsov AA (2004) Science 306:666
2. Chen D, Tanga L, Li J (2010) Chem Soc Rev 39:3157
3. Liu Y, Dong X, Chen P (2012) Chem Soc Rev 41:2283
4. Yao J, Sun Y, Yang M, Duan Y (2012) J Mater Chem 22:14313
5. Guo S, Dong S (2011) J Mater Chem 21:18503
6. Ratinac KR, Yang W, Gooding JJ, Thordarson P, Braeta F (2011) Electroanalysis 23:803
7. Shao Y, Wang J, Wu H, Liu J, Aksay IA, Lin Y (2010) Electroanalysis 22:1027
8. Pumera M (2011) Mater Today 14:308
9. Du A, Zhu Z, Smith SC (2010) J Am Chem Soc 132:2876
10. Chen H-Y, Appenzeller J (2012) Nano Lett 12:2067

11. Wu Y, Jenkins KA, Valdes-Garcia A, Farmer DB, Zhu Y, Bol AA, Dimitrakopoulos C, Zhu W, Xia F, Avouris P, Lin Y-M (2012) Nano Lett 12:3062
12. Dai L (2013) Acc Chem Res. 46:31
13. Hou J, Shao Y, Ellis MW, Moored RB, Yie B (2011) Phys Chem Chem Phys 13:15384
14. Huang C-K, Ou Y, Bie Y, Zhao Q, Yu D (2011) Appl Phys Lett 98:263104
15. Lee SW, Lee SS, Yang E-H (2009) Nanoscale Res Lett 4:1218
16. Wassei JK, Kaner RB (2010) Mater Today 13:52
17. Sharma PS, D'Souza F, Kutner W (2012) In: D'Souza F, Kadish KM (eds) Handbook of carbon nano materials, vol 3. Singapore, World Scientific, Chapter 5
18. Sherigara BS, Kutner W, D'Souza F (2003) Electroanalysis 15:753
19. Jacobs CB, Peairs MJ, Venton BJ (2010) Anal Chim Acta 662:105
20. Yang W, Ratinac KR, Ringer SP, Thordarson P, Gooding JJ, Braet F (2010) Angew Chem Int Ed 49:2114
21. Wang J, Yang S, Guo D, Yu P, Li D, Ye J, Mao L (2009) Electrochem Commun 11:1892
22. Alwarappan S, Boyapalle S, Kumar A, Li C-Z, Mohapatra S (2012) J Phys Chem C 116:6556
23. Hummers WS, Offeman RE (1958) J Am Chem Soc 80:1339
24. Mattevi C, Kima H, Chhowalla M (2011) J Mater Chem 21:3324
25. Kosynkin DV, Higginbotham AL, Sinitskii A, Lomeda JR, Dimiev A, Price BK, Tour JM (2009) Nat Lett 458:872
26. Rangel NL, Sotelo JC, Seminario JM (2009) J Chem Phys 131:031105
27. Poh HL, Sanek F, Ambrosi A, Zhao G, Sofer Z, Pumera M (2012) Nanoscale 4:3515
28. Ambrosi A, Bonanni A, Sofer Z, Cross JS, Pumera M (2011) Chem Eur J 17:10763
29. Dikin DA, Stankovich S, Zimney EJ, Piner RD, Dommett GHB, Evmenenko G, Nguyen ST, Ruoff RS (2007) Nature 448:457
30. Chen D, Feng H, Li J (2012) Chem Rev 112:6027
31. Georgakilas V, Otyepka M, Bourlinos AB, Chandra V, Kim N, Kemp KC, Hobza P, Zboril R, Kim KS (2012) Chem Rev 112:6156
32. Dreyer DR, Park S, Bielawski CW, Ruoff RS (2010) Chem Soc Rev 39:228
33. Su Q, Pang S, Alijani V, Li C, Feng X, Mullen K (2009) Adv Mater 21:3191
34. Kaminska I, Das MR, Coffinier Y, Niedziolka-Jonsson J, Woisel P, Opallo M, Szunerits S, Boukherroub R (2012) Chem Commun 48:1221
35. Lomeda JR, Doyle CD, Kosynkin DV, Hwang W-F, Tour JM (2008) J Am Chem Soc 130:16201
36. Sun Y, Wu Q, Shi G (2011) Energy Environ Sci 4:1113
37. Pumera M (2011) Energy Environ Sci 4:668
38. Brownson DAC, Kampouris DK, Banks CE (2011) J Power Sources 196:4873
39. Ratinac KR, Yang W, Ringer SP, Braet F (2010) Environ Sci Technol 44:1167
40. Shang NG, Papakonstantinou P, McMullan M, Chu M, Stamboulis A, Potenza A, Dhesi SS, Marchetto H (2008) Adv Funct Mater 18:3506
41. Li J, Kuang D, Feng Y, Zhang F, Xu Z, Liu M (2012) J Hazard Mater 201–202:250
42. Tang L, Feng H, Cheng J, Li J (2010) Chem Commun 46:5882
43. Guo CX, Lei Y, Li CM (2011) Electroanalysis 23:885
44. Goh MS, Pumera M (2011) Anal Bioanal Chem 399:127
45. Guo CX, Lu ZS, Lei Y, Li CM (2010) Electrochem Commun 12:1237
46. Guo S, Wen D, Zhai Y, Dong S, Wang E (2011) Biosens Bioelectron 26:3475
47. Chen T-W, Xu J-Y, Sheng Z-H, Wang K, Wang F-B, Liang T-M, Xia X-H (2012) Electrochem Commun 16:30
48. Shi J-J, Zhu J-J (2011) Electrochim Acta 56:6008
49. Fan H, Li Y, Wu D, Ma H, Mao K, Fan D, Du B, Li H, Wei Q (2012) Anal Chim Acta 711:24
50. Xu C, Wang J, Wan L, Lin J, Wang X (2011) J Mater Chem 21:10463
51. Guo Y, Guo S, Li J, Wang E, Dong S (2011) Talanta 84:60
52. Wei Q, Zhao Y, Du B, Wu D, Cai Y, Mao K, Li H, Xu C (2011) Adv Funct Mater 21:4193
53. Kim TH, Lee BY, Jaworski J, Yokoyama K, Chung WJ, Wang E, Hong S, Majumdar A, Lee SW (2011) ACS Nano 5:2824
54. Snow ES, Perkins FK, Houser EJ, Badescu SC, Reinecke TL (2005) Science 307:1942

55. Robinson JA, Snow ES, Perkins FK (2007) Sens Actuators A 135:309
56. Kong L, Wang J, Fu X, Zhong Y, Meng F, Luo T, Liu J (2010) Carbon 48:1262
57. Kuang Z, Kim SN, Crookes-Goodson WJ, Farmer BL, Naik RR (2010) ACS Nano 4:452
58. Park M, Cella LN, Chen W, Myung NV, Mulchandani A (2010) Biosens Bioelectron 26:1297
59. Robinson JT, Perkins FK, Snow ES, Wei Z, Sheehan PE (2008) Nano Lett 8:3137
60. Wu C, Sun D, Li Q, Wu K (2012) Sens Actuators B 168:178
61. Cremisini C, Sario SD, Mela J, Pilloton R, Palleschi G (1995) Anal Chim Acta 311:273
62. Mulchandani P, Chen W, Mulchandani A (2006) Anal Chim Acta 568:217
63. Karnati C, Du H, Ji HF, Xu X, Lvov Y, Mulchandani A, Mulchandani P, Chen W (2007) Biosens Bioelectron 22:2636
64. Vidal JC, Esteban S, Gil J, Castillo JR (2006) Talanta 68:791
65. Liu T, Xu M, Yin H, Ai S, Qu X, Zong S (2011) Microchim Acta 175:129
66. Wang Y, Zhang S, Du D, Shao Y, Li Z, Wang J, Engelhard MH, Li J, Lin Y (2011) J Mater Chem 21:5319
67. Gong J, Miao X, Zhou T, Zhang L (2011) Talanta 85:1344
68. Yang M, Choi BG, Park TJ, Heo NS, Hong WH, Lee SY (2011) Nanoscale 3:2950
69. Jin E, Lu X, Cui L, Chao D, Wang C (2010) Electrochim Acta 55:7230
70. Zhang L, Zhang A, Du D, Lin Y (2012) Nanoscale 4:4674
71. Liu T, Su H, Qu X, Ju P, Cui L, Ai S (2011) Sens Actuators B 160:1255
72. Wang K, Li H-N, Wu J, Ju C, Yan J-J, Liu Q, Qiu B (2011) Analyst 136:3349
73. Wu S, Lan X, Cui L, Zhang L, Tao S, Wang H, Han M, Zhiguang L, Meng C (2011) Anal Chim Acta 699:170
74. Choi BG, Park H, Park TJ, Yang MH, Kim JS, Jang S-Y, Heo NS, Lee SY, Kong J, Hong WH (2010) ACS Nano 4:2910
75. Ohno Y, Maehashi K, Yamashiro Y, Matsumoto K (2009) Nano Lett 9:3318
76. Ohno Y, Maehashi K, Matsumoto K (2010) Biosens Bioelectron 26:1727
77. Zhang B, Cui T (2011) Appl Phys Lett 98:073116
78. Mao S, Lu G, Yu K, Bo Z, Chen J (2010) Adv Mater 22:3521
79. Myung S, Solanki A, Kim C, Park J, Kim KS, Lee K-B (2011) Adv Mater 23:2221
80. Yang M, Gong S (2010) Chem Commun 46:5796
81. Kong F-Y, Xu M-T, Xu J-J, Chen H-Y (2011) Talanta 85:2620
82. Li H, Wei Q, He J, Li T, Zhao Y, Cai Y, Du B, Qian Z, Yang M (2011) Biosens Bioelectron 26:3590
83. Jung JH, Cheon DS, Liu F, Lee KB, Seo TS (2010) Angew Chem Int Ed 49:5708
84. Mohanty N, Berry V (2008) Nano Lett 8:4469
85. Wan Y, Lin Z, Zhang D, Wang Y, Hou B (2011) Biosens Bioelectron 26:1959
86. Huang Y, Dong X, Liu Y, Li L-J, Chen P (2011) J Mater Chem 21:12358
87. Ang PK, Li A, Jaiswal M, Wang Y, Hou HW, Thong JTL, Lim CT, Loh KP (2011) Nano Lett 11:5240
88. Wang L, Zhang X, Xiong H, Wang S (2010) Biosens Bioelectron 26:991
89. Zhang L, Long L, Zhang W, Du D, Lin Y (2012) Electroanalysis 24:1
90. Enyashin AN, Ivanovskii AL (2011) Phys Status Solidi B 248:1879
91. Sofo JO, Chaudhari AS, Barber GD (2007) Phys Rev Lett B 75:153401
92. Wen X-D, Yang T, Hoffmann R, Ashcroft NW, Martin RL, Rudin SP, Zhu J-X (2012) ACS Nano 6:7142
93. Cranford SW, Buehler MJ (2011) Carbon 49:4111
94. Narita N, Nagai S, Suzuki S, Nakao K (1998) Phys Rev B 58:11009
95. Peng Q, Ji W, De S (2012) Phys Chem Chem Phys 14:13385
96. Li G, Li Y, Liu H, Guo Y, Lia Y, Zhu D (2010) Chem Commun 46:3256
97. Srinivasu K, Ghosh SK (2012) J Phys Chem C 116:5951–5956
98. Zheng Q, Luo G, Liu Q, Quhe R, Zheng J, Tang K, Gao Z, Nagasec S, Lu J (2012) Nanoscale 4:3990
99. Jiao Y, Du A, Hankel M, Zhu Z, Rudolph V, Smith SC (2011) Chem Commun 47:11843

Index